

Design and Development of Particle-Loaded Ocular Microneedle Arrays Prepared Using 3D Printing

Rawan A Fitaihi

A thesis submitted in partial fulfilment of the requirements of UCL School of Pharmacy
for the degree of
Doctor of Philosophy

School of Pharmacy
University College London

2023

Declaration of Authorship

I, Rawan Fitaihi confirm that the work presented in this thesis is my own. Where information has been derived from other sources, I confirm that this has been indicated in the thesis.

Rawan Fitaihi

Abstract

Microneedle-based systems have emerged as a minimally invasive method to enhance drug delivery. While this approach has been primarily designed for transdermal uses, new applications of microneedles (MN) have recently been developed, including the delivery and localisation of therapeutic agents within ocular tissue. Ocular diseases may represent a significant challenge for drug delivery, as penetration of drugs into the ocular tissues is a major limiting factor in the treatment of vitreoretinal diseases. In this PhD project, a novel ocular drug delivery system was developed by formulating a dissolvable MN array loaded with biodegradable polylactic-glycolic acid (PLGA) particles for scleral drug deposition.

Moulds with a range of geometric features were prepared using a stereolithography 3D printer. The optimised moulds were used to prepare PVP/PVA dissolvable MN arrays loaded with PLGA particles. The mechanical strength and the insertion force were tested *ex-vivo* on porcine scleral tissue. The MN array was strong enough to penetrate scleral tissue and subsequently dissolve within the tissue.

Dexamethasone was selected in this study as a model drug to be loaded into the PLGA particles. The permeation through scleral tissue was tested; the MN arrays showed a significantly higher permeation than topically administered dexamethasone suspension. Additionally, more than 10% of the dexamethasone in the MN array was detected in the vitreous humour of excised porcine eye one hour post application.

The effect of size and surface charge on the particle's distribution diffusion in the sclera was assessed by applying fluorescent labelled micro- and nano- particles and PLGA particles. All particle types were found to diffuse within the scleral tissue. Thus, this platform can be potentially tailored to prepare a minimally invasive drug delivery system for a wide range of therapeutics. *In-vivo* studies have also been performed to evaluate ocular irritancy and assess the behaviour of the systems in endotoxin-induced

uveitis rabbit model. The *in-vivo* study demonstrated that the system has minimal irritation to rabbit eyes and could serve as a safe and effective drug delivery platform.

Impact Statement

Drug delivery to the posterior segment of the eye is challenging because of the ocular anatomical and physiological barriers. Therefore, intravitreal injection has become the standard practice for administering therapeutic agents to the back of the eye. However, the utilization of this route is limited to patient tolerance and possible complications. To combat the negative consequences, recent research has been directed to develop advanced drug-delivery systems to fulfil the demand for treating posterior eye diseases in a minimally invasive manner.

This PhD thesis presented a novel drug delivery platform comprised of a dissolving microneedle array loaded with controlled drug release carrier, i.e. PLGA particles, to investigate a self-administered and minimally invasive drug delivery platform. This system can potentially overcome ocular barriers, increase ocular bioavailability, and improve patient adherence. In addition, this PhD investigated micromould creation by a quick and affordable 3D printing process since the use of 3D printing renders pharmaceutical customisation more attainable as compared to conventional manufacturing methods.

The potential impact of this research, from an academic standpoint, includes the novelty of the platform displaying the feasibility of particle deposition using a dissolving microneedle. Although microneedle systems have been studied for decades for transdermal delivery, their ocular application has recently emerged, allowing for several relevant research opportunities. Moreover, the limited understanding of the employability of ocular dissolving microneedles, the permeability of microparticles and nanoparticle distribution within ocular tissue has not been comprehensively investigated.

The results obtained from this thesis can further validate the use of dissolving microneedles for ocular drug delivery, which may promote academic and industrial research to advance delivery platforms to reach the market.

The model drug for this research was dexamethasone. It is a glucocorticoid that is administered to treat many eye conditions via multiple routes, including intravitreal injection. Newly approved dexamethasone-containing drug delivery systems, such as ocular implants, are available in the market. Due to the intrusive application of the systems, research to develop minimally invasive alternatives demonstrates pharmaceutical impact. Over the years, pharmaceuticals has undergone a significant transition. The development of novel dosage forms is an essential element to feed the research and development (R&D) pipeline. Future medication prospects may be transformed into more therapeutically effective formulations through the R&D of novel molecular entities in combination with cutting-edge delivery systems.

Acknowledgement

First and foremost, I would like to thank God for all the blessings in my life and for giving me the strength and guidance throughout the challenging time of completing this research.

I would like to express my deepest gratitude to my supervisor Professor Duncan Craig, for accepting me to be part of his group and for always being supportive, encouraging, and patient. Thanks for all the wisdom and knowledge he shared. Without his guidance and insightful feedback, this work would not have been possible.

I would like to extend my sincere thanks to Professor Susan Barker for welcoming me and supporting me at the beginning of my studies, and I would like to thank Professor Mine Orlu for her support.

I am very blessed and lucky to be part of the great group in B15 for the good times, the waves of laughter and all the food we have shared. Their company have always made me feel like home. I would like to thank Dr Hend Abdelhakim, Ms Zoe Whiteley, Dr Shorooq Abukhamees, Ms Amal Abdulghani, Mr Antony Omita, Dr Hei Ho, Mr Se Hun, Ms Charitini Volitaki, Ms Beshair Alsaffar, Ms Scheilly Tsilova, Ms Widyan Alamoudi, Ms Nura Alharbi, Dr Maryam Parhizkar and Dr Asma Buanz for all the help and support throughout the time of my studies.

I'm also thankful to Dr Stephan Hilton for helping me in conceptualising the 3D printing part of this work and to Dr James Philips, Dr Andrew Weston, Dr Satinder Sembi, and Dr Isabel Goncalves for their help during my studies.

I'm so much grateful to Professor Aws Alshamasn for being such a great inspiration. I'm thankful for all his support and encouragement to pursue my education at UCL. I would also like to extend my thanks to his research team in the College of Pharmacy at King Saud University for their contribution to this work by conducting the animal study.

Last but not least, I would like to express my deepest gratitude to my family. My mom and my dad, I can't thank them enough for everything they have done for me; their prayer and love are what kept me going. My husband Mustafa and my daughters Ayla, Wid, and Deem, I couldn't have done it without them. Their love, patience, and support have made everything possible. I would like to thank my sisters, Samar, Reem, Rana, Zainab, and Ghalia and I would like to thank my dearest friend Ghaliah and her family for being the best companion in this journey and for always being by my side.

Table of Contents

Declaration of Authorship.....	2
Abstract	3
Impact Statement	5
Acknowledgement	7
Table of Contents.....	9
List of Figures	15
List of Tables	24
Scientific Presentation	26
Chapter 1 Introduction.....	27
1.1 General overview	28
1.2 Anatomy and physiology of the eye.....	29
1.3 Ocular delivery barriers.....	31
1.4 Routes of ocular drug delivery	32
1.4.1 Topical administration	32
1.4.2 Intravitreal injection	33
1.4.3 Periocular injection	33
1.4.4 Systemic administration	34
1.5 Recent advances in ocular drug delivery system	34
1.5.1 Intraocular Implants.....	35
1.5.2 Contact lenses	39
1.5.3 Topical inserts	39
1.5.4 Iontophoresis	40
1.5.5 Microneedle technology	40
1.6 Overview of microneedles	41
1.6.1 Types of microneedles	41
1.6.2 Methods of microneedle fabrication	42

1.6.3	Microneedles in ocular drug delivery	43
1.7	3D printing overview	45
1.7.1	3D printing in pharmaceutical applications.....	49
1.8	Polymers used for ocular drug delivery	49
1.8.1	PLGA in ocular delivery	51
1.8.2	PLGA particles fabrication methods	51
1.9	Corticosteroid overview	54
1.9.1	Dexamethasone in ocular delivery	54
1.10	Thesis aim.....	55
1.11	Thesis graphical overview	57
Chapter 2	Materials and methods	58
2.1	Materials	59
2.1.1	Poly (vinyl alcohol)	59
2.1.2	Polyvinylpyrrolidone	60
2.1.3	Poly (lactic-co-glycolic acid)	62
2.1.4	Polydimethylsiloxane	63
2.1.5	Coumarin-6	64
2.1.6	Dexamethasone	65
2.1.7	Clear resin	67
2.2	Methods	68
2.2.1	Methods of processing	68
2.2.2	Methods of characterisation and assessment.....	77
Chapter 3	Design and 3D printing of microneedle masters and reverse mould preparation 97	
3.1	Introduction.....	98
3.1.1	Aim and objectives.....	100

3.1.2	Chapter graphical overview	100
3.2	Materials	101
3.3	Methods	101
3.3.1	Design and optimisation of the MN masters.....	101
3.3.2	Printing microneedle array masters	103
3.3.3	Post-printing treatment.....	105
3.3.4	Examining of MN masters.....	105
3.3.5	3D scanning of MN masters.....	106
3.3.6	Printing accuracy.....	106
3.3.7	Reverse mould fabrication.....	106
3.3.8	Insertion depth	107
3.3.9	Statistical analysis	108
3.4	Results	108
3.4.1	CAD design and 3D printing of MN masters	108
3.4.2	MN design parameters	112
3.4.3	3D printing parameters.....	118
3.4.4	3D accuracy study	127
3.4.5	MN insertion depth.....	132
3.5	Conclusions.....	134
Chapter 4	Formulation and characterisation of PLGA particles	136
4.1	Introduction.....	137
4.1.1	Aim and objectives.....	138
4.1.2	Chapter graphical overview	139
4.2	Materials	140
4.3	Methods	141
4.3.1	Preparation and optimisation of PLGA particles	141
4.3.2	Particle size analysis.....	143

4.3.3	Surface charge measurement.....	143
4.3.4	Morphology analysis.....	144
4.3.5	Fluorescent imaging.....	144
4.3.6	Percentage of production yield	144
4.3.7	Analytical quantification of dexamethasone	145
4.3.8	Encapsulation efficiency and drug loading capacity.....	149
4.3.9	Solubility Study	149
4.3.10	<i>In-vitro dexamethasone</i> release study.....	150
4.3.11	Thermal Analysis	150
4.3.12	X-ray powder diffraction.....	150
4.3.13	Fourier transform infrared spectroscopy	151
4.3.14	Cell culture	151
4.3.15	Determination of inhibitory concentration	151
4.3.16	Cell viability assay	152
4.3.17	Cellular uptake	152
4.3.18	Statistical analysis	154
4.4	Results	155
4.4.1	Preparation and optimisation of PLGA particles	155
4.4.2	Particle size and surface charge.....	162
4.4.3	% Yield	167
4.4.4	Analytical quantification of dexamethasone	168
4.4.5	Encapsulation efficiency and drug loading capacity.....	177
4.4.6	Solubility Study	179
4.4.7	<i>In-vitro</i> release study	180
4.4.8	Differential scanning calorimetry	183
4.4.9	X-ray powder diffraction.....	185
4.4.10	Fourier transforms infrared spectroscopy.....	186
4.4.11	Cell viability assay	187
4.4.12	Cellular uptake	190

4.5	Conclusions.....	192
Chapter 5	Preparation and characterisation of microneedle arrays and <i>ex-vivo</i> studies	
	194
5.1	Introduction.....	195
5.1.1	Aim and objectives.....	196
5.1.2	Chapter graphical overview	196
5.2	Materials	197
5.3	Methods	197
5.3.1	Microneedle array preparation	197
5.3.2	Dissolution study.....	200
5.3.3	Mechanical strength testing	200
5.3.4	Preparation of ocular tissue.....	201
5.3.5	Microneedle array adhesion test.....	202
5.3.6	MN array scleral insertion test	202
5.3.7	Analytical quantification of dexamethasone in ocular tissue.....	203
5.3.8	Dexamethasone transscleral permeation.....	204
5.3.9	<i>Ex-vivo</i> transscleral particles diffusion.....	205
5.3.10	Dexamethasone ocular biodistribution	205
5.3.11	Statistical analysis	206
5.4	Results	207
5.4.1	Preparation and optimization of the dissolvable polymeric base	207
5.4.2	Preparation and characterisation of particle loaded MN arrays.....	215
5.4.3	Microneedle array scleral insertion test.....	218
5.4.4	Analytical quantification of dexamethasone in ocular tissue.....	220
5.4.5	Dexamethasone transscleral permeation.....	225
5.4.6	<i>Ex-vivo</i> trans-scleral particles diffusion	228
5.4.7	Dexamethasone ocular biodistribution	232

5.5	Conclusions.....	235
Chapter 6	<i>In-vivo</i> studies of dexamethasone-loaded microneedle patches	237
6.1	Introduction.....	238
6.1.1	Aim and objectives.....	240
6.1.2	Graphical overview	240
6.2	Materials	241
6.3	Methods	241
6.3.1	Preparation of animal microneedle moulds	241
6.3.2	Preparation of microneedle patches	242
6.3.3	Animals.....	243
6.3.4	Ocular irritancy	244
6.3.5	<i>In-vivo</i> activity of dexamethasone in LPS-induced uveitis.....	246
6.3.6	Histopathological evaluation	248
6.3.7	Statistical analysis	249
6.4	Results	249
6.4.1	Preparation of microneedle patch.....	249
6.4.2	Ocular irritation.....	252
6.4.3	<i>In-vivo</i> activity of dexamethasone in LPS-induced uveitis.....	258
6.4.4	Histopathological evaluation	264
6.5	Conclusions.....	267
Chapter 7	Conclusions and future direction	269
7.1	Conclusions.....	270
7.2	Future direction.....	275
References	277

List of Figures

Figure 1-1 Graphical illustration of the MN insertion into ocular tissue and the release of PLGA particles from the dissolvable polymeric base (created by Biorender).	29
Figure 1-2 Diagrammatic view of the (a) eye anatomy, (b) corneal layers [8].	29
Figure 1-3 Schematic representation showing the sites of periocular routes of drug administration [1].	34
Figure 1-4 Ozurdex® intravitreal implant and ten cent US coin (17.91 mm in diameter) [37].	37
Figure 1-5 Vitrasert® front view (left) and schematic diagram (right) [40].	38
Figure 1-6 I-vation™ non-biodegradable drug delivery implant [41].	39
Figure 1-7 TODDD™ ocular insert and ten cent US coin (17.91 mm in diameter) [46].	40
Figure 1-8 Suprachoroidal injection using hollow MN [86].	44
Figure 1-9 Configuration of SLA 3D printer [96].	47
Figure 1-10 Schematic illustration of (a) top-down and (b) bottom-up SLA printer [99].	47
Figure 1-11 The uses of synthetic and natural polymers to prepare micro and nanoscale formulations to enhance and control ocular drug delivery [114].	50
Figure 1-12 Thesis Graphical overview (created by Biorender).	57
Figure 2-1 Chemical structure of PVA (a) fully hydrolysed, (b) partially hydrolysed, (created by ChemSketch).	59
Figure 2-2 Chemical structure of PVP, (created by ChemSketch).	61
Figure 2-3 Chemical structure of PLGA, (created by ChemSketch).	62
Figure 2-4 Chemical structure of PDMS, (created by ChemSketch).	63
Figure 2-5 Chemical structure of coumarin-6, (created by ChemSketch).	64
Figure 2-6 Chemical structure of dexamethasone, (created by ChemSketch).	66
Figure 2-7 3D printed objects using Formlabs® clear resin [162].	67
Figure 2-8 Fusion 360™ interface components.	69
Figure 2-9 Schematic illustration of SLA 3D printing process, (LPU is the light processing unit) [170].	70
Figure 2-10 Component of Preform 3D printing software.	71
Figure 2-11 Pure water pressure vs. temperature phase diagram in a closed system [181].	74
Figure 2-12 Illustration of freeze dryer basic components [181].	75
Figure 2-13 Illustration of the formation of the pellets in the tubes with a horizontal rotor and a fixed angle rotor [187].	76

Figure 2-14 Demonstration of PLGA particles concentrated the MN tip in 90° vs 45° degree rotors, (created by Biorender).	77
Figure 2-15 Schematic diagram of DLS setup [190].	79
Figure 2-16 Diagram of the particle surrounding ionic concentration and potential differences [193].	80
Figure 2-17 Illustration of heat-flux DSC. A is the furnace and B is the thermocouple [198].....	81
Figure 2-18 DSC data diagram constructed from the difference in heat flow between the reference and the sample [197].	82
Figure 2-19 Schematic illustration of an XRD instrument [200].	84
Figure 2-20 Schematic diagram of FTIR [203].	85
Figure 2-21 Schematic illustration of HPLC instrument [204].	86
Figure 2-22 Schematic illustration of different mechanical testing configurations (A) tensile, (B) compression, and (C) flexural loading [214].	90
Figure 2-23 Schematic illustration of typical UTM [215].	90
Figure 2-24 Schematic illustration of a Franz diffusion cell [218].....	92
Figure 2-25 Schematic illustration of the mitochondrial reduction of yellow MTT to purple formazan [220].	94
Figure 3-1 Chapter 3 graphical overview (created by Biorender).	101
Figure 3-2 The shapes of the MN designed by CAD software (a) triangular pyramid, (b) pyramid, and (c) cone needles. The designs present shapes in a 1:2 aspect ratio.	102
Figure 3-3 Preparation of the CAD model in preform software before uploading the design on the 3D printer.	104
Figure 3-4 Illustration of adjusting the object at 0° and 45° orientation with support structure before the printing using Preform software.	105
Figure 3-5 Digital images of (a) reverse mould, (b) pre-filled Falcon™ tube with lightweight silicon rubber.....	107
Figure 3-6 Preliminary master designs showing CAD design, 3D printed master, and PDMS reverse mould, (a) square mould, (b) circular mould, (c) polymeric MN array.	109
Figure 3-7 Master of MN array displaying a dome-shaped base and a two-part system consisting of a base holding the array and a cup to fit in the base. (a) CAD design, (b) 3D printed masters, (c) reverse mould (23 mm in diameter), (d) polymeric MN array (4x4 mm).	110
Figure 3-8 Inspection of MN array master post-curing by digital camera.....	111

Figure 3-9 Microscopic images of MN array masters before curing, (a) uncured resin trapped in the interneedle space, (b) uncured resin completely removed.....	112
Figure 3-10 CAD design of a 1x4 MN array for height printability testing (in the image, 500 μm MN height in 1:2 aspect ratio is shown).	113
Figure 3-11 3D printed MN (C 1-2) in height ranged from 100 μm to 900 μm (obtained by Infiniprobe high-focus digital camera).	113
Figure 3-12 Comparison of the input design and output print heights of the MN printed in a cone shape and 1:2 aspect ratio (C 1-2). Data are reported as mean \pm SD (n=6).	114
Figure 3-13 3D printed MN in cone, pyramid, and triangular pyramid shapes in 1:3, 1:2, and 1:1 aspect ratio (MN are 900 μm in height).....	115
Figure 3-14 Top and side view SEM images of MN in a cone (C), pyramid (P), and triangular pyramid (T) shape with 1:1, 1:2, and 1:3 aspect ratios. Scale bar () 300 μm	116
Figure 3-15 Accuracy (output/input %) of height with different shapes and aspect ratios. (C) cone, (P) pyramid, and (T) triangular pyramid (dotted line indicates 100% accuracy). Data are reported as mean \pm SD (n=4 arrays).	116
Figure 3-16 Accuracy (output/input %) of base size with different shapes and aspect ratios. (C) cone, (P) pyramid, and (T) triangular pyramid (dotted line indicates 100% accuracy). Data are reported as mean \pm SD (n=4 arrays).	117
Figure 3-17 Digital images of 3D printed MN with 25, 50, and 100 μm layer thicknesses (MN are 900 μm in height).	119
Figure 3-18 Adjusting the MN array at 0°, 45°, 67.5°, and 90° orientation angles using support structure to investigate the effect of changing the layers outline on the printing resolution.	119
Figure 3-19 Adjusting the printing orientation of the CAD model in Preform software. (a) editing the support structure points (b) support structure generated at the selected point.	120
Figure 3-20 Printing needles at different orientation angles displaying the layer at which the MN tip is printed (a) side view, (b) top view.....	121
Figure 3-21 SEM images of 3D printed cone shaped (C 1-2) MN at different orientation angles (0°, 45°, 67.5°, and 90°) front, top, and side views. Scale bar () 300 μm	122
Figure 3-22 Accuracy (output/input %) of the MN height and base printed at 0°, 45°, 67.5°, and 90° orientation angles (dotted line indicates 100% accuracy). Data are reported as mean \pm SD (n=6 needles).....	123

Figure 3-23 Effect of the orientation angles on the tip size of a cone shape MN. Data are reported as mean \pm SD (n=6 needles).	124
Figure 3-24 Digital images of MN (C 1-2) ranged in height from 100 μ m to 800 μ m printed at 0°, 45° and 67.5° angles.	125
Figure 3-25 Comparison of the input and output heights of the MN (C 1-2) printed at 45° and 67.5° angles. Data are reported as mean \pm SD (n=6).	126
Figure 3-26 3D scans of MN (C 1-2) printed at different orientation angles (0°, 45°, 67.5°, and 90°).	128
Figure 3-27 Accuracy (output/ input %) of the height (Z-max), volume, and surface area of MN printed at 0°, 45°, 67.5°, and 90° orientation angles (dotted line indicates 100% accuracy) Data are reported as mean \pm SD (n=4).	128
Figure 3-28 Surface area to volume ratio (S:V) of MN and tip (100 μ m length from the top) printed at different orientation angles (0°, 45°, 67.5°, and 90°). Data are reported as mean \pm SD (n=4).	129
Figure 3-29 3D scans of MN printed with different shapes at 1:2 aspect ratio and 0°. Cone (C 1-2), pyramid (P 1-2), and triangular pyramid (T 1-2).	131
Figure 3-30 Accuracy (output/input %) of the height (Z-max), volume, and surface area of MN printed with different shapes at a 1:2 aspect ratio and 0°. Cone (C 1-2), pyramid (P 1-2), and triangular pyramid (T 1-2), (dotted line indicates 100% accuracy). Data are reported as mean \pm SD (n=4).	131
Figure 3-31 Percentage of holes created in parafilm M® layers following the insertion of cone (C 1-2) MN printed at different orientation angles (0°, 45°, 67.5°, and 90°) means \pm SD (n=4 arrays).	133
Figure 3-32 Percentage of holes created in parafilm M® layers following the insertion of different 3D printed MN shapes, cone (C 1-2), pyramid (P 1-2), and triangular pyramid (T 1-2) means \pm SD, (n=4 arrays).	134
Figure 4-1 Chapter 4 graphical overview (created by Biorender).	140
Figure 4-2 Demonstration of ImageJ fluorescence analysis by calculating the corrected total cell fluorescence (CTCF) by selecting (a) background, (b) cell.	154
Figure 4-3 SEM images of blank PLGA particles (MP-02) prepared by low viscosity PLGA (PURAC®, PDLG 7502), (a) lower magnification overview, (b) higher magnification overview.	156

Figure 4-4 SEM images of blank PLGA particles (MP-07) prepared by high viscosity PLGA (PURAC®, PDLG 7507), (a) lower magnification overview, (b) higher magnification overview.	156
Figure 4-5 SEM images of Dex-loaded PLGA particles prepared with acetone and DCM mixture as an organic phase, (a) using low viscosity PLGA grade, (b) using high viscosity PLGA grade. The orange arrows point out the free Dex.....	158
Figure 4-6 SEM images of Dex-loaded PLGA particles prepared with methanol and DCM mixture as an organic phase, (a) using low viscosity PLGA grade, (b) using high viscosity PLGA grade.	159
Figure 4-7 SEM images of Dex-loaded PLGA particles prepared with DMSO and DCM mixture as an organic phase, (a) low viscosity PLGA grade, (b) high viscosity PLGA grade.....	159
Figure 4-8 SEM images of Fluorescent labelled PLGA microparticles prepared (a) using low viscosity PLGA grade (MP-02-Flu), (b) using high viscosity PLGA grade (MP-07-Flu).	160
Figure 4-9 Images of fluorescent labelled PLGA microparticles prepared using low viscosity PLGA grade (MP-02-Flu), (a) fluorescence microscopy, (b) optical microscopy image.....	161
Figure 4-10 SEM images of PLGA nanoparticles (a), (b) Dex-loaded PLGA nanoparticles (NP-Dex) (c), (d) fluorescence labelled PLGA nanoparticles (NP-Flu).....	162
Figure 4-11 Percentage of the production yield of microparticles (MP), Nanoparticles (NP), and Dex-loaded micro- and nano- particles (MP-Dex, NP-Dex) (**** $p < 0.00001$).	168
Figure 4-12 Chromatograms of standard Dex solution (100 µg/mL), (a) dissolution assay, (b) content assay.	170
Figure 4-13 Chromatograms acquired in the specificity study of a spiked sample (50 µg/mL).	173
Figure 4-14 Standard calibration curves for Dex on three days (1, 2, and 3) the regression line equation and the correlation coefficient are shown on the top of the curve (mean ±SD, n=3).	176
Figure 4-15 Standard calibration curve of Dex in ACN, the regression line equation and the correlation coefficient are shown on the top of the curve (overall mean ±SD, n=3).	176
Figure 4-16 DL% of Dex in PLGA microparticles prepared by low (MP-Dex-02) and high viscosity (MP-Dex-07) PLGA grades using different organic mixtures.	178
Figure 4-17 EE% of Dex in PLGA microparticles prepared by low (MP-Dex-02) and high viscosity (MP-Dex-07) PLGA grades using different organic mixtures.	178
Figure 4-18 Comparisons of the DL% and EE% in Dex-loaded nanoparticles (NP-Dex) and Dex-loaded microparticles (MP- Dex-02) prepared by DCM/methanol organic solvent.	179

Figure 4-19 <i>In-vitro</i> Dex release profiles from microparticles prepared by low viscosity (MP-Dex-02) and high viscosity (MP-Dex-07) PLGA grades.	181
Figure 4-20 <i>In-vitro</i> Dex release profiles from nanoparticles (NP-Dex) and microparticles prepared by low viscosity PLGA (MP- Dex-02).....	182
Figure 4-21 DSC thermograms of pure Dex, PLGA (PLDG 7502), physical mixture, MP-Dex-02, and MP-02.	184
Figure 4-22 XRD diffractograms of Dex, PLGA, physical mixture, MP-Dex-02, and MP-Dex-02.....	186
Figure 4-23 FTIR spectra of free Dex, PLGA (PLGD 7502) powder, physical mixture, MP-Dex-02.	187
Figure 4-24 Digital image of ARPE-19 cell line adhered to the bottom of the culture flask after 48 h incubation.	188
Figure 4-25 The IC20 and IC50 values determined by MTT reagent for Dex in 96 well plates treated with different concentrations at 24 and 48 h.	189
Figure 4-26 Effect of Dex-loaded particles (NP-Dex and MP-Dex) and blank particles (NP and MP) on ARPE-19 % viability.....	190
Figure 4-27 Cellular uptakes of NP-Flu and MP-Flu after exposing ARPE-19 cells for 1 h (a) the fluorescent intensity detected extracting the fluorescent markers, (b) CTCF measured in ARPE-19 cells.	191
Figure 4-28 Fluorescent microscope images of ARPE-19 cells after 1 h of incubation with (a) NP-Flu, (b)MP-Flu. The cell nucleus was stained blue by DAPI and green, indicating the uptake of the fluorescent marker in the particles.....	192
Figure 5-1 Chapter 5 graphical overview (created by Biorender).	197
Figure 5-2 MN array mechanical testing setup using an Instron tensile tester. A cylindrical probe attached to the upper instrument frame.....	201
Figure 5-3 Illustration of the instrumental set-up of MN array insertion into porcine scleral tissue (a) graphical illustration, (b) Instron tensile tester.	203
Figure 5-4 Before and after images of MN array dissolution prepared by different ratios of PVP/PVA blend. P5A1, P1A1, and P1A5 MN arrays were inserted in gelatine for 30 sec. (MN are 900 µm in height before insertion).	208
Figure 5-5 Percentage of height reduction of MN arrays formulated by different PVP/ PVA blend (P5A1, P1A1, and P1A5) MN arrays after insertion in gelatine. Data presents mean ±SD (n=18), (**** $p < 0.00001$).	209

Figure 5-6 Force exerted on MN array prepared by different ratios of PVP/PVA to reach 0.5 mm displacement. The values represent mean \pm SD (** $p < 0.001$, *** $p < 0.0001$, **** $p < 0.00001$).	210
Figure 5-7 Before and after images of MN array dissolution in gelatine after 30 sec prepared by different ratios of PVP/PVA blend (MN are 900 μ m in height before insertion).	210
Figure 5-8 Percentage of height reduction of MN formulated by different grades of PVP and ratio of PVP/PVA blend. Data present mean \pm SD (n=18) (* $p < 0.01$, ** $p < 0.001$, *** $p < 0.0001$, **** $p < 0.00001$).	211
Figure 5-9 MN array (3x3) mechanical strength test of various PVP/PVA blends. In the box, the force exerted to reach 0.5 mm displacement. All values represent mean \pm SD (n=3) (* $p < 0.01$, ** $p < 0.001$).	213
Figure 5-10 Forces recorded to detach MN array prepared by various PVP/PVA blends from porcine scleral tissue. All values represent mean \pm SD (n=3).	214
Figure 5-11 Digital images of MN array of (a) top view of the blank MN array compared to British one penny coin (diameter =20.3 mm), (b) side view, (c) MP concentrated at the tip of the MN, and (d) fluorescent microscope image of MP-Flu incorporated MN array.	216
Figure 5-12 SEM images of MN arrays, (a) interneedle space of blank MN array, (b) tip of the blank MN array, (c) interneedle space of microparticles incorporated MN array, (d) MN tip of microparticles incorporated MN array.	217
Figure 5-13 MN array (3x3) mechanical strength test of blank polymeric MN (MN) and MP-MN arrays. In the box, forces exerted to reach 0.5 mm displacement. All values represent the mean \pm SD (n=3).	218
Figure 5-14 Ex-vivo scleral insertion test of MN and MP-MN arrays. The data represents mean values \pm SD (n=3 arrays).	219
Figure 5-15 Chromatograms of standard Dex solution (100 μ g/mL) and IS (100 μ g/mL). (a) original developed method, (b) mobile phase gradient change over 14 min, (c) flow rate of 0.9 mL.	222
Figure 5-16 Chromatogram of scleral tissue extract. (a) Dex spiked sample (50 μ g/mL) of scleral extract, (b) blank scleral extract.	223
Figure 5-17 Standard calibration curve of Dex/IS in ACN, the regression line equation and the correlation coefficient are shown on the top of the curve (data present mean \pm SD, n=3) ...	225

Figure 5-18 <i>In-vitro</i> transscleral permeation profile of Dex from Dex suspension, Dex-loaded microparticles (MP-Dex), and MP-Dex incorporated MN array (Dex-MN) (* $p < 0.01$, ** $p < 0.001$, and *** $p < 0.0001$).	226
Figure 5-19 Dex retained in sclera post the permeation study. Values are mean \pm SD (** $p < 0.001$).	227
Figure 5-20 Images of <i>ex-vivo</i> particle diffusion in scleral tissue (a) light microscope image of MN produced crack wound on the scleral surface, (b) fluorescent microscopy image of MP-Flu release on the scleral surface, (c) fluorescent microscopy image of DAPI stained cross-sectioned sclera post MN array loaded with NP-Flu insertion, (d) MP-Flu insertion, (e) light microscopy image of cross-sectioned haematoxylin and eosin stained sclera post MN array loaded with MP-Flu insertion showing MN-produced crack and MP-Flu dispositioning, (f) MP-Flu detected within the tissue (indicated by orange arrows).	229
Figure 5-21 Fluorescent microscope images of middle and bottom region transverse sections of <i>ex-vivo</i> MP-Flu diffusion study 1 h post insertion. Blue represents nucleus and green represents MP-Flu. The green channel shows MP-Flu and the blue channel shows the tissue nucleus (scale bar=400 μ m).	230
Figure 5-22 Fluorescent microscope images of middle and bottom region transverse sections of <i>ex-vivo</i> NP-Flu diffusion study 1 h post insertion. Blue represents nucleus and green represents NP-Flu. Green channel shows MP-Flu and blue channel shows the tissue nucleus (scale bar=400 μ m).	231
Figure 5-23 Schematic illustration of the segmentation of the eye globe for Dex extraction (created by Biorender).	233
Figure 5-24 Dex ocular diffusion presented as a percentage of Dex detected in each region post MN application (a) MP-Dex-loaded MN array and NP-Dex-loaded MN array, and (b) represent a comparison between MP-Dec and NP-Dex, (Sc= sclera, AS= anterior segment, VH= vitreous humour, MN= MN insertion site). Data presented as mean \pm SD.....	234
Figure 6-1 Chapter 6 graphical overview (created by Biorender).	240
Figure 6-2 CAD design of the master to prepare the mould to fabricate MN patches for animal use, (a) sketch of the MN array, (b) 3D design of the MN array, (c) MN array on cylinder filleted top on 23 mm disk, (d) the final design of the master.....	242
Figure 6-3 Digital images of moulds prepared for <i>in-vivo</i> animal studies (a) 3D printed master (base 23 mm in diameter) (b) PDMS reverse mould (23 mm in diameter).	250

Figure 6-4 Preparation of customised animal MN patch (a) the dried polymeric base containing nanoparticles in the MN removed from the moulds, (b) a 5x5 MN patch prepared by punch tool (7 mm in diameter), (c) MN patches in a glass container.....	250
Figure 6-5 The remaining portion of the MN patches without an insoluble PMMA backing layer on the rabbit ocular surface.....	251
Figure 6-6 The MN patch remaining with an insoluble PMMA backing layer maintained the shape and integrity of the patch 2 h after application. The MN are visible under the patch.	252
Figure 6-7 Images of rabbit eye (a) NaCl treated eyes, (b) MN patch treated eye, at the time of the patch insertion (0 h). Green arrows indicate the normal features of the eye.....	254
Figure 6-8 Images taken during irritation study on albino rabbit eyes. Post insertion of Blank-MN and Dex-MN patches over 24 h. Red arrows indicate visible signs of inflammation, orange arrow indicates mild signs, and green arrows indicate the normal features of the eye.	256
Figure 6-9 The effect of Dex-MN on LPS-induced uveitis. (a) clinical scores of LPS-induced uveitis in rabbit eyes (b) polymorphonuclear infiltration cytology in AqH samples. All values represent mean \pm SD of three animals per group * $p < 0.05$ (Blank-MN); # $p < 0.05$ (LPS + Blank-MN). ...	258
Figure 6-10 Effect of Dex-MN on LPS-induced uveitis on inflammatory cytokines (a) TNF- α , (b) IL-6, (c) pro-inflammatory marker MPO, and (d) NF- κ B DNA-binding. All values represent mean \pm SD of three animals per group * $p < 0.05$ (Blank-MN); # $p < 0.05$ (LPS + Blank-MN).	260
Figure 6-11 Effect of Dex-MN on LPS- induced uveitis on apoptotic markers in ocular tissues of rabbit. (a) the protein expression of Bax, (b) Caspase-3, (c) NF- κ B phosphorylation proteins, (d) BCL-2 β -actin, and (e) protein levels in AqH, and (f) western blot of all proteins. All values represent mean \pm SD of three animals per group * $p < 0.05$ (Blank-MN); # $p < 0.05$ (LPS + Blank-MN).....	262
Figure 6-12 Images and micrographs of hematoxylin and eosin–stained sections of rabbit eyes for <i>in-vivo</i> activity in LPS-induced uveitis. (a) Group-I, normal control group (Blank-MN). No cellular infiltrate, and conjunctival hyperaemia were observed, (b) LPS-induced uveitis (24 h),(c) Group-II, numerous inflammatory cells infiltrated the extravascular uveal tissue in the LPS + Blank-MN and (d) Group-III, inflammatory cellular infiltration was reduced by treatment with Dex-MN. Section magnification $\times 100$	266
Figure 6-13 Histological score of the normal control group, LPS-induced uveitis with Blank-MN and Dex-MN administration. (The values represent mean \pm SD of three animals per group * $p < 0.05$ (Blank-MN); # $p < 0.05$ (LPS + Blank-MN).	267

List of Tables

Table 1-1 FDA approved ocular implant products.....	36
Table 1-2 Summary of MN types and fabrication methods and materials.....	43
Table 2-1 Poly(vinyl alcohol) properties provided by the manufacturer.....	60
Table 2-2 Properties of Kollidon®30 and Kollidon®90F, provided by the manufacturer.....	61
Table 2-3 Properties of PURASORB PDLG, provided by the manufacturer.	63
Table 2-4 SYLGARD®184 silicon properties.....	64
Table 2-5 Properties of coumarin-6 provided by the manufacturer.	65
Table 2-6 Properties of dexamethasone provided by the manufacturer.....	67
Table 2-7 Properties of Clear resin provided by the manufacturer.....	68
Table 3-1 Dimensions and specifications of the MN array designs.	103
Table 3-2 Comparison between needle input and 3D printed output height.	114
Table 3-3 Outcome height and accuracy (output/input %) of MN (C 1-2) printed at 45°and 67.5° angles. Data are reported as mean \pm SD (n=6).	126
Table 4-1 Name and composition of the organic phase used for the preparation of blank and Dex- loaded microparticles.....	142
Table 4-2 Chromatographic conditions used for the analysis of Dex.	146
Table 4-3 SEM images, particle size histograms, PDI, and Zeta potential data of microparticles prepared by low viscosity PLGA (PDLG 7502).	164
Table 4-4 SEM images, particle size, PDI, histograms, and Zeta potential data of microparticles prepared by high viscosity PLGA (PDLG 7507).	165
Table 4-5 SEM images, particle size histograms, PDI, and Zeta potential distribution of nanoparticles prepared by low viscosity PLGA (PDLG 7502).	167
Table 4-6 System suitability parameters for the Dex content and dissolution assays.	169
Table 4-7 precision and accuracy analysis of Dex samples performed intra- and inter-day. (n=3)	171
Table 4-8 The limit of detection determined by the signal-to-noise approach.....	172
Table 4-9 Statistical calculation of the specificity by a Student's t-test, of the areas of the peaks of standard and spiked samples (50 μ g/mL) (n=3).....	173
Table 4-10 Robustness of the HPLC method analysing 100 μ g/mL by changing the temperature, flow rate, and pH.....	174
Table 4-11 HPLC mean peak area of Dex concentrations (μ g/mL) of three sets (n=3).	175

Table 5-1 Formulations composition of MN array polymeric base solution (30% w/v) prepared by various ratios of PVP and PVA.	198
Table 5-2 Formulation composition of MN array polymeric base solution (30% w/v) prepared by PVA with PVP-K30 or PVP-K90.	198
Table 5-3 Specifications of PLGA particles incorporated in dissolvable MN array.	199
Table 5-4 Compression force per MN array (3x3) and per needle of various PVP/PVA blends to reach 0.5 mm displacement. values represented as mean value \pm SD (n=3).	213
Table 5-5 Estimation of insertion force into scleral tissue for MN and MP-MN arrays.....	220
Table 5-6 Effect of HPLC method modification on peaks separation R_s and R_T of Dex and IS.	221
Table 5-7 System suitability parameters for Dex and IS standard samples.....	223
Table 5-8 Statistical calculation of the specificity by a Student's t-test, of the areas of the peaks of standard solution and Dex spiked samples (50 μ g/mL) (n=3).....	224
Table 5-9 Mean ratios of peak area (Dex/IS) of Dex concentration (μ g/mL) of three sets (n=3)...	224
Table 6-1 Formulation of the MN patches prepared for <i>in-vivo</i> animal study	243
Table 6-2 Grading system for ocular lesion severity in irritation tests [320].	245
Table 6-3 Classification of the eye irritation scoring system.	246
Table 6-4 Weighted scores for the eye irritation test of the Dex-MN patch and Blank-MN patch.	253
Table 6-5 Calculation of MMTS for the Blank-MN and Dex-MN patches according to the scores mentioned in Table 6-4.	257

Scientific Presentation

Oral Communications:

- Formulation and Characterization of Dissolvable PLGA-Loaded Microneedles for Ocular Drug Delivery. UCL School of Pharmacy Research Day, 14th of July 2021, (London, UK).

Poster presentation:

- 3D-Printed Micromould to Prepare Microneedles Loaded with PLGA Microspheres. The APS 10th International PharmSci Conference. University of Greenwich (Maritime Campus), 11th – 13th September 2019, (Greenwich, UK)
- Formulation and Characterization of Dissolvable PLGA-Loaded Microneedles for Ocular Drug Deliver. The 12th PBP World Meeting and the ResearchPharm[®] exhibition 7th -11th February 2021, (Vienna, Austria).
- Dissolvable Microneedle Array Containing Dexamethasone-Loaded PLGA Microparticles for Scleral Drug Delivery. The 13th PBP World Meeting 28th -31st March 2022, (Rotterdam, The Netherlands).

Chapter 1 Introduction

1.1 General overview

Ocular diseases vary from self-limiting conditions, as simple as conjunctivitis, to more complicated diseases that lead to irreversible visual impairments [1]. Diseases of the posterior segment, such as wet and dry age-related macular degeneration (AMD), diabetic macular oedema (DME), cytomegalovirus (CMV), proliferative diabetic retinopathy (PDR), endophthalmitis and uveitis are the most prevalent [2]. In order to treat posterior segment conditions, an effective delivery strategy must be employed. Topically-applied ophthalmic medications such as eye drops and ointments suffer from extremely low bioavailability (<5%) [3]. This is attributed to the anatomical and physiological mechanisms of drug elimination, including tear fluid turnover, blinking reflex, and tear drainage. Therefore, large and frequent doses are required to achieve effective concentrations [4]. Similarly, the systemic route requires the administration of a large dose to deliver an effective concentration at the target site, hence an off-target adverse effect is expected. Intraocular injection, on the other hand, can directly deliver a high dose at the target site. However, along with patients' inconvenience, the intravitreal route has been associated with serious side effects, including infection and retinal detachment [5]. Thus, an alternative efficient, localised, and minimally invasive approach is highly desirable. Recently, microneedles (MN) have gained a great deal of interest in ocular drug delivery. The MN can be utilised to deliver a wide range of therapeutics due to their minimally invasive nature. MN can penetrate the ocular barrier for site-specific drug localisation [1]. Ocular application of MN has been mainly focused on the use of hollow, solid, and dissolvable MN [6]. Dissolvable polymeric MN is a patient-friendly drug delivery system that can be self-applied. Hydrophilic, dissolvable, and biodegradable polymers are used to fabricate these MN.

In this study, a dissolvable polymeric MN array to deliver dexamethasone-loaded PLGA particles for ocular drug delivery was developed (Figure 1-1). MN mould fabrication will be studied in Chapter 3, fabrication and characterisation of the PLGA particles and the MN array will be discussed in Chapters 4 and 5, respectively. And finally, the *in-vivo* assessment of the fabricated MN array is presented in Chapter 6.

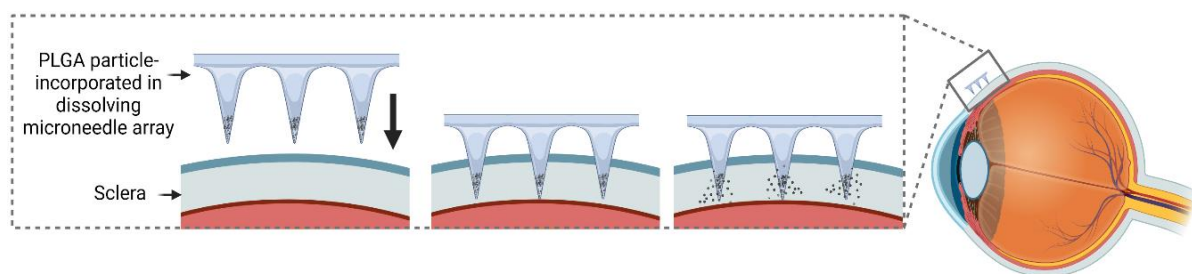


Figure 1-1 Graphical illustration of the MN insertion into ocular tissue and the release of PLGA particles from the dissolvable polymeric base (created by Biorender).

In the following sections, the fundamental concepts, challenges, and literature review regarding the foundation of this research are presented.

1.2 Anatomy and physiology of the eye

The eye is one of the most complex body organs. It has unique anatomical and physiological properties that render it a highly protected organ. Generally, the ocular globe is divided into anterior and posterior segments, as shown in Figure 1-2, a. The anterior segment is composed of the conjunctiva, cornea, iris, ciliary body, lens, and aqueous humour, while the posterior segment comprises the sclera, retina, choroid and vitreous humour [7].

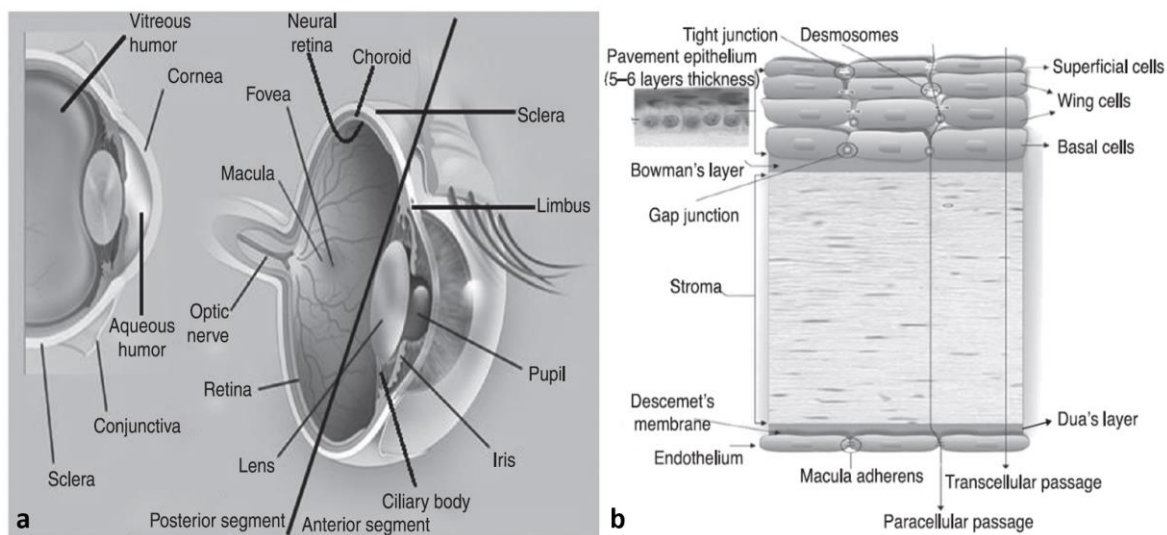


Figure 1-2 Diagrammatic view of the (a) eye anatomy, (b) corneal layers [8].

The conjunctiva is the outer mucous layer that coats the visible part of the sclera and the inner part of the eyelid that facilitates eye lubrication. While the human cornea measures around 12 mm in diameter and 0.5 mm in thickness. It is composed of six distinctive layers: epithelium layer, Bowman's membrane, stroma, Dua's layer, Descemet's membrane, and endothelium layer (Figure 1-2, b) [8]. It is connected to the sclera by the limbus, and its primary function is refraction. The iris is the anterior part of the uvea. It consists of pigmented epithelial tissue that gives the eye its colour and a thin circular muscular disc that is perforated by the pupils. The iris sphincter controls the diameter of the pupils and the light entrance to the eye. The space between the iris and the cornea is known as the anterior chamber. The ciliary body is a part of the uvea, and it is composed of triangular-shaped muscles attached to the iris to provide support and focus for the lens. The lens, the focusing accessory of the eye, is a clear flexible structure that lies behind the iris. It is suspended from the ciliary muscles by a thin ligament called the zonule. The aqueous humour is a clear solution approximately 0.3 mL in volume, rich in electrolytes, secreted by the ciliary body in the posterior segment and enters the anterior chamber through the pupils to nourish the lens and the cornea. It circulates in the anterior chamber and drains through the extraocular venous network [7, 8].

The posterior segment, on the other hand, includes all the structures located posterior to the lens, namely: the sclera, retina, choroid, vitreous humour, and optic nerve. The sclera, the white of the eye, is the outermost layer of the eye. It consists of haphazardly arranged collagen bundles, which give it an opaque white colour. The outer layer of the sclera, the episcleral, is consist of vascularised loose connective tissue. The sclera is thinnest, at about 0.3 mm, posterior to the corneoscleral limbus and substantially thickens to reach about 1 mm near the optic nerve [9]. The retina is a multi-layered photosensitive sensory tissue that lines the inner surface of the eye. It consists of outer pigment epithelium and inner sensory tissue that contains millions of rods and cones, photoreceptors, bipolar cells, and ganglion cells. The choroid layer is located between the sclera and the retina. It is a highly vascularized layer that provides nourishment to

the retinal photoreceptor. The vitreous humour is a clear gel-like matrix approximately 3 mL in volume, which fills the space between the retina and the lens. It consists of long-chain collagen molecules that retain a large amount of water (99%) and hyaluronic acid (1%). The optic nerve consists of axons that arise from the retinal ganglionic cells [7, 10-12].

1.3 Ocular delivery barriers

Delivery to the ocular tissue is challenging to overcome due to the distinctive anatomical and physiological barriers [13]. To deliver drugs to the anterior segment, the outermost tear film dilutes the instilled topical formulation, and the flow of the lacrimal fluid drains the drug to the nasolacrimal ducts in minutes [14]. With a nearly 1.2 $\mu\text{L}/\text{min}$ lacrimal turnover rate and normal blinking reflex (5-7 blinks/min), 95% of the topically applied drugs are eliminated systemically through the blood capillaries in the conjunctival sac or the nasolacrimal duct [15, 16]. Additionally, anatomical barriers comprise corneal epithelium, stroma, and blood-aqueous barrier (BAB). BAB is located in the anterior segment of the eye, and it consists of endothelial cells of the iris blood vessels and the non-pigmented ciliary epithelium. It limits drug entry into the aqueous humour [13]. The corneal epithelium is approximately 500 μm in thickness and negatively charged at physiological pH. Thus, negatively charged molecules permeate faster than positively charged ones [17].

For the posterior segment delivery, the sclera, choroid, and conjunctiva oppose an anatomical barrier for drug permeation. The blood-retinal barrier (BRB) is composed of retinal capillary endothelial cells (inner part) and the retinal pigment epithelial cells (outer part), BRB has tight junctions that limit molecule transportation from choroidal blood to the vitreous humour [18]. Furthermore, BRB efflux transporters such as P-glycoprotein (P-gp), multidrug resistance protein (MRP), and breast cancer resistance protein (BCRP) represent an important barrier for molecule permeation of systemically administered drugs to the vitreous humour [13, 17, 19].

1.4 Routes of ocular drug delivery

Designing an effective ocular drug delivery system to overcome the ocular-protective anatomical and physiological barriers has been the main challenge to pharmaceutical scientists. To attain ocular drug delivery, multiple routes for ocular drug administration have been employed, ranging from conventional topical instillation to invasive intraocular injection [10].

1.4.1 Topical administration

This is one of the most preferred routes of ocular drug administration due to ease of administration and high patient compliance. Topical ocular dosage forms such as eye drops, ointment, and gel require frequent and large doses of administration since more than 90% of the applied dose is lost as a result of nasolacrimal drainage, tear dilution, and blinking reflex leaving less than 5% of the dose available in the aqueous humour. Absorption of topically instilled medications occurs through corneal or non-corneal routes, i.e., conjunctival and scleral routes, and is mainly affected by the drug's physicochemical properties. The corneal apical epithelial cells form a tight junction that prevents paracellular drug transport. Therefore, the cornea is more permeable to small lipophilic drugs than its hydrophilic counterparts. Despite the corneal epithelial layer tightness, trans-corneal permeation is the major route of drug absorption for topically instilled drugs [16, 20]. Meanwhile, the sclera and conjunctiva are more permeable than the cornea to drugs with larger molecular weight regardless of their hydrophilicity level [16]. The sclera offers a large and easily accessible surface area with high water content. Studies have demonstrated that the sclera is permeable to molecules as large as 150 kDa [16, 21]. However, topical transscleral delivery suffers from many drawbacks, such as orbital clearance, intraocular pressure, choroidal blood flow and restriction of the BRB that may limit drug permeability to the posterior segment of the eye [21].

1.4.2 Intravitreal injection

This route involves direct drug administration into the vitreous and retina. However, the injected drug is not presumably uniformly distributed in vitreous fluid. Small molecules tend to diffuse rapidly throughout the vitreous fluid, while the motility of larger macromolecules is highly restricted [16]. After injection, drugs are eliminated by anterior or posterior routes [15, 22]. In the anterior elimination, the drug diffuses from the vitreous to the aqueous humour and, thereafter, is eliminated by aqueous turnover and uveal blood flow. On the other hand, posterior elimination occurs by passive permeability of small lipophilic drugs or active transport through the BRB. On these grounds, large molecular weight drugs have longer half-lives in the vitreous humour than small molecular weight drugs [10, 16, 22]. Despite the relatively high bioavailability, frequent administration of intravitreal injections can lead to endophthalmitis, retinal detachment and vitreous haemorrhage [1]. Therefore, neither patients nor doctors prefer this route of administration.

1.4.3 Periocular injection

This route enables drug injection to the external surface against the sclera allowing for posterior segment delivery through transscleral permeation, systemic circulation, and through the anterior surface by the tear film and corneal penetration. This route includes peribulbar, retrobulbar, subtenon, and subconjunctival routes (Figure 1-3) [1, 10, 23]. However, reflux of the administered drug through the needle-punctured site may contribute to initial loss and, hence, lower bioavailability. The application of optimum needle size, injection volume, and formulation properties can improve bioavailability. Moreover, conjunctival lymphatic pathways, episcleral veins, and choroidal blood flow can also contribute to periocular drug loss [1].

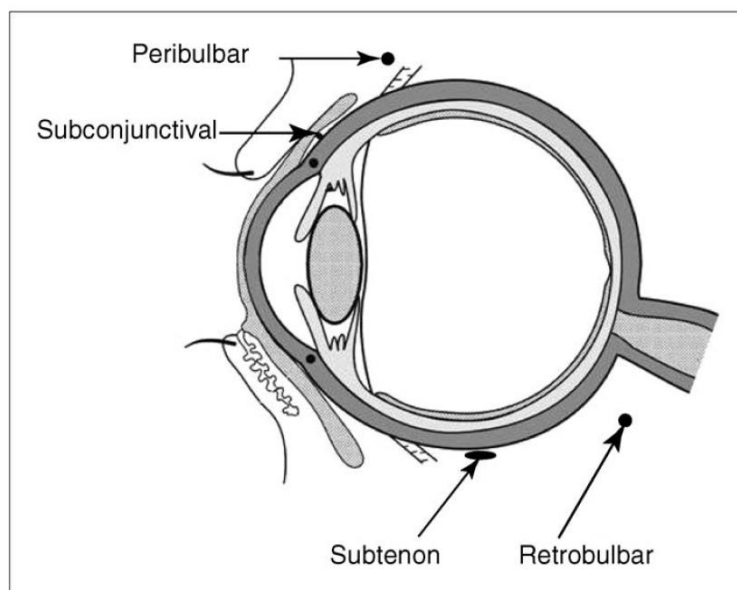


Figure 1-3 Schematic representation showing the sites of periocular routes of drug administration [1].

1.4.4 Systemic administration

Systemic ocular delivery by oral or intravenous administration is sometimes selected to treat posterior segment diseases. However, due to the restriction of the BRB and the BAB, only 1-5% of the administered drug reaches the vitreous humour [10]. The BRB and BAB ocular barriers limit the entry of drugs to the anterior and posterior segments by their tight junctions and limited blood flow [10, 20, 24]. To overcome the limited ocular availability following orally or intravenously administered drugs, a high or frequent doses are required to observe a therapeutic effect. Therefore, an assessment of the safety and toxicity needs to be considered before systemic administration [25].

1.5 Recent advances in ocular drug delivery system

To meet the increasing demand to treat chronic ocular diseases, various drug delivery systems have been developed. Different strategies have been introduced to access the anterior segment of the eye. In recent advances in topical dosage forms, improve the bioavailability by the use of prodrugs, increase drug solubility by cyclodextrins, increase the permeability by penetration enhancers, and other ocular drug delivery formulations

such as hydrogels, bioadhesive polymeric formulation, *in-situ* thermo-sensitive or ion-activated gelation, colloidal and nanosized systems were explored [18, 26]. In another line, delivery to the posterior segment of the eye has been studied to develop systems capable of overcoming the ocular barrier and delivering drugs to treat conditions related to vitreoretinal diseases [1, 27]. In this section, the new approaches in ocular drug delivery are briefly highlighted.

1.5.1 Intraocular Implants

Ocular implants offer a sustained release platform to deliver drugs from biodegradable or non-biodegradable matrices over months to years period[28]. These implants are physically settled onto the sclera through a surgical suture or direct injection to the vitreous for transscleral or intravitreal delivery [1]. Despite the invasiveness of the device implantation, this drug delivery platform has gained increasing interest due to the positive long-term outcome. Ocular implants have been classified as biodegradable and non-biodegradable according to the materials used. Table 1-1 summarizes all the Food and Drug Administration (FDA) approved marketed implant products.

Table 1-1 FDA approved ocular implant products.

Product	Implant material	Drug	Indication	Release time	Year approved
Vitrasert®	PVA, EVA	Ganciclovir	AIDS-related CMV retinitis	5–8 months	1996
Retisert®	PVA, silicone	Fluocinolone acetonide	Non-infectious uveitis	2.5 years	2004
Ozurdex®	PLGA	Dexamethasone	DME, posterior uveitis	6 months	2009
Iluvien®	Polyimide	Fluocinolone acetonide	DME	3 years	2014
Yutiq®	Polyimide	Fluocinolone acetonide	Chronic non-infectious uveitis	3 years	2018
DEXYCU®	Acetyl triethyl citrate P	Dexamethasone	Postoperative inflammation	2-3 weeks	2018
DURYSTA™	PLGA/PGA/PEG	Bimatoprost	Open-angle glaucoma	12-24 months	2020
Susvimo™	Polysulfone body coated in silicone	Ranibizumab	Wet AMD	6 months	2021
Dextenza®	PEG-Fluorescein	Dexamethasone	Eye itching associated with allergic conjunctivitis	1 month	2021

Biodegradable implant or polymeric implant does not require post-treatment removal and provide sustained drug-release profiles without the need for frequent administration. However, movement of the implant to the anterior chamber or front of the retina can cause complications. Fabrication of these devices is based on the use of bulk eroding polymers such as poly lactic acid (PLA), poly glycolic acid (PGA), PLGA, and

polycaprolactone (PCL) or surface eroding polymers such as polyanhydride, poly(trimethylene carbonate), and poly(ortho ester) are commonly used materials to fabricate these implants [29, 30]. Ozurdex[®] (Figure 1-4) is an FDA approved dexamethasone intravitreal implant to treat DME, macular oedema (swelling of the macula) and non-infectious uveitis [31]. This implant uses a rod-shaped PLGA polymeric matrix to release the drug over six months period [30, 32]. Surodex[™] is another dexamethasone implant that has been approved in Mexico, China and Singapore to control post-surgery inflammation in patients with cataracts [33]. Similar to Ozurdex[®], Surodex[™] is a PLGA-based rod-shaped implant (1mm 0.5mm) that is injected into the vitreous [30]. Dextenza[®] is an ocular insert to be administered in the lower lacrimal punctum to release 400 µg of dexamethasone over 30 days [34]. Durysta[™] is a biodegradable PLGA implant to deliver bimatoprost to treat open angle glaucoma [35]. Another recently FDA approved intraocular implant is DEXYCU[®] (Icon Biosciences Inc.), a dexamethasone injectable suspension in acetyl triethyl citrate that settles into a sphere and slowly releases the drug over 2-3 weeks [36].

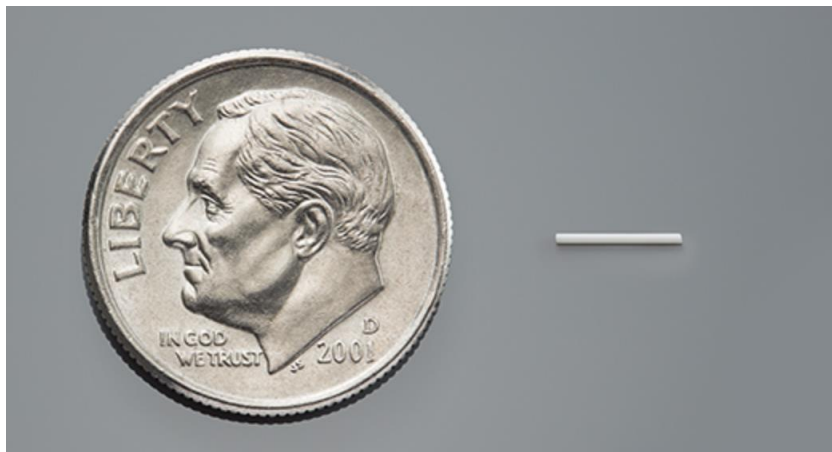


Figure 1-4 Ozurdex[®] intravitreal implant and ten cent US coin (17.91 mm in diameter) [37].

On the other hand, non-biodegradable implants require surgical implantation of the device into a convenient position and post-treatment surgical removal. Polymers used in the fabrication of non-biodegradable implants include hydrophobic matrices such as silicon and ethylene-vinyl acetate copolymer (EVA) and hydrophilic membranes such as

poly(vinyl alcohol) (PVA), and clear plastic such as poly(methyl methacrylate) (PMMA) can also be incorporated to allow the permeability of the loaded drug [30]. Retisert® is an FDA approved non-biodegradable implant for non-infectious posterior uveitis. It contains fluocinolone acetonide coated with PVA and silicon laminate [38]. Iluvien™ is another FDA approved fluocinolone acetate non-biodegradable implant composed of PVA matrix within a polyimide to treat DME over 36 months period [30, 39]. Vitrasert® is an implant for ganciclovir delivery, approved by the FDA, to treat CMV retinitis in acquired immunodeficiency syndrome (AIDS) patients. The device is made of PVA/EVA, which allows slow drug release for a period ranging from 5 to 8 months (Figure 1-5).

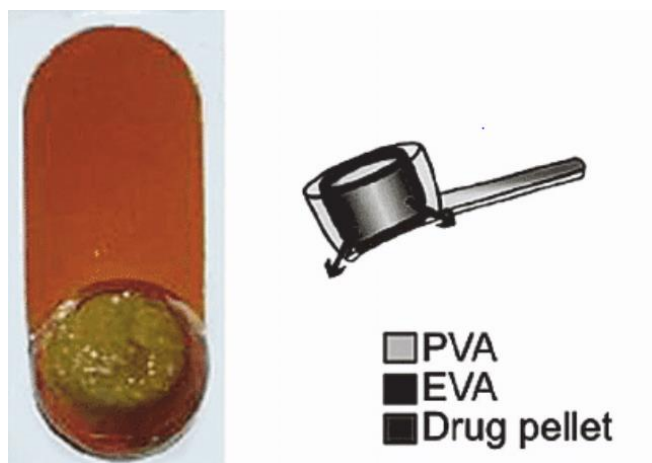


Figure 1-5 Vitrasert® front view (left) and schematic diagram (right) [40].

I-VATION™ is another non-biodegradable implant that consists of three main components; a titanium helical coil, a top cap, and a drug-loaded polymer coating that encapsulates the helix, as shown in Figure 1-6. The helical shape coil is designed to increase the surface area, and it is expected to release the drug for two years [41].

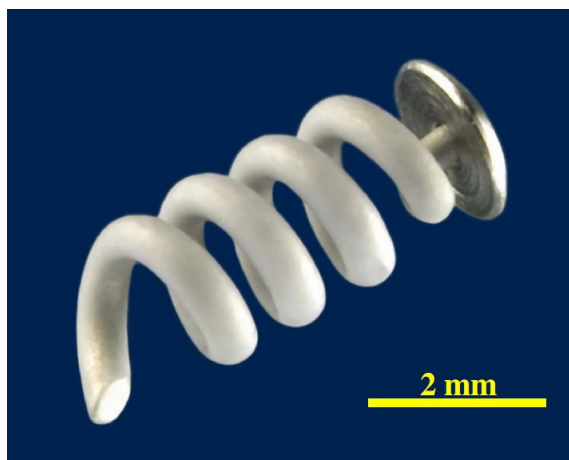


Figure 1-6 I-vation™ non-biodegradable drug delivery implant [41].

1.5.2 Contact lenses

Contact lenses have been used for decades, and they offer an attractive ocular drug delivery platform in which drugs can be released over a long period of time; these systems improve drug bioavailability by more than 50% [42]. Contact lenses have several advantages, such as high patient compliance, long contact time and lower tear mixing between the lens and the cornea [43]. Timolol maleate and dorzolamide hydrochloride loaded contact lens has completed phase I clinical trial to assess the safety and effectiveness in treating glaucoma (NCT02852057) [44]. Dexamethasone incorporated in contact lenses showed 200 times greater retinal concentration than hourly administered dexamethasone eye drops [45].

1.5.3 Topical inserts

It is a device that is inserted under the eyelid or into the sclera to release the drug over several months. Helios™, developed by ForSight Vision5, Inc., is a non-invasive bimatoprost insert which has completed a phase II clinical trial to evaluate the effectiveness compared to topical timolol solution in patients with glaucoma or ocular hypertension (NCT01915940). The company is conducting an open label extension study to assess the safety of the insert [43]. TODDD™ developed by Amorphex Therapeutics is another non-invasive device in a pre-clinical trial placed on the scleral

and concealed under the eyelid (Figure 1-7). This device can deliver up to three drugs [46].



Figure 1-7 TODDD™ ocular insert and ten cent US coin (17.91 mm in diameter) [46].

1.5.4 Iontophoresis

It is a non-invasive method that applies a small electric current to facilitate the penetration of charged drug molecules into the tissue [47]. Recently, studies demonstrated that iontophoresis could enhance transscleral penetration. It has been shown that this method improved the transscleral permeability of many drugs, including small molecular weight steroids [48] to large molecular weight proteins [49] and DNA molecules up to 8 million Dalton [50]. Iontophoresis has been coupled with MN technology to deliver negatively charged particles through the suprachoroidal space to the posterior segment [51]. However, at higher electric current, iontophoresis causes choroid and retinal damage and epithelial oedema, which limit its application [1].

1.5.5 Microneedle technology

MN is an attractive minimally invasive approach for ocular drug delivery. This technology is based on the capacity to deliver drugs into the inner layers of ocular

tissue, overcoming the ocular barrier and increasing the therapeutic outcomes [32]. This technology will be discussed thoroughly in the following sections.

1.6 Overview of microneedles

The MN system was first proposed back in 1976 for transdermal drug delivery [52]. Since then, MN fabrication has made massive progress in the drug delivery industry [53]. MN are micron-sized needles arranged on a backing layer. Several types of MN have been designed to overcome many obstacles associated with the route of drug delivery, such as tissue barrier, first-pass metabolism, pain, and patient compliance [6]. The MN drug delivery systems have been fabricated and studied for multiple applications [54]. Each type of MN has its own specific mode of drug delivery into any given biological tissue [55]. MN has been classified based on various aspects such as applications (e.g. therapeutic, diagnostic) [56, 57], route of delivery (e.g. transdermal, ocular, buccal) [58-60], structure (e.g. solid, hollow, dissolving) [58, 59, 61], needle shape (e.g. conical, pyramid) [62, 63] and fabrication method (e.g. micro-moulding, lithography, or etching) [63, 64].

1.6.1 Types of microneedles

1.6.1.1 Solid microneedle

Solid MN follows a two-step application process in which the MN is inserted to create holes in the tissue. Next, the drug is administered topically to passively diffuse through the created holes. Solid MN is usually fabricated by silicon [61] or stainless steel [65]. However, this approach has been limited by the inherent inconvenience of the two-step process and the difficulty in controlling the delivered drug amount [55].

1.6.1.2 Hollow microneedle

Hollow MN is used to deliver liquid drug formulations to the tissue in relatively large doses compared to solid MN. This system allows drugs to be continuously injected through the hollow MN channel within the MN using different assisting techniques such

as pressure or electrical force [55]. Hollow MN is fabricated using various materials, including silicon, metal, and ceramic. However, the major drawback in hollow MN is the possibility of needle clogging during insertion and the risk of fracture due to insufficient mechanical strength [59].

1.6.1.3 Coated microneedle

Coated MN has been used to pierce the skin and deliver the deposited drug on the MN surface to the applied tissue. Coated MN have been studied to deliver DNA, vaccines, and biotherapeutics to the skin, eye, and buccal cavity [60, 66, 67]. The major limitation of coated MN is the inefficient drug loading, which mainly depends on the coating thickness [53].

1.6.1.4 Dissolvable microneedle

Dissolvable MN requires single-step application with no need for removal, leading to higher patient compliance. Upon insertion, the MN start to dissolve and release its payload. This method has been widely studied for transdermal delivery and recently for ocular delivery [62, 63, 68]. Biodegradable and biocompatible polymeric materials are used in its fabrication. Furthermore, using swellable or hydrogel-forming polymers have an additional advantage by absorbing body fluids into their three-dimensional structure and serving as a drug reservoir once they are inserted [69].

1.6.2 Methods of microneedle fabrication

Several methods have been employed for the MN fabrication. Etching is one of the traditional ways for MN fabrication. Wet etching uses 20-30% potassium hydroxide as an etchant, while dry etching uses sulfur hexafluoride/oxygen. The concentration of the etchant and the rate of etching are key steps in the fabrication of this type of MN [54, 70]. Micromoulding, lithography, two-photon polymerization and laser cutting have been commonly used in MN fabrication [71]. Recently, three-dimensional (3D) printing has emerged as a new technique to fabricate MN [72-74]. The materials used in MN

fabrication extensively varied among metal, ceramic, silicon, and polymer. The used material is expected to meet specific criteria depending on its intended use, such as biocompatibility, availability, and mechanical strength [55]. Table 1-2 summarises the different methods and materials used in MN fabrication.

Table 1-2 Summary of MN types and fabrication methods and materials.

Type of MN	Fabrication methods	Materials	Ref
Solid	Dry etching, wet etching, 3D printing, laser ablation, micromoulding, magnetorheological drawing lithography, electroplating	Metal, glass, silicone, acrylic	[61, 73, 74]
Coated	Dry etching, wet etching, 3D printing, laser ablation, micromoulding, magnetorheological drawing lithography, electroplating	Metal, glass, silicone	[67, 73, 75]
Hollow	Lithographic moulding, x-ray photolithography, 3D printing, micromachining	Metal, glass, silicone, ceramic	[59, 76-78]
Dissolvable	Micromoulding, ultrasonic welding, 3D printing, micromachining, ion etching, piezoelectric dispensing (i.e. voltage pulse dispensing)	Carboxy methyl-cellulose, hyaluronic acid (HA), PVP, sugar, dextran, PVA, PLA, chitosan, PLGA, and poly(methyl-vinylether-co-maleic anhydride)	[69, 79-81]

1.6.3 Microneedles in ocular drug delivery

The use of MN for ocular drug delivery is an emerging area of research particularly to treat posterior segment diseases like age-related AMD, diabetic retinopathy (DR), retinitis pigmentosa and uveitis [82]. MN overcome anatomical and physiological ocular barriers and deposits drug into the internal ocular tissue. Several types of MN have been studied for ocular delivery. A coated solid MN (140 μm in length) pen has been designed to locally deliver drugs to corneal stromal tissue [83], and metal solid coated MN (500–750 μm in length) also has been tested for DNA and protein delivery via

intracorneal and intrascleral routes [75]. Although solid coated MN offers a minimally invasive alternative for ocular drug delivery, the system has a drawback of limited drug loading capacity that can be incorporated on the MN surface.

Suprachoroidal injection of triamcinolone acetonide using a hollow MN system developed by Clearside's Biomedical is in phase III trial for patients with macular oedema, the hollow MN based system ensures consistent insertion and reduces the risk associated with intravitreal injection as demonstrated in Figure 1-8 [84, 85].

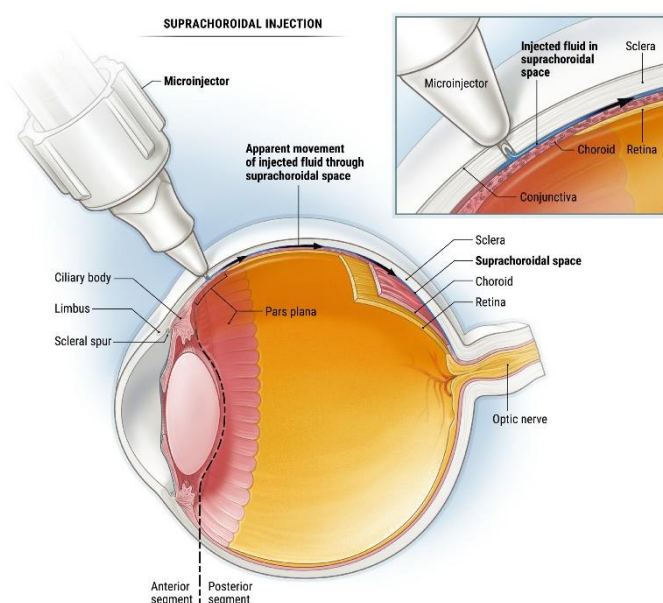


Figure 1-8 Suprachoroidal injection using hollow MN [86].

Additionally, hollow MN (800–1,000 μm in length) have been tested to deliver nanoparticle and microparticle suspensions into the posterior segment by infusion of the suspension into the suprachoroidal space [77, 87]. In another study, scleral delivery with hollow MN was investigated to infuse fluorescent tagged particles to the sclera. The particles were able to permeate the scleral tissue in the presence of hyaluronidase and collagenase enzymes [76]. However, solid and hollow MN require two-step treatment that involves MN application followed by drug administration which results in poor patient compliance.

Dissolvable polymeric MN utilises biodegradable and biocompatible polymers in which the drug is incorporated. PLA, HA, PVA, and PVP polymers have all been used to fabricate ocular dissolvable MN [58, 62, 63, 88]. Corneal delivery of besifloxacin-loaded MN showed greater antibacterial activity against *Staphylococcus aureus* infected cornea in comparison to topical besifloxacin solution [58]. Another study demonstrated superior effectiveness in treating corneal neovascularization by applying anti-angiogenic monoclonal antibody-loaded MN against topical eye drops through corneal application [63]. In a different approach, a dissolving MN array has been attached to a contact lens. A study displayed the potential of delivering high molecular weight cyclosporin A in a controlled manner using a PVP MN array attached to a contact lens [89]. While another study investigated the delivery of pilocarpine to the corneal membrane using MN patch fabricated by PVA and PVP mixture fixed on a contact lens. The MN array showed greater permeation of pilocarpine compared to the drug solution [90]. A study investigated the feasibility of delivering various molecular weight drugs through scleral and corneal MN application, high degree of permeation of large molecular weight (150 kDa) was observed [62]. In another study, a strategy of computational design by central composite design-response surface methodology (CCD-RSM) was used to design and optimize dissolvable MN arrays for ocular delivery [91]. Furthermore, a dissolvable MN system containing PLGA nanoparticles loaded with ovalbumin protein to release the particles within the ocular tissue displayed a sustained release of the protein to treat neovascular ocular diseases [92]. In general, MN application has shown great potential for drug retention within the selected ocular tissues, unlike topical application.

1.7 3D printing overview

In 1960 an experiment was performed to polymerise resin by using two different wavelength laser beams, and more studies investigated rapid prototyping using laser beams were conducted. Later, in 1984 Charles Hull submitted a patent for stereolithography and subsequently coupled the invention by the 3D system to produce the first commercial 3D printer [93].

3D printing or additive manufacturing includes several techniques that enable the construction of 3D solid structures from computer-aided design (CAD). CAD file contains the geometrical outlines of the 3D structure designed by specific CAD generating software. This CAD file is next converted to a file that can be interpreted by the printer. Standard tessellation language (.STL) files and object wavefront (.OBJ) files, are commonly used for 3D printing. These files are broken down by the printer system into a series of horizontal layers. The printer head moves in X-Y coordinates to print each layer on top of the previous layer to project in a vertical (Z-axis) orientation [94]. Different 3D technologies require additional considerations with respect to the type of material and 3D printer specifications [94, 95]. 3D printing has been utilised in many pharmaceutical and medical applications, including the fabrication of laboratory hardware, microfluidic chips, moulds and templates, catalytically active surfaces and biomedical engineering [94]. In the last decade, a variety of 3D printing technologies have been introduced. A brief description of the types of 3D printing technologies will help to compare and explore application possibilities. The principle of 3D printing is mainly based on three concepts, liquid solidification (e.g. drop on drop deposition, stereolithography), powder solidification (e.g. selective laser sintering or melting, powder bed fusion), and extrusion (e.g. fused deposition modelling, pressure assisted syringe) [96].

Among the various 3D printing techniques, photopolymerization, which is a liquid solidification 3D printing technique that works by photopolymerizing a photosensitive liquid resin by high energy light, e.g. laser beam. The photopolymerization concept includes various techniques such as stereolithography (SLA) digital light processing (DLP), continuous liquid interface production (CLIP) and two-photon polymerization (2PP) [97].

Recently, the SLA 3D printer has become one of the most used photopolymerization technology [98]. SLA uses a laser beam that cures the resin point by point, tracing the model's cross-sectional layers. The laser cures the resin layer by layer on the building platform (Figure 1-9). The laser beam is directed by a lens or mirror at the surface for

top-up printing or directed to the bottom of the tank for bottom-down printing, as shown in Figure 1-10.

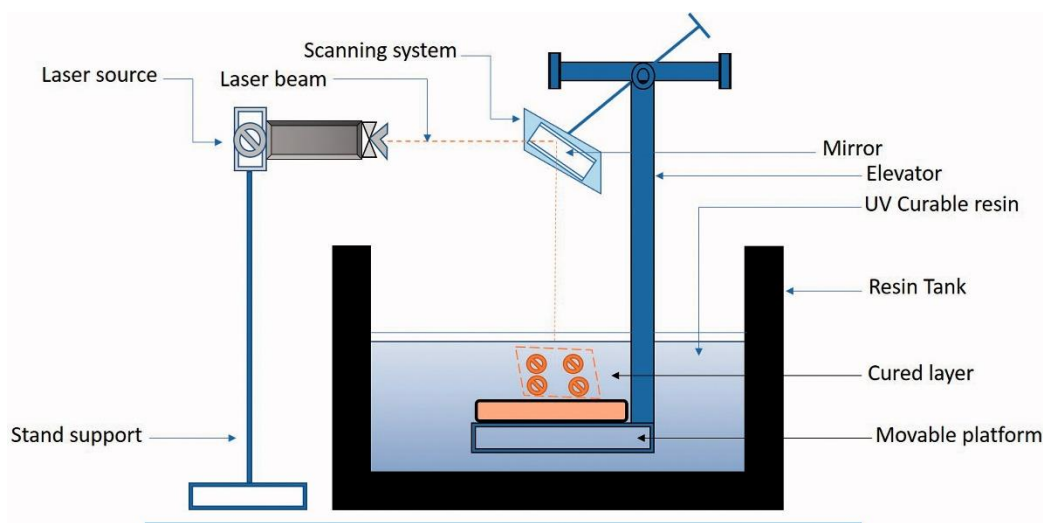


Figure 1-9 Configuration of SLA 3D printer [96].

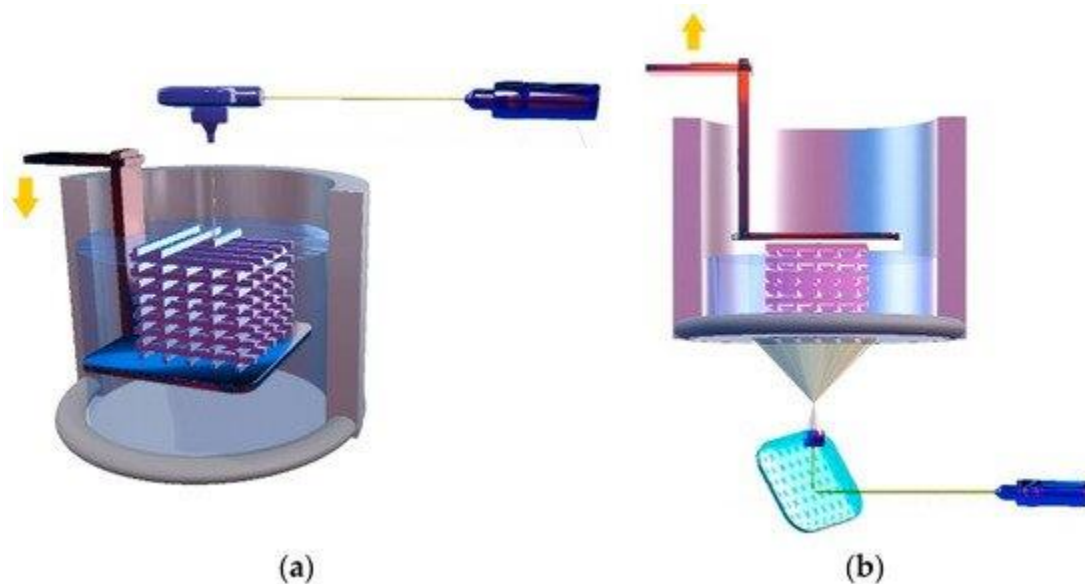


Figure 1-10 Schematic illustration of (a) top-down and (b) bottom-up SLA printer [99].

SLA has some key advantages which make it one of the most popular printers today. It consists of the high precision of the laser beam allows for printing objects with high resolution and relatively smooth surfaces [100]. The choice of liquid resin is crucial for the overall printing resolution. Although the FDA has approved several biocompatible

3D printing resins for dental purposes, no resins have yet been approved for use in pharmaceutical applications [101]. The most used photo-curable materials are acrylates, epoxides, and urethanes. Another component of the liquid resin is the photo-initiators, poly(ethylene glycol) diacrylate (PEGDA), poly(2-hydroxyethyl methacrylate) (pHEMA), poly(ethylene glycol) dimethacrylate (PEGDMA), and diphenyl(2,4,6-trimethylbenzoyl) phosphine oxide are used as photo-initiators [100, 102]. Investigational MN patches were also fabricated by SLA 3D printing to transport solutes with different molecular weights [72]. In a recent study, two different 3D printing technologies were used to fabricate MN patches to deliver insulin. The MN was SLA printed, then coated by insulin mixed with other excipients such as trehalose, mannitol, and xylitol by inkjet printing [73, 103]. Recently, SLA 3D printing was utilised to generate masters for MN preparation [104].

In contrast to SLA printers, DLP and CLIP printers use a projector light source instead of a laser beam, curing a whole layer at once and hence, providing faster printing compared to SLA. DLP printers use a glass window to cure the resin, whereas CLIP printers use an oxygen-permeable window. The limitation relies on the accuracy of printing, which mainly depends on the projector's light pixel resolution [99]. Meanwhile, in the two-photon polymerization technique absorption of NIR light is used to excite the photoinitiator by two-photon absorption in a liquid monomer solution at the focal point, initiating a polymerization reaction in a very small volume known as a "voxel" [13]. Using this technology, the material is no longer deposited "layer by layer," allowing the fabrication of complex 3D microstructures. Up until now, the 2PP printer has been the most accurate and precise 3D printing technology. However, the utilization of 2PP for pharmaceutical applications is constrained by the toxicity of many feedstock materials [105]. Besides, the equipment is more expensive than other photopolymerisation based 3D printers [99].

1.7.1 3D printing in pharmaceutical applications

3D printing is increasingly prevalent in the pharmaceutical industry. This versatile technology provides the ability to design, prototype, and produce pharmaceutical products [95]. The recent progress in 3D printing technologies facilitates the production of simple laboratory hardware to more complicated organ implants [94]. In the drug delivery field, approaches to design personalised medicine to meet comprehensive patient needs are now possible [101, 106]. 3D printing was utilised to create templates, masters, moulds, and microfluidic devices [94]. In 2016, the FDA approved the first 3D printed tablet, SPRITAM® (levetiracetam). The tablets were printed by the patented 3D printing technology ZipDose®, which was designed to produce rapidly disintegrating dosage form [107]. Fabrication of personalised high-resolution MN by 3D printing was also reported [64, 108]. The use of 3D printing for implant and prosthesis fabrication has revolutionized the area by delivering simple and cost-effective manufacturing techniques [109, 110]. Recently, bioprinting of biological material and cells to produce functional 3D living tissue has been introduced. The technology has already succeeded in creating humane-scale tissue for transplantation [111, 112].

1.8 Polymers used for ocular drug delivery

Polymers are large macromolecules composed of repeating subunits known as monomers. Generally, polymers are classified as natural or synthetic. Synthetic polymers are based on chemically obtained monomers, while natural polymers, also known as biopolymers, are composed of naturally occurring monomers. Recent studies have demonstrated the employment of both synthetic and natural polymers in the fabrication of ocular drug delivery to control the release, increase the drug solubility, improve the mechanical properties, and regulate pharmacokinetic performance [113, 114].

The FDA has approved numerous synthetic and natural polymers for ocular delivery, including PVA, PGA, PLGA, PCL, poly[2-(dimethylamino)ethyl methacrylate] (DMAEM), poly(ethylene glycol) (PEG), poly(acrylic acid) (PAA), and poly(amidoamine) (PAMAM)

as synthetic polymers [114]. In addition, chitosan, hyaluronic acid, collagen, carboxymethyl cellulose (CMC), gelatine, and inulin natural polymers have also been approved [113, 114].

Due to their versatility, synthetic and natural polymers are utilised in the preparation of numerous drug delivery vehicles used in the realm of micro- and nano- technology, including micelles, liposomes, microparticles, and nanoparticles. These drug delivery systems have been incorporated into drug delivery platforms such as hydrogel, contact lenses, and MN to facilitate and enhance ocular delivery [114]. Several micro and nanoscale systems including nanospheres, nanocapsules, liposomes, micelles, hydrogel, and dendrimer fabricated using polymers were used in ocular delivery. These nanosystems can also be loaded into a delivery carrier such as contact lenses and MN (Figure 1-11).

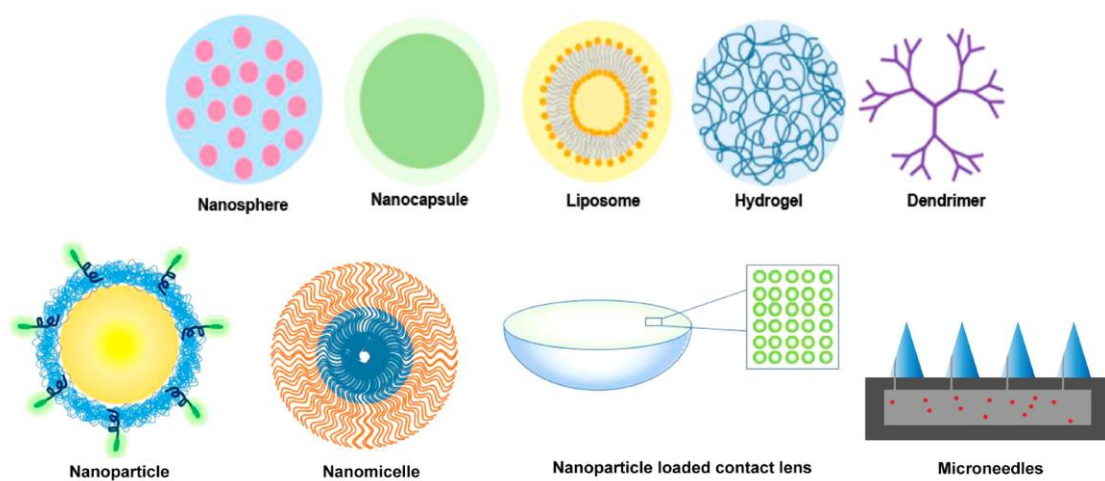


Figure 1-11 The uses of synthetic and natural polymers to prepare micro and nanoscale formulations to enhance and control ocular drug delivery [114].

Typically, a single polymer may not provide the essential characteristics required, hence combining two or more polymers to modulate features such as mechanical strength, swelling behaviour, drug release rate, and degradation time is necessary to reach optimal performance [113].

1.8.1 PLGA in ocular delivery

Owing to its favourable physicochemical and biological attributes, PLGA has been commonly employed to fabricate several systems for ocular delivery purposes, either alone or in combination with other polymers [114, 115]. Implementation of PLGA in ocular delivery is intended to produce a controlled release vehicle. The polymer's mechanical and biodegradation properties can be controlled by modifying the relevant physicochemical parameters such as molecular weight, functional groups, and the ratio of lactide to glycolide [114]. Several PLGA-based drug delivery systems were prepared to target both anterior and posterior segments. This includes a plethora of payloads ranging from small molecules such as dexamethasone [116] and fluocinolone acetonide [117] to macromolecules such as bevacizumab [118], infliximab [119], and ranibizumab [120]. PLGA-based ocular delivery systems were fabricated to form a variety of structures such as nanoparticles [121], microparticles [12], *in-situ* hydrogels [122], and implants, including the commercially available Ozurdex® and DURYSTA™ [31]. Moreover, PLGA can be versatile enough to allow for a relatively shorter release time, as proven in the commercially available product Surodex™ intraocular biodegradable implant. Suradex is a rod-shaped implant composed of dexamethasone in PLGA and hydroxypropyl methylcellulose matrix. It is intended to treat postoperative inflammation after cataract surgery over the course of 7-10 days [30]. Hence, all PLGA-based formulations add an advantage to controlling drug release intraocularly by providing a new drug pharmacokinetic profile. Even large molecules, such as monoclonal antibodies, showed extended intraocular half-life when delivered in PLGA microparticles formulation [120].

1.8.2 PLGA particles fabrication methods

PLGA is an FDA-approved biodegradable and biocompatible polymer for medical applications [123]. It has shown great potential in fabricating versatile drug delivery carriers, scaffolds in tissue engineering, and surgical sutures [124]. As a drug carrier,

PLGA microparticles and nanoparticles have been produced by several methods as outlined below.

1.8.2.1 Emulsion solvent evaporation method

Emulsion solvent evaporation is one of the most commonly used methods in preparing PLGA particles [125]. This approach is suitable for preparing micro- or nano- particles loaded with hydrophilic or lipophilic drugs. It can be prepared as single oil in water (o/w) emulsion or double emulsion as water in oil in water (w/o/w). The single emulsion approach is mainly used to encapsulate hydrophobic drugs (e.g. corticosteroids) [12]. The drug and the PLGA are dissolved in a suitable organic solvent to prepare a solution, and then the solution is gradually added to water phase containing a stabilising/emulsifying agent (e.g. PVA). The two solutions are mixed at specified stirring speed, time, and temperature. The dispersion is then kept under continuous stirring to evaporate the organic solvent. The resultant PLGA particles are washed several times to remove the excess stabilising/emulsifying polymer. On the other hand, the double emulsion (w/o/w) approach is best suited for hydrophilic drugs (e.g. proteins). The preparation starts with dissolving the drug in water to prepare an aqueous solution, which is later added to the organic solution of PLGA, then, the mixture is vigorously stirred to prepare the primary w/o emulsion. Next, the primary emulsion is added to an aqueous solution of stabilising/emulsifying polymer and stirred at high speed to prepare w/o/w emulsion. The organic solvent is then allowed to evaporate then the particles are finally washed. Adjusting the process parameters like the choice of solvent and the mixing speed will affect the PLGA particle size and encapsulation efficiency [124].

1.8.2.2 Phase separation

Phase separation, also known as coacervation is a process of preparing micro-sized particles encapsulation by liquid-liquid phase separation method. The PLGA is dissolved in an organic solvent in a specific ratio. If the drug is hydrophilic, it will be dissolved in

water and dispersed in the PLGA solution, and if the drug is hydrophobic, it will be dissolved in the PLGA organic solution. Different organic solvents will be added to the polymer-drug phase while stirring. Soft coacervate of drug-polymer droplets will be formed by phase separation. Later, the mixture will be dipped into an insoluble medium to quench the formed microdroplet. Microparticles are extracted from the system by washing, filtration, or freeze-drying. The method parameters like the concentrations, the quenching temperature and time will affect the shape and size of the particles [124, 126].

1.8.2.3 Spray drying

Spray drying is a fast and efficient method to prepare PLGA particles on a large scale. In this process, the drug-loaded particles are prepared by spraying w/o emulsion or drug in an oil dispersion in a stream of hot air. The choice of the solvent used in the process will be governed by the hydrophilicity of hydrophobicity of the loaded drug. This method can be employed to encapsulate the drug in micro- or nano- particles without affecting their activity. In addition, changing the process parameters such as the orientation of jets, heat flow rate, and solvent type can develop uniform particles with controllable shell thickness [124, 127].

1.8.2.4 Electrospraying

The process is based on injecting a conductive solution containing the PLGA and the drug by a syringe pump. The drug/polymer solution is subjected to electrical potentials that generate an electric stress that accelerates the liquid flow from the syringe to create a jet. The jet then breaks to small particles due to the repulsion of the opposite charges generated at the jet surface. Depending on the processing conditions, electrospray can produce nanosized and micronized particles [128].

1.8.2.5 Direct Precipitation

In this method, PLGA particles are formed by interfacial deposition of the polymer following the displacement of water miscible organic solvent with an aqueous solution [129]. PLGA is co-dissolved with the drug in water-miscible organic solvents such as acetone. The organic phase is added dropwise to a larger volume of the aqueous phase with continuous stirring until the organic solvent is completely evaporated [130].

1.9 Corticosteroid overview

Since 1949, corticosteroids have been among the most effective anti-inflammatory medication used to treat ocular inflammations [131]. Dexamethasone, triamcinolone acetonide, fluorometholone, prednisolone, and loteprednol etabonate are among the most widely used corticosteroid for the management of ocular diseases [132]. The anti-inflammatory effect of corticosteroids relies mainly on the direct impact on gene expression. Their therapeutic action is activated by the interaction with cytosolic glucocorticoid receptors (GR). Signalling the GR receptors inhibits the expression of inflammatory associated molecules such as cytokines, chemokines, and adhesion molecules by inhibiting the activity of the transcription factor NF- κ B [133]. Additionally, corticosteroids work by reducing the levels of IL-1 α and IL-1 β mRNAs in a dose-related manner [134]. However, the major complication associated with corticosteroid ocular therapy is the increase in intraocular pressure (IOP), which mainly depends on the dose and the frequency of administration [135].

1.9.1 Dexamethasone in ocular delivery

Dexamethasone is one of the most prescribed corticosteroids for ocular delivery [136]. It is commonly prescribed to treat ocular inflammation in the anterior and posterior segments, such as conjunctivitis, uveitis, and macular oedema. It is also prescribed for the management of postoperative inflammation [132]. Commercially available dexamethasone ocular dosage forms include topical solutions, topical suspensions, ointments, intraocular suspensions, and ocular implants. Dexamethasone has a potent

immunosuppressant activity, and hence, a very low concentration of dexamethasone is required to treat the eye locally. A concentration as low as 1 µg/mL is sufficient to produce an anti-inflammatory effect [137]. A lower concentration of the drug can minimise corticosteroid related side effects. The two main side effects associated with dexamethasone ocular administration are cataracts and IOP elevation. Studies have confirmed that IOP elevation was lower in patients treated with dexamethasone implants compared to other corticosteroids such as fluocinolone acetonide and triamcinolone acetonide implants [138].

Dexamethasone was the drug of choice to formulate most of the marketed long acting implants such as Ozurdex®, Dextenza®, and DEXYCY® which is mainly due to its potency, safety, and low solubility in water (89 mg/L) [132]. The main challenge in dexamethasone ocular delivery is to design a dosage form that maintains a longer ocular resident time with less invasive application and minimal local side effects [132].

1.10 Thesis aim

Through the above literature, it is excerpted that ocular drug delivery opposes major challenges to overcoming the eye anatomical and physiological barrier in a minimally invasive manner. This study aims to develop a novel minimally invasive drug delivery system composed of drug-loaded biodegradable PLGA particles incorporated in a dissolvable polymeric microneedle array using a flexible and customisable 3D printed mould. The system aimed to pierce the scleral surface and deposit the loaded particles within the scleral tissue to serve as a drug reservoir allowing controlled drug delivery of the loaded drug, in this case, dexamethasone, to the back of the eye.

In order to achieve the aim of this thesis, studies to optimise a 3D printed mould using a cost-effective widely available SLA 3D printer to be used in the fabrication of the MN array were conducted. Then, PLGA particles were prepared to be incorporated into an optimised polymeric base composed of a PVP and PVA blend. The capacity of the MN system to successfully deposit and deliver the loaded PLGA particles into the sclera

inner tissue was investigated. Comprehensive *ex-vivo* and *in-vivo* studies were performed to assess the particle deposition and the drug delivery capability of the system.

1.11 Thesis graphical overview

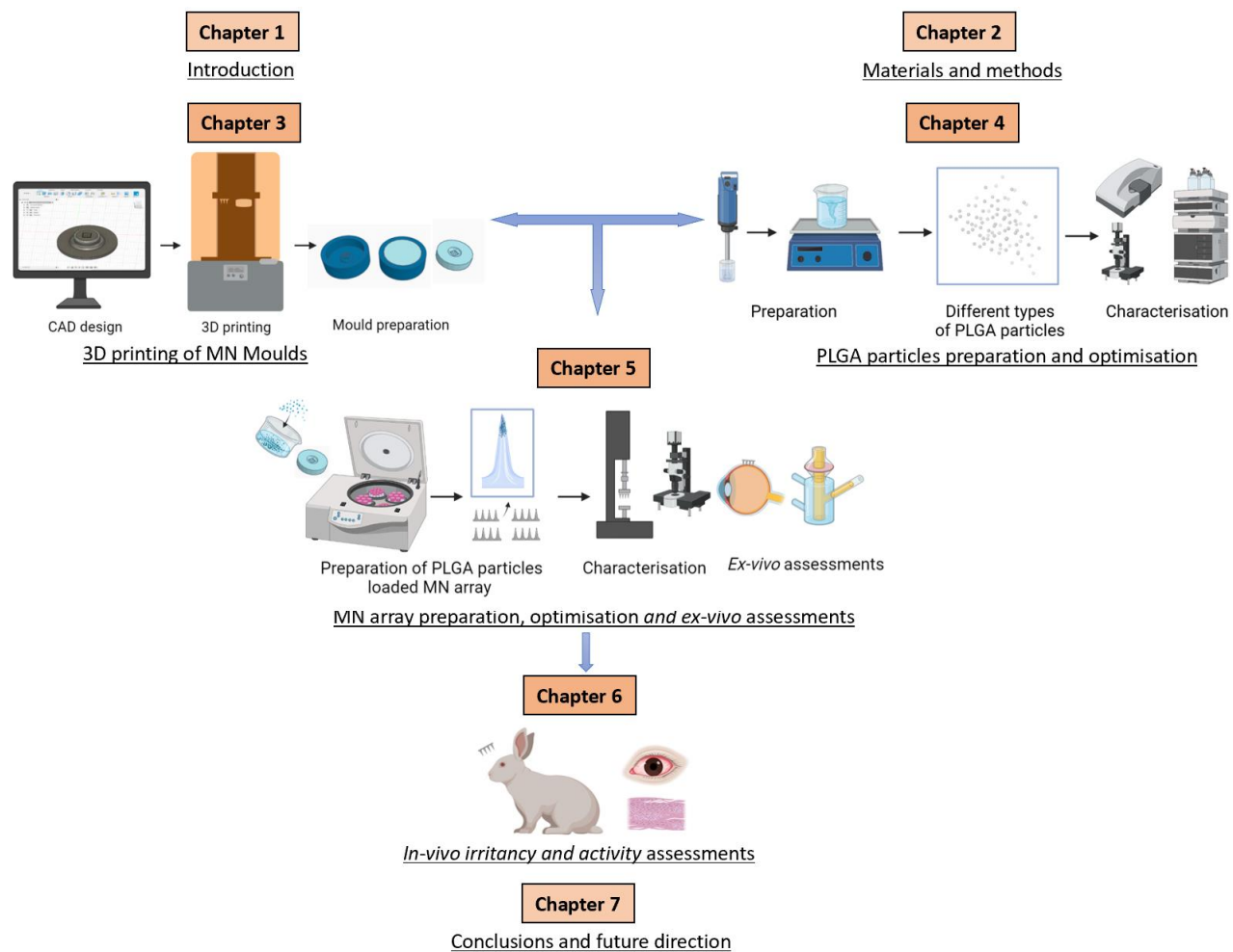


Figure 1-12 Thesis Graphical overview (created by Biorender).



Chapter 2 Materials and methods

2.1 Materials

The main materials used in this thesis are briefly described in the following sections. Further information regarding the materials and the reagents used are given in the materials section in each experiment chapter.

2.1.1 Poly (vinyl alcohol)

Poly(vinyl alcohol) (PVA), $(C_2H_4O)_n$ is a synthetic polymer obtained from partial or full hydrolysis of polyvinyl acetate by removing the acetate groups (Figure 2-1). The degree of hydroxylation determines the physicochemical properties of the polymer. The molecular weight depends on the initial length of the polyvinyl acetate chain, which ranges between 20 and 400 kDa [139]. PVA is soluble in water and insoluble in most organic solvents. The degree of hydrolysis and the molecular weight affect its water solubility. The high degree of hydrolysis necessitates high temperature over a long time to break inter- and intra- molecular hydrogen bonds [140].

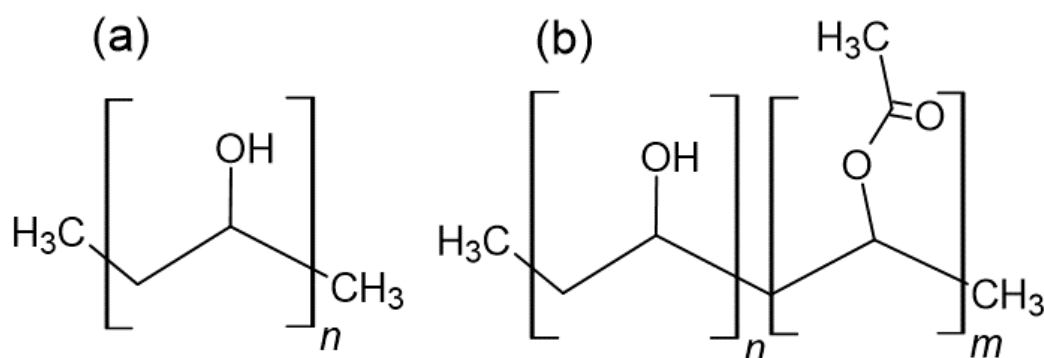


Figure 2-1 Chemical structure of PVA (a) fully hydrolysed, (b) partially hydrolysed, (created by ChemSketch).

PVA is a biodegradable, biocompatible, nontoxic, and noncarcinogenic polymer that has been widely used in biomedical and pharmaceutical applications as a stabiliser, viscosity enhancer, and lubricant. Blending PVA with other biopolymers or hydrophilic polymers has been utilised to modify the mechanical properties of pharmaceutical dosage forms such as corneal implants and oral films [141, 142].

It has been frequently used in ophthalmic preparations such as eye drops, artificial tears, ocular implants, contact lenses, and as an excipient in many formulations [141]. PVA is one of the most efficient stabilisers (0.25-3% w/v) for emulsions, especially in the preparation of PLGA micro- nano- particles [141, 143].

In this study, PVA was used in the preparation of PLGA particles as a stabilising agent and in the fabrication of MN array polymeric base. PVA was purchased from Merck Sigma Aldrich and the specification data are presented in Table 2-1.

Table 2-1 Poly(vinyl alcohol) properties provided by the manufacturer.

Property	Information
Form	White to light yellow powder
Manufacturer	Merck Sigma Aldrich, USA
Formula	$[-CH_2CHOH-]_n$
Mwt	31,000-50,000
% Hydrolysed	98-99%
Viscosity	5.5- 6.6 cps
pH	5.0-7.0

2.1.2 Polyvinylpyrrolidone

Polyvinylpyrrolidone (PVP), $(C_6H_9NO)_n$ or povidone is a synthetic polymer obtained by free radical polymerization of linear 1-vinyl-2-pyrrolidinone groups (Figure 2-2). The different degrees of polymerization give the polymer a range of molecular weights from 2500 to 3 million [141, 144]. PVP polymer is usually characterized by its aqueous viscosity. PVP has been used in a variety of pharmaceutical formulations; it is frequently used as a coating agent, solubilising agent, suspending agent, binder, disintegrant, and viscosity-enhancing agent. It has been commonly employed in ophthalmic preparations, such as hydrogels [145], moisturizing eye drops (e.g. Refresh™), and dissolvable MN fabricated for ocular [62] and transdermal [56] delivery.

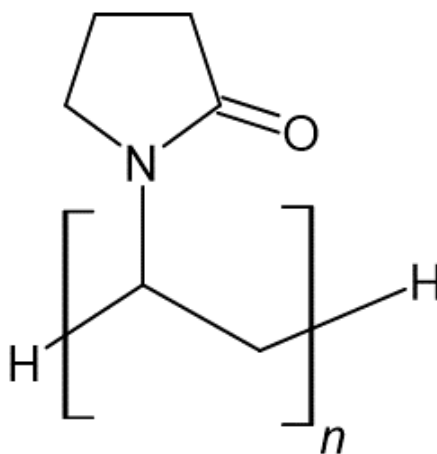


Figure 2-2 Chemical structure of PVP, (created by ChemSketch).

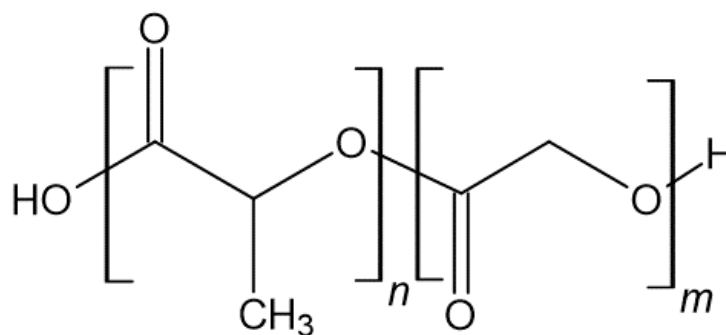
Two grades of PVP were used in this study, Kollidon® 90F and Kollidon® 30 (BASF Pharma, Germany). The soluble grade of Kollidon® is a white to yellowish, free-flowing powder. Kollidon® 90F has a high degree of viscosity in water due to the high molecular weight of the polymer chain, which can serve as a good candidate for the formulation of dissolving MN [146]. Kollidon® 30 has a relatively low viscosity in aqueous solution, and it is also used in the preparation of dissolving MN [147]. The properties of the two grades of Kollidon® are summarized in Table 2-2.

Table 2-2 Properties of Kollidon®30 and Kollidon®90F, provided by the manufacturer.

Property	Information	
	Kollidon® 30	Kollidon® 90F
Form	White powder	
Manufacturer	BASF, Germany	
Formula	[-CH ₂ CHOH-] _n	
Mwt	44000 – 54000	900000 – 1200000
pH	3-5	4-7
Viscosity (1% in water)	1.201 – 1.281 mPa.s	3.310 – 5.195 mPa.s
Solubility	Soluble in chloroform, ethanol, n-propanol and water	
Tg₂ [°C]	171	177

2.1.3 Poly (lactic-co-glycolic acid)

Poly (lactic-co-glycolic acid) (PLGA) is a synthetic biodegradable polyester, mostly synthesized by ring-opening polymerization of lactide and glycolide (Figure 2-3). PLGA degrades in the body by hydrolysis to produce its original monomers, which can be completely metabolized by hydrolysis to lactic and glycolic acids that are naturally eliminated *in-vivo*. The degradation time of PLGA varies from days to years, depending on the ratio of lactide to glycolide. The presence of methyl groups in lactide makes it more hydrophobic than glycolide, and hence the higher the content of lactide in the copolymer, the less water hydrolysis occurs, and subsequently more extended degradation period is required [148, 149]. PLGA has been widely used in drug delivery as a biodegradable carrier and in tissue engineering as a scaffold [150]. The FDA has approved the use of PLGA for ophthalmic preparation [114].



n: number of lactic acid units
m: number of glycolic acid units

Figure 2-3 Chemical structure of PLGA, (created by ChemSketch).

PURASORB PDLG 7507 and 7502 were used in this project to prepare micro- and nano-particles for ocular delivery. The PLGA used has a 75:25 molar ratio of lactide to glycolide that has a slower degradation rate compared to the 50:50 molar ratio [151]. Low (7502) and high (7507) viscosity PLGA has been used for particle fabrication. Product specifications are listed in Table 2-3.

Table 2-3 Properties of PURASORB PDLG, provided by the manufacturer.

Property	Information
Form	White to light tan granules
Composition	75/25 DL-lactide/glycolide copolymer
Manufacturer	Corbion Purac, Netherlands.
Formula	$[(C_6H_8O_4)_x(C_4H_4O_4)_y]_n$
Viscosity	7507 0.5% in chloroform at 25 °C 0.56-0.84 dL/g 7502 1% in in chloroform at 25 °C 0.16-0.24 dL/g

2.1.4 Polydimethylsiloxane

Polydimethylsiloxane (PDMS) or dimethicone is a mixture of fully methylated linear siloxane polymers containing repeating units of the formula $[-(CH_3)_2SiO-]_n$ (Figure 2-4) [141].

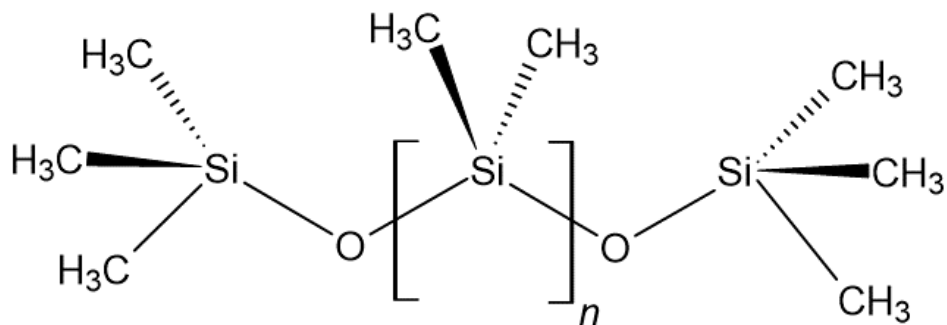


Figure 2-4 Chemical structure of PDMS, (created by ChemSketch).

PDMS has a wide range of viscosity, from liquid (low n) to semi-solid (high n), depending on the size of the polymer chain. Crosslinked PDMS cures to form a hydrophobic elastomer structure. PDMS is insoluble in both water and ethanol. The liquid phase is soluble in benzene, chloroform, and ether. It has been widely used as an antifoaming, emollient and water-repelling agent. Cured PDMS has been used for mould casting, microfluidic chip fabrication and prototyping [152].

In this project, SYLGARD™ 184 silicone elastomer kit from Dow Corning was used to prepare flexible reverse moulds. It is a clear silicone flowable liquid that cures when mixed with a curing agent to form a flexible elastomer structure. The kit contains two parts to be mixed in a 10:1 ratio (w/w or v/v) base to curing agent. The mixture is poured into the desired container. It can be cured at room temperature for 48 h or at a higher temperature for fast curing (45 min at 100 °C, 20 min at 125 °C, and 10 min at 150 °C) [153].

Table 2-4 SYLGARD®184 silicon properties.

Property	Information
Form	Base and curing agents are colourless liquid
Manufacturer	Merck Sigma Aldrich, USA
Formula	C ₂₀ H ₁₈ N ₂ O ₂ S
Viscosity	4000.00 - 6500.00 cSt
Tensile strength	~5.2 MPa

2.1.5 Coumarin-6

3-(2-benzothiazolyl)-N,N-diethylumbelliferylamine, 3-(2-benzothiazolyl)-7-(diethylamino)coumarin (Figure 2-5).

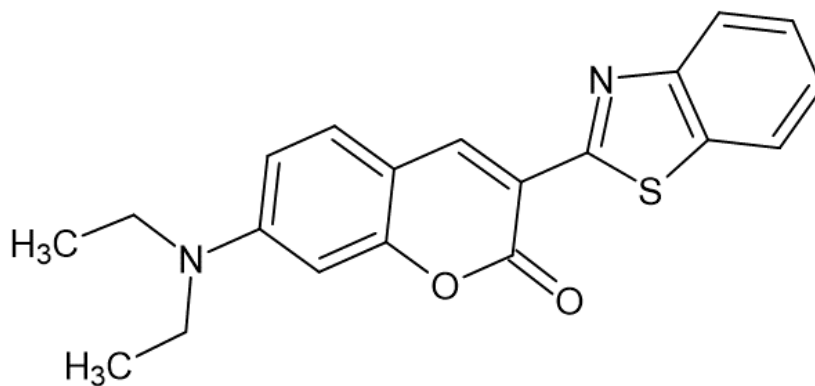


Figure 2-5 Chemical structure of coumarin-6, (created by ChemSketch).

Coumarin-6 is a heterocyclic benzo- α -pyrone resulting from the fusion of a pyrone ring with a benzene nucleus. Coumarin derivatives have been widely found in many plants. It has been frequently used in the pharmaceutical field as a model for poorly-soluble drugs, as a fluorescence probe, as a traceability marker of *in-vitro* drug delivery testing, and as an indicator for microenvironments such as viscosity and pH change due to its solvatochromic shift [154]. Coumarin-6 is water insoluble orange powder with stable fluorescence activity, which makes it a suitable fluorescence probe for encapsulation in PLGA particles prepared by the single emulsion method. In this project, coumarin-6 from Merck Sigma Aldrich was used as a marker to prepare fluorescent labelled PLGA particles. Table 2-5 shows the properties of coumarin-6 provided by the supplier.

Table 2-5 Properties of coumarin-6 provided by the manufacturer.

Property	Information
Form	Orange to very dark orange powder
Manufacturer	Merck Sigma Aldrich, USA
Formula	$C_{20}H_{18}N_2O_2S$
λ_{max}	444 nm
Fluorescence	λ_{em} 505 nm in ethanol
Purity	> 97.5 %

2.1.6 Dexamethasone

Dexamethasone is 9 α -fluoro-11 β ,17 α ,21-trihydroxy-16 α -methylpregna-1,4-diene-3,20-dione or 1-dehydro-9 α -fluoro-16 α -methylhydrocortisone (Figure 2-6). Dexamethasone is a synthetic adrenal member of glucocorticoids, a subclass of corticosteroids. It has a significantly more potent anti-inflammatory, immunosuppressive, and anti-allergic activity compared to other corticosteroids [155].

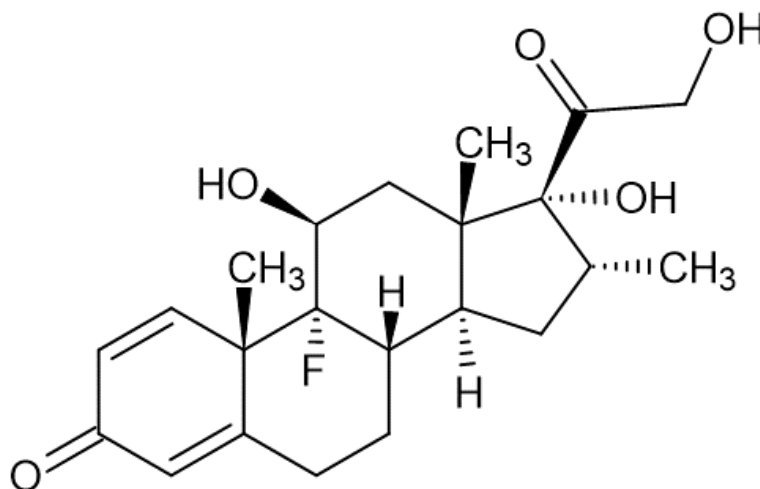


Figure 2-6 Chemical structure of dexamethasone, (created by ChemSketch).

Among corticosteroids, dexamethasone is one of the most commonly prescribed drugs to treat a variety of anterior and posterior segment ocular conditions, such as conjunctivitis, keratitis, uveitis, dry eye, age-related macular degeneration, and macular oedema [132, 156]. It has also been used as an immunosuppressant to manage corneal graft rejection [157]. Dexamethasone has a high affinity to intracellular GR α that subsequently activates the expression of anti-inflammatory effect [132, 158, 159]. It is very effective in inhibiting the expression of inflammatory cytokines and chemokines and downregulating the production of matrix metalloproteinase (MMP-3) [160]. In this project, dexamethasone was loaded into biodegradable PLGA particles. It is available as a white odourless crystalline powder with a slightly bitter taste and partial solubility in water (89 mg/L at 25 °C) [161]. Specifications of dexamethasone are listed in Table 2-6.

Table 2-6 Properties of dexamethasone provided by the manufacturer.

Property	Information
Form	White powder
Manufacturer	Merck Sigma Aldrich, USA
Formula	$C_{22}H_{29}FO_5$
Melting point	262-264 °C
solubility	Soluble in DMSO Sparingly soluble in acetone, ethanol, and methanol. Slightly soluble in chloroform, ether. Practically insoluble in water.

2.1.7 Clear resin

Clear® is a photoactive resin purchased from Formlabs®. Clear is a light yellowish viscous liquid composed of a mixture of methacrylic acid esters and a photoinitiator. Uncured resin is slightly soluble in water and soluble in organic solvents. Printed and cured resin is compatible with most aqueous solutions, including 5% acetic acid, isopropyl alcohol, 3.5% NaCl solution, and water. However, cured resin cracks in acetone and distorts in strong acids [162]. The printed objects are transparent, displaying the internal features as shown in Figure 2-7. This resin offers high-resolution printing (25 μm) with a strong and smooth surface [162].



Figure 2-7 3D printed objects using Formlabs® clear resin [162].

Table 2-7 Properties of Clear resin provided by the manufacturer.

Property	Information
Form	Liquid
Manufacturer	Formlabs, Inc., USA
Ingredients	Methacrylated oligomer ($\geq 75\%$ - $\leq 90\%$) Methacrylated monomer ($\geq 25\%$ - $\leq 50\%$) Diphenyl (2,4,6-trimethylbenzoyl) phosphine oxide ($< 1\%$)
Tensile Strength	38 MPa (uncured) 65 MPa (cured)
Viscosity	Dynamic viscosity at 25 °C is 850 to 900 mPa-s

2.2 Methods

In the following section, a brief overview is given of the basic principles of the methods used for the development, characterization, and activity testing of the fabricated drug delivery system. The parameters of the experiments are discussed in the methods section of each experimental chapter.

2.2.1 Methods of processing

2.2.1.1 3D design

To design a 3D model, a computer-aided design (CAD) is used to create, modify, and analyse 2D and 3D models. CAD program offers a coordinate (X-Y-Z axis) virtual drawing space with programmed functions to generate a drawing. There are various types of CAD software available in the market, varying in functions, operation properties and cost [163]. Here in this study, Fusion 360™ (Autodesk®, USA) was used. Fusion 360™ is a cloud-based 3D designing CAD with comprehensive modelling tools and advanced analysis methods. The software interface is shown in Figure 2-8.

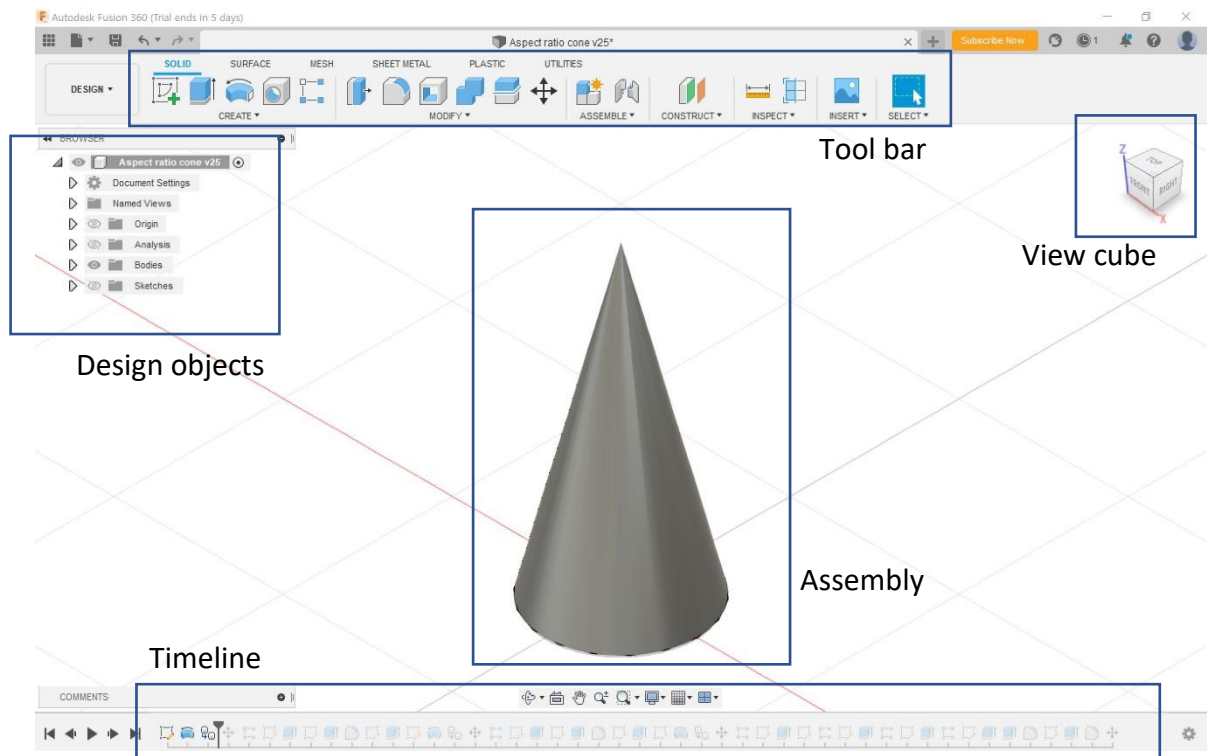


Figure 2-8 Fusion 360™ interface components.

2.2.1.2 Stereolithography 3D Printing

As mentioned in section 1.7, photocuring printing is the first developed 3D printing technique [164]. SLA is an additive manufacturing process that enables the fabrication of solid objects from CAD files. The 3D design is created by computer software that uses mathematical equations to create the internal and external geometry of the 3D object. The CAD design is saved as printable .STL or .OBJ file, the file is uploaded to 3D printing software to slice the 3D structure into 2D slices to be used as a pattern for the layer-by-layer printing process. The slice thickness is determined by the 3D printer software, which usually ranges from 25 to 100 μm . The processed data are then transferred to the SLA printer, and the structure is fabricated accordingly [165, 166]. The fabrication of 3D structures by SLA 3D printer is based on digitally controlled layer-by-layer solidification of photosensitive liquid resin by a laser beam. In the SLA printer, the liquid resin is filled into a tank that is activated when exposed to sufficient photo energy. The laser beam illuminates at a specified wavelength to solidify the resin spot by spot to

form the first layer. This first solid layer adheres to the building platform, and subsequently, the building platform moves in the Z axis at a distance equal to the layer thickness, allowing the next layer to cure on the previous layer. The process is repeated to finally build a 3D structure, as shown in Figure 2-9. Once the printing is completed, the object is separated from the building platform and then washed to remove excess resin adhered to the object surface. The object is further cured by UV light to neutralize the remaining reactive group. This post-curing step improves the mechanical strength and stability of the printed objects [166, 167].

SLA compatible resin is the main limitation of the technique. The resin must be a flowable liquid that rapidly solidifies upon exposure to the illuminating source. Resins used in SLA printers are composed of low molecular weight functionalized monomers, usually mixed with photoinitiators and photoinhibitors to initiate and terminate the photopolymerization and crosslinking reactions. Biodegradable resin made of functionalised oligomers with ester or carbonate hydrolysable bonds has been developed [168, 169].

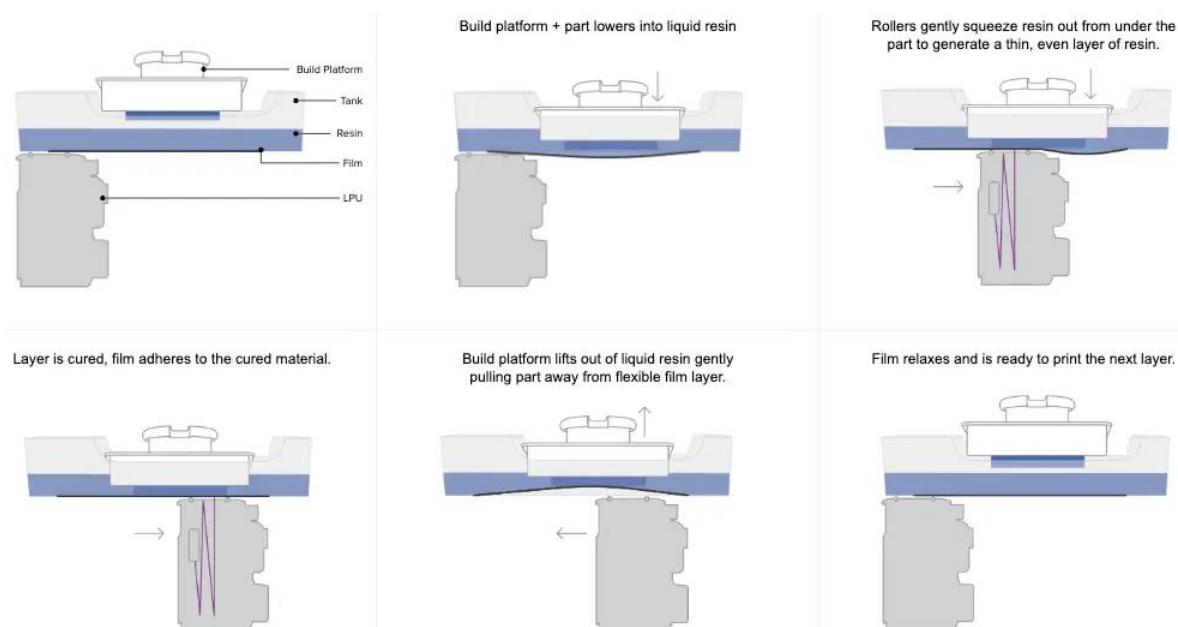


Figure 2-9 Schematic illustration of SLA 3D printing process, (LPU is the light processing unit) [170].

SLA 3D printers are one of the most robust, fast, efficient, and cost-effective 3D printing techniques, with the highest printing accuracy and resolution. It has been extensively used for rapid prototyping, laboratory tools, moulds, and microfluidic chips manufacturing. It has been investigated in biomedical applications such as tissue engineering scaffolds, implantable parts, and customised patient devices [171].

In this project, an SLA 3D printer was used (Form3, Formlabs, USA) to create masters for MN array fabrication. These masters were used to prepare PDMS flexible reverse moulds to be filled with the polymeric base for the MN array production. Form3 is an upside-down (inverted) SLA printer that uses 250 mW laser power, with an 85 μm laser spot size and 25 μm XY resolution. The model is uploaded to Preform software (Formlabs, USA) to adjust and add support to the model as shown in Figure 2-10. The printed parts were further cured by Form Cure (Formlabs, USA), which is a 13 multidirectional LED light chamber emitting 405 nm UV light and rotating at 1 rpm for even UV exposure [170].

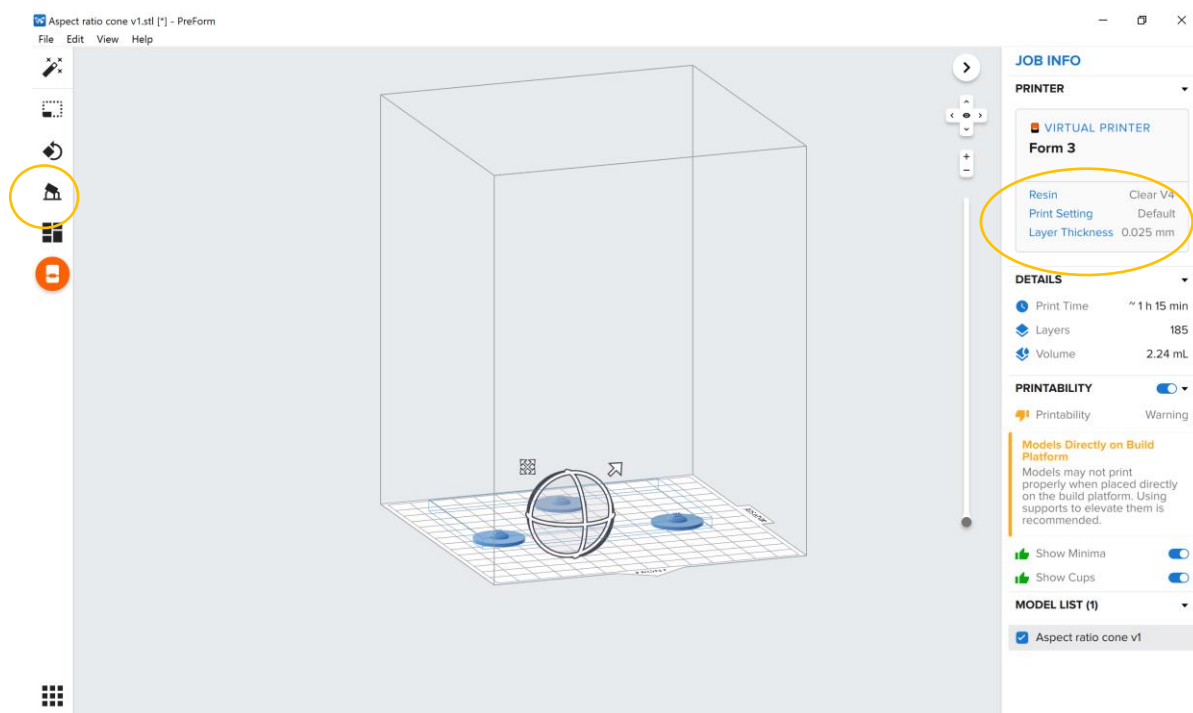


Figure 2-10 Component of Preform 3D printing software.

2.2.1.3 PLGA particle preparation

The different methods utilised for particles preparation were mentioned in section 1.8.2. Emulsion solvent evaporation technique has been commonly used to prepare PLGA microparticles and nanoparticles. This method can be used to encapsulate hydrophilic and hydrophobic drugs by single or double emulsion method. Here, a single emulsion method was used to encapsulate the hydrophobic dexamethasone. Typically, the process first starts with dissolving a polymer (e.g. PLGA) in a water immiscible organic solvent. The drug or the dye to be loaded into the particles is added to the polymer organic solution (oil phase). The polymer-drug solution is then gradually added to an aqueous solution (water phase) containing a stabiliser such as PVA and mixed at high speed to produce small droplets of the oil phase in the water phase [172]. A wide range of effective stabilisers has been used in o/w emulsion preparation, such as PVA, PVP, gelatine, and tweens [172]. The addition of a low percentage of stabiliser reduces the surface tension and provides a thin protective layer surrounding the emulsion droplets to reduce droplet coalescence and aggregation [173, 174].

The solvent is removed from the emulsion to harden the particles by either evaporation under reduced pressure or by extraction and evaporation at atmospheric pressure. In the latter method, the emulsion is added to a larger volume of water medium with or without a stabiliser and stirred [175]. The solvent entrapped in the particle diffuses to the aqueous media before it is removed by evaporation. The particles are washed to remove the excess stabiliser and then collected by centrifugation or filtration [176]. The particles are subsequently dried under ambient conditions or by freeze drying [175].

The size of the produced particles is determined initially during the emulsion droplet formation. To produce nano- or micro-sized particles, the process parameters such as the emulsion water to oil ratio, stirring speed, stabiliser and polymer concentration must be controlled to obtain various sizes of droplets [172].

In this study, micro- and nano- particles were fabricated by a single emulsion solvent evaporation method using different mixing devices. High shear homogeniser and ultrasonic homogeniser were used to prepare micro- and nano- particles, respectively. A high shear mixer generates rotational shear force in the fluid creating large droplets of the oil phase in the water phase forming a coarse emulsion [177]. While in an ultrasonic homogeniser, the ultrasonic energy is transmitted through the liquid medium producing a cavitation field that results in oil phase disruption and the production of nanosized emulsion droplets [178].

2.2.1.4 Freeze drying

Freeze drying or lyophilisation is a low temperature drying process. It is commonly used to improve the stability of pharmaceutical products such as colloidal systems, vaccines, vitamins, proteins, and peptides. Freeze drying was first developed during the Second World War to preserve blood serum [179, 180]. The principle of freeze drying is based on sublimation. Sublimation is the conversion from a solid state to a gas state without the transition to a liquid state. The sublimation of water takes place when the ice temperature and the vapour pressure are lower than the triple point. To understand the triple point, Figure 2-11 illustrates the phase diagram of water three phases of thermodynamic state in a closed system. The phases are solid (ice), gas (steam), and liquid separated by lines. The lines D-A, D-B, and D-C show the two adjacent phases equilibrium. D is the triple point where the three thermodynamic states coexist at specific temperatures and pressure (0.6 kPa and 273.16 K).

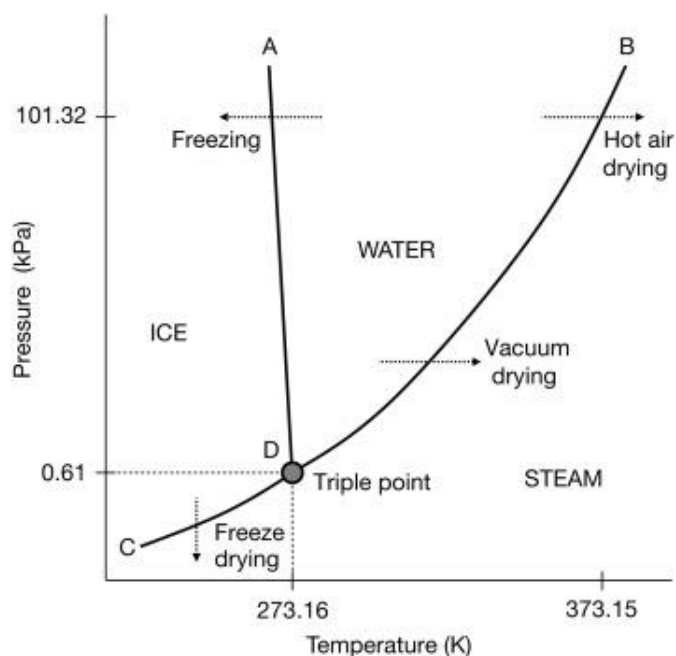


Figure 2-11 Pure water pressure vs. temperature phase diagram in a closed system [181].

Freeze dryer apparatus consists of a drying chamber equipped with a vacuum pump, a heating source and connector to a condenser (Figure 2-12). The frozen product is placed in the drying chamber; at this step, all the water molecules are frozen; the vacuum pump is required to remove gases from the chamber to reach the vacuum level, of less than 0.61 kPa. Once the product is under vacuum, the heating source provides the sublimation temperature. [181].

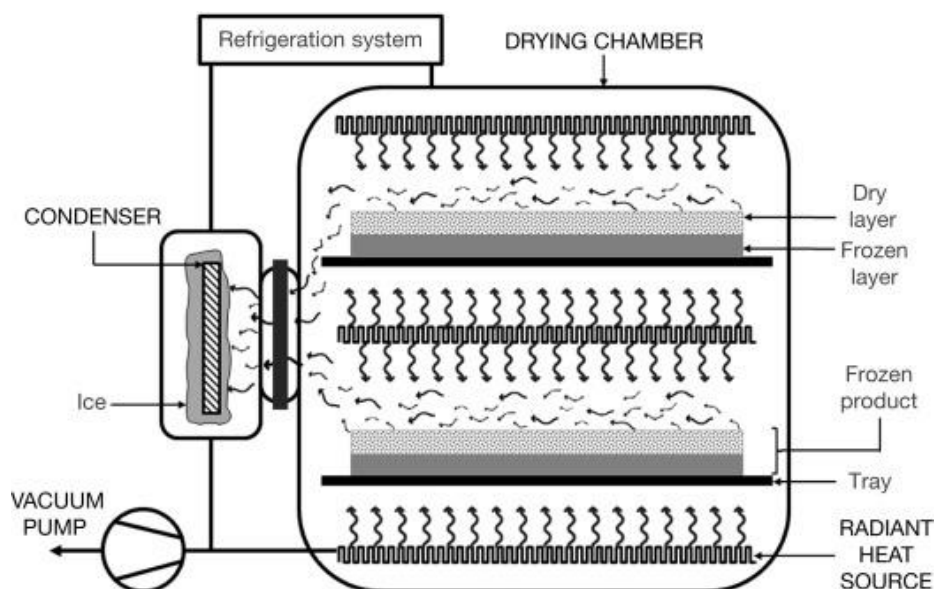


Figure 2-12 Illustration of freeze dryer basic components [181].

Generally, the process comprises three steps, freezing, primary drying, and secondary drying. Firstly, the product is frozen to form a pure water crystal, and then exposing the ice crystal to a high vacuum for sublimation to take place [181]. Subsequently, the primary drying step will take place, then the product is heated under vacuum to convert the ice to a gas. Around 90% of the water content is removed at this stage. Finally, at the secondary drying phase, bound water is removed by desorption through the surface layer by increasing the temperature and lowering the pressure [179, 180, 182].

In this project, the formulated PLGA particles are suspended in deionised water. The particles water dispersion is dried by freeze drying using (VirTis Advantage, SP, USA) to be further characterized and used.

2.2.1.5 Centrifugation

Centrifugation is a mechanical separation process that involves the sedimentation of particles in a liquid medium by centrifugal (rotational) forces [183]. The separation mainly depends on the size and density of the mixture components [184]. Typically, sedimentation of particles or separation of two immiscible liquids occurs as a result of gravitational force over time. Still, small particles may remain suspended if not

subjected to a centrifugal field. Applying centrifugal field forces speeds up the sedimentation process by directing denser particles to migrate away from the rotor axis while small particles migrate toward the axis [185]. The force applied to the particles compared to earth's gravitational force is known as relative centrifugal force (RCF), also known as xG, and is calculated by the following formula:

$$RCF = 11.17(r) \left(\frac{RPM}{1000} \right)^2$$

Equation 2-1

where r is the radius in cm from the centreline and RPM is rotor speed in rounds per minute or revolutions per minute [184-186].

The centrifuge is an instrument used to conduct the centrifugal force field. It mainly consists of an electric motor and a sample rotor; the motor spins the rotor that holds the samples. Several types of rotors are available, including fixed angle, horizontal rotors (i.e., swinging buckets), and vertical rotors. The pellet or the sedimented material moves directly to the bottom of the sample tube in vertical and swinging buckets rotor, while it usually collects at an angle in fixed angle rotor as shown in Figure 2-13. The pellets are collected perpendicular to the centrifugal forces.

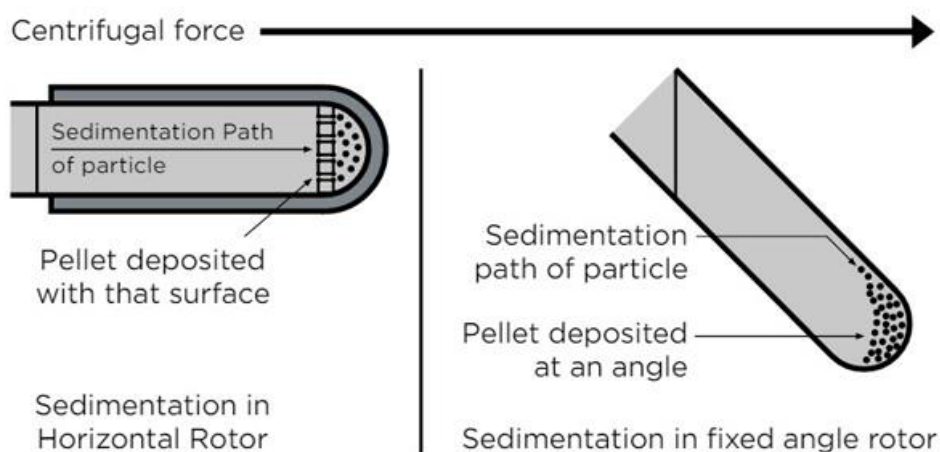


Figure 2-13 Illustration of the formation of the pellets in the tubes with a horizontal rotor and a fixed angle rotor [187].

In this study, a centrifuge with a fixed angle rotor (45 °degree) was used to wash the fabricated PLGA particles, and a swinging bucket rotor was used for the MN mould filling. A swinging bucket rotor (90 °degree angel) was required to evenly fill the moulds and concentrate the PLGA particles at the tip of the MN, as demonstrated in Figure 2-14.

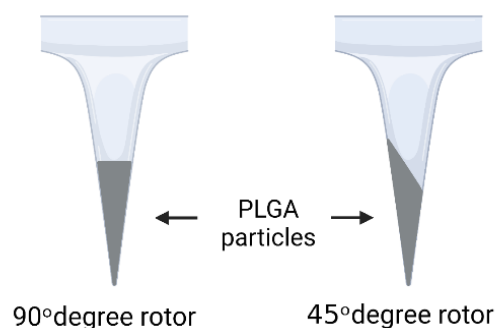


Figure 2-14 Demonstration of PLGA particles concentrated the MN tip in 90° vs 45° degree rotors, (created by Biorender).

2.2.2 Methods of characterisation and assessment

In this section, an overview of the main principals of the characterisation and assessment methods used in this project are discussed below. The specific parameters of each experiment are mentioned in each experimental chapter.

2.2.2.1 Scanning electron microscopy

Scanning electron microscopy (SEM) is an advanced microscope capable of producing detailed 3D images showing the surface morphology and topology at magnification power extended to 300,000x. SEM is used to scan the sample surface only, providing no information on the internal structure of the samples [188].

The principle of SEM is based on generating a stream of accelerating electron beams through high voltage. This beam passes through the condenser and lenses to focus on the sample to scan it in a raster pattern. The electron beam interacts with surface atoms

producing various signals. Consequently, secondary electrons and/or backscattered electrons are emitted by the surface atoms collected by detectors to produce the image [189]. The SEM operates under vacuum to avoid the interaction of the electron beam with the gas molecules to obtain high-resolution images. The samples with a low atomic number are coated with a thin layer of metal such as gold to enhance the secondary electron intensity and thus produce higher resolution images [188].

SEM images in this study were acquired by high-performance SEM (FEI Quanta 200F, FEI, Netherlands) or by desktop SEM (Phenom Pro, USA). Dr Andrew Weston performed the SEM analysis using a FEI Quanta 200F SEM. The samples were fixed on double-sided carbon adherent tabs and then gold coated for 60 sec in a Quorum Q150T Sputter Coater (Quorum Technologies Ltd, UK) and analysed at 5Kv acceleration voltage.

2.2.2.2 Dynamic light scattering

Dynamic light scattering (DLS) or photon correlation spectroscopy is a technique used to measure particle size, particularly by applying a laser beam to quantify the hydrodynamic size of particles in a liquid medium [190]. DLS setup is shown in Figure 2-15. The visible laser light passes through an attenuator to detect the polarization of the laser light; the light is focused on the sample, and the intensity of the scattered light is measured by a detector [191]. The fluctuation of small particles in the intensity profile is smaller than large particles due to their faster Brownian motion [191].

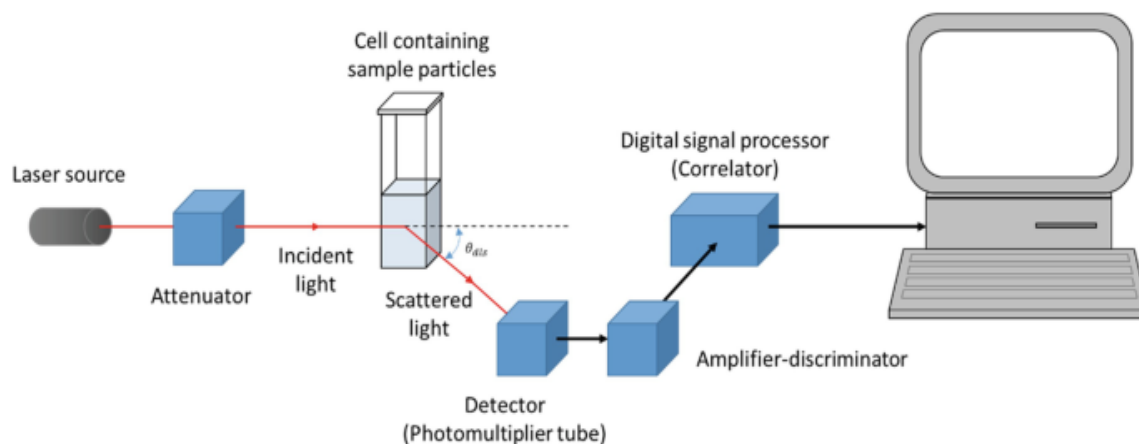


Figure 2-15 Schematic diagram of DLS setup [190].

DLS results are presented as Z-average. The Z-average or cumulant mean, is the harmonic intensity averaged diameter size of the particles in the sample. It is only relevant for spherical, monodispersed, and monomodal systems [190]. The polydispersity index (PDI) is another parameter measured by DLS. It indicates the heterogeneity in the particle's distribution. The lower the PDI value, the highly monodispersed the system, while a higher PDI value indicates wide size distribution in the sample [191].

In this study, a Zetasizer (nano-zs DLS, Malvern) was used to measure the fabricated PLGA particles Z-average and PDI. The particles were dispersed in deionised water.

2.2.2.3 Zeta potential analysis

Zeta potential is the measurement of the surface charge of particles in a colloidal system [192]. The surface of the particles attracts a thin liquid layer of opposite charge, known as the stern layer, that is strongly bound to the surface. An outer layer less strongly bound to the surface is known as the diffused layer, whereas an interface within the diffuse layer is known as the slipping plane, as shown in Figure 2-16. The Zeta potential is the potential at the slipping plane [193, 194]. The Zeta potential value

indicates the magnitude of the colloidal stability. High potential magnitude indicates greater electrostatic repulsion, thus higher stability.

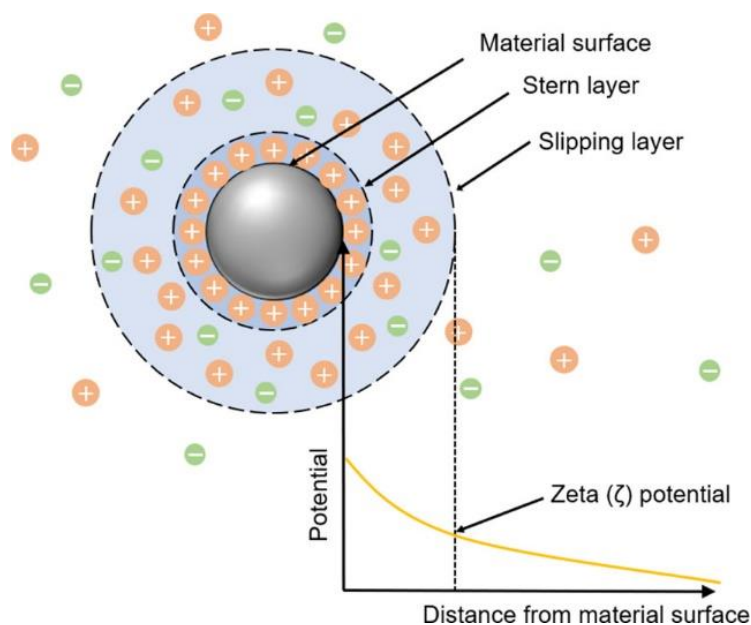


Figure 2-16 Diagram of the particle surrounding ionic concentration and potential differences [193].

In the Zeta potential analyser, the sample is placed in a special cuvette with a built-in electrode where the electric field is applied i.e., electrophoresis. During electrophoresis, charged particles move to the opposite electrode. The particles surface charge cannot be measured directly and instead determined from the electrophoretic mobility of particles when applying an electric field [192]. The pH of the medium has the main impact on the Zeta potential. Other factors, including ionic strength, temperature, and concentration, may also affect the Zeta potential reading [195].

In this study, a Zetasizer (Nano-zs, Malvern, UK) was used to measure the PLGA particle's surface charge. The reading was repeated 100 times for each sample, and the average Zeta potential was calculated.

2.2.2.4 Differential scanning calorimetry

Differential scanning calorimetry (DSC) is a thermoanalytical method of measuring the heat energy uptake in materials as a function of temperature and time. The instrument detects the temperature exchange, whether it is absorbed or emitted by the material relative to a reference sample. Based on the operation technique, DSC is categorized as heat-flux DSC and power-compensated DSC [196]. In heat-flux DSC, as shown in Figure 2-17, the sample and the reference are both placed in a furnace heated at a linear rate through a thermoelectric disk [197]. The temperatures of the sample and the reference are monitored and the difference is recorded by the thermocouple using the thermal equivalent of Ohm's Law:

$$q = \Delta T / R$$

Equation 2-2

where q is the heat flow in the sample, ΔT is the temperature difference between the sample and the reference, and R is the thermoelectric disk resistance [197, 198].

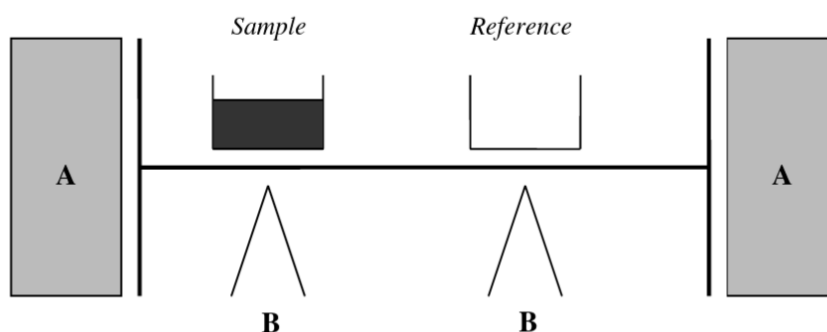


Figure 2-17 Illustration of heat-flux DSC. A is the furnace and B is the thermocouple [198].

Whilst in power compensated DSC, the sample and the reference pans are placed in separate furnaces and the power required to maintain the same temperature is recorded.

DSC data are typically recorded in terms of energy as a function of temperature. An example of a typical DSC experiment is illustrated in Figure 2-18. The temperature of the sample and the reference is raised over time at the same rate. However, the heat flow required to increase the sample temperature (q_s) is higher in the sample than in the reference (q_r). The recorded DSC curve represents the excess heat absorbed by the sample molecules (Δq) [197].

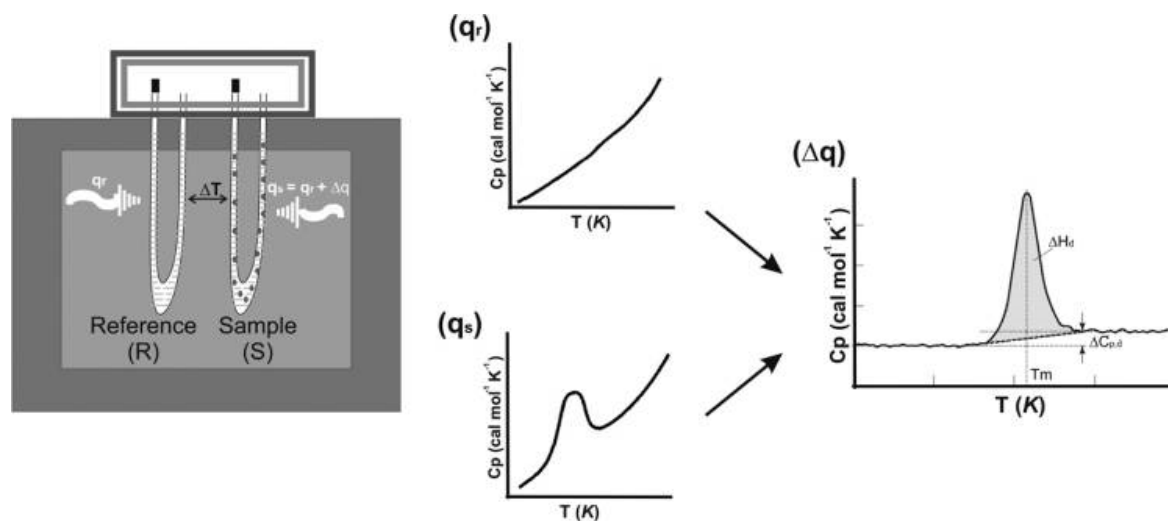


Figure 2-18 DSC data diagram constructed from the difference in heat flow between the reference and the sample [197].

The baseline indicates the power required to maintain the sample temperature to the set temperature, which is reflected by the sample heat capacity (C_p). This is expressed in joules per gram kelvin. C_p is a physical characteristic of the sample; it represents the amount of energy required to increase the temperature by 1 K and it is calculated via [198]:

$$C_p = q/H$$

Equation 2-3

where (q) is the heat flow and (H) is the heating rate.

However, the C_p measurement in DSC is based on the relationship between the calorimetric sensitivity (K), the baseline difference in the presence and absence of the sample (ΔY), and the heating rate (b) and is presented as follows [198]:

$$C_p = K\Delta Y/b$$

Equation 2-4

DSC offers a range of applications in material characterisation; it has been commonly used to identify and quantify the crystalline and amorphous phases of materials. Thermal properties such as heat capacity, melting point, and glass transition temperature are obtained by DSC analysis [197].

This method was used in this research for the thermal characterization of the pure dexamethasone, the polymer used, and the formulated PLGA particles using a Discovery DSC (TA Instruments, UK).

2.2.2.5 X-ray powder diffraction

X-ray powder diffraction (XRD) uses x-rays to investigate the structure of monocrystal or polycrystalline materials at atomic scale [199, 200]. The x-ray enters between the lattice plane of the crystal, and consequently, the rays are scattered or diffracted by the electron cloud around the atoms. The x-ray is diffracted in specific patterns corresponding to the crystal position, size, and arrangement. This pattern serves as a 'fingerprint' for the crystalline structure. The scattered x-ray occurs as a reflection through the sample and into the detector, where these scattered x-rays interfere with each other. This interference is observed by applying Bragg's law [200]. The law states that the angle, θ , of an incident x-ray onto a crystal reflects back with the same angle, θ [199, 201]. It is represented as follows:

$$2d\sin\theta = n\lambda$$

Equation 2-5

where d is the interplane space, θ is the angle of the incident x-ray, n is an integer order of reflection, and λ is the incident x-ray wavelength [200].

Typical XRD instruments rely on three basic components, an x-ray source, a sample holder, and a detector, as shown in Figure 2-19. The data are collected as a diffractogram, where the y-axis is the intensity, and the x-axis is the scanning angle. XRD is commonly used in the evaluation of the crystalline and amorphous phase status of materials, investigation of sample stress and strains, measurement of sample purity and determination of crystal dimensions. This technique was used in this research to characterise the solid state of dexamethasone, PLGA, and the prepared PLGA particles using MiniFlex 600 benchtop diffractometer (Rigaku, Japan).

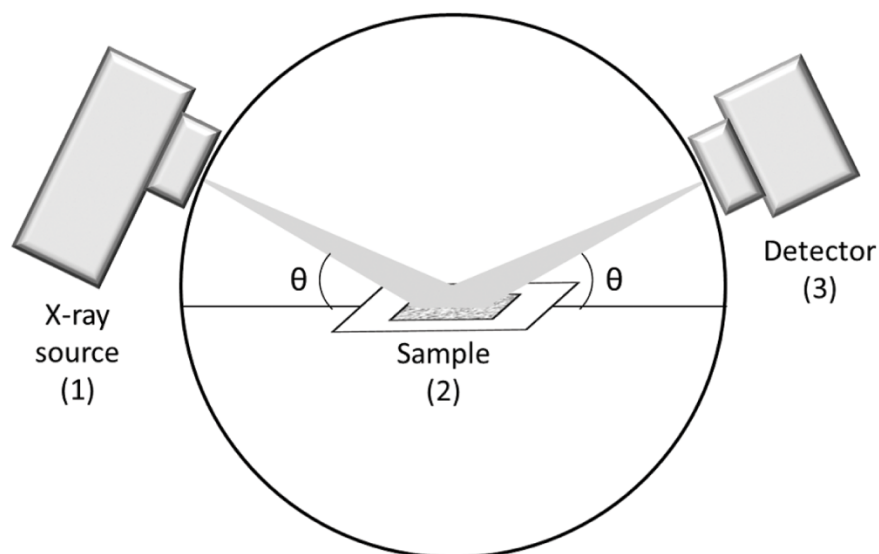


Figure 2-19 Schematic illustration of an XRD instrument [200].

2.2.2.6 Fourier transform infrared spectroscopy

Fourier transform infrared spectroscopy (FTIR) is a non-destructive analytical technique used to obtain a high-resolution infrared (IR) spectrum of absorption or emission of materials. The resultant IR spectrum represents molecular absorption or transmission, creating a unique “fingerprint” of the sample [202]. FTIR uses interferometry that

performs measurements over a broad spectrum of IR frequencies to produce signals over a period of seconds [203].

The main components of the FTIR spectrometer are shown in Figure 2-20. It consists of an IR radiation source, an interferometer, a sample cell, a detector, and a computer. The interferometer consists of three parts, two mirrors perpendicular to each other, a moving mirror and a fixed mirror, and a beam splitter. The IR radiation enters the interferometer for spectral encoding. The beam then passes through the sample, where it is reflected or transmitted. Additionally, the sample absorbs specific frequencies of radiation encoded by the sample structure. The absorbed radiation is converted to vibrational and rotational energy to be detected by the detector. Generally, the obtained IR spectrums are from 4000 to 400 cm^{-1} [202, 203].

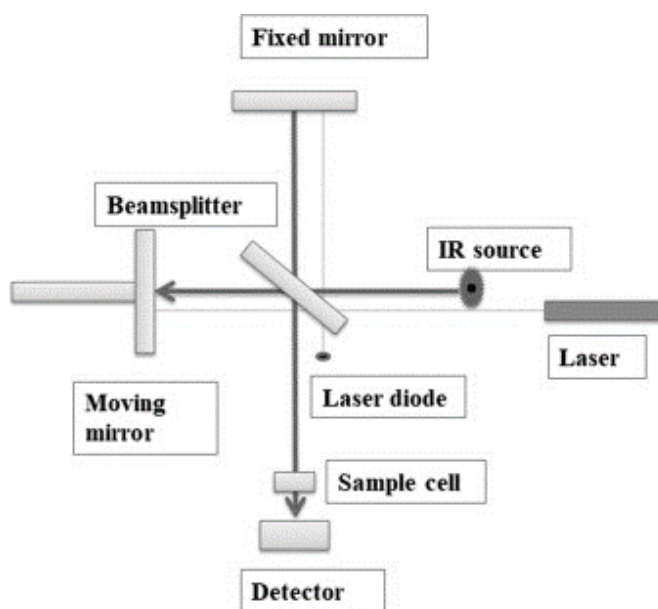


Figure 2-20 Schematic diagram of FTIR [203].

In this study, the technique was used to analyse the raw materials and the formulated PLGA particles to assess any sort of interaction between the drug and the polymers used. The study was performed using Vertex 70 FTIR spectrometer (BRUKER, UK).

2.2.2.7 High-performance liquid chromatography

High-performance liquid chromatography (HPLC) is a chemical analytical technique used to separate, identify, and quantify non-volatile compounds in a sample [204]. Liquid chromatography (LC) is a type of chromatographic technique in which the mobile phase is liquid. This technique has constantly evolved into two distinct methods, including a low-pressure system that uses disposable open columns and high-pressure system that uses reusable columns. The latter represented the vast majority of LC and was referred to as HPLC [205]. The instrumentation of HPLC comprises a pump, degasser, injector, column, and detector, as shown in Figure 2-21. The pump passes the mobile phase under pressure through the system; once the pressure is stabilised, the sample is injected into the column, where the separation occurs [206]. The separated components are eluted at a different time i.e., retention time (T_R), then analysed by the detector and presented as a peak in the chromatogram [204].

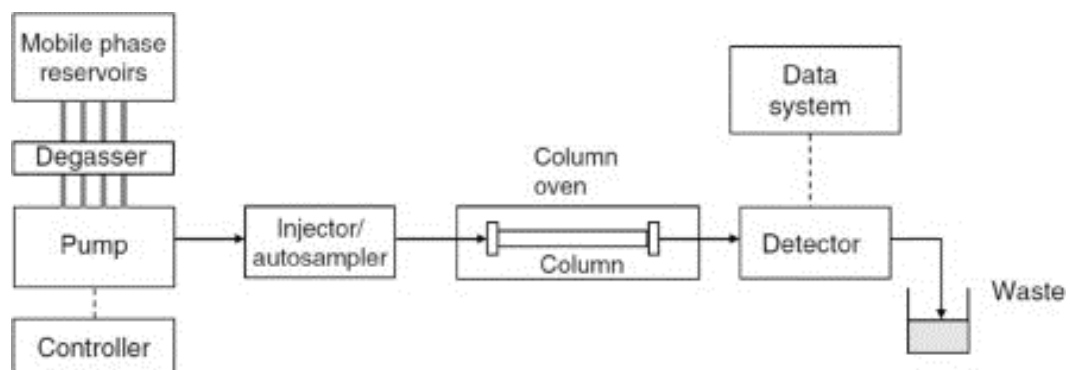


Figure 2-21 Schematic illustration of HPLC instrument [204].

Several separation techniques have been used mainly based on the established equilibration between the molecules in the mobile phase and the stationary phase. The main types of separation are partition, adsorption, ion exchange, and size exclusion [205].

The column is packed with the stationary phase, where the interaction with the analyte in the mobile phase takes place. The particle size, shape and porosity affect the

performance of the HPLC column. Solid silica-packed columns are the most commonly used type with adsorption and reversed-phase chromatography [205]. In reversed phase, which is the type of chromatography used in this study, the separation is based on the partitioning of the analyte between the mobile phase and the stationary phase. The stationary phase is non-polar and most likely composed of hydrophobic hydrocarbon chains (e.g. C8 and C18) bonded on the silica particles. The separation is mainly based on hydrophobic interaction. The T_r is longer for less polar molecules, while polar molecules are eluted more rapidly. Using a hydrophilic mobile phase can increase the T_r of the hydrophobic analyte by increasing its affinity to the hydrophobic stationary phase [204, 205].

When the mobile phase composition remains constant, it is known as isocratic elution, and when the ratio of the mobile phase changes during the separation, it is known as a gradient elution. To enhance the separation of the sample component, the composition, flow rate, temperature, and pH of the mobile phase must be controlled. HPLC detectors such as UV-visible, fluorescence, and mass spectrometer are mostly used to analyse the sample. It must be sensitive, consistent, and reliable with a low baseline noise [206].

The data are presented as a graphic output known as a chromatogram. The separated components are displayed as peaks. Each peak represents a different component; the height and the area of the peaks reflect the amount of each component [204]. Based on the nature of the sample, the column and the mobile phase are selected to achieve the separation. When developing an HPLC method, the method is validated for specificity, accuracy, selectivity, precision, linearity, and limit of detection in order to ensure reliable analytical data [207].

In this study, a reversed-phase column (C18) with an HPLC system coupled with a UV detector, 1200 HPLC (Agilent Technologies, USA) was used. A method was developed and validated to analyse the amount of dexamethasone loaded in the PLGA particles and the amount of dexamethasone released from the formulated PLGA particles. The

method was further adjusted to quantify the amount of dexamethasone extracted from biological tissue.

2.2.2.8 Dissolution test

Dissolution is the process of dissolving a substance into a solution. Dissolution testing is a method used to assess the *in-vitro* drug release from a delivery system. The release of the drug from the carrier is mainly affected by different factors, including the excipient, the manufacturing process, the drug's physicochemical properties, and the dissolution medium [208]. Dissolution testing is commonly used to predict *in-vivo* performance. When planning a drug release study, the choice of the apparatus depends on the physiological factors at the delivery site, such as the pH, movement of the organ, fluid content, enzymatic effect, protein binding, and anatomical barrier [208, 209]. Currently, the USP dissolution apparatus is generally used for dissolution testing. However, in some situations where the available compendial apparatus are not suitable for the tested dosage form, a modified or non-compendial setup is employed with justification and validation of the process [208, 210].

The underlying principle of the dissolution process of a solid dosage form is demonstrated by the detachment of the drug molecule, followed by solvation by the medium, and finally, transport of the solvated molecule from the stagnant layer to the bulk media. Noyes- Whitney developed a basic mathematical equation to describe the dissolution rate as follows:

$$dC/dT = kS (C_{sat} - C_{sol})$$

Equation 2-6

where dC/dT is the dissolution rate, k is the dissolution rate constant, S is the surface area, C_{sat} is the concentration of the saturated solution, C_{sol} is the concentration of the solution at any given time [208, 210].

Generally, dissolution testing involves the dosage form immersed in the dissolution medium at a temperature-controlled environment with controlled mechanical movement to mimic the site of application. Samples from the dissolution media are collected at a specified time interval and analysed by a suitable analytical method.

In this project, *in-vitro* dexamethasone release from the PLGA micro- and nano-particles was performed using a non-compendial method to mimic the pH and the dynamic of the ocular region.

2.2.2.9 Mechanical testing

Mechanical testing for pharmaceutical products is essential to ensure product quality, safety, performance, and cost-effectiveness. As a part of product characterisation and quality assurance, materials are usually tested for failures such as fracture, bending, and deformation. [211, 212]. The most important tests used to assess the mechanical properties of a product or a material in pharmaceutical application include tensile, compression, and flexural testing, which is illustrated in Figure 2-22. Tensile testing is a uniaxial method to pull on the sample; it is performed by stretching the sample at a fixed rate, as shown in Figure 2-22, A. Conversely, the compression test is a test that determines the material's behaviour when subjected to a compressive load (Figure 2-22, B). The flexural test is to determine the force required to bend a beam of material under three-point loading (Figure 2-22, C). Flex modulus measures how much material can flex before permanent deformation occurs [211, 213].

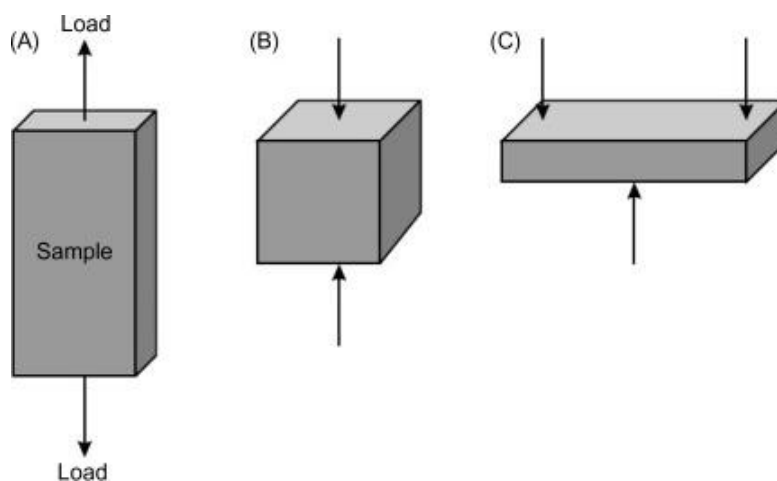


Figure 2-22 Schematic illustration of different mechanical testing configurations (A) tensile, (B) compression, and (C) flexural loading [214].

The most widely used instrument in pharmaceutical mechanical testing is the universal test machine (UTM). Standard UTM is either screw-driven, electromechanical, or hydraulic and it comes with a range of variations like different load cell capacities, uniaxial or multiaxial arrangement, and add-on fixtures. Typically, it consists of a rigid frame, a fixed crosshead, a movable crosshead, a load cell, and a controller, as shown in Figure 2-23. The load cell attached to the moving crosshead measures the force corresponding to the displacement [212].

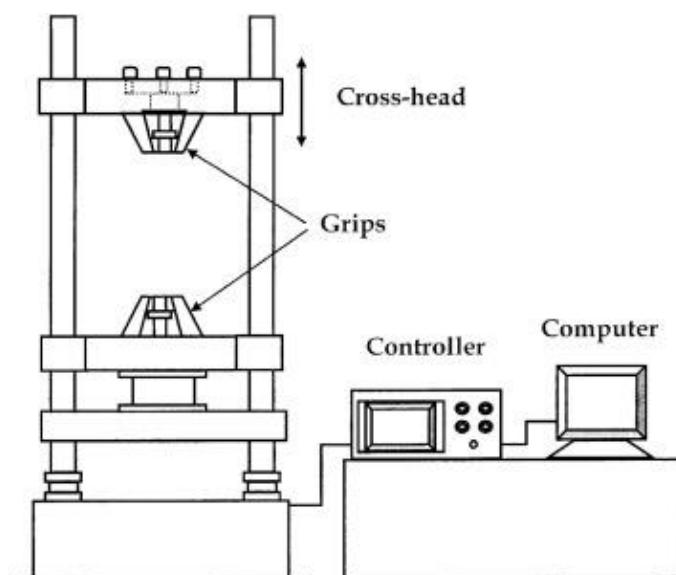


Figure 2-23 Schematic illustration of typical UTM [215].

The data are typically collected as stress as a function of strain or load as a function of extension. The stress is expressed by the formula:

$$\sigma = F/A$$

Equation 2-7

where σ is the stress, F is the load, and A is the area [213]. And the strain formula is

$$\varepsilon = \Delta L/L$$

Equation 2-8

where ε is the strain, ΔL is the total extension, and L is the original length.

Young's modulus defines the material's elastic behaviour; it is calculated from the stress-strain curve. In addition, mechanical parameters such as yield, break point, and ultimate strength are also calculated from the stress-strain plot.

In this study, mechanical testing of the MN array was performed using UTM, Instron universal system (Instron, USA) and TA plus texture analyser (Stable micro system, UK). UTM was also used to determine the adhesion properties and the insertion force in ocular tissue.

2.2.2.10 Permeation study

Permeation or diffusion is defined as the transport of adsorbed molecules through a membrane from a region of high concentration to a region of lower concentration. Permeability is the key factor in drug absorption and distribution within biological tissue. Several *in-vitro* models with high throughput capacity are used to assess the permeation and absorption of drug molecules based on the transport through artificial membranes, cells, or tissue [216]. The underlying theory describing drug transport is Fick's law of diffusion.

$$J = D \cdot C_v / h$$

where J is the flux, C_v is concentration, h is the membrane thickness, D is the diffusion coefficient [217].

Factors such as the permeation membrane, pH, and diffusion surface area are carefully considered in the permeation model. In this study, a Franz diffusion cell was used as an *ex-vivo* permeation model. It comprises of a donor chamber, membrane, sampling port, and acceptor chamber, as shown in Figure 2-24. The sample is placed in the donor chamber while the acceptor chamber is maintained under continuous stirring at a controlled temperature. The permeation kinetics is determined by quantifying the sample concentration at specified time intervals and then analysed by a quantification method, e.g. HPLC.

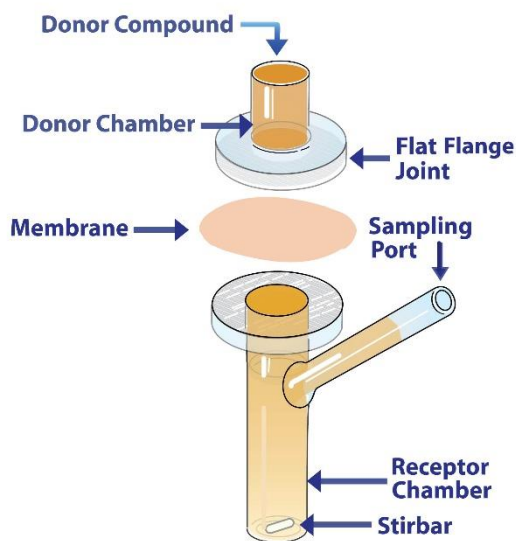


Figure 2-24 Schematic illustration of a Franz diffusion cell [218].

2.2.2.11 Cellular study

Cell culture is an *in-vitro* method of growth and reproduction of cells cultivated outside a living organism under controlled conditions. Cell culture has served in many medical fields such as vaccines, new drug development, toxicology, genetics, and enzymes [219].

A cell culture study is carried out under controlled aseptic working conditions. The cells proliferate in a culture medium that provides the essential nutrients, minerals, and growth factors. Cells are subcultured in media and regularly monitored by eye or inverted microscope until they reach around 70-80% confluency for adherent cells or 10^6 cells/mL in suspension cells. The cells are later collected and centrifuged for counting and viability detection. Counting the cells can be done by staining the cells with trypan blue, which differentiates between the viable and the dead cells using the Thoma slide method or the automated cell counter [219].

2.2.2.11.1 Cell viability assay

Cell viability is an assay carried out to measure the proportion of live healthy cells to dead cells in a population. It is used to screen the cytotoxic effect of a tested molecule on cell proliferation. There are different viability markers used as indicators for metabolically active cells (living cells), including measuring the ATP level, identifying specific enzymatic activity, and reduction of substrate [220].

In this study, a tetrazolium reduction cell viability assay was used. It is a colourimetric assay employed in high throughput screening; it is based on the measurement of mitochondrial activity [219, 220]. In viable eukaryotic cells, monotetrazolium salts are reduced by NADPH and dehydrogenases to insoluble formazans. Reduction of the yellow tetrazolium salt (MTT) in metabolically active cells results in the formation of an insoluble purple formazan dye, as shown in Figure 2-25. The formazan dye is solubilised, and the intensity of the dye is measured with a spectrophotometry plate reader [220].

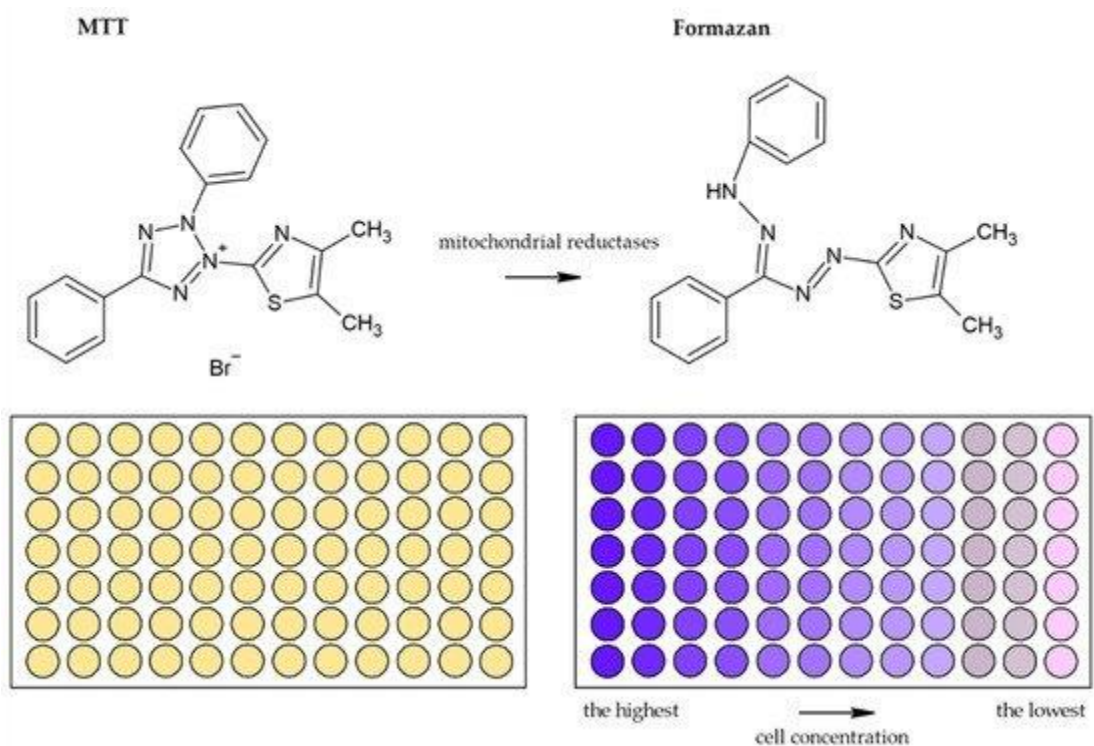


Figure 2-25 Schematic illustration of the mitochondrial reduction of yellow MTT to purple formazan [220].

2.2.2.11.2 Cellular uptake

Several factors influence cellular uptake, including size, shape, surface charge, rigidity, texture, and protein corona [221]. Additionally, cell type and concentration in the population play an important role in cellular uptake. There are two main mechanisms for cellular particle uptake. Phagocytosis, also known as cell eating. It is associated with certain types of cells, such as macrophages, neutrophils, monocytes, and dendritic cells. Particles up to 3 μm in size can be internalized by phagocytosis. The second mechanism of cellular uptake is endocytosis, also known as cell drinking. It occurs in most cell types. It is subdivided into receptor-mediated endocytosis, caveolae-mediated endocytosis, and micropinocytosis [221, 222]. In the cellular uptake test, the particles interact with the cellular organelle, which results in cellular internalization.

The assessment method is important to analyse and quantify cellular uptake. SEM and transmission electron microscopy (TEM) are used to examine the intracellular structure

and visualize the particle uptake. However, these electron-based microscopy methods require extensive preparation and offer only qualitative data. Quantification of cellular uptake might also be attainable by flow cytometry and fluorescent microscopy; both methods are suitable for fluorescent labelled particles [223, 224].

In this study, fluorescent labelled PLGA particles of different sizes were tested for cellular uptake in a human retinal pigment epithelial cell line (ARPE-19) and visualized by fluorescent microscopy (EVOS, ThermoFisher, USA).

2.2.2.12 *In-vivo* animal study

2.2.2.12.1 Eye irritancy test

The eye irritancy test, also known as the 'Draize eye test', is an ocular toxicity test developed in 1944 by FDA toxicologists John Draize and Jacob Spines [225]. It is a method of evaluating the irritation potential in the eye after exposure to a substance in one eye while the other eye serves as a control [226]. The eye is examined and scored at every interval of 1, 24, 48, and 72 h post application. The grading scores cover the following aspects: corneal opacity, iris appearance and response to light, conjunctival redness, and eyelid swelling. The eyes of Albino rabbits are preferred to perform this test since their iris lacks pigmentation, which makes it easier to interpret the results [227]. In this project, an *in-vivo* irritancy test was performed on an albino rabbit to assess the irritation potential of the MN array.

2.2.2.12.2 Animal disease model and *in-vivo* activity

Animal disease model is an important method for studying the pathophysiology of a disease. Several ocular disease models have been experimentally exploited to study the efficacy of a proposed drug delivery system in the lab. From infectious and parasitic disease models to non-infectious ocular inflammatory disease, experimentally induced ocular disease models elucidate greater understanding of human disease and facilitate the investigation of new therapies [228, 229].

Uveitis exemplifies a various range of intraocular inflammatory conditions that can be linked to autoimmune diseases, bacterial or viral infections, and chemical injuries. For the assessment of the *in-vivo* pharmacological activity of dexamethasone and the study of the pathological mechanisms, endotoxin-induced uveitis is an efficient *in-vivo* model that causes short uveal inflammation [230]. Lipopolysaccharide (LPS) is a pro-inflammatory mediator released on the cell wall of gram-negative bacteria such as *Escherichia coli*. LPS pro-inflammatory endotoxin acts through autocrine and paracrine signalling, triggering the release of inflammatory cytokines such as TNF- α and IL-1 [230, 231]. In this study, LPS-induced uveitis was used to assess the *in-vivo* activity of the dexamethasone-loaded MN array.

Chapter 3 Design and 3D printing of microneedle masters and reverse mould preparation

3.1 Introduction

The fabrication of MN utilises a variety of materials, including metal, glass, ceramic and polymers [55]. Based on the material of the MN, several manufacturing techniques have been employed for pharmaceutical applications. More details about the manufacturing techniques were previously mentioned in Chapter 1, section 1.6.2. Among these techniques is the method of micro-moulding, in which microstructure is replicated using moulds [232]. The fabrication of dissolvable MN arrays is commonly achieved by solvent casting, in which a polymeric solution is filled into a flexible silicon mould and left to solidify by solvent evaporation [233]. These silicon moulds are prepared by the microfabrication of masters. The masters are fabricated with the precise shape and geometry of the intended product outcome. Subsequently, the masters are used to generate an unlimited number of reverse copies, i.e. the silicon moulds. These reverse moulds are created by pouring PDMS solution onto the masters which are then cured to be used for MN production [234].

Lithography, 3D printing, and laser cutting have been commonly used in the fabrication of MN masters [104, 109, 235, 236]. Various 3D printing technologies, such as fused deposition modelling (FDM), two-photon polymerisation (2PP), digital light processing (DLP), and stereolithography (SLA) were utilised for MN fabrication [232, 235, 237, 238]. FDM printers are based on hot-melt extrusion for layer-by-layer deposition of material. However, the relatively low resolution of FDM printers has made it difficult to manufacture a sufficiently precise MN. SLA, DLP, and 2PP printing are based on the photopolymerization of UV sensitive resin [53]. 2PP has superior nanoscale accuracy, which is suitable for fabricating intricate and complex microstructures. However, the method is time consuming and expensive [64]. In contrast, DLP and SLA printers are more economical and offer a high-speed printing process which make them widely available for manufacturing and prototyping. The techniques provide relatively accurate and precise printing at the micrometre scale [53].

Due to the delicate nature of the eye, MN intended for ocular delivery should be in the microscale (<1 mm in length) to accommodate eye tissue thickness. Therefore, the main challenge in preparing the moulds is to prepare accurate and precise masters. SLA 3D printers are accessible, flexible, and low-cost 3D printing technology that has superior accuracy and attainable level of performance compared to other low-cost 3D printers [103, 232]. The technology is based on layer-by-layer solidification of photosensitive liquid resin by a laser beam or other light source. The laser beam moves in the X-Y direction following the layer pattern. The laser spot size has a great influence on the resolution of the printing. Commercially available SLA 3D printers have a laser spot size ranging from 30 to 140 μm . Therefore, the smallest feature on the printed object is limited by the laser spot size [239]. Recently, some reported studies have used SLA printers for MN masters' fabrication. The studies have emphasised the printing of MN in the millimetre range, which is more suitable for transdermal application [104, 232, 238]. Normally, the ocular tissue thickness ranges from $\sim 500 \mu\text{m}$ in the cornea to $\sim 900 \mu\text{m}$ in parts of the sclera [9]. Therefore, the fabrication of MN arrays in the micron range is investigated in this study. Affordable SLA 3D printers have limited resolution capacity and attempts to improve the resolution of the printed MN have been reported [104, 238]. A study investigated of pyramid shaped MN arrays 3D printed at a tilted position has demonstrated a reduction in the MN tip size [238]. While a different study implemented a new approach to improve the resolution by printing a 3 mm conical needle with a high aspect ratio in the basin and then reducing the MN length by filling the basin with a curable material, keeping only the tip exposed to produce micro sized needle. This approach is a complex and time-consuming process. Neither any of the reported studies have investigated the feasibility of the methods to print different MN shapes nor studied the accuracy of the method on the volume and geometry of the produced MN.

The size of the array and the geometry of the MN, including the height and the tip size, have a great impact on the insertion force and the pain level when a MN array is applied [240]. Decreasing the number of the MN in the array and reducing the tip size improve

tissue penetration and reduce the pain significantly [240, 241]. Furthermore, studies have confirmed the relationship between the insertion force and the surface area of the MN. The insertion force increases linearly with the surface area of the MN and the MN tip size [242, 243].

3.1.1 Aim and objectives

The aim of this chapter was to use a simple, cost-effective, and easily customisable SLA 3D printing method to develop sub-millimetre MN array masters with optimal shape and geometry for scleral application by controlling the design and the printing parameters.

The objectives of the study are:

- Optimise the overall master design to produce mould suitable for preparing the particles incorporated dissolving MN array.
- Study the effect of shape and aspect ratio on the accuracy of the SLA printing.
- Optimize the 3D printing process parameters to improve the printing resolution of the MN array and study the 3D accuracy of the prints by comparing the printed MN array geometry with the input CAD model dimension.
- Study the effect of shape and tip size on the MN insertion.
- Prepare a reverse mould from the optimised 3D printed masters.

3.1.2 Chapter graphical overview

A summary of the work conducted in this chapter is illustrated in Figure 3-1.

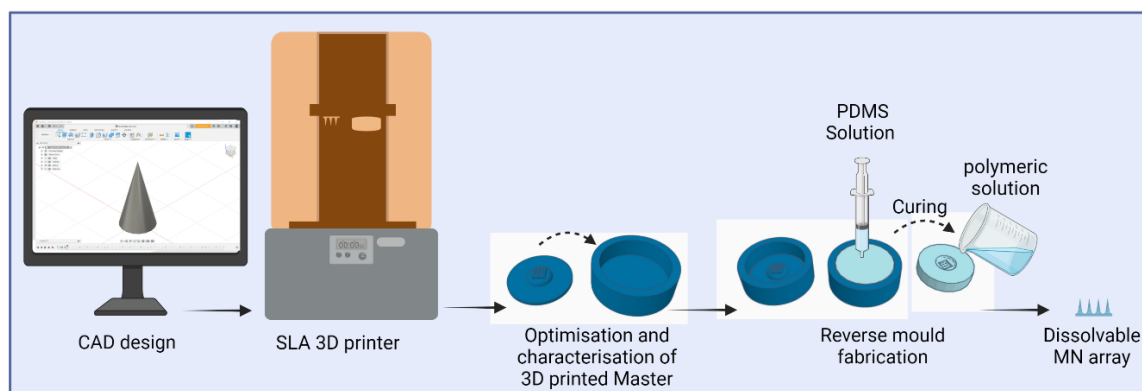


Figure 3-1 Chapter 3 graphical overview (created by Biorender).

3.2 Materials

UV curable liquid resin, Clear® was purchased from Formlabs®, USA. Polydimethylsiloxane (PDMS) SYLGARD™184 Silicone Elastomer kit purchased from Dow, USA. Silicon Rubber GP-3481-F purchased from MB Fiberglass, UK. Isopropyl alcohol (IPA) and Parafilm® 'M' were all purchased from Merck Sigma Aldrich, France.

3.3 Methods

3.3.1 Design and optimisation of the MN masters

Masters were designed using Fusion 360™, CAD software, Autodesk®, USA. The limit of height printability was first tested. MN arrays 1X4 with conical-shaped needles ranging in height from 100 μm to 900 μm were designed on a 200 μm thick base. Printing MN with diverse shapes and various aspect ratios was also tested. Conical, pyramid and triangular pyramid-shaped MN were selected as they represent shapes with zero angles (cone), three angles (triangular pyramid), and four angles (pyramid) (Figure 3-2). The MN with different shapes was designed at a 1:1, 1:2, and 1:3 (base width to height) aspect ratio in a 1X4 or 3x3 array. Table 3-1 shows the dimensions of the MN designed in different shapes and aspect ratios. Arrays 1x4 set on a 2x4 mm rectangle, 200 μm thick base was designed for imaging, while a 3x3 array set on a 4x4 mm, 200 μm thick square base was used for testing the MN insertion. All the masters were designed as

two-part, consisting of a base holding the array and a basin to be assembled before creating the reverse moulds.

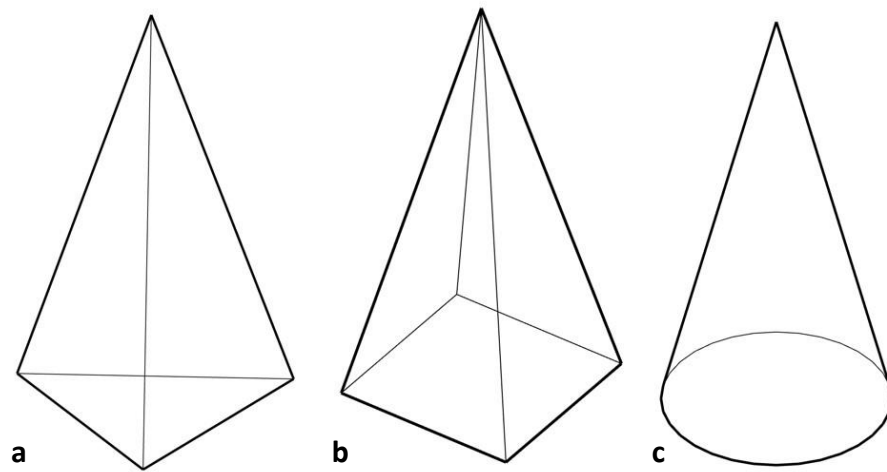


Figure 3-2 The shapes of the MN designed by CAD software (a) triangular pyramid, (b) pyramid, and (c) cone needles. The designs present shapes in a 1:2 aspect ratio.

Table 3-1 Dimensions and specifications of the MN array designs.

Shape	Design code	Slant angle θ	Volume (mm ³)	Diameter / Side (μ m)	Base surface area (mm ²)	Body surface area (mm ²)	Aspect ratio	Tip to tip distance (mm)
Cone	C 1-1	63.43	0.191	900	0.64	2.06	1:1	1.15
	C 1-2	75.96	0.048	450	0.16	0.82	1:2	1.00
	C 1-3	80.53	0.021	300	0.07	0.50	1:3	1.00
Pyramid	P 1-1	66.09	0.240	900	0.81	2.62	1:1	1.20
	P 1-2	76.58	0.062	450	0.20	1.05	1:2	1.00
	P 1-3	80.92	0.027	300	0.09	0.64	1:3	1.00
Triangular pyramid	T 1-1	64.62	0.107	900	0.35	1.63	1:1	1.25
	T 1-2	76.54	0.027	450	0.09	0.72	1:2	1.00
	T 1-3	81.05	0.012	300	0.04	0.47	1:3	1.00

3.3.2 Printing microneedle array masters

The CAD designs were saved as an .STL file format to be uploaded to the 3D printer model preparing software (Preform software, Formlabs®, USA) to adjust the model layout as shown in Figure 3-3. The model orientation and layer thickness were specified before printing. The printing layer thickness was tested on 900 μ m height MN by printing with 25, 50, and 100 μ m thick layers.

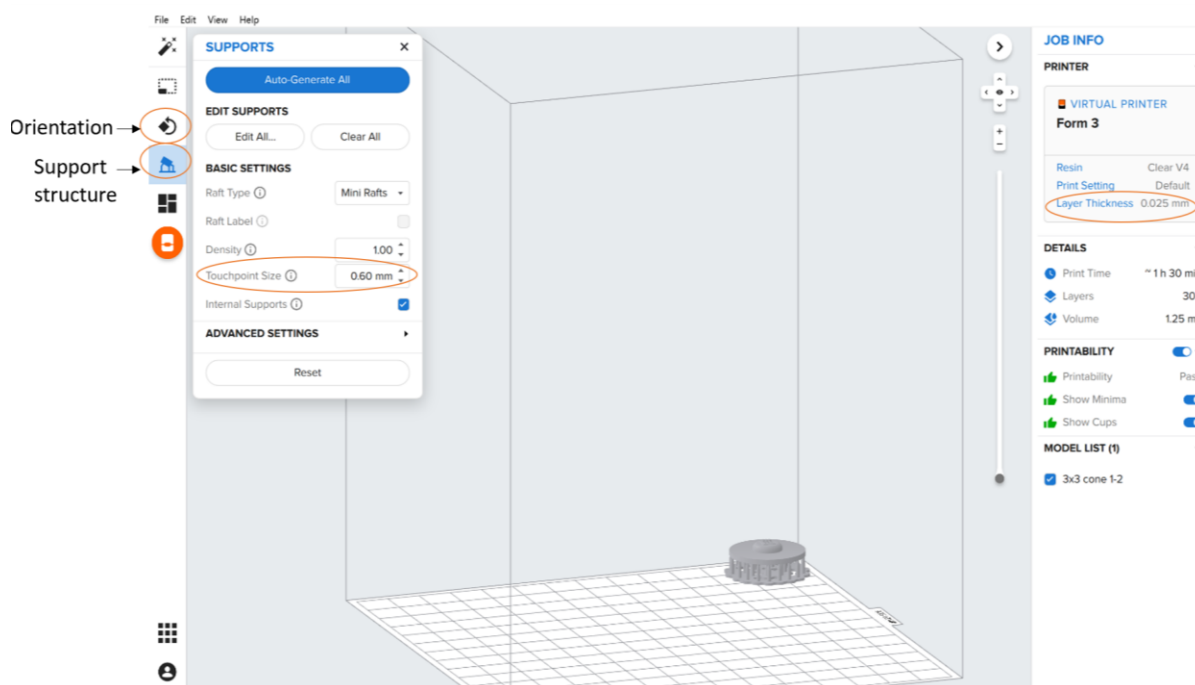


Figure 3-3 Preparation of the CAD model in preform software before uploading the design on the 3D printer.

Moreover, the model was adjusted at 0, 45°, 67.5°, and 90° angles in the X-Z or Y-Z direction. When adjusting the model orientation angle, support structures were added to support the model on the building platform, as shown in Figure 3-4. The support structure looks like columns or branches attached to the model. The location, density and touch point size were controlled by the software features. All the support structures were set at a 40 μm touch point and added to the back surface of the MN array base, avoiding the top surface and the MN body to prevent leaving marks on the MN surface. Then the printing order was uploaded to the 3D printer (Form 3, Formlabs®, USA). The software converts the model into bitmaps representing each layer individually. When the model was uploaded, the printer filled the tank with the resin and kept it heated while printing to maintain the optimum temperature, which is close to 35 °C. The 3D printing was initiated automatically when the resin tank was heated.

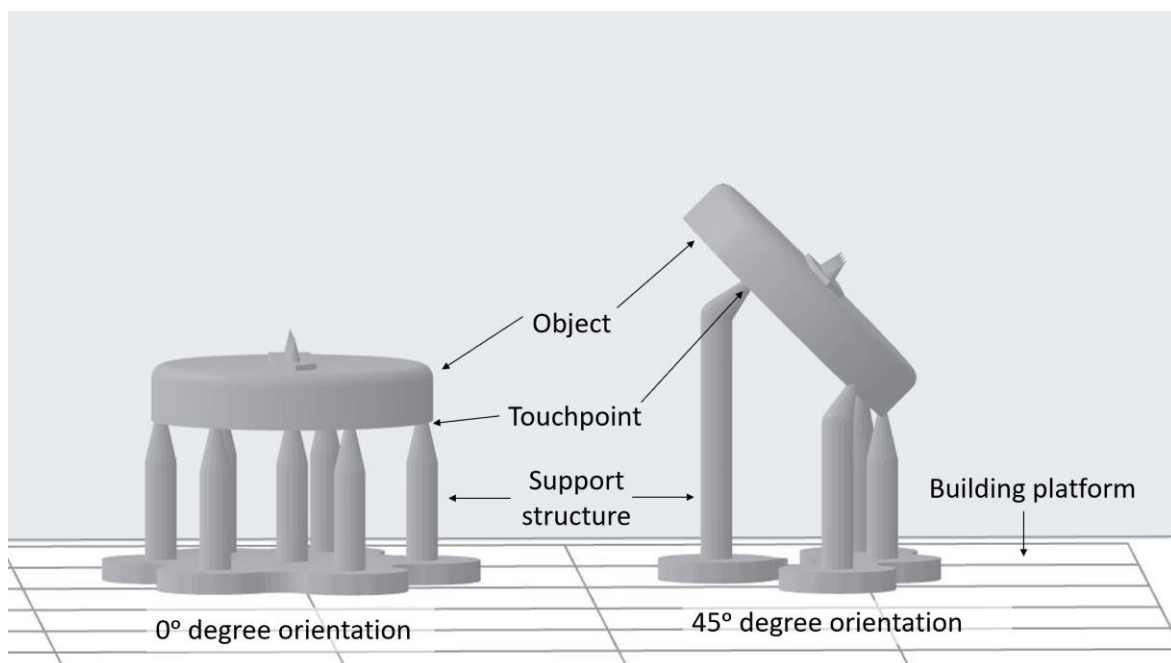


Figure 3-4 Illustration of adjusting the object at 0° and 45° orientation with support structure before the printing using Preform software.

3.3.3 Post-printing treatment

Once the 3D printing process ended, the printed objects were carefully removed from the building platform by applying force with a scraper beneath the support structure. The objects were then washed in an IPA tub for 30 min to remove the excess uncured resin. The MN array master was inspected by a handheld digital microscope (Dino-lite, USA) prior to curing to ensure that uncured resin was completely removed from the tight inter-needle spaces. To improve the object strength and performance, washed masters were cured at 60°C for 30 min using a multidirectional LED light curer (405 nm) (Form Cure, Formlabs®, USA).

3.3.4 Examining of MN masters

Cured masters were examined by a digital microscope (Dino-lite, USA) and imaged using a benchtop SEM (Phenom Pro, USA), and a high-focus digital camera (Infiniprobe Infinity, USA).

For SEM imaging, the MN array was attached to an SEM stub (TAAB Laboratories, UK) using a double-sided electrically conductive carbon adhesive tab (Agar Scientific, UK). The samples were then gold coated for one min by a sputter coater (Quarum, Lambdaphoto, UK). Defected masters or failed prints were excluded from further use.

3.3.5 3D scanning of MN masters

An optical digital microscope (Keyence Digital Microscope VHX-7000) was used to inspect the body and tip size of 3D-printed MN array masters. The 3D scan of the MN was acquired by the control software's depth-up feature, which captures every focused pixel through scans along the z-axis and combines them into a single image. Then the maximum point height, volume, and surface area of each needle in the fully focused image were measured by specifying the designated flat region of the printed MN parts as the reference base plane. The 3D scan of the masters and the measurement of the MN dimensions (height, volume, surface area) from the control software were performed by a group member, Se Chung, at the engineering and physical sciences research council, UCL.

3.3.6 Printing accuracy

The printing accuracy was calculated to determine the differences in dimension between the CAD design (input size) and the 3D printed MN (output size). The study was performed to ensure the efficiency and reproducibility of the process.

The dimensional accuracy was assessed by calculating the percentage of the ratio of output to input dimensions. Percentage > 100% means the dimension was larger than the proposed design and vice versa. The input dimensions were obtained from the CAD software, and output dimensions were obtained from the SEM images, the digital images, or the 3D scanning measurements of the masters.

3.3.7 Reverse mould fabrication

To create the reverse moulds, the master was assembled then the PDMS solution was poured into the basin, the PDMS solution was degassed under vacuum for 10 min

(Nuve, EV 018, Turkey) and then cured at 65°C for 4 h or left at room temperature for 48 h. Subsequently, the solidified moulds were carefully separated from the wall of the basin using a stainless-steel micro-spatula and gently pulled out using a tweezer. Finally, the reverse moulds were left to be further cured under ambient conditions for 24 h, then washed with deionised water and dried before use. The reverse moulds were made to create several copies of the dissolvable MN array using a hydrophilic polymeric mixture. The moulds were created to fit inside 50 mL Falcon™ tubes (28 mL outer diameter) to be centrifuged, as shown in Figure 3-5-a. To maintain the moulds stable during centrifugation, the Falcon™ tubes were filled with light weight silicon rubber, then levelled and cured at room temperature, as shown in Figure 3-5-b. One mould or three stacked moulds were placed in the tube and centrifuged for mould filling.

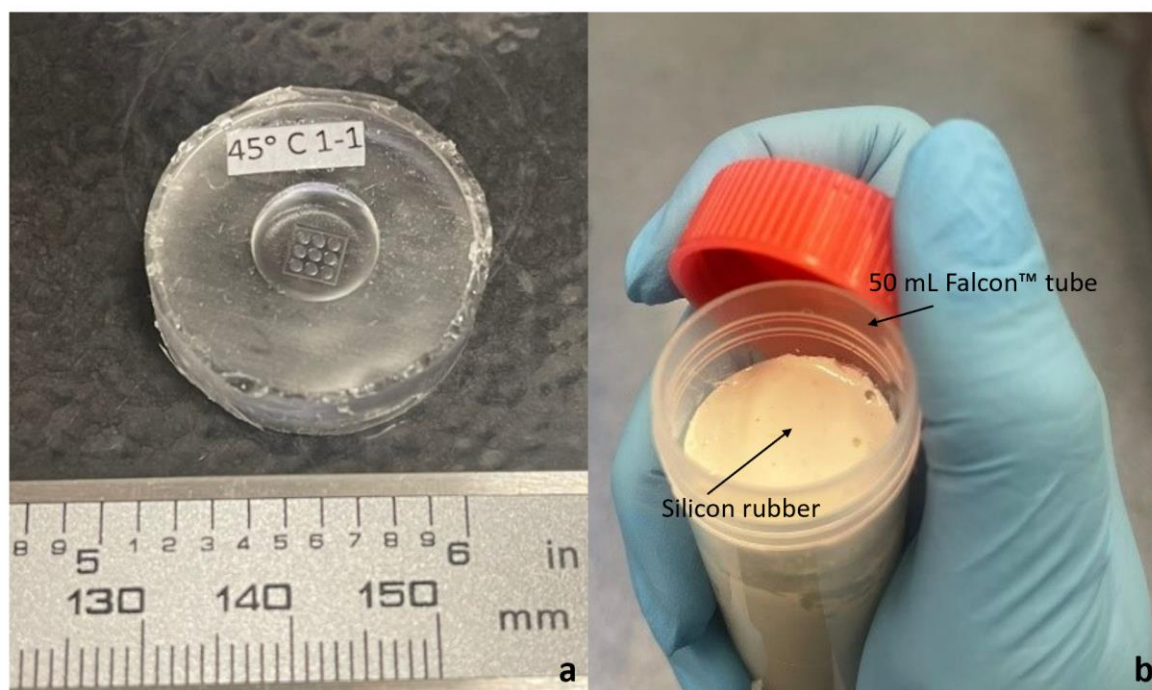


Figure 3-5 Digital images of (a) reverse mould, (b) pre-filled Falcon™ tube with lightweight silicon rubber.

3.3.8 Insertion depth

To assess the effect of MN shape and tip size on the insertion depth, Parafilm® M thermoplastic film was used. The film is around 127 μm in thickness. Eight layers of the

film were folded around a glass slide to reach ~ 1 mm thickness [80]. The test was conducted using a texture analyser (TA plus texture analyser, Stable Micro System, UK). The MN array was fixed on a plastic probe by double-sided adhesive tape attached to a movable arm to exert a linear force perpendicular to the film layers at a speed of 100 $\mu\text{m}/\text{sec}$ until 1 mm distance was reached. After the insertion, the films were carefully removed, and the number of holes pierced on each layer was counted.

3.3.9 Statistical analysis

Data are reported as mean \pm standard deviation (SD). The means were compared by T-test or by one-way analysis of variance (ANOVA) followed by Tukey's multiple comparison test. *P*-values < 0.05 indicate statistical significance. Statistical analysis was conducted by statistical software Prism 9 (GraphPad, USA).

3.4 Results

3.4.1 CAD design and 3D printing of MN masters

This study aimed to prepare a high-resolution 3D printed master that produces a MN array with optimum geometry for scleral application. Several designs were tested to optimize the MN array fabrication. In the optimisation of the 3D printing process, two key elements were considered. First, the overall design of the master and the resultant reverse mould, regardless of the MN included in the design. Features including the space or depot to fill the polymeric solution, mould size and shape that facilitate centrifugation of the mould, and accessibility to examine the quality of the MN prints were considered. Second, the shape and size of the MN. The effect of the shape and the aspect ratio on the 3D printing resolution and, ultimately, the insertion performance was assessed. This was achieved by optimising the printing parameters. Improving the resolution of the printing without compromising the overall accuracy of the needles was the main goal in the optimisation process.

In the development of the master, a 3x3 MN array setting on a 4x4 mm and 5 mm thick, square base fitted inside a square basin was initially designed (Figure 3-6-a). Next, a

reverse mould was created and subsequently, the polymeric MN was fabricated. To fill the mould with the polymeric solution, the moulds were centrifuged by placing them in the modified Falcon™ tubes. The square-shaped mould was not securely fit in the tube. Subsequently, the design was adjusted to a circular basin to fit inside the centrifugal tube (Figure 3-6-b).

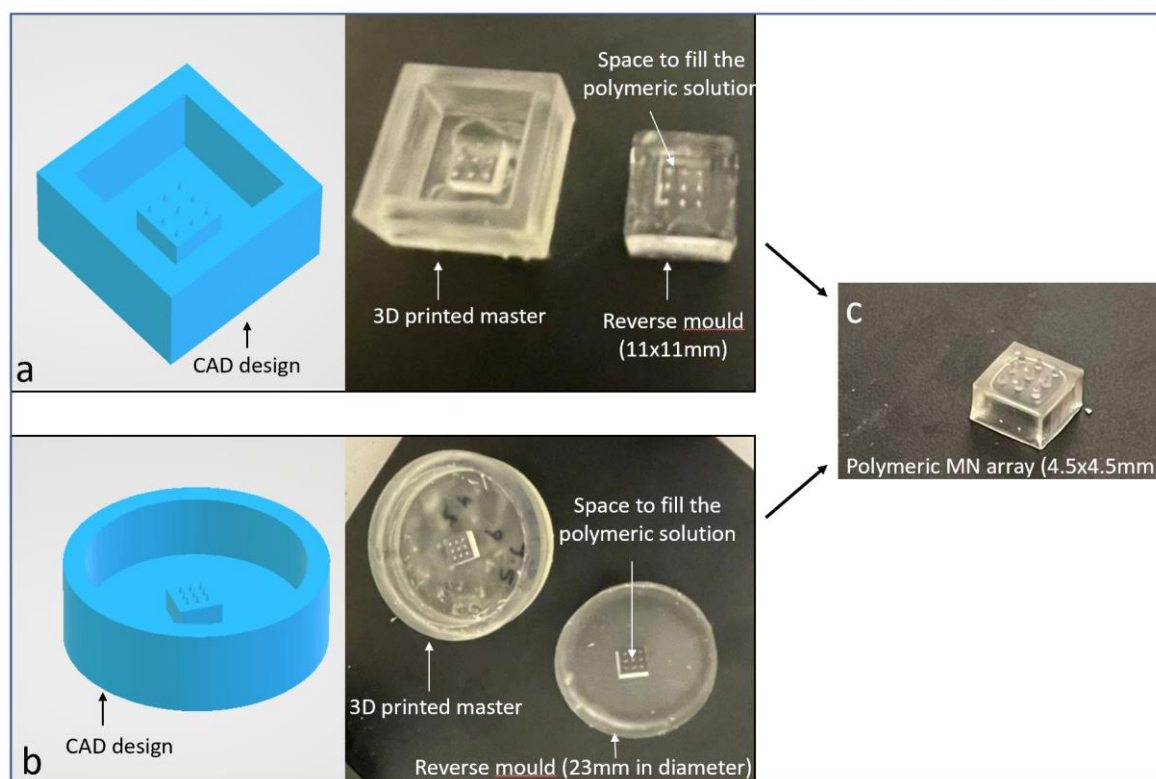


Figure 3-6 Preliminary master designs showing CAD design, 3D printed master, and PDMS reverse mould, (a) square mould, (b) circular mould, (c) polymeric MN array.

The MN array was designed to be set on a 5 mm thick base; this extra depth was required to give sufficient space to fill the polymeric solution in the moulds. The deep base resulted in MN arrays sitting on thick square walls that were hard to cut or remove (Figure 3-6-c). This thick, deep wall will impede the reliability of the mechanical testing where force must be evenly distributed on the MN base. Similar shaped MN patches with deep walls or thick bases were observed [63, 244]. However, methods to remove the edges have not been reported.

Thus, further improvements were required to provide a reservoir for the polymeric solution filling and to eliminate the hard, thick walls created by the polymer solution. In consequence, a MN array was placed on a 200 μm in thick base. This thin square base was fitted on a hemispherical-shaped dome, $\sim 86.5 \text{ mm}^3$ in volume and $\sim 9 \text{ mm}$ in diameter (Figure 3-7-a, b). This dome created a tub-like reservoir in the reverse mould that served as a space for placing the polymeric solution before centrifugation. Additionally, upon application of centrifugal force, the curvature of the inverted dome directed the solution towards the MN holes, avoiding any spillage (Figure 3-7-c). After drying, the excess polymeric base was easily removed without damaging the MN array (Figure 3-7-d).

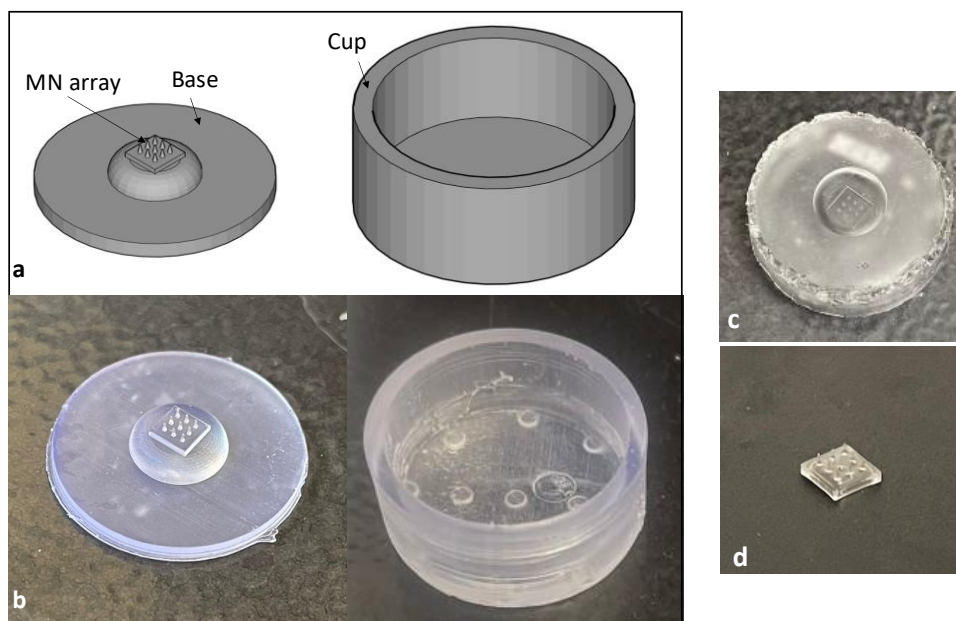


Figure 3-7 Master of MN array displaying a dome-shaped base and a two-part system consisting of a base holding the array and a cup to fit in the base. (a) CAD design, (b) 3D printed masters, (c) reverse mould (23 mm in diameter), (d) polymeric MN array (4x4 mm).

Another design element that was also considered was the feasibility of the master design to allow the inspect the printed MN before use. To be able to inspect the MN array from a side view, a two-part system was constructed. As shown in Figure 3-7, the master design was comprised of a circular base 23 mm in diameter, holding the

microstructure of the MN array and a basin 25 mm in internal diameter. This design facilitates the inspection and assessment of the printed MN to ensure the quality of the prints, and to exclude faulty prints before preparing the reverse PDMS mould (Figure 3-8). A similar approach was observed with 2PP 3D printed master, where a MN array was printed on a 0.5 mm thick square baseplate and then glued on a holder [74].

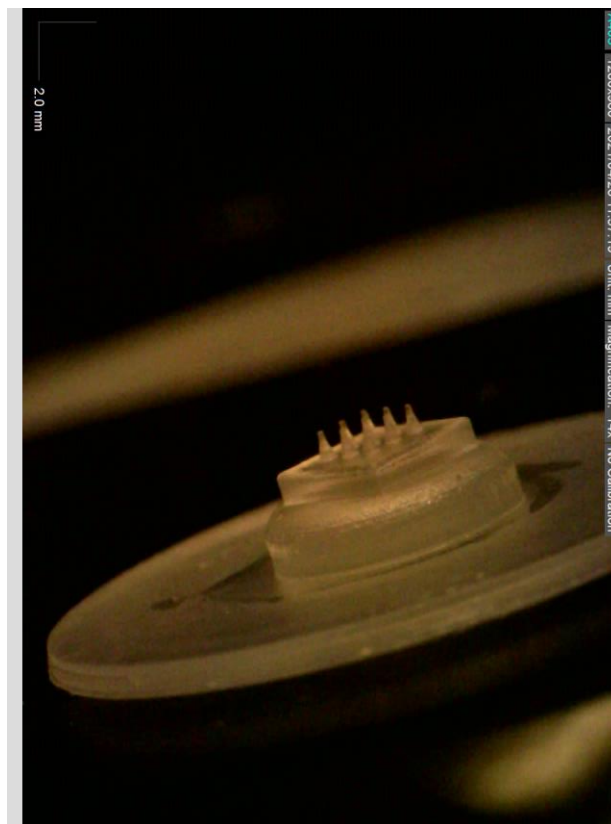


Figure 3-8 Inspection of MN array master post-curing by digital camera.

Post-printing, the uncured resin can be trapped between the needles, washing the printed object in IPA will usually remove most of the uncured resin. However, due to the small interneedle spacing, the uncured resin may remain trapped. Further cleaning and washing are required to remove all excess resin before curing, as shown in Figure 3-9.

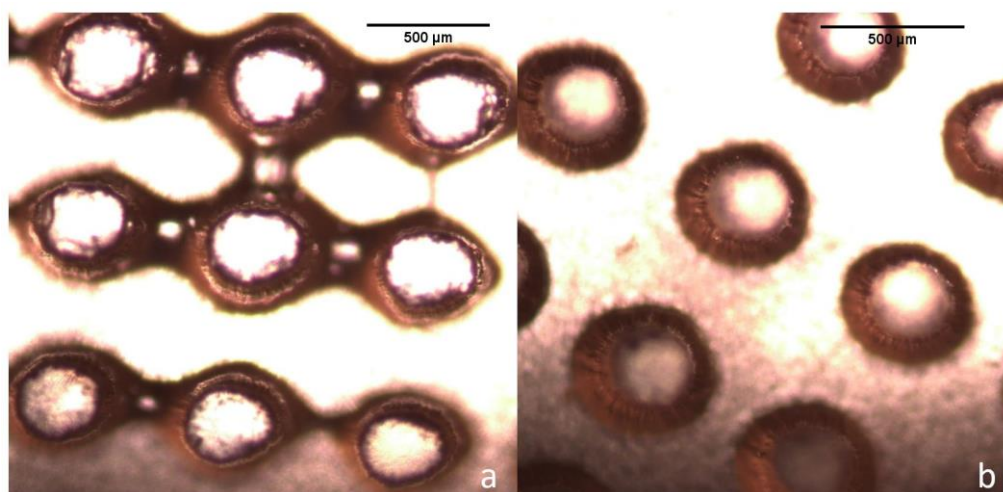


Figure 3-9 Microscopic images of MN array masters before curing, (a) uncured resin trapped in the interneedle space, (b) uncured resin completely removed.

3.4.2 MN design parameters

MN designs were tested to produce 3D-printed MN with optimal needle properties. An assessment of the effect of shape and geometry on the printing outcome was conducted to produce MN suitable for the ocular application. Three parameters of the needle's design were evaluated as part of the parametric study to measure the printing success, including the needle height, the needle shape, and the aspect ratio.

For the height printability study, MN 1X4 arrays in a cone shape and 1:2 aspect ratio ranging from 100 to 900 μm in height were printed at vertical orientation (Figure 3-10).

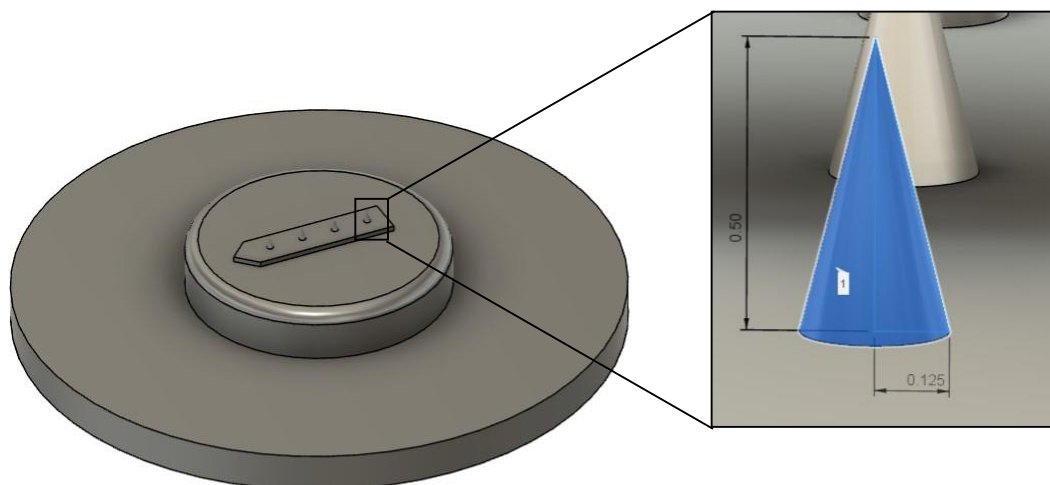


Figure 3-10 CAD design of a 1x4 MN array for height printability testing (in the image, 500 μm MN height in 1:2 aspect ratio is shown).

The printing outcome of the MN is shown in Figure 3-11, and a comparison between the height of the input design and the output prints is presented in Table 3-2 and Figure 3-12. From the table and the figure, it was confirmed that the printing was highly accurate in terms of the MN height (z-direction) in the range of 100 μm to 900 μm . All the printed heights have less than a 1% difference from the input height (100%).

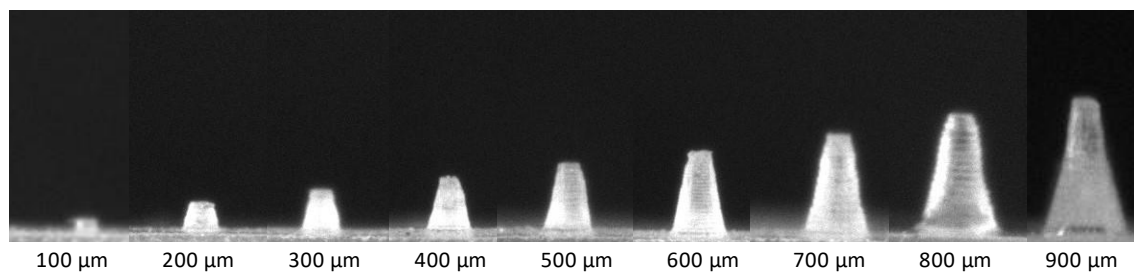


Figure 3-11 3D printed MN (C 1-2) in height ranged from 100 μm to 900 μm (obtained by Infiniprobe high-focus digital camera).

Table 3-2 Comparison between needle input and 3D printed output height.

Input height	Outcome height	\pm SD	Accuracy (output/input %)
100	100.13	11.44	100.13
200	200.00	10.23	100.00
300	302.81	11.68	100.94
400	401.50	14.86	100.38
500	500.26	17.46	100.05
600	601.14	12.41	100.19
700	702.28	16.88	100.33
800	807.93	19.60	100.99
900	901.50	26.97	100.17

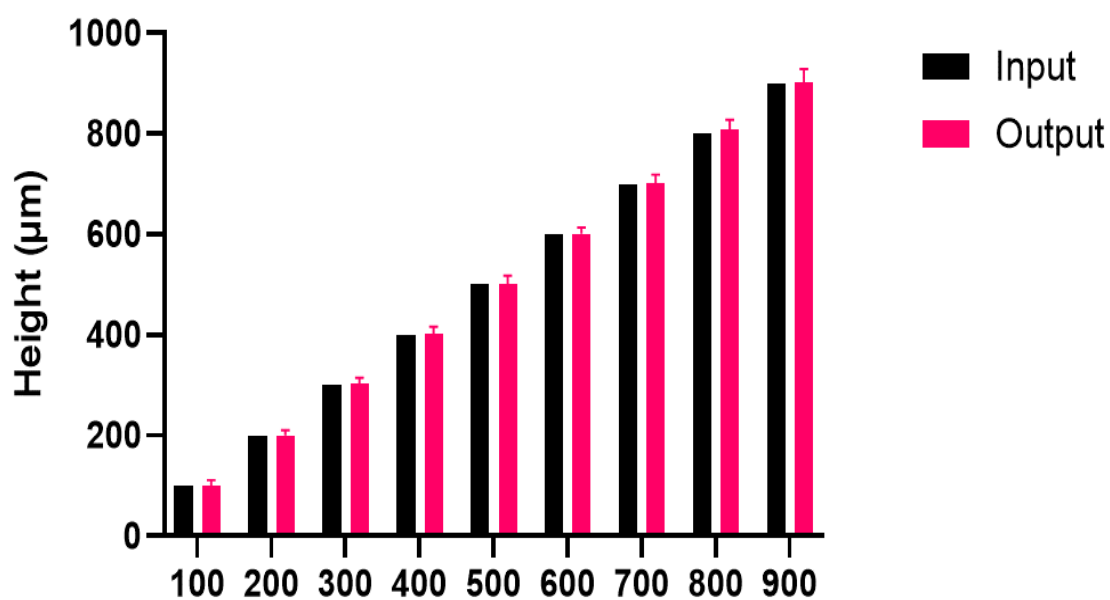


Figure 3-12 Comparison of the input design and output print heights of the MN printed in a cone shape and 1:2 aspect ratio (C 1-2). Data are reported as mean \pm SD (n=6).

Although the MN height was accurately printed, the tips of the MN were wide and blunt, which was expected due to the printer's limited resolution and the laser spot size

of 85 μm . The accurate height of the printed MN indicates that the printer was printing all the layers entirely regardless of their surface area. Thus, layers with a diameter of less than 85 μm were still printed with single-spot printing. The measurement of the tip size will be investigated in more detail in the following section.

Furthermore, the effect of the shape and aspect ratio of the MN was investigated in terms of printing accuracy. Cone, pyramid, and triangular pyramid shapes were designed with three aspect ratios of 1:3, 1:2, and 1:1, as presented in Figure 3-13. These shapes were selected as they represent shapes with zero angles (cone), three angles (triangular pyramid), and four angles (pyramid). The MN were imaged by SEM, and the accuracy of the height and the side length or the diameter dimensions were assessed by ImageJ. A top and a side view are presented in Figure 3-14. All the MN shapes and sizes had blunted rather than pointed sharp tips due to the limited printer resolution. Pyramid and triangular MN shapes lack the sharp lateral edge displaying curved slants. Likewise, the corners of the square and triangular bases were rounded in the pyramid and the triangular pyramid MN respectively. The lack of sharp edges and base corners was due to the rounded shape of the laser beam, which is incapable of producing defined outlines at such a small scale. Yet, the height and base were accurate, and no more than 1% variation from the input measurements was observed in all cases (Figure 3-15, Figure 3-16). Indicating that the geometric shape and aspect ratio have a minimum influence on the printing accuracy.

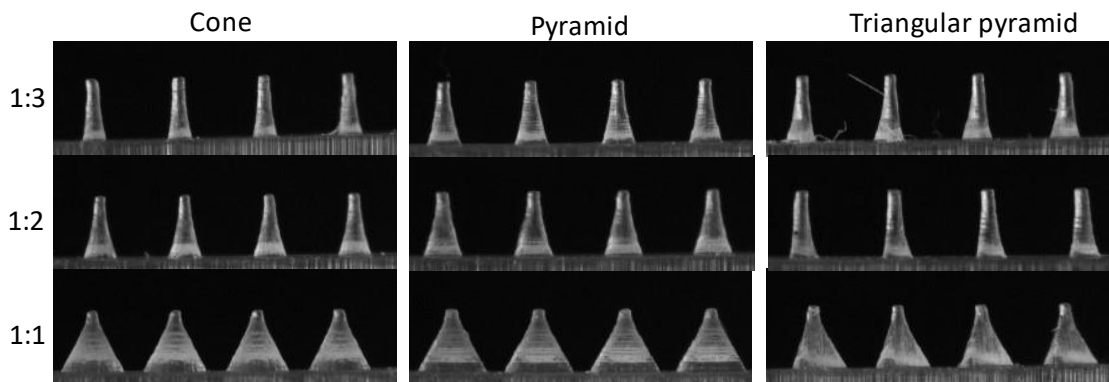


Figure 3-13 3D printed MN in cone, pyramid, and triangular pyramid shapes in 1:3, 1:2, and 1:1 aspect ratio (MN are 900 μm in height).

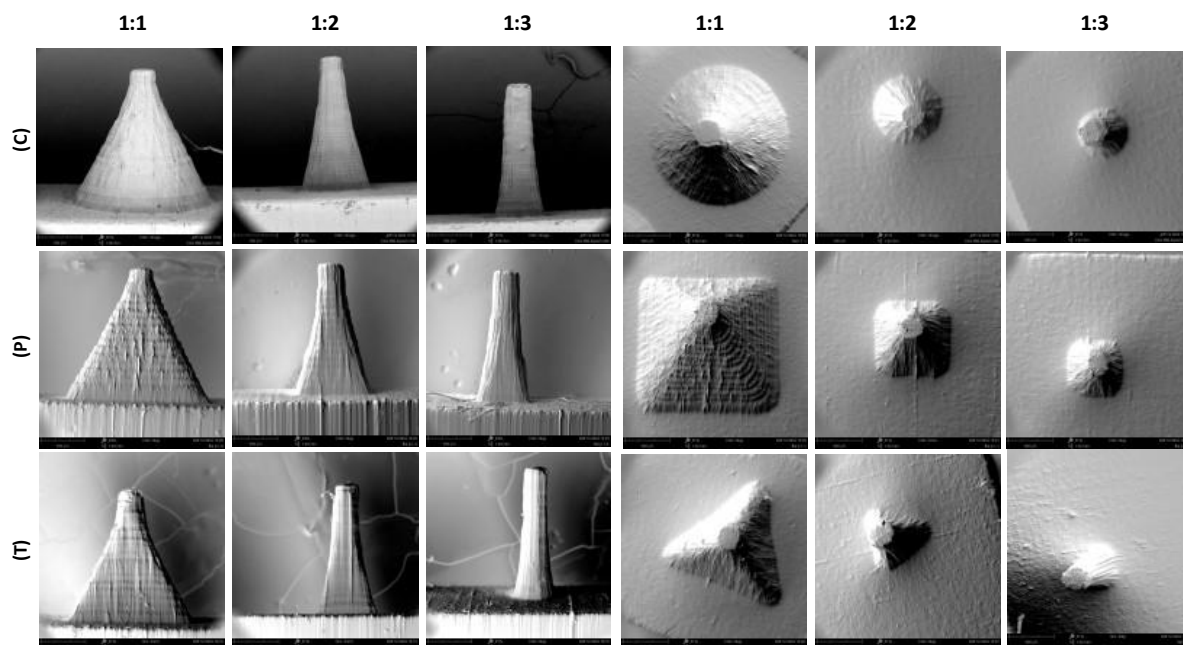


Figure 3-14 Top and side view SEM images of MN in a cone (C), pyramid (P), and triangular pyramid (T) shape with 1:1, 1:2, and 1:3 aspect ratios. Scale bar (—) 300 μm .

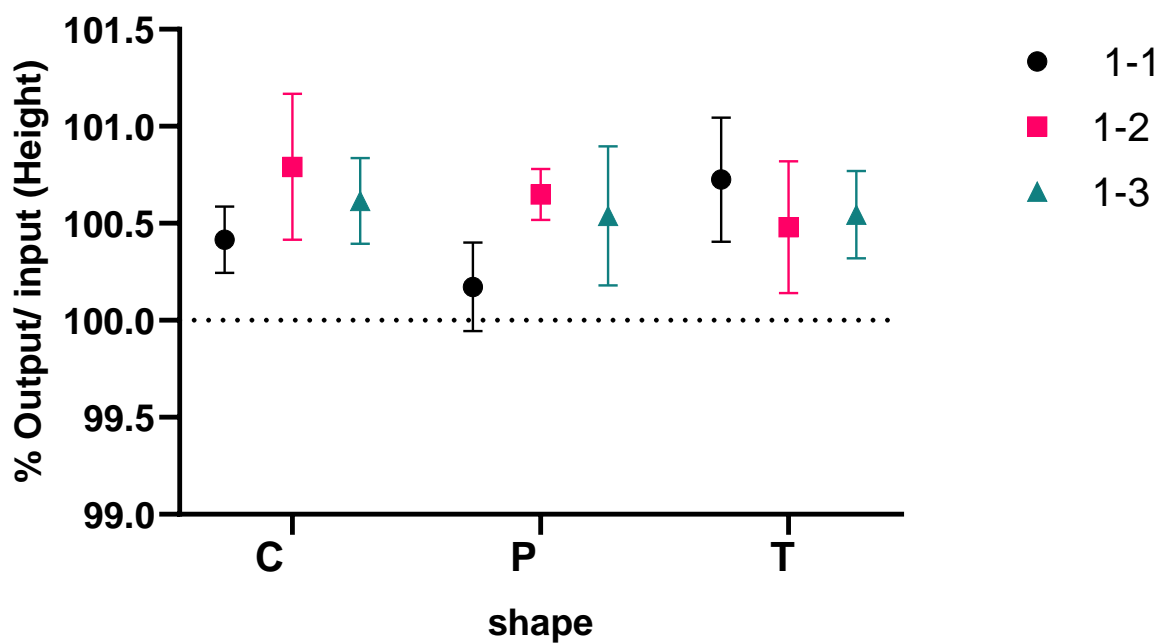


Figure 3-15 Accuracy (output/input %) of height with different shapes and aspect ratios. (C) cone, (P) pyramid, and (T) triangular pyramid (dotted line indicates 100% accuracy). Data are reported as mean \pm SD (n=4 arrays).

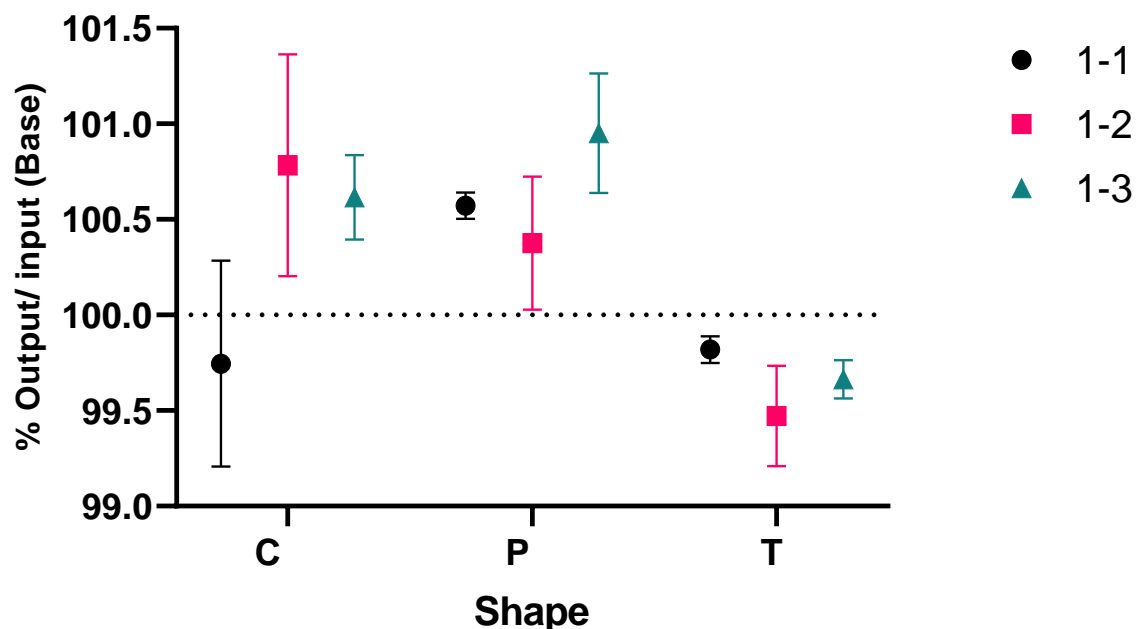


Figure 3-16 Accuracy (output/input %) of base size with different shapes and aspect ratios. (C) cone, (P) pyramid, and (T) triangular pyramid (dotted line indicates 100% accuracy). Data are reported as mean \pm SD (n=4 arrays).

The relatively high resolution and accuracy of SLA and DLP 3D printers have enabled the utilization of the technologies in MN fabrication [101]. A study has reported $\pm 5\%$ dimensional fidelity of pyramidal MN printed by DLP 3D printer [232], and no significant error in the SLA printed conical MN was also reported in another study [104].

In clinical practice, needles in the size range of 27 to 30G (0.413–0.312 mm diameter) are usually used for intravitreal injection [6]. Retinal detachment, retinal hole, and haemorrhage are complications that could be associated with intravitreal injection. Using MN in a micron scale with a small outer diameter could avoid such a complication [245]. Thus, MN with a 1:1 aspect ratio is probably not ideal for ocular application due to the large base diameter/side (900 μ m). Meanwhile, MN with a 1:3 aspect ratio was deemed to be of insufficient quality, specifically with the pyramid and triangular pyramid, due to the absence of the distinct geometrical characteristic resulting in a featureless shape MN (Figure 3-14). These MN showed cylindrical shafts through the top part of the MN since the high aspect ratio (1:3) resulted in a narrow variation in the

surface area between the layers, which mostly lies beyond the resolution capacity of the printer. The lack of edges sharpness is commonly associated with MN printed by SLA and DLP 3D printers [232, 238, 246].

The 1:1 aspect ratio was excluded from further study because of the bulkiness of the needle body, which could possibly damage the tissues upon application. Also, the 1:3 ratio was excluded because the printed MN shape lacked the input design definition. The optimization continued further on the 1:2 aspect ratio since it showed a reasonably defined geometry.

3.4.3 3D printing parameters

An investigation of the printing parameters on the MN resolution was conducted. The 3D printer allows the printing with 25, 50, and 100 μm layer thickness in the Z-direction. Before printing, the printer software breaks up the CAD design into a series of layers to be printed layer by layer consequently. Therefore, when a 25 μm layer height is selected, a greater number of layers is generated, and a lengthier printing time is required. On the other hand, thicker layers will reduce the total number of layers, and a faster printing time will be obtained. Here, a cone-shaped MN with a 1:2 aspect ratio was printed at 25, 50, and 100 μm thick layers in order to examine the effect of layer thickness on the printing quality. As seen in Figure 3-17, the needle surface was smoother and more defined at 25 μm thick layers. Conversely, low-resolution printing with a stair-stepping effect was observed when printing with 100 μm thick layers. The literature reported mismatched edge ridges with MN printed at 100 μm thick layers [104]. The stair-stepping phenomenon can be mitigated by printing with lower layer thickness [97]. Consequently, printing with 25 μm thick layers was chosen to print the MN for the rest of the study.

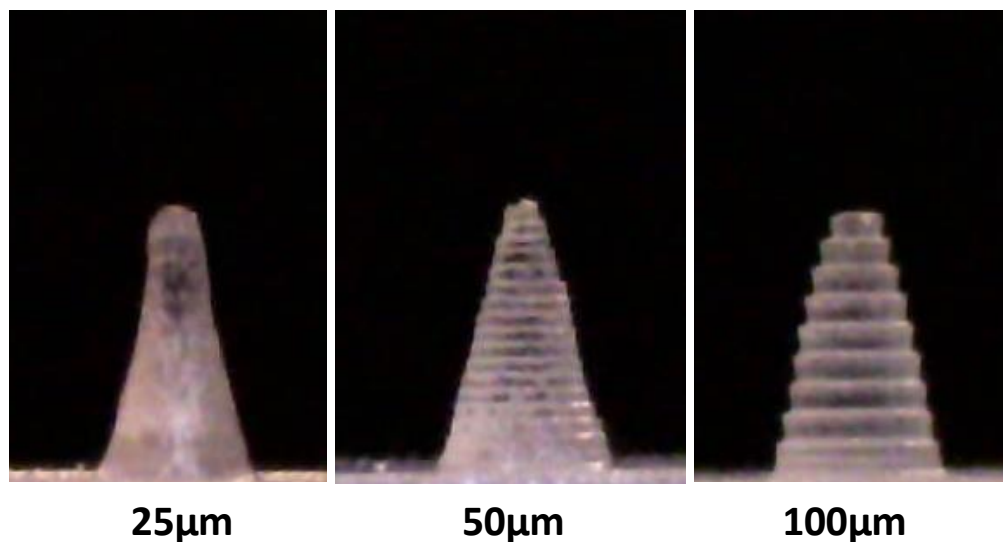


Figure 3-17 Digital images of 3D printed MN with 25, 50, and 100 μm layer thicknesses (MN are 900 μm in height).

Furthermore, the effect of printing orientation on the printing quality was studied. Using the 3D printer software that prepares the model before printing (Preform, Formlab®, USA), the MN arrays were adjusted at 0°, 45°, 67.5°, and 90° angles using printing support structures (Figure 3-18).

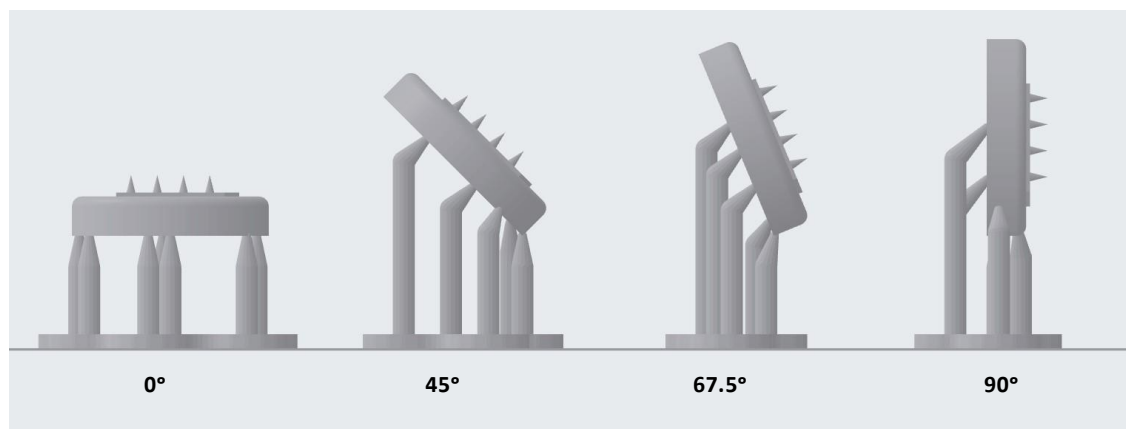


Figure 3-18 Adjusting the MN array at 0°, 45°, 67.5°, and 90° orientation angles using support structure to investigate the effect of changing the layers outline on the printing resolution.

The support structures are not part of the model; they are simply employed to support the model components, such as overhangs and bridges, during printing. After the

printing is completed, the support structures are removed at the touch point. In this study, the support structures were always attached at the back of the circular base holding the MN array to avoid any support touchpoint marks on the MN surface, as shown in Figure 3-19.

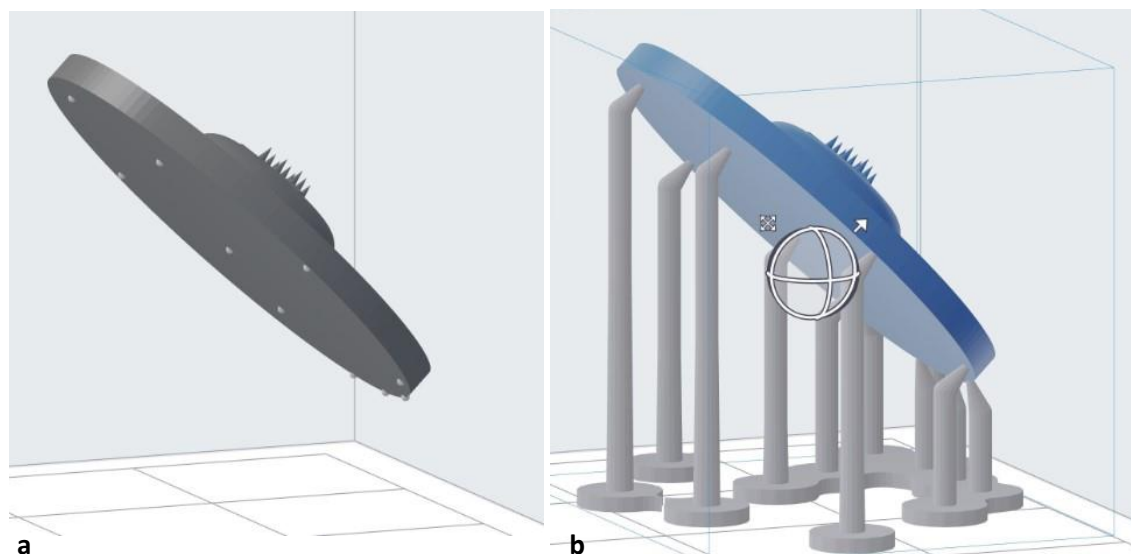


Figure 3-19 Adjusting the printing orientation of the CAD model in Preform software.
(a) editing the support structure points (b) support structure generated at the selected point.

The 3D printer software slices the model into a series of layers to prepare it for printing. Changing the orientation will affect the model slices. The master model was adjusted vertically (0°) on the building platform, which resulted in a higher number of layers with a smaller surface area. While rotating the needles at X-Z or Y-Z axis to 45° , 67.5° , and 90° progressively increased the surface area of the layer corresponding to print the MN tip (Figure 3-20-a). A comparative view of the outlines of the layer at which the needle tip was printed at the different orientation angles is presented in Figure 3-20.

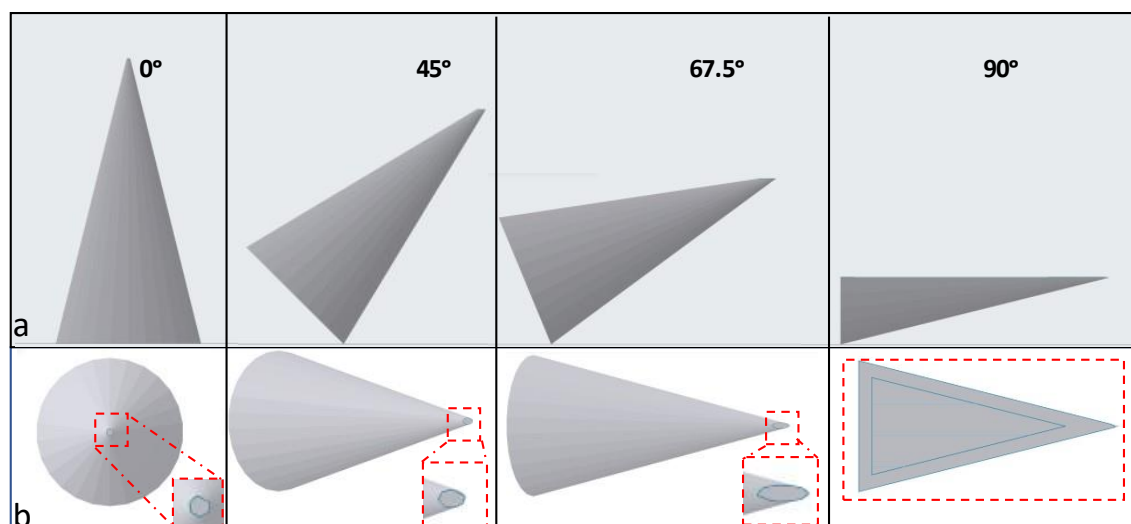


Figure 3-20 Printing needles at different orientation angles displaying the layer at which the MN tip is printed (a) side view, (b) top view.

First, a cone-shaped MN 900 μm in height with a 1:2 aspect ratio was printed at different orientation angles. The side, front, and top views of the printing outcome are presented in Figure 3-21. The MN tip size was noticeably reduced with increasing the orientation angle. However, the shape of the MN body was also impacted by printing at elevated angles. The MN tip size at different orientation angles is presented in Figure 3-23, it was observed that the tip shape has changed from a cylindrical shape at 0° to a bevelled tip at 45° to a more pointed tip at 67.5° and 90° . The % accuracy of the height and the base dimensions of the needles are presented in Figure 3-22. From the SEM images and the bar chart, it was seen the height decreased with increasing the orientation angle from a nearly accurate 901.50 μm average height at 0° to 864.17, 872.22, and 811.41 μm at 45° , 67.5° , and 90° respectively. This could be due to the lack of support at the MN body and the effect imposed by the gravitational force during the 3D printing process. The MN base diameter, on the other hand, has changed from a rounded shape at 0° to an elliptical shape at 45° , then to a more elongated elliptical shape at 67.5° and 90° orientations. The overall base dimension was calculated as the average of the minor axis and the major axis. The input MN base diameter was 450 μm , at 0° the diameter was 453.52 ± 2.614 μm and at 45° , 67.5° , and 90° orientation angles, the base diameter was 499.42 ± 26.43 , 493.12 ± 22.86 , and 594.16 ± 22.75 μm

respectively. The percentages of accuracy of the base and height are presented in Figure 3-22. MN printed at 90° showed a significant deviation from the base diameter ($p < 0.05$), where a 32.036% increase in the base diameter was recorded. The MN height was also significantly shortened, with a 9.85% decrease from the input dimensions observed.

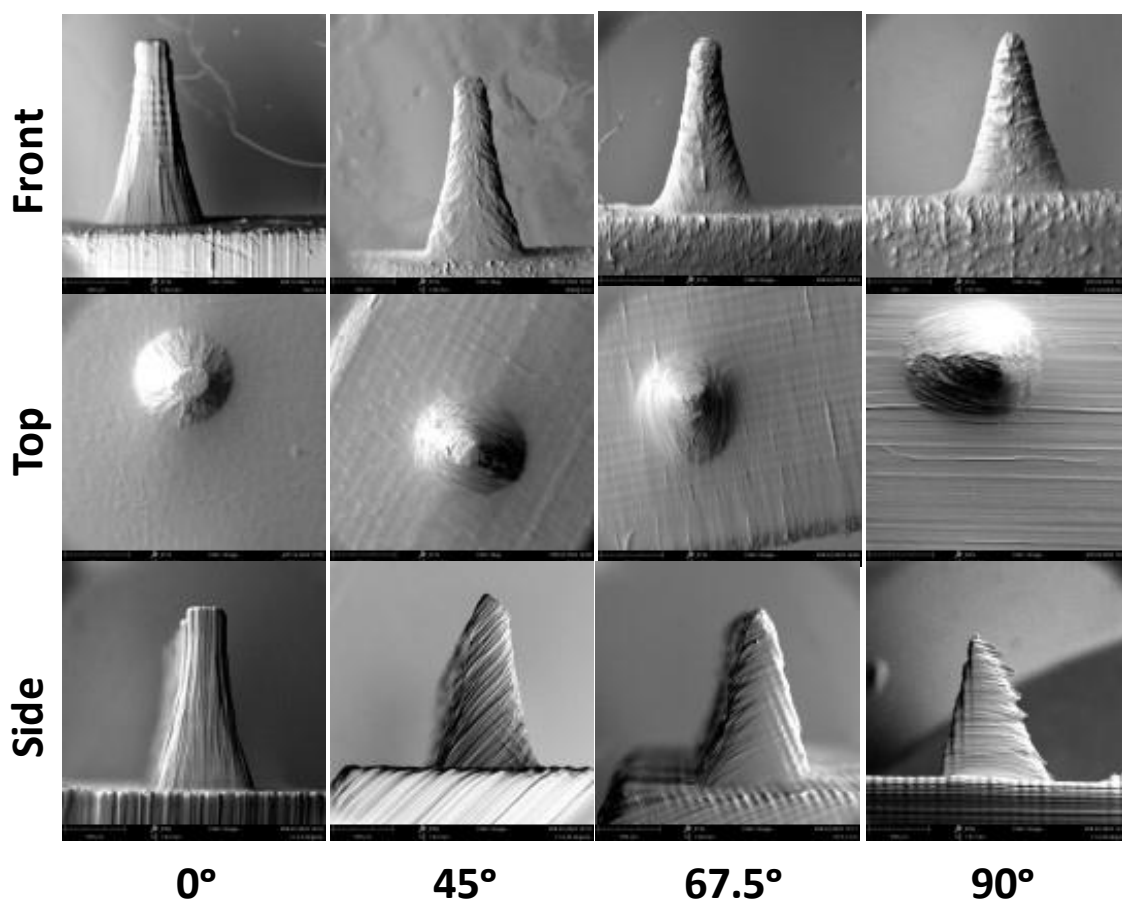


Figure 3-21 SEM images of 3D printed cone shaped (C 1-2) MN at different orientation angles (0°, 45°, 67.5°, and 90°) front, top, and side views. Scale bar (—) 300 μm .

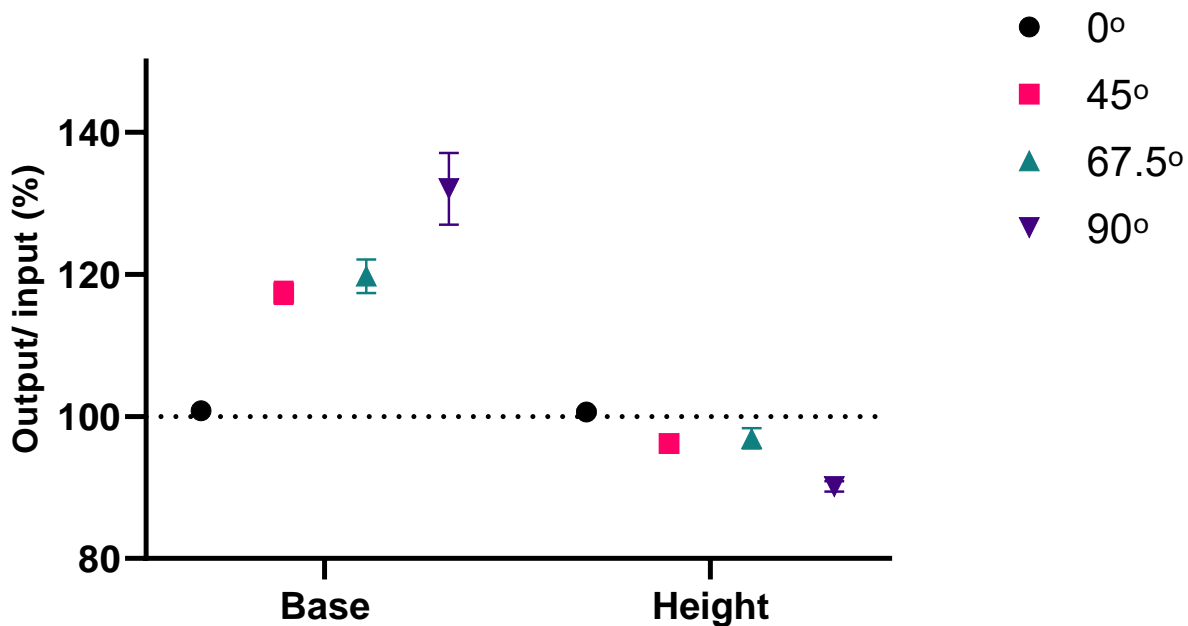


Figure 3-22 Accuracy (output/input %) of the MN height and base printed at 0°, 45°, 67.5°, and 90° orientation angles (dotted line indicates 100% accuracy). Data are reported as mean \pm SD (n=6 needles).

The average tip sizes collected from SEM images of the MN printed at different angles are shown in Figure 3-23. The mean tip size significantly decreased when tilting the MN array to 45° and continued to decrease with elevating the orientation angle. Changing the printing orientation changes the area of the layer corresponding to the tip printing. A similar observation was reported in a study with a 3D printed pyramid-shaped MN using an SLA printer, tilting the MN at 45° and 60° angles towards the corner of the pyramid produced a sharper needle tip [238]. Here, the conical shape of the MN allows more flexibility in the orientation in any direction due to the lack of corners in the cone design.

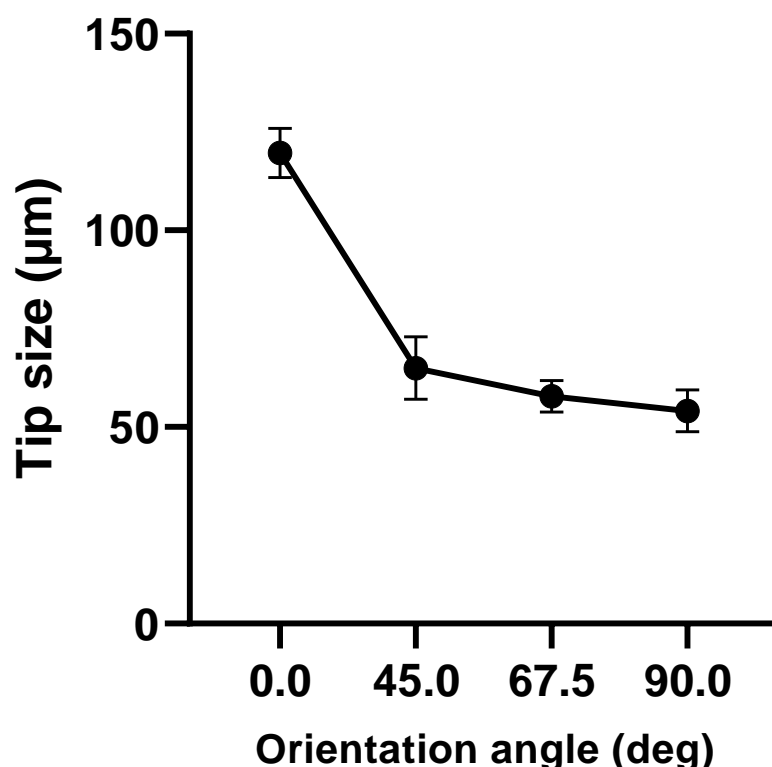


Figure 3-23 Effect of the orientation angles on the tip size of a cone shape MN. Data are reported as mean \pm SD (n=6 needles).

Furthermore, the effect of printing orientation on the limit of height printability was tested on a range of MN height. At 0°, the height of the printed MN was highly accurate in MN as low as 100 μ m. MN printed in the range of 100- 800 μ m at 45° and 67.5° angles are shown in Figure 3-24. A comparison of the input height and the printing outcome are presented in Figure 3-25 and Table 3-3. At 45° orientation, the printing failed to print at 100 μ m and 200 μ m input heights. Whereas at 67.5°, no printing was detected with 100 μ m input and needles 33.3 ± 9.92 μ m were detected at 200 μ m. Thus, printing at an angled position is only applicable with an input height of 300 μ m and above. Printing on 67.5° was slightly more accurate than printing at 45°. A study was conducted to test the percentage of accuracy on MN heights ranging from 600 μ m to 2000 μ m upon printing at a 60° angle [238]. In the referenced study, the accuracy of MN printed heights increased with the MN input height. While in this study, the height accuracy

relationship was not proportional at the studied height range. The data indicate that the proposed approach is sensitive to the input MN size, and to overcome such a limitation, the input height can be adjusted to achieve the desired MN dimension outcome.

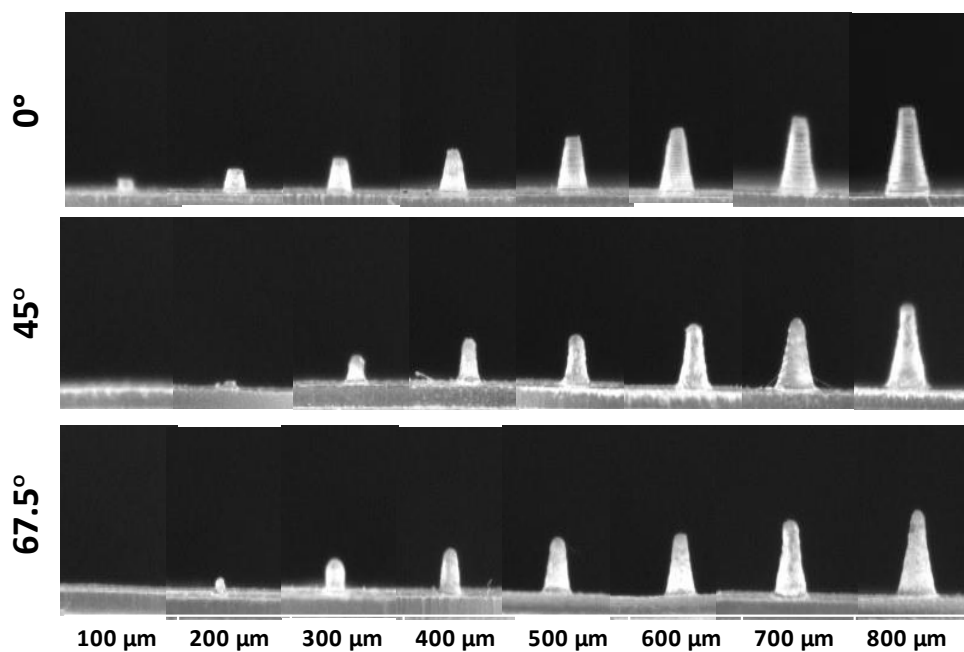


Figure 3-24 Digital images of MN (C 1-2) ranged in height from 100 μm to 800 μm printed at 0°, 45° and 67.5° angles.

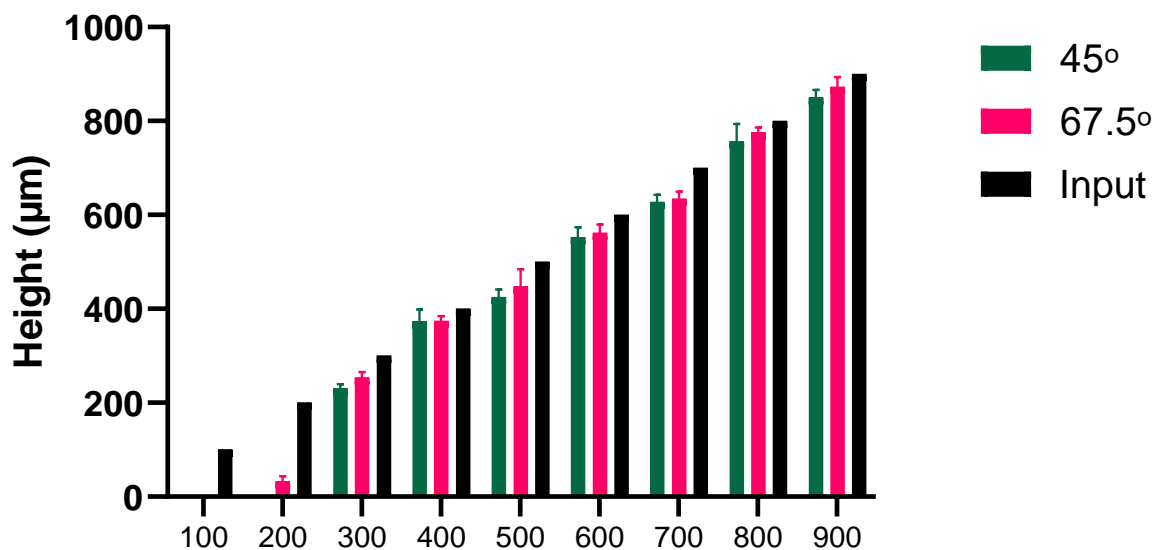


Figure 3-25 Comparison of the input and output heights of the MN (C 1-2) printed at 45° and 67.5° angles. Data are reported as mean \pm SD (n=6).

Table 3-3 Outcome height and accuracy (output/input %) of MN (C 1-2) printed at 45° and 67.5° angles. Data are reported as mean \pm SD (n=6).

Height (μm)	Height at 45° (μm)	Accuracy (%)	Height at 67.5° (μm)	Accuracy (%)
100	0.00	0.00	0.00	0.00
200	0.00	0.00	33.3±9.92	16.65
300	230.17 ±9.39	76.72333	253.63 ±11.92	84.54
400	373.75 ±25.48	93.4375	374.56 ±10.21	93.64
500	425.75 ±15.65	85.15	447.56 ±36.74	89.51
600	552.75 ±21.08	92.125	562.13 ±17.34	93.69
700	627.50 ±15.07	89.64286	634.50 ±15.18	90.64
800	757.00 ±36.96	94.625	776.13 ±10.13	97.02
900	850.13 ±15.54	94.45889	872.60 ±21.16	96.96

3.4.4 3D accuracy study

3.4.4.1 Accuracy of angled printing

Printing at an angled position without adding support structures to the projecting needles can affect the needle posture and silhouette. Coned shaped MN (C 1-2) 900 μm in height are individually 3D scanned to measure the height in the Z-direction, the MN surface area, the MN volume, and the tip size. For proper estimation of the MN tip size, the volume and the surface areas of the top 100 μm were determined. The images of the 3D scans of the MN printed at 0°, 45°, 67.5°, and 90° are displayed in Figure 3-26. The acquired MN height, surface area, and volume are calculated in terms of accuracy (%) in reference to the absolute values of the input design as shown in Figure 3-27. The images and the data confirm the previously reported data, the percentage of accuracy of the printing outcome deviates from the input values as the printing angles increase. At 0° orientation, the height and the surface area were almost accurate, with +0.83% \pm 0.41 and +3.62% \pm 4.39 change, respectively. However, the volume was slightly larger (+12.09% \pm 0.87) than the CAD design determined volume. This could be due to the larger volume of the tip. The needles were slightly shorter, with -5.15% \pm 1.40 at 45° and -2.02% \pm 1.16 at 67.5°, which could be explained by the insufficient support at the tip of the needle; thus, the printer possibly failed to print the last layer. Conversely, the volume and the surface area increased by increasing the angle of printing due to the needles sagging. The lowest accuracy was recorded with 90° printing, where +87.26% \pm 8.71 and +50.21% \pm 2.68 increases were recorded in the volume and surface area, respectively, accompanied by a -12.83% \pm 1.54 decrease in height.

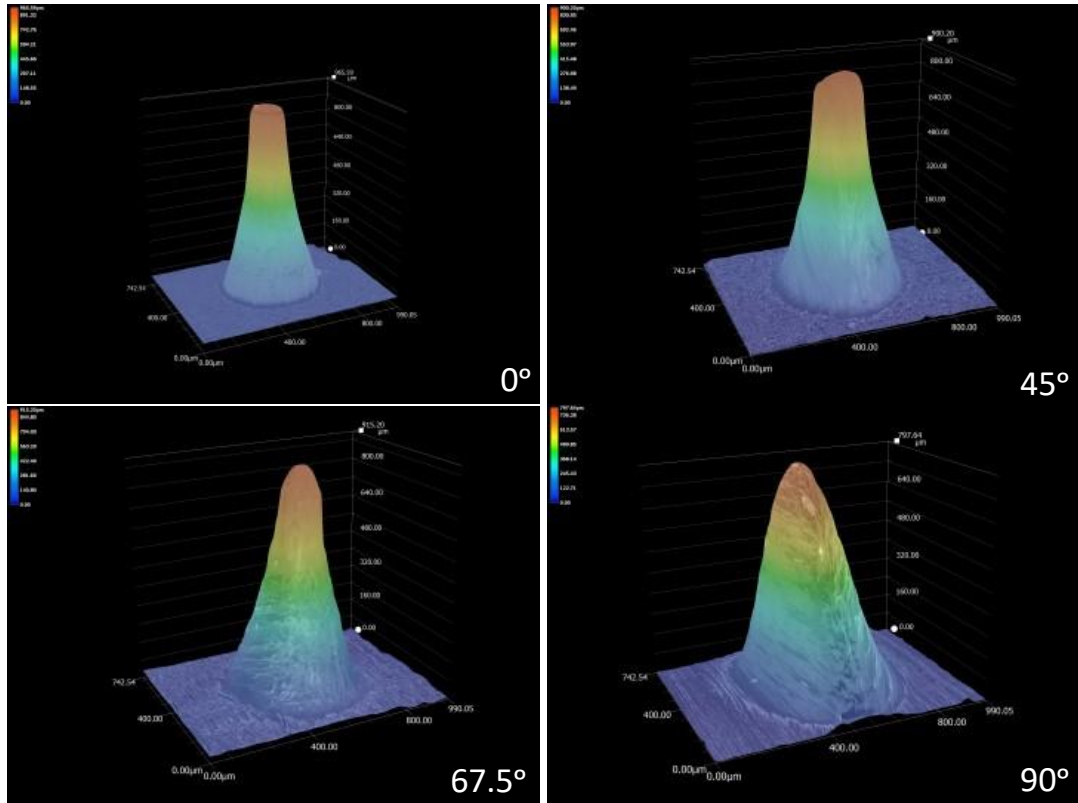


Figure 3-26 3D scans of MN (C 1-2) printed at different orientation angles (0°, 45°, 67.5°, and 90°).

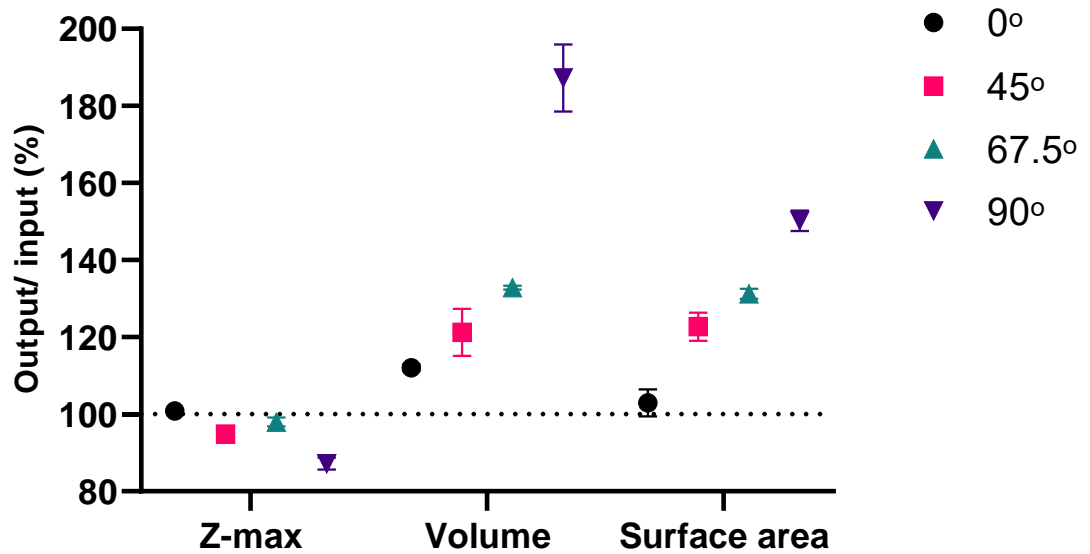


Figure 3-27 Accuracy (output/ input %) of the height (Z-max), volume, and surface area of MN printed at 0°, 45°, 67.5°, and 90° orientation angles (dotted line indicates 100% accuracy) Data are reported as mean ± SD (n=4).

The value of surface area per unit volume of an object is known as the surface-area-to-volume ratio (S:V). In physical dimensions, the surface-area-to-volume ratio is given in a unit of inverse distance (μm^{-1}) [247]. The S:V ratio is inversely related to the size of a particular object. It is a tool to measure how compact an object is, the higher the value, the more compact the object [248]. The S:V ratio of the whole MN body and the tip (measured at 100 μm from the top) are displayed in Figure 3-28. Comparing the S:V values of the MN bodies, the MN printed at 0° showed the highest S:V value with $14.91 \pm 0.50 \mu\text{m}^{-1}$. At 45° and 67.5°, the values slightly decreased, with 13.28 ± 0.23 and $12.89 \pm 0.68 \mu\text{m}^{-1}$, respectively. The lowest S:V value of $10.53 \pm 0.24 \mu\text{m}^{-1}$ was recorded at 90°, indicating that the MN has the largest body size. The recorded data suggests that increasing the printing angles increases the deformation of the MN shape. A study showed a similar finding of a reduced percentage of accuracy when printing cylindrical specimens at 45° using an FDM 3D printer [249].

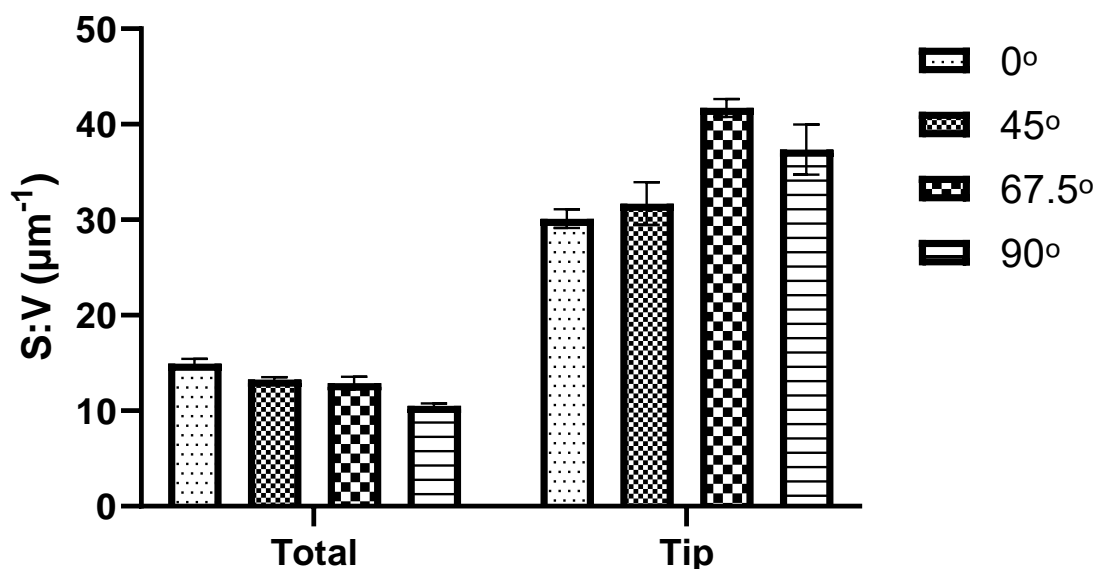


Figure 3-28 Surface area to volume ratio (S:V) of MN and tip (100 μm length from the top) printed at different orientation angles (0°, 45°, 67.5°, and 90°). Data are reported as mean \pm SD (n=4).

Meanwhile, the effect of the printing orientation on the MN tip size is displayed in Figure 3-28. The highest S:V ratio value was observed with MN printed at 67.5° with $41.71 \pm 0.95 \mu\text{m}^{-1}$, indicating and confirming previously observed smaller tips. At 90°, the S:V of the tip was $37.36 \pm 2.63 \mu\text{m}^{-1}$, and at 45° S:V was $31.70 \pm 2.24 \mu\text{m}^{-1}$. Finally, the largest tip was at 0° with $30.12 \pm 0.97 \mu\text{m}^{-1}$. Although the previously reported tip measurement from the SEM images suggested that the MN printed at 90° had the smallest tip size, here S:V ratio is based on two parameters, the surface area and the volume of the top 100 μm which collectively provided a higher value compared to the 67.5° orientation. In the literature, a study has reported a decrease in the MN tip size when printing at 60° orientation [238].

Overall, the data suggest that printing at 67.5° produced the pointiest MN tip with minimum impact on the MN body. Calculations to adjust the design can be performed to achieve the desired dimensions of the MN and hence the amount of drug loaded.

3.4.4.2 Accuracy of MN shape printing

SLA 3D printer has demonstrated a high level of printing accuracy. However, printing MN with various shapes in the sub-millimeter range may compromise the expected level of performance. In this study, MN in a cone, pyramid, and triangular pyramids with a 1:2 aspect ratio printed at 0° were 3D scanned (Figure 3-29). The mean values of height (Z-direction), volume, and surface area are presented in Figure 3-30. The highest accuracy measured in all the parameters was observed with C 1-2. While T 1-2 showed the lowest accuracy, the plane triangle-shaped layers in T 1-2 have collectively narrower angles compared to square-shaped layers in P 1-2. SLA printer resolution is based on the spot size and the increments of laser movement, which draw a rounded line. Therefore, it could be challenging to follow a triangular pattern with narrow angles precisely. This possibly could explain a higher deviation from input design in the T 1-2, and a higher accuracy observed with C 1-2.

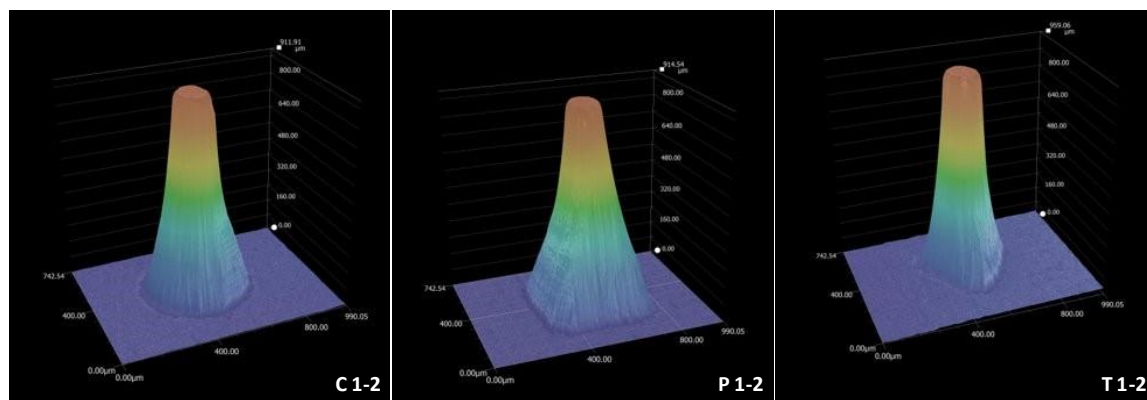


Figure 3-29 3D scans of MN printed with different shapes at 1:2 aspect ratio and 0°. Cone (C 1-2), pyramid (P 1-2), and triangular pyramid (T 1-2).

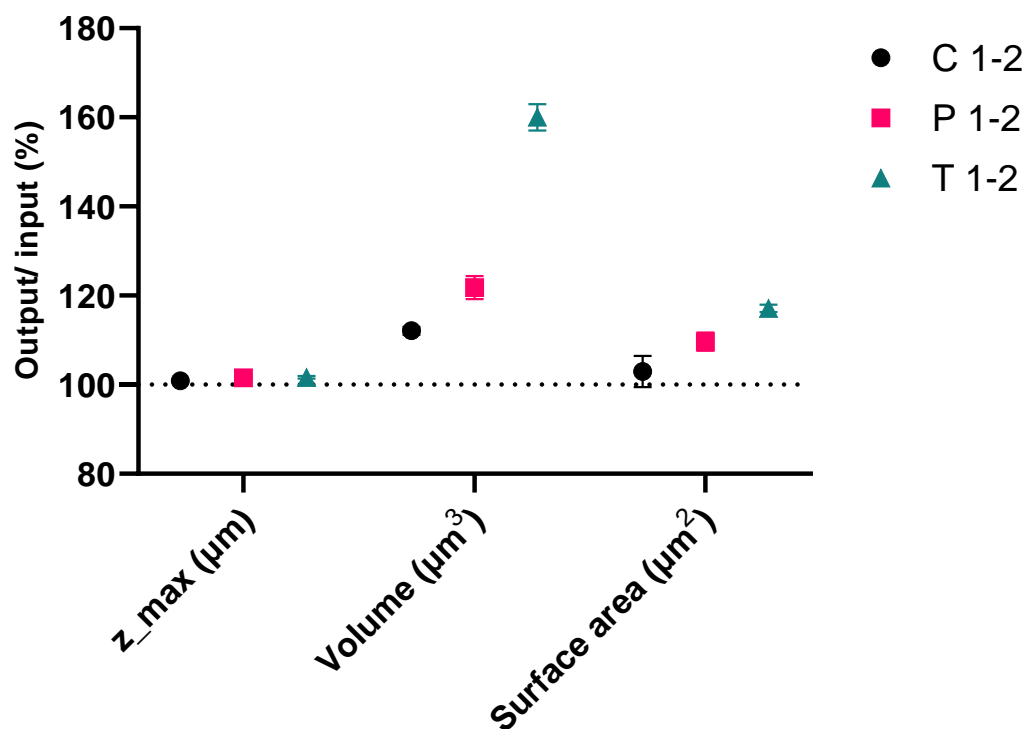


Figure 3-30 Accuracy (output/input %) of the height (Z-max), volume, and surface area of MN printed with different shapes at a 1:2 aspect ratio and 0°. Cone (C 1-2), pyramid (P 1-2), and triangular pyramid (T 1-2), (dotted line indicates 100% accuracy). Data are reported as mean \pm SD (n=4).

3.4.5 MN insertion depth

The effectiveness of MN as a drug delivery system relies on the permeability through biological tissue and MN insertion behaviour [60]. The insertion capability of a MN system is a result of several factors, including the mechanical strength, tip size, and geometrical shape of the MN [250]. According to previously reported studies, parafilm can function as a verified artificial membrane for MN insertion testing. This technique is commonly used to estimate the insertion depths in biological membranes such as skin. By multiplying the number of layers penetrated by the MN by the thickness of each parafilm layer (127 μm) to predict the overall penetration distance [80, 251]. MN arrays (3x3) printed at 0°, 45°, and 67.5° angles have been perpendicularly pressed on 8 layers of parafilm for a 1mm distance. Figure 3-31 shows the percentage of holes pierced on each layer by MN (C 1-2) printed at different orientation angles. All the MN have penetrated the first and second layers, while only the MN printed 67.5° has penetrated the third layer (381 μm depth) by 100%. While MN printed at 45° and 0° penetrated the third layer by 72.22% \pm 26.44 and 25% \pm 36.71 respectively. MN printed at 0° has failed to penetrate beyond the 3rd layer. At the fourth layer (508 μm depth), the MN printed at 45° reached by 25.00% \pm 42.91 and the array printed at 67.5° reached by 33.33% \pm 39.54 representing the effect of tip size on the penetration distance. The smaller the tip the greater the distance of penetration. It was reported that blunt MN requires higher force for skin penetration while sharper MN penetrate the tissue more smoothly [252].

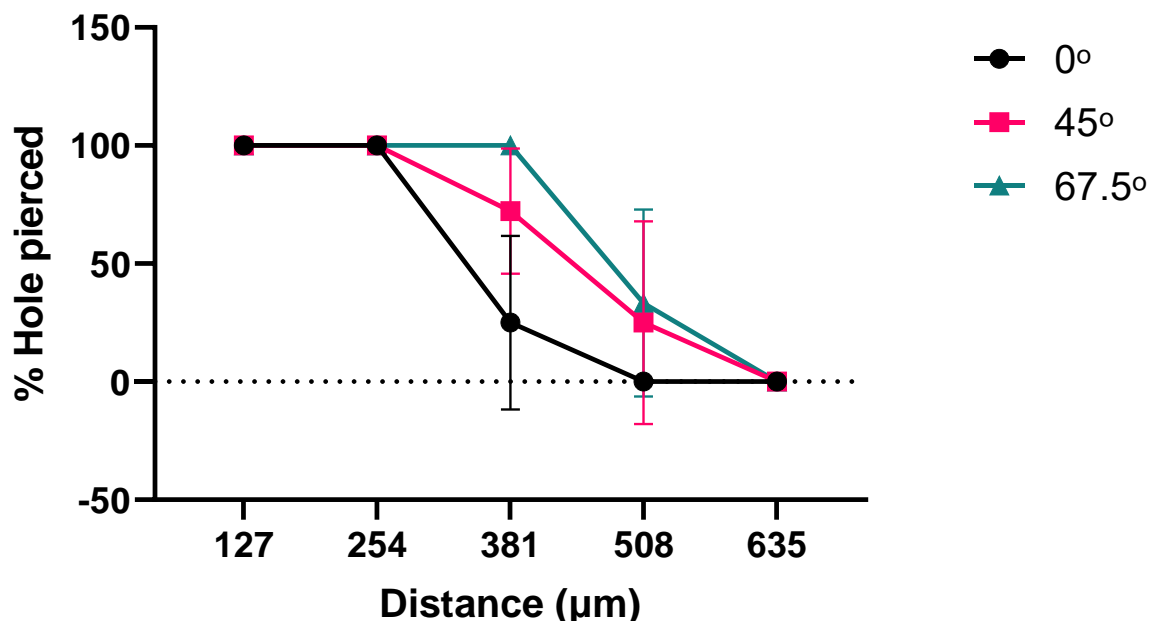


Figure 3-31 Percentage of holes created in parafilm M® layers following the insertion of cone (C 1-2) MN printed at different orientation angles (0°, 45°, 67.5°, and 90°) means \pm SD (n=4 arrays).

Furthermore, the effect of MN geometry on the insertion depth was also investigated. Figure 3-32 displayed the percentage of holes created on parafilm layers by the cone (C 1-2), pyramid (P 1-2), and triangular pyramid (T 1-2) printed at 0° to exclude the effect of tip size on the data collected. Unlike the cone-shaped MN (previously discussed), the pyramid and triangular pyramid created a lower percentage of holes at 127μm. P 1-2 created 58.33% \pm 29.22 at the first layer (127 μm depth) and 25.00% \pm 50.00 at the second layer (254 μm depth) and was unable to reach the third layer. Meanwhile, the percentage of the holes created by T 1-2 was higher than P 1-2, reaching the second layer by 52.77% \pm 42.91 and the third layer at 33.33% \pm 47.14. This comes in alignment with the recent study that reported the effect of the MN shape on skin insertion. A cone-shaped MN showed optimum geometry for tissue insertion and mechanical strength [253].

In the literature, a study was conducted to study the effect of the MN shape on the skin insertion force. Tapered cone MN demonstrated a lower insertion force compared to

bevelled tip MN [244]. Furthermore, a study that compared the insertion forces of different shapes of MN prepared by 2PP 3D printing found that conical shaped MN with a 1:3 aspect ratio displayed the highest insertion depth and drug deposition on neonatal porcine skin [74].

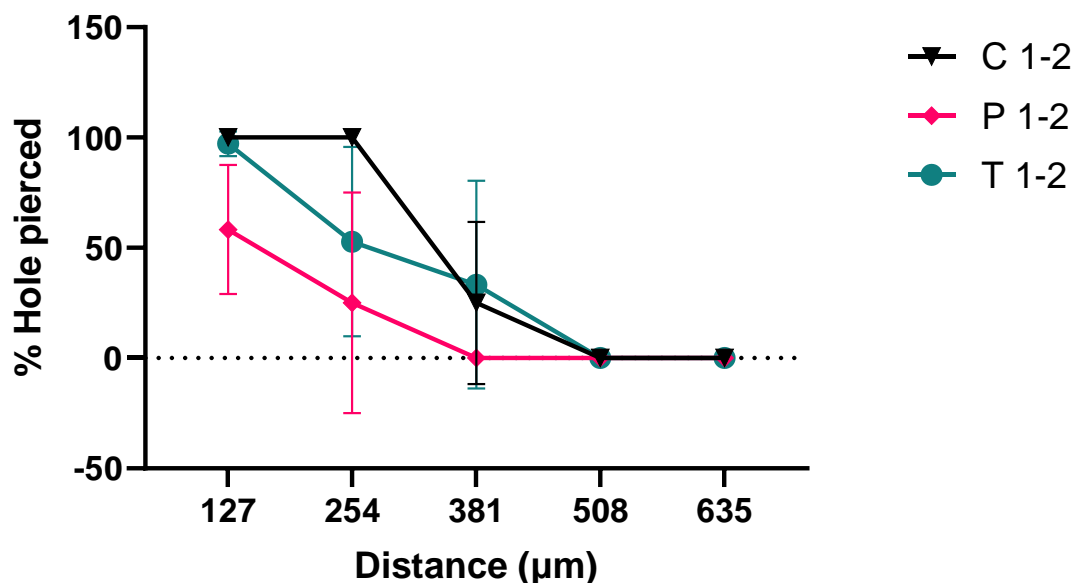


Figure 3-32 Percentage of holes created in parafilm M® layers following the insertion of different 3D printed MN shapes, cone (C 1-2), pyramid (P 1-2), and triangular pyramid (T 1-2) means \pm SD, (n=4 arrays).

Thus, MN in a cone shape with a 1:2 aspect ratio (C 1-2) was used in the rest of the study and the printing orientation will be addressed in the method section of the experiments.

3.5 Conclusions

This chapter demonstrated a simple, and easily customisable method for creating reusable MN master moulds for ocular application using a widely available and inexpensive SLA 3D printer. 3D printed masters were optimised to print MN with the highest resolution possible after extensive consideration of the complete process. The

model design, the 3D printer used, the type of resin, the printing parameters, and post-printing processing altogether affect the quality of the printed object. Masters to produce MN moulds were optimized to fit in a centrifugal tube and equipped with a reservoir for polymeric solution casting of an individual dose per mould.

MN are microstructure that require accurate and precise fabrication methods to achieve the optimal outcome. Design elements, including MN height, aspect ratio, and shape, were investigated. With typical vertical printing, MN was accurately printed in terms of height and base dimensions with heights ranging from 100 to 900 μm , various shapes (cone, pyramid, and triangular pyramid) and aspect ratios (1:1, 1:2, and 1:3). However, all the MN produced had blunt tips.

When optimizing a 3D printing process, many factors were considered to enhance the printing resolution' The layers' thickness was tested. Printing at 25 μm layers produced MN with smoother surfaces compared to 50 μm and 100 μm layers. The effect of the printing orientation was also studied. Adjusting the model at 45°, 67.5°, and 90° angles resulted in smaller and sharper MN tips. However, the overall geometry of the needles and the printing accuracy have been considerably affected by shifting the orientation of the printing to an elevated position. Thus, printing at 90° was eliminated from the study.

The MN insertion capacity, of the cone-shaped (C 1-2) showed the deepest penetration compared to the pyramid (P 1-2) and triangular pyramid (T 1-2) with the same height and aspect ratio. The tip size has also influenced the penetration capacity. Sharper tips produced with MN printed at 45° and 67.5° reached deeper layers.

In conclusion, masters including cone-shaped MN with a 1:2 aspect ratio showed superior printing accuracy. Adjusting the printing angle to 45° and 67.5° produced sharper tips and better insertion capacity.

Chapter 4 Formulation and characterisation of PLGA particles

4.1 Introduction

The polyester PLGA is a copolymer composed of PLA and PGA. PLGA is one of the most commonly used biodegradable polymers as a drug delivery vehicle for ocular formulation [114]. This hydrophobic polymer has been used to deliver API like small molecules (e.g. dexamethasone) and large molecules (e.g. proteins and genes) [124]. The use of PLGA as an ocular drug delivery carrier is intended to improve bioavailability while regulating the release of the payload through modifiable polymer characteristics. *In-vivo* biodegradation rate is based on the length and the monomer ratio of the polymer chains [114, 254]. The payload in PLGA delivery devices is released by diffusion through the polymeric matrix, by erosion of the polymer, or by a combination of both [124]. For ocular delivery, PLGA has been formulated as an implant, as electrospun fibre, and as micro- and nano- particles for topical and intravitreal application [121-123, 136, 255].

Various methods have been utilized to prepare PLGA drug delivery carriers, amongst which is the single emulsion (o/w) solvent evaporation method. In this method, PLGA is dissolved in a water immiscible organic (oil) phase, which is dispersed in the water phase [124]. The organic phase is emulsified in an aqueous phase in the presence of a suitable surfactant [256]. The characteristics of the PLGA particles synthesized by emulsion solvent evaporation methods have been shown to depend on the initial emulsion fabrication process, (including PLGA viscosity grade, PLGA concentration, type of organic solvent, type of surfactant or stabiliser, rate of mixing, time and temperature) and subsequently the solvent extraction step (including the volume of water, concentration of surfactant, mixing rate, and temperature) [254, 256].

Dexamethasone (Dex) is a commonly prescribed anti-inflammatory corticosteroid to treat anterior and posterior ocular conditions [132]. It is available on the market as a topical solution, suspension, ointment, and intravitreal implant [132]. Due to the high potency of Dex and the challenges associated with its delivery to the posterior segment of the eye, the drug was selected for this research. Dex-loaded PLGA micro- and nano-

particles prepared by emulsion solvent evaporation have been studied in the literature for ocular and non-ocular applications [257-265]. Studies to improve the Dex encapsulation efficiency and control the release have been reported. Mixing predegraded and standard Dex-loaded microparticles was studied to modulate the release of Dex over a 1-month period. [259], while another study has included vitamin E and human serum albumin as excipients in the formulation of Dex-loaded microparticles to improve the properties of the particles and regulate the drug release [136]. A design of experiment (DoE) approach was utilised to control the fabrication parameters to optimise the drug loading and the drug release profile of Dex-loaded PLGA microspheres prepared using polymer blends [266]. Furthermore, studies investigating the effect of blending different grades of PLGA on the properties of the particles and the drug release performance were reported [264, 267].

The principal aim of this thesis was to deliver and deposit PLGA particles into the scleral tissue using a minimally invasive dissolving MN system to overcome transocular barriers. Biodegradable micro- and nano- particles were prepared with PLGA polymer using o/w emulsion solvent evaporation method to prepare Dex-loaded, blank and fluorescent labelled particles. In this chapter, a parameter such as solvent type and viscosity of PLGA grades for preparing PLGA particles have been used to assess their influence on the percentage of drug loading, release profile, and size distribution.

The incorporation of the particles prepared and characterised in this chapter into the MN system will be studied in the following chapters. Dex-loaded micro- and nano- particles were prepared to test the *ex-vivo* performance and *in-vivo* pharmacological activity of the system. Furthermore, fluorescent labelled micro- and nano- particles were additionally prepared to study the particles cellular uptake and to assess the particle's distribution within the scleral tissue.

4.1.1 Aim and objectives

The aim of this chapter was to optimise the preparation of different types of PLGA micro- and nano- particles (blank, Dex-loaded and fluorescent labelled PLGA particles)

by oil-in-water solvent evaporation method using two grades of PLGA. The work also aimed to focus on the development of Dex-loaded particles that could offer a controlled Dex release profile.

The objectives of the study are:

- Optimise the preparation of PLGA particles by testing different viscosities of PLGA polymer for preparing various types of PLGA particles.
- Preparation of blank and fluorescent labelled PLGA micro- and nano- particles with identical composition but contrasting particle sizes.
- Preparation and optimisation of the Dex encapsulation in micro- and nano-particles.
- Characterise the different particles produced using variety of analytical techniques to understand the properties of each formulation.
- Assess the Dex release behaviour from the prepared Dex-loaded particles using an *in-vitro* dissolution method.
- Study the cytotoxicity and the cellular uptake on human retinal pigmented cells (ARPE-19).

4.1.2 Chapter graphical overview

A summary of the experiments conducted in this chapter is summarised in Figure 4-1.

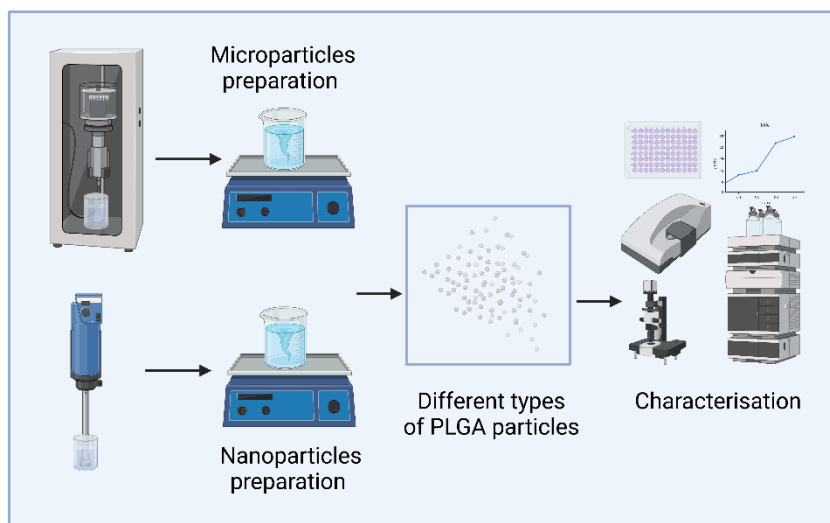


Figure 4-1 Chapter 4 graphical overview (created by Biorender).

4.2 Materials

PLGA 75:25 grades, Purasorb® PDLG 7507 and PDLG 7502 were obtained from Corbion Purac Biomaterials, Netherlands. Dimethyl sulfoxide, dichloromethane, methanol, ethanol, acetone, and trifluoroacetic acid were purchased from Merck Sigma Aldrich, France. Dexamethasone, polyvinyl alcohol, tween 80, sodium azide, phosphate buffered saline tablets, and tritons X-100 were purchased from Merck Sigma Aldrich. Acetonitrile was purchased from Fisher Scientific, UK. Coumarin-6 was purchased from Acros organic, USA.

Cell culture reagents:

Dulbecco's modified eagle medium/nutrient mixture F-12, Dulbecco's phosphate-buffered saline, fetal bovine serum, penicillin-streptomycin (10,000 U/mL), trypsin-EDTA, and trypan blue were purchased from Gibco, ThermoFisher Scientific, UK. Paraformaldehyde, 4% in PBS, was purchased from Alfa Aesar, UK. DAPI (diamidino-2-phenylindole) was purchased from Merck Sigma Aldrich, UK. CellTiter 96® Non-Radioactive Cell Proliferation Assay (MTT) was purchased from Promega, UK.

4.3 Methods

4.3.1 Preparation and optimisation of PLGA particles

4.3.1.1 Microparticle preparation

PLGA microparticles were prepared using oil in water (o/w) emulsion solvent evaporation method, using PVA aqueous solution as a stabilising agent. To prepare the blank PLGA microparticles, 140 mg of PLGA (75:25) was dissolved in 5 mL of dichloromethane (DCM). PVA 1% and 0.1% (w/v) solutions were prepared by mixing PVA powder in deionised water under continuous stirring at 80°C until completely dissolved then cooled at 4°C. The organic DCM/ PLGA solution was added dropwise to 15 mL of the 1% PVA solution, while subjected to homogenisation at 18,000 rpm for 60 sec using a high-speed homogeniser (Yellow line DI 18 basic, Ika, Germany) to produce a PVA stabilised o/w emulsion with small particle size. The homogenisation of the dispersion was carried out on an ice bath. The emulsion was added to 250 mL 0.1% PVA solution stirred with a magnetic stirrer at 600 rpm for 4 h, to evaporate the organic solvent at room temperature. Thereafter, the dispersion was washed by centrifugation at 9,000 rpm for 15 min using a centrifuge (Sigma 3-16K, Sigma, UK) in three cycles. The supernatant was removed each time and replaced with deionised water to remove the excess PVA solution. PLGA particle dispersion was then pre-frozen (−80 °C) for 12 h and subsequently lyophilised using (VirTis Advantage, SP, USA) for 48 h with hold and ramp cycles from −40 °C to 20 °C.

Furthermore, for the preparation of Dex-loaded PLGA microparticles, 100 mg of PLGA and 40 mg of Dex were dissolved in 5 mL of organic solvent, followed by the same steps mentioned above. The organic solvents used are listed in Table 4-1.

Table 4-1 Name and composition of the organic phase used for the preparation of blank and Dex-loaded microparticles.

Formulation code	Organic solvent (5mL)	PLGA grade
Blank microparticle		
MP-02	DCM	PDLG 7502
MP-07	DCM	PDLG 7507
Dex-loaded microparticles		
MP-02-Dex act	1:4 of Acetone:DCM	PDLG 7502
MP-07-Dex act		PDLG 7507
MP-02-Dex met	1:9 of Methanol:DCM	PDLG 7502
MP-07-Dex met		PDLG 7507
MP-02-Dex DMSO	1:9 of DMSO:DCM	PDLG 7502
MP-07-Dex DMSO		PDLG 7507

To prepare the fluorescent labelled PLGA microparticles, 0.5% w/w coumarin-6 was dissolved with 140 mg PLGA dissolved in 5 mL DCM followed by the steps used to prepare the blank PLGA microparticles.

4.3.1.2 Nanoparticle preparation

Similar to the method used for the preparation of the microparticles, PLGA nanoparticles were prepared by oil in water (o/w) emulsion solvent evaporation method, using PVA aqueous solution as a stabilising agent. To prepare the blank PLGA particles, 140 mg of PLGA (75:25) was dissolved in 5 mL of dichloromethane (DCM). PVA 1% and 0.1 (w/v) solutions were prepared by mixing PVA powder in deionised water under continuous stirring at 80°C until completely dissolved then cooled at 4°C. The organic DCM/ PLGA solution was added dropwise to 15 mL of the 1% PVA solution, while subjected to ultrasonication by dipping a probe sonicator (Soniprep 150, MSE,

UK) at 18 amplitude microns for 60 s. The emulsion was added to 250 mL 0.1% PVA solution and stirred with a magnetic stirrer for 4 h. The dispersion was then washed thrice by centrifugation at 9,000 rpm for 25 min using a benchtop centrifuge (Sigma 3-16K, UK). The supernatant was replaced with deionised water to remove the excess PVA solution. The PLGA particle dispersion was then pre-frozen (-80°C) for 12 h and subsequently lyophilised using (VirTis Advantage, SP, USA) for 48 h with hold and ramp cycles from -40°C to 20°C .

Likewise, for the preparation of Dex-loaded PLGA nanoparticles, 100 mg of PLGA and 40 mg of Dex were dissolved in 5 mL of DCM and methanol mixture (9:1). Then followed by the previously mentioned steps. Fluorescent labelled PLGA nanoparticles were prepared by dissolving 0.5% w/w coumarin-6 in the PLGA/DCM solution followed by the same steps employed to prepare the blank PLGA nanoparticles.

4.3.2 Particle size analysis

The mean particle size, the size distribution and the polydispersity index (PDI) were measured by dynamic light scattering (DLS) (Zetasizer, nano-zs, Malvern, UK). The freeze-dried PLGA particles were resuspended in deionised water and then sonicated for five minutes until a homogenous suspension was achieved. The suspension was later diluted with deionised water and then placed in the plastic disposable cuvette. The stabilising time was 60 seconds, and the measurement was repeated 10 times for each run. The mean particle size, size distribution and PDI were measured for each batch of PLGA particles prepared. The measurements were carried out in triplicate for each sample.

4.3.3 Surface charge measurement

The magnitude of the electrostatic charge was measured by a Zeta potential analyser (Zetasizer, nano-zs, Malvern, UK). The samples used in particle size measurement were placed in folded capillary cells with electrodes. An average of 100 measurements was

taken post one min of equilibration for each sample. The measurements were carried out in triplicate for each sample.

4.3.4 Morphology analysis

The surface morphology of the prepared PLGA particles was assessed by scanning electron microscopy (SEM). A small amount of the freeze-dried particles was mounted on an SEM stub (TAAB Laboratories, UK) using a double-sided electrically conductive adhesive carbon tab (Agar Scientific, UK). The samples were then gold coated for one min by a sputter coater (Quarum, Lambdaphoto, UK). The coated samples were imaged by a high-performance SEM (FEI Quanta 200F, FEI, Netherlands) or by a desktop SEM (Phenom Pro, USA) at 5Kv acceleration voltage. The acquired images were then analysed by an image processing software (ImageJ, USA).

4.3.5 Fluorescent imaging

Cumarine-6 loaded particles were imaged by a fluorescent microscope with a 12v mercury lamp (Nikon Microphot-FXA microscope, Nikon, Japan). Samples were placed on a glass slide and examined by halogen light and fluorescent light at 340 nm wavelength.

4.3.6 Percentage of production yield

Oil-in-water emulsion solvent evaporation method is a multistep formulation technique. In the last step of preparation, an empty bottle was weighed without the cap (W1). The particle dispersion was added to the bottle for freeze-drying. The bottle was reweighed after lyophilisation (W2) and the weight of the dry particles was calculated from the formula:

$$\text{Weight of the particles} = W2 - W1$$

Equation 4-1

To calculate the yield of the particles produced, the percentage yield (Y%) was calculated according to the following equation:

$$Y\% = \frac{\text{weight of the particles}}{\text{Total weight of the initial ingredients}} \times 100$$

Equation 4-2

The average % yield of microparticles and nanoparticles was calculated. A minimum of 4 batches were reported. If any spills or accidental losses occurred during the fabrication process the batch yield was excluded.

4.3.7 Analytical quantification of dexamethasone

Chromatographic quantification was utilised to detect and analyse the concentration of Dex in the samples. High-performance liquid chromatography (HPLC) (Agilent® 1200, Agilent Technologies, USA) equipped with a UV-visible detector, autosampler, quat pump and degasser was used. The method was developed and validated to quantify Dex dissolved in acetonitrile (ACN) and PBS. To analyse the Dex release and content in the particles, a calibration curve was constructed. The experimental conditions are summarized in Table 4-2. A C18 HPLC reverse phase column with 5 µm particle size, 15 cm length and 4.6 mm internal diameter (ASCENTIS®, Supelco, USA) was used for the analysis. The standard solution was prepared by accurately weighing 100 mg of Dex in 100 mL of ACN to prepare a mg/mL stock solution, then 1mL of the stock solution was diluted to 10 mL of ACN to prepare 100 µg/mL standard solution.

A gradient mobile phase was used to optimise retention time (RT) and the Dex elution peak by using a mobile phase comprised of a mixture of ACN and acidified water (0.1% TFA water, pH 2.1). The run starts at 30:70 ACN to 0.1% TFA water for 3 min (0-3 min), followed by a gradual change in the ratio to 70:30 ACN:0.1%TFA water over 12 min (3-15 min). Thereafter, the ratio was returned to the initial gradient (30:70, ACN: 0.1%TFA water) over 3 min (15-18 min) then stabilised for 5 min (18-23 min). A flow rate of 1 mL/min was maintained at 25 °C. The injection volume was 10 µL and the UV detection wavelength was set at 240 nm. The data acquired were analysed and processed with OpenLab software (Agilent Technologies, USA).

Table 4-2 Chromatographic conditions used for the analysis of Dex.

Experimental conditions			
Column	Supelco™ C18 HPLC column (150x4.6 mm, 5µm)		
Detection	UV at 240 nm		
Mobile phase	A: ACN B: 0.1% TFA water		
	Time (min)	% A	% B
	0-3	30	70
	3-15	30-70	70-30
	15-18	70-30	30-70
	18-23	30	70
Injection volume	10 µm		
Flow rate	1 mL/min		
Column temperature	25 °C		

4.3.7.1 Method of validation

The developed HPLC method was validated for system suitability, specificity, linearity, accuracy, precision, and robustness [207].

- System suitability

To test an integral part of the developed procedure by routinely checking the suitability of the system to execute accurate and precise chromatograms. The standard solution (100 µg/mL) was injected 6 times and the chromatograms were recorded and compared to the standard validated chromatogram.

- Linearity

To test the ability of the method to obtain results proportional to the concentration of the analyte within the working range. The linearity was determined by calculating the linear regression of the peak area vs the concentration of the analyte at the given range.

The linearity was measured for Dex in the range of 5 µg/mL to 150 µg/mL. The equation of the regression line and the correlation coefficient were calculated.

- Precision

Precision and repeatability are to measure the method's reproducibility under normal operating conditions and expressed as relative standard deviation (%RSD):

$$\%RSD = \frac{SD}{Mean} \times 100$$

Equation 4-3

Samples of standard Dex solutions of 50, 100, and 150 µg/mL were tested 6 times on the same day (intraday precision) and 3 consecutive days (interday precision).

- Accuracy

Accuracy is used to express the closeness of the acquired data to the true value and it is calculated as the percentage recovery of the analyte. Spiked pre-analysed samples were tested for the % recovery of the added Dex amount.

- Limit of detection and limit of quantification

The limit of detection (LOD) is to determine the lowest detectable concentration of the analyte, albeit not always quantitated. According to ICH guidelines, LOD can be measured by different methods. Among which signal-to-noise approach. This approach is performed by determining the lowest concentration of analyte that produces a signal-to-noise ratio (s) of 3:1 and it is calculated by the following formula:

$$s = H/h$$

Equation 4-4

where H is the height of the peak and h is the absolute value of the highest peak detected in the baseline of a blank solution chromatogram.

The limit of quantitation (LOQ) is essential for several pharmaceutical applications. LOQ is the lowest concentration of analyte that can be adequately identified with acceptable precision ($RDS \leq 5\%$). It is generally accepted as a 10:1 signal-to-noise ratio or based on the SD of the response and slope, calculated by the following formula:

$$LOQ = \frac{10 SD}{b}$$

Equation 4-5

where SD is the standard deviation of the regression line intercept, and b is the slope of the calibration curve.

- Specificity

Specificity is used to express the ability of the method to detect the analyte in the presence of other components expected to be present in the analysed samples. Blank PLGA particles were dissolved in ACN. The solution was mixed with different ratios of PBS 1:9 and 9:1 PBS:ACN and spiked with 50 µg/mL Dex.

- Robustness

The robustness of a method is to confirm the developed method is unaffected by deliberate alteration in the method parameters and confirms the reliability of the method during routine analysis. The standard solution of Dex was tested 3 times for each varied parameter of flow rate, column temperature, and pH of the mobile phase acidified water.

4.3.7.2 Standard calibration curve

To test the linearity of the HPLC method, a standard calibration curve was constructed by analysing serial dilution of known concentration of Dex in ACN (150, 100, 75, 50, 25, 10, 5 µg/mL). Each concentration was analysed using the developed HPLC method and a curve of Dex concentrations vs chromatogram peak areas was plotted, and a line was

fitted to measure the degree of linearity. The regression line equation was used as a reference to quantify the unknown concentration of Dex. A series of replicates (x4) were performed to ensure the robustness of the calibration curve [268]. The equation of the regression line and the correlation coefficient (r^2) were calculated. An r value close to unity ($r^2=1$) indicates a linear relationship between the concentration and the response.

4.3.8 Encapsulation efficiency and drug loading capacity

To determine the encapsulation efficiency and drug loading of the prepared Dex-loaded particles a direct method of quantification was used. An accurately weighed Dex-loaded particles was completely dissolved in ACN. Samples from the solution were filtered by polytetrafluoroethylene (PTFE) 0.22 μm filters. The samples were subsequently analysed by HPLC to determine the amount of Dex in the particles.

Then, the percentage of encapsulation efficiency (EE%) and the percentage of drug loading (DL%) were calculated by the following equations:

$$EE\% = \frac{\text{Actual amount of Dex in the particles}}{\text{Theoretical Dex amount}} \times 100$$

Equation 4-6

$$DL\% = \frac{\text{Actual amount of Dex in the particles}}{\text{total amount of the particles}} \times 100$$

Equation 4-7

4.3.9 Solubility Study

To assess the saturated solubility of Dex in deionised water and PBS (pH 7.4), a solution of 1 mg/mL of Dex in water or PBS was prepared and kept at $37 \pm 0.5^\circ\text{C}$ shaking incubator (100 rpm) for 48 h to reach equilibrium [122]. Samples were filtered using a 0.45 μm PES filter and analysed by HPLC to determine Dex concentration. The solubility was analysed in triplicate and the means \pm SD were reported.

4.3.10 *In-vitro* dexamethasone release study

The *in-vitro* release of Dex from the PLGA particles was carried out using a modified release study. In a 15 mL Falcon™ tube, 10 mg of the Dex-loaded particles were added with 10 mL preheated at 37 °C PBS containing 0.05% tween 80 and 0.02% sodium azide. The tube was placed in a shaking incubator (Sciquip, UK) at 37 °C and 100 rpm. At specified time intervals, the tubes were centrifuged for 5 min at 5000 rpm then a 1 mL sample was withdrawn from the dissolution media and replaced with fresh buffer. The collected samples were kept at -20 °C until the end of the experiment. The amount of Dex was analysed by HPLC. Three batches of the particles were analysed in triplicate and the means \pm SD were reported.

4.3.11 Thermal Analysis

Thermal analysis of the raw materials, physical mixture, and Dex-loaded and blank PLGA particles was performed using a Discovery TA Q2000 differential scanning calorimeter. Data collection was performed from 0 °C to 300 °C, at a heating rate of 10 °C/min and an empty aluminium pan was used as a reference standard. 3-5 mg of sample was placed in an aluminium pan (Perkin-Elmer, USA), then crimped by an aluminium lid. The sealed pan was punched to put a pinhole in the lid. Analysis was performed under nitrogen purge at a 50 mL/min rate. The equipment underwent routine calibration procedures using high purity indium to ensure accurate measurement of the sample tested. The data collected were analysed by TRIOS data analysis software (TA instruments, USA).

4.3.12 X-ray powder diffraction

XRD is a non-destructive testing instrument used to characterise the solid state of materials. Free polymer, Dex, physical mixture, and Dex-loaded and blank PLGA particles were analysed by benchtop X-ray diffractometer (MiniFlex 600, Rigaku, Japan). The sample was placed and pressed on a crystal quartz sample holder. The instrument uses copper K- α radiation and the scan was operated at 40 mV and 15 mA at a diffraction angle (2θ) from 3° to 50°. Data was collected at a step size of 0.02° and

4° per min. Patterns were generated from raw data using Origin 2019 (OriginLab Corporation, USA).

4.3.13 Fourier transform infrared spectroscopy

To obtain an infrared spectrum of the initial materials, a physical mixture and Dex-loaded and blank PLGA particles FT-IR spectrometer (Spectrum 100, Perkin-Elmer, USA) was used. Each sample was scanned 16 times in the range of 4000 cm^{-1} to 500 cm^{-1} at 2 cm^{-1} resolution. A background scan was performed before each run.

4.3.14 Cell culture

Human retinal pigment epithelial cell line (ARPE-19) purchased from American Type Culture Collection (ATCC®, CRL-2302™, USA). Passage number 12 was maintained in culture media comprised of DMEM/F12 supplemented with 10% FBS and 1% antibiotic (streptomycin/penicillin). The cells were incubated in a humidified atmosphere of 5% CO_2 and 95% O_2 at 37 °C. Once the cells reached 70% confluency (~ 72 h), culture media was gently removed and replaced with DPBS for washing. The cells were detached with 0.05% trypsin-EDTA the cells were incubated for 7 min until the cells were fully detached then centrifuged at 1100 rpm for 7 min. The supernatant was gently removed and resuspended in 2 mL media. 100 μL of the cell suspension was mixed with 100 μL Trypan blue for cell counting. Brightfield automated cell counter (LUNA-II™, Logos Biosystems, Korea) was used to quantify and differentiate between the live and the dead cells. The cells were further diluted with media and seeded in multi-well plates and cultured to yield 70% confluency.

4.3.15 Determination of inhibitory concentration

To identify the 50% inhibitory concentration, the cells were seeded at 5×10^3 cells per well in 96 well plates and incubated at 37 °C and 5% CO_2 . After 48 h incubation, 70% confluency was reached. A serial dilution of 100 μL Dex solution ranging from 3.9 to 500 $\mu\text{g/mL}$ was added to each well which was then further incubated for 24 and 48 h. Untreated cells were used as a control for the experiment. Cells proliferation activity

was checked by CellTiter 96® Non-Radioactive Cell Proliferation Assay (MTT), 15 µl of the dye solution was added in each well and incubated at 37°C and 5% CO₂ for 2 h, then a 100 µl of the stop solution (solubilising solution) was added to each well. The plates were kept at 4 °C for 1 h, then the absorbance was recorded at 570 nm using a 96 well microplate reader (Spectramax® M2, Molecular Devices, USA). The percentage of the cell viability was recorded in reference to the control wells where they were considered 100% viable. The data were presented as a mean ±SD of at least three replicas.

4.3.16 Cell viability assay

The particles were tested for cellular toxicity using an MTT assay. ARPE-19 cells were seeded with 100 µL culture media at 5x 10³ cells/ well in 96 well plates and cultured to confluence. Thereafter, the cells were incubated with blank media, blank and Dex-loaded micro- and nano- particles for 24 and 48 h. At the end of the treatment, the media and the particles were removed, and the cells were washed thrice with DPBS to completely remove the particles. The cells were then incubated with 100 µL MTT reagent for 4 h at 37 °C 5% CO₂. Later, 100 µL of the solubilising solution was added to each well to solubilise the formed formazan crystals for 60 min. To calculate the viability of the cells the absorbance was measured at an optical density of 570 nm using a microplate reader (Spectramax® M2, Molecular Devices, USA). Untreated cells were considered 100% viable. The relative cell viability was calculated according to the equation:

$$Cell\ viability = \frac{Abs\ of\ test}{Abs\ of\ control} \times 100$$

Equation 4-8

All assays were performed in triplicate and presented as a mean ±SD.

4.3.17 Cellular uptake

Fluorescent labelled particles were used to study the cellular uptake in ARPE-19 cells. The cells were cultured to 70% confluency then seeded in 24 well plates at 10 x 10³ cell

density/ well and incubated with culture media to confluence. The media was then removed, and the cells were treated with 20 µg/mL suspension of the fluorescent labelled micro- and nano- particles then incubated for 2 h in 5% CO₂ and 95% O₂ at 37 °C. The experiment was terminated by washing the cells 6 times with DPBS to remove the excess unattached particles. The cells were either fixed and stained or lysed by non-ionic surfactant.

To assess the uptake, the cells were fixed with 4% paraformaldehyde and the nucleus was stained with 100 µL DAPI (0.1 µg/mL) for 5 min. Then, washed by DPBS and observed with a cell imaging system (EVOS, ThermoFisher, UK). The obtained images of the cells are analysed by ImageJ (USA) to quantify the fluorescence intensity of the cells. Cells were selected and outlined by the software selection tools along with an adjacent background area as shown in Figure 4-2. Subsequently, the selection was analysed to measure the area, the mean fluorescence, and the integrated density. To subtract the fluorescence of the background and neutralize the error of manual cell selection, the corrected total cell fluorescence (CTCF) was calculated according to the following formula [269, 270].

$$CTCF = \text{integrated density} - (\text{area} \times \text{mean of background fluorescence})$$

Equation 4-9

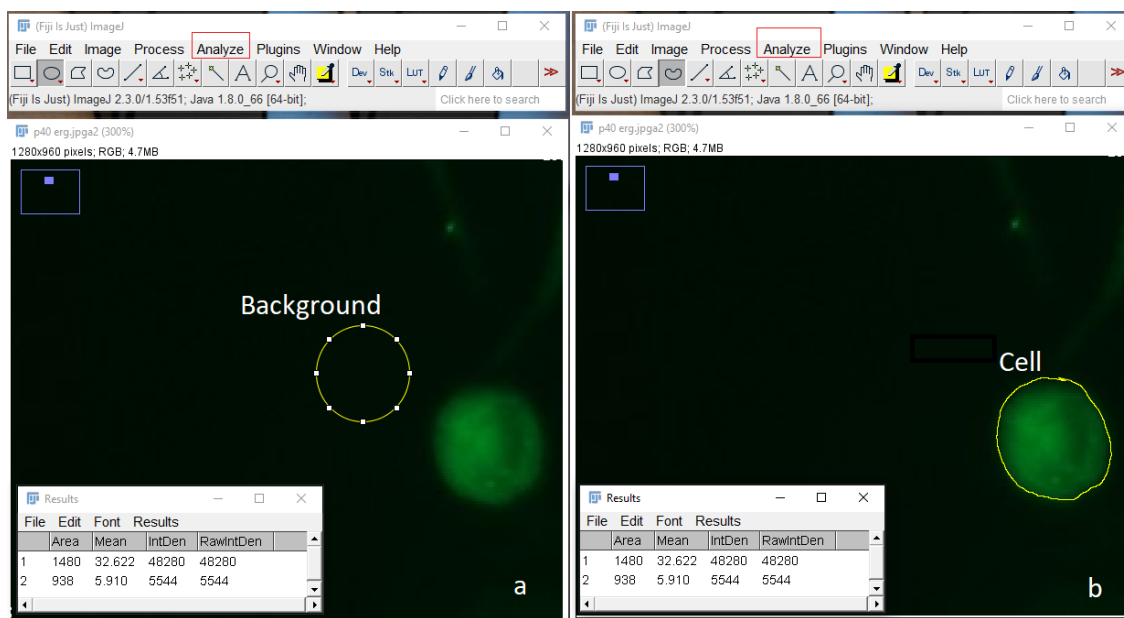


Figure 4-2 Demonstration of ImageJ fluorescence analysis by calculating the corrected total cell fluorescence (CTCF) by selecting (a) background, (b) cell.

Alternatively, the washed cells were treated with 100 μ L 0.5% Triton X-100 in 0.2N NaOH solution, a nonionic surfactant that permeabilises the cell membrane rendering the internal particles exposed for quantitative measurement. The plates were measured for fluorescent intensity by a microplate reader (Spectramax® M2, Molecular Devices, USA) at λ_{ex} 430 nm, λ_{em} 485 nm. The uptake was presented as the % of fluorescence of the cells correlated with the fluorescence of the treating solution. Untreated cells were used as a negative control.

4.3.18 Statistical analysis

Statistical analysis was conducted by the statistical software Prism 9 (GraphPad, USA). Data reported as mean \pm SD. The means were compared by T-test or by one-way ANOVA followed by Tukey's multiple comparison test. *P*-values <0.05 indicate statistical significance.

4.4 Results

4.4.1 Preparation and optimisation of PLGA particles

4.4.1.1 Microparticle preparation

In this study, PLGA microparticles were formulated by the o/w emulsion solvent evaporation method. Initially, the microparticles were prepared and characterised, and then the optimised formulation parameters were used to prepare the nanoparticles. This work aimed to study the effect of PLGA viscosity on the prepared microparticles. In addition to the PLGA viscosity, the effect of the organic phase composition on the Dex encapsulation was also investigated.

Two grades of PLGA were used to prepare blank and Dex-loaded microparticles, Purac® PDLG 7502 (low viscosity) and Purac® PDLG 7507 (high viscosity). For the preparation of the blank microparticles, DCM was used as an organic (oil) phase, whereas in Dex-loaded microparticles a mixture of solvents was used to improve Dex solubility in the organic phase since Dex is insoluble in DCM. For the preparation of the Dex-loaded microparticles, a mixture of DCM with acetone, methanol, or DMSO was used as an organic phase to prepare the o/w emulsion (Table 4-1). The microparticles were assessed based on their shape, encapsulation efficiency, and release profile. Consequently, the formula with a uniform shape, high Dex encapsulation, and controlled release was selected for further examination.

Figure 4-3 and Figure 4-4 show SEM images of the blank particles. From images, it was clear that the two grades of PLGA made microparticles that were spherical in shape and had a smooth surface. However, the high viscosity grade demonstrated a wide range of particle sizes. The molecular weight of PLGA is manifested in the viscosity, which in turn, has a large influence on the droplet formation and the resulting droplet size distribution [254].

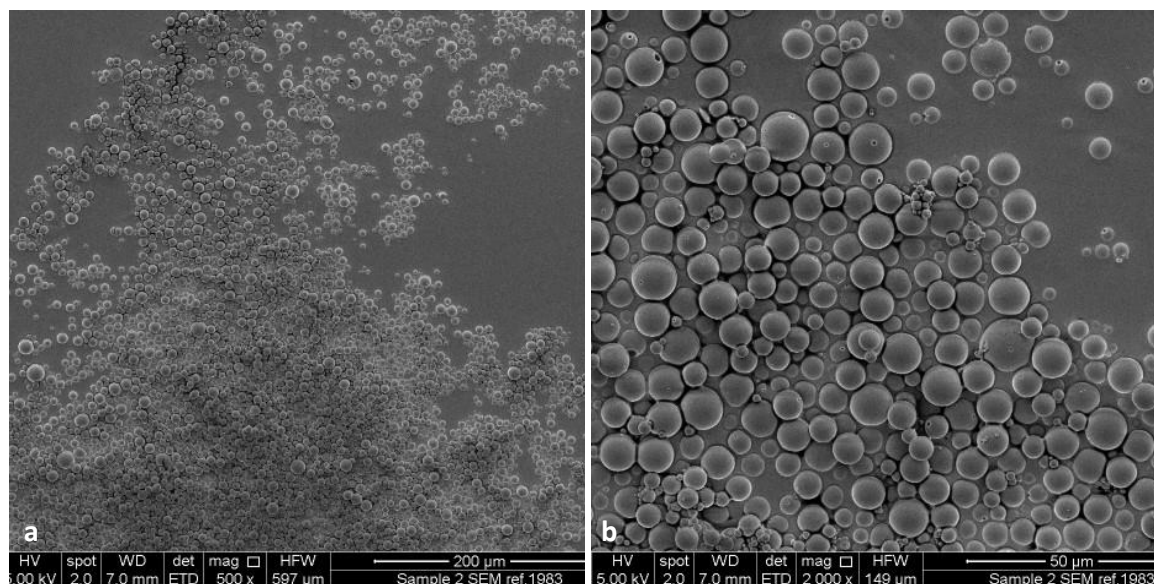


Figure 4-3 SEM images of blank PLGA particles (MP-02) prepared by low viscosity PLGA (PURAC®, PDLG 7502), (a) lower magnification overview, (b) higher magnification overview.

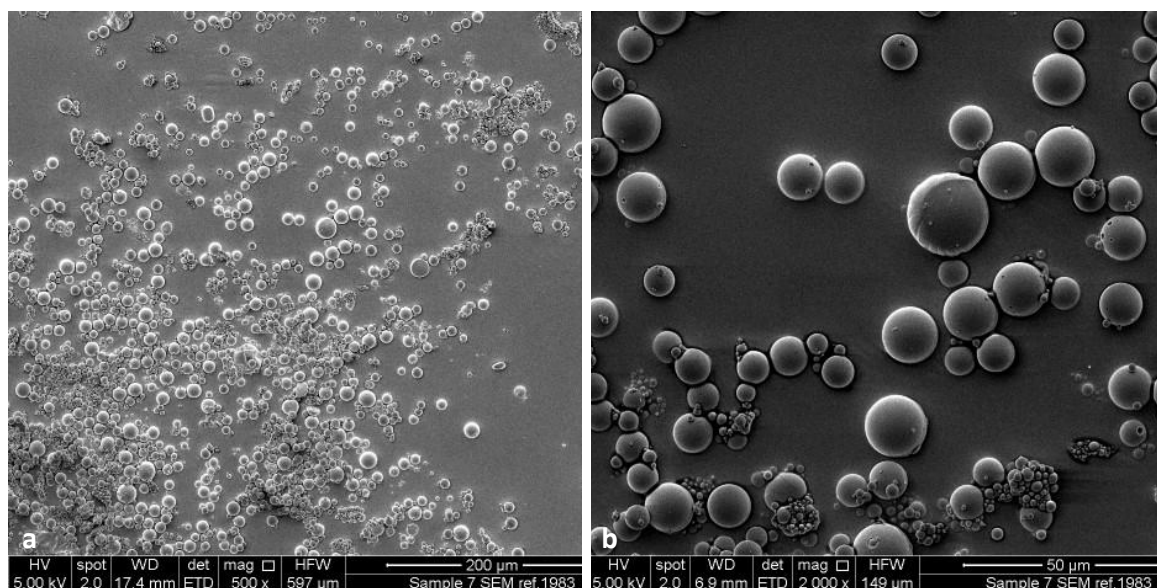


Figure 4-4 SEM images of blank PLGA particles (MP-07) prepared by high viscosity PLGA (PURAC®, PDLG 7507), (a) lower magnification overview, (b) higher magnification overview.

Based on the theory of emulsification, two immiscible liquids are mixed in the presence of a stabiliser to disperse the oil phase in the water phase [151]. In the preparation of the Dex-loaded microparticles, the insolubility of Dex in DCM and most of the water immiscible organic solvents necessitate the use of organic solvents mixture. Dex is freely soluble in DMSO and methanol, and sparingly soluble in acetone [271]. Since these solvents (DMSO, methanol, and acetone) are water miscible, a mixture with DCM was prepared for each solvent. In the literature, the use of a combination of solvents has been reported to prepare Dex-loaded PLGA micro- and nano- particles [261, 265, 266].

Both the low viscosity and high viscosity PLGA grades were used with each solvent mixture as listed in Table 4-1. In the acetone and DCM mixture, Dex was not fully soluble in the mixture; therefore, a dispersion of Dex in the mixture was prepared. The SEM images of the resultant microparticles are shown in Figure 4-5. The microparticles were spherical in shape with a wide range of size distribution. However, with the two grades of PLGA used irregularly shaped particles were observed in the sample (indicated by orange arrows). These particles seemed to be free Dex particles as Dex was initially dispersed and not solubilised in the organic phase. A similar observation was reported where free Dex was detected in a PLGA microparticle sample when Dex was dispersed in DCM for microparticle preparation by o/w emulsion solvent evaporation method [266].

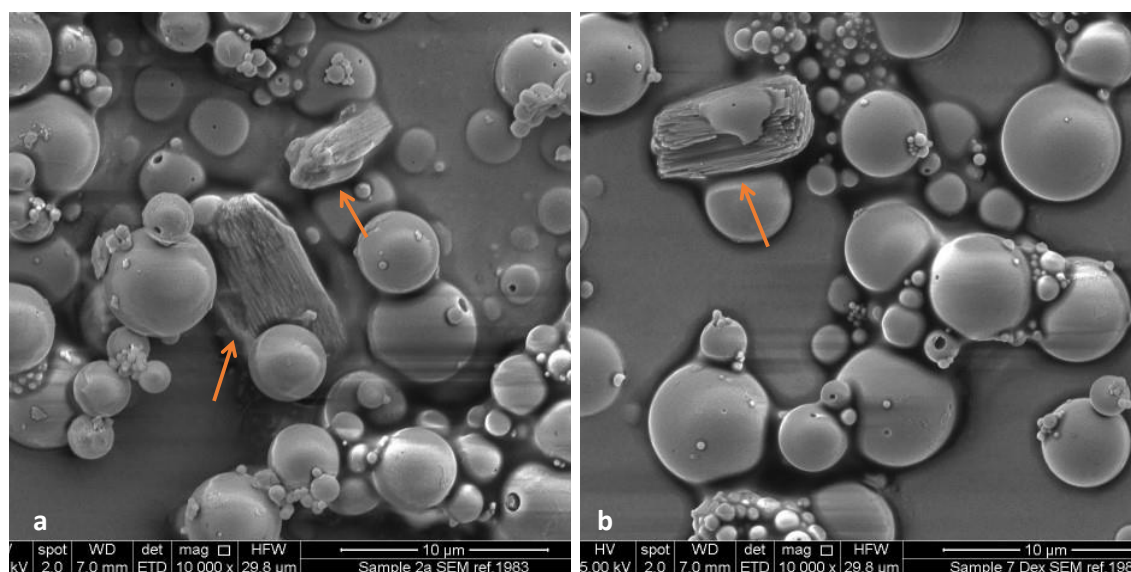


Figure 4-5 SEM images of Dex-loaded PLGA particles prepared with acetone and DCM mixture as an organic phase, (a) using low viscosity PLGA grade, (b) using high viscosity PLGA grade. The orange arrows point out the free Dex.

Meanwhile, Dex is highly soluble in both methanol and DMSO. Preparation of the organic phase with methanol/DCM and DMSO/DCM in a 9:1 ratio has rendered a clear solution of Dex and PLGA rather than dispersion. Figure 4-6 and Figure 4-7 show the particles prepared by the methanol/DCM mixture and DMSO/DCM mixture, respectively. The microparticles were all spherical in shape with pinholes appearing on the surface of some of the particles. A study reported the effect of the polymer concentration, temperature, and composition of the organic phase on the shape and surface morphology of PLGA microparticles [272]. Interfacial tension and polymer phase separation simultaneously affect the microparticle morphology. In addition, the polymer concentration and the emulsion temperature influence the rate of particle solidification by solvent extraction at which the holes might be created.

Free Dex was not observed in the samples but again, a wide range of particle size was observed in the high viscosity PLGA grade Figure 4-6, b and Figure 4-7, b.

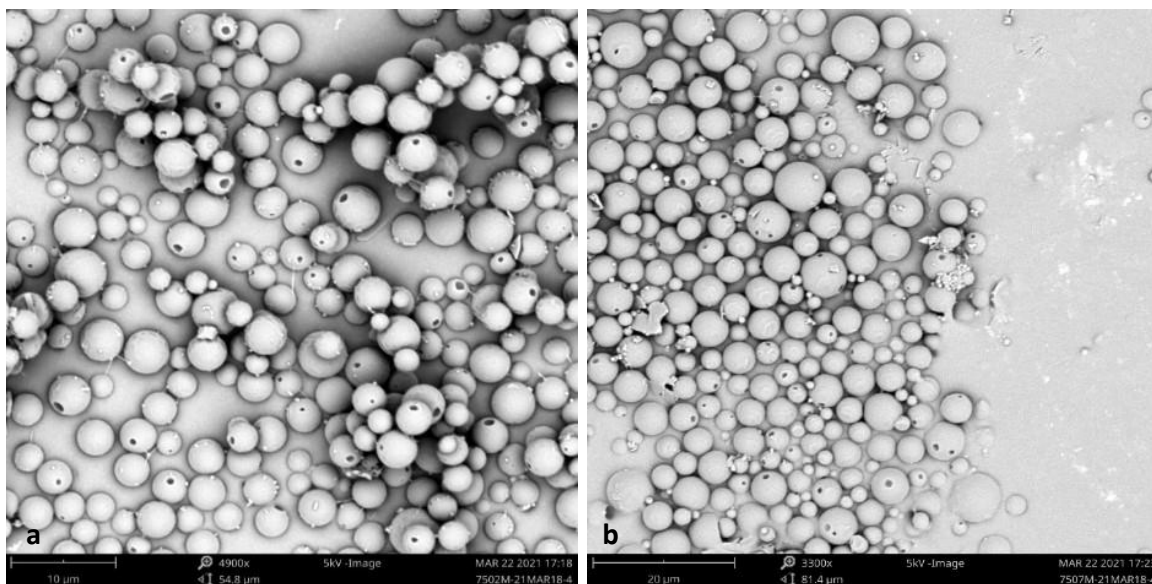


Figure 4-6 SEM images of Dex-loaded PLGA particles prepared with methanol and DCM mixture as an organic phase, (a) using low viscosity PLGA grade, (b) using high viscosity PLGA grade.

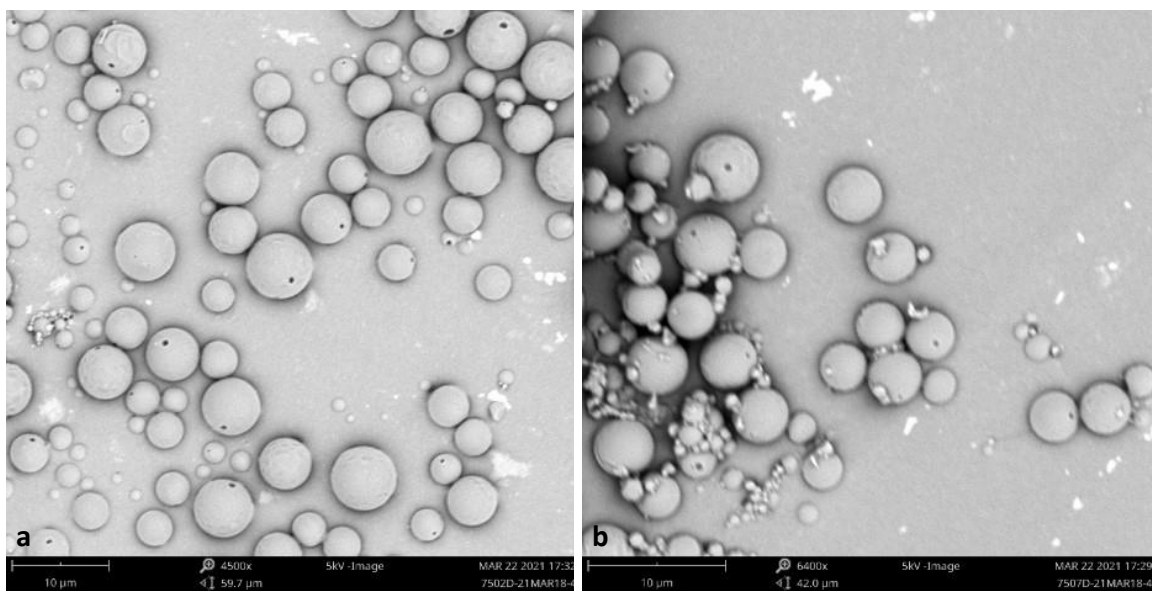


Figure 4-7 SEM images of Dex-loaded PLGA particles prepared with DMSO and DCM mixture as an organic phase, (a) low viscosity PLGA grade, (b) high viscosity PLGA grade.

Fluorescent-labelled PLGA microparticles were prepared using coumarin-6 as a fluorescent agent. The organic solvent was prepared by dissolving coumarin-6 in DCM. Figure 4-8 displays fluorescent labelled PLGA microparticles prepared by the two grades of PLGA. From the surface morphology obtained, the surface was smooth and spherical microparticles were prepared, the pinhole was also observed on the surface of the microparticles. The fluorescent microparticles were also images by fluorescent microscope as shown in Figure 4-9.

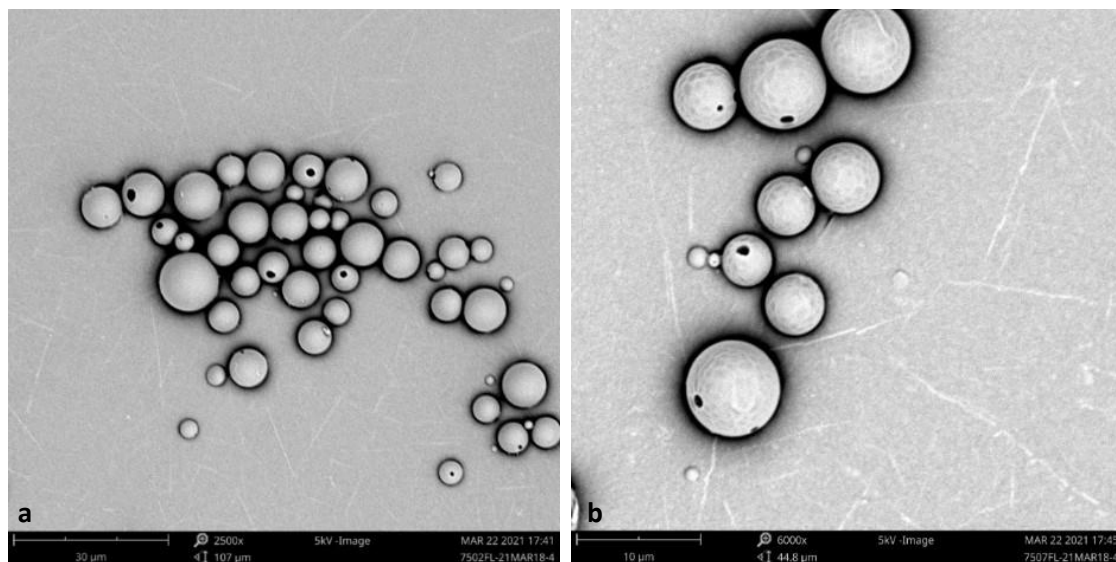


Figure 4-8 SEM images of Fluorescent labelled PLGA microparticles prepared (a) using low viscosity PLGA grade (MP-02-Flu), (b) using high viscosity PLGA grade (MP-07-Flu).

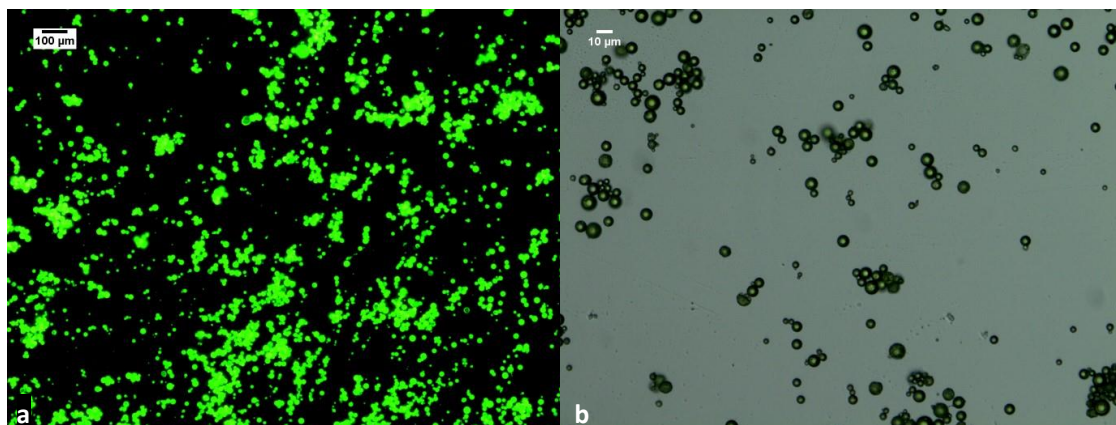


Figure 4-9 Images of fluorescent labelled PLGA microparticles prepared using low viscosity PLGA grade (MP-02-Flu), (a) fluorescence microscopy, (b) optical microscopy image.

4.4.1.2 Nanoparticles preparation

The preparation of PLGA nanoparticles was carried out using only the low-viscosity PLGA grade. A probe sonicator was used to generate cavitation and compression in the system to generate nanosized droplets that were stabilised by PVA solution. Disrupt droplets were generated by shear forces, inertial forces, or cavitation forces. Therefore, the choice of the mixing tool in the preparation of emulsion has a great influence on the particle size [151]. This method has successfully produced PLGA nanoparticles as shown in Figure 4-10. The nanoparticles were spherical, and the surface morphology showed no cracks or pinholes on the surface. Dex-loaded particles were prepared using DCM and methanol mixture in a 9:1 ratio.

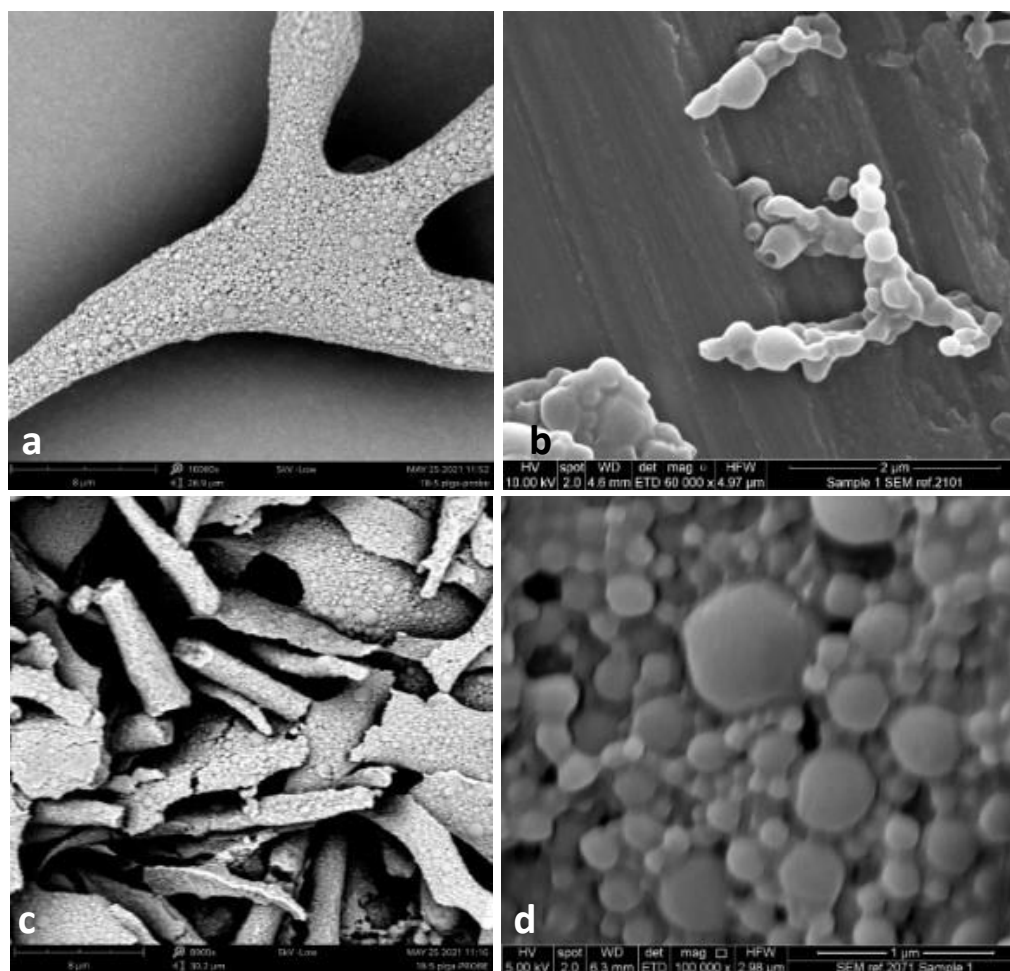


Figure 4-10 SEM images of PLGA nanoparticles (a), (b) Dex-loaded PLGA nanoparticles (NP-Dex) (c), (d) fluorescence labelled PLGA nanoparticles (NP-Flu).

4.4.2 Particle size and surface charge

The particle size and the distribution analysis of blank, Dex-loaded, and fluorescent labelled PLGA micro- and nano- particles were assessed by laser diffraction method. Particle size, PDI, Zeta potential and SEM images of Dex-loaded, blank, fluorescent labelled microparticles prepared low viscosity PLGA are presented in Table 4-3 and microparticles prepared with high viscosity PLGA are presented in Table 4-4. The particles formulated using the homogeniser have produced particles in the range $1860 \text{ nm} \pm 215$ to $3740 \text{ nm} \pm 100$ with generally high PDI values. Microparticles prepared with low viscosity PLGA produced slightly smaller microparticles ranging from $1860 \text{ nm} \pm 215$ to $2690 \text{ nm} \pm 596$, while high viscosity produced microparticles in the range of 2667 nm

± 111 to $3740 \text{ nm} \pm 100$, which is justified by the effect of the organic phase higher viscosity. The viscosity of the PLGA solution significantly impacts the droplet breakage and the emulsion droplet size [273]. Moreover, all the microparticles produced by the low and high viscosity grade PLGA had a negative Zeta potential value. The surface charge is strongly influenced by the stabiliser used in the fabrication process. PVA has a negative hydroxyl group (-OH) [274], and the PLGA chain has terminal carboxylic groups [275], which collectively contribute to the negative surface charge values.

Table 4-3 SEM images, particle size histograms, PDI, and Zeta potential data of microparticles prepared by low viscosity PLGA (PDLG 7502).

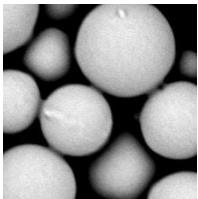
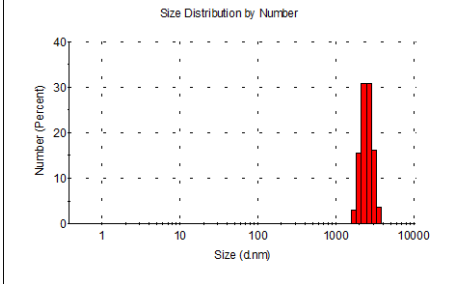
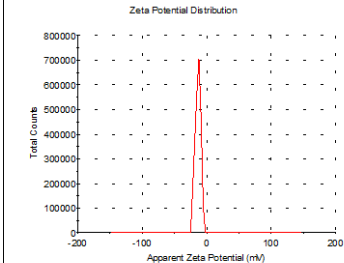
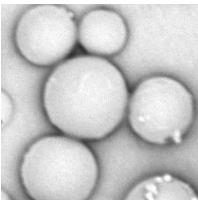
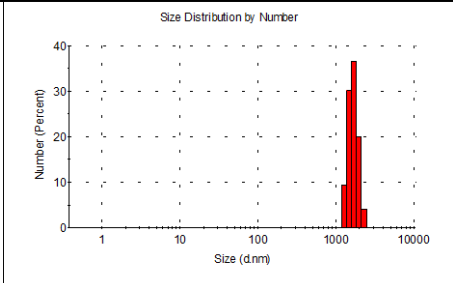
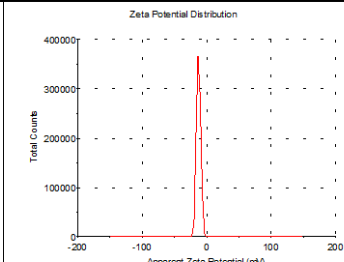
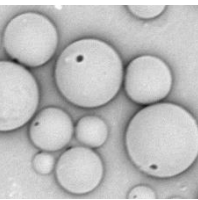
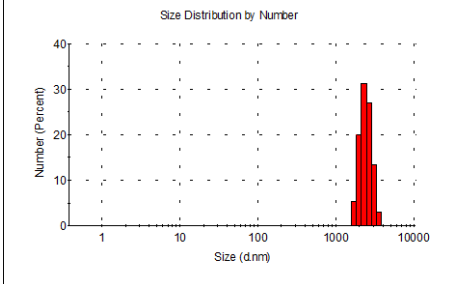
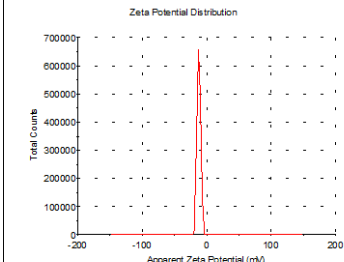
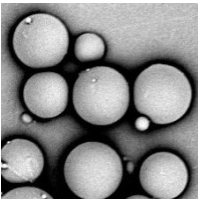
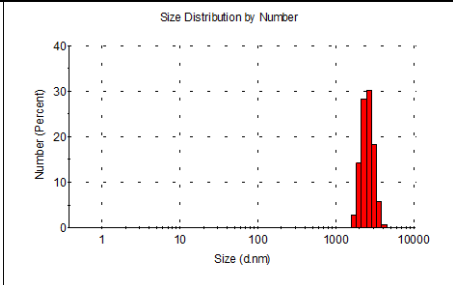
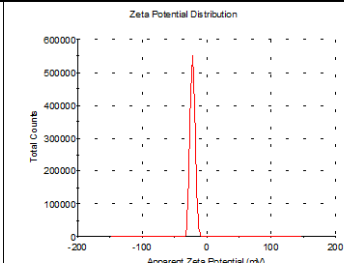
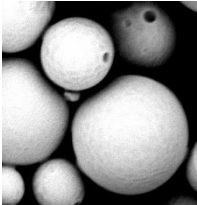
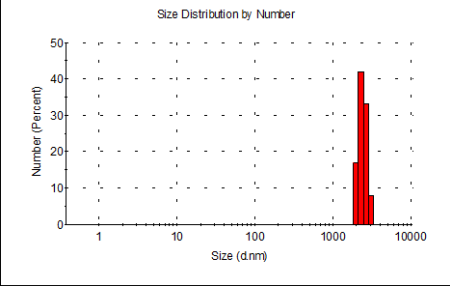
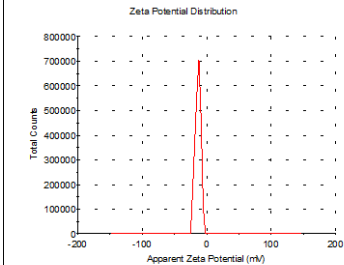
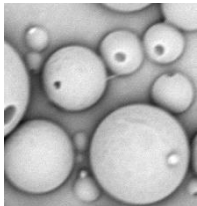
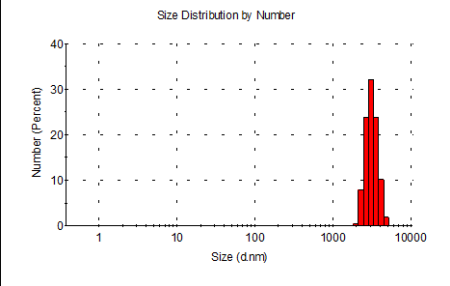
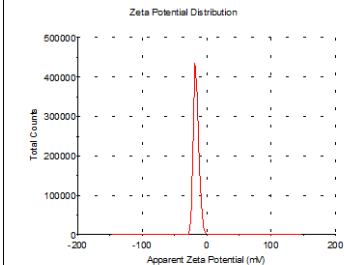
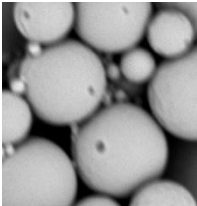
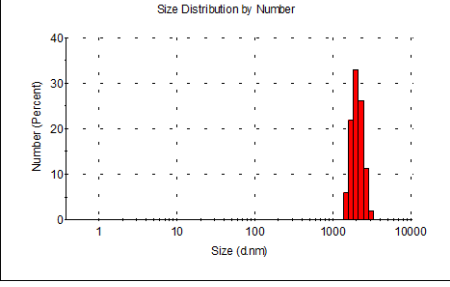
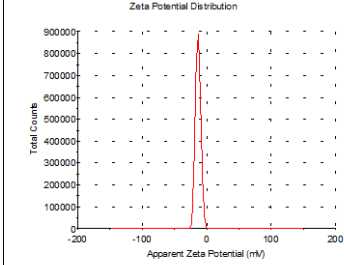
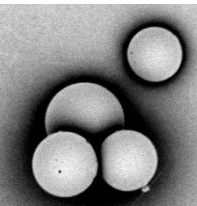
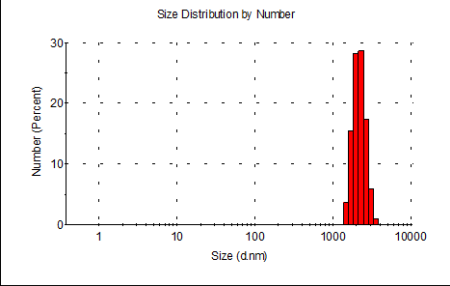
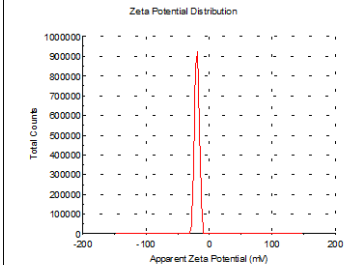
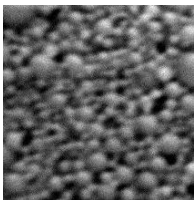
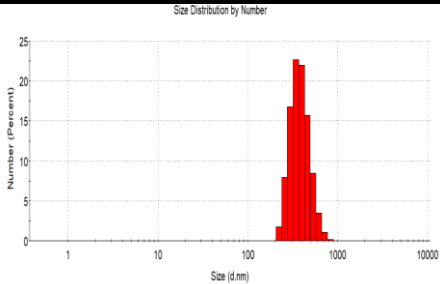
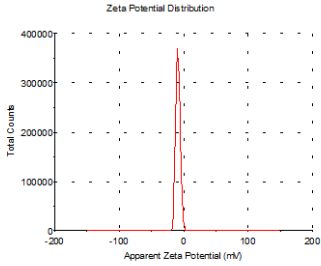
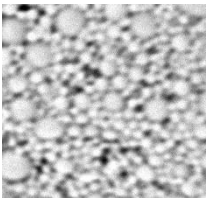
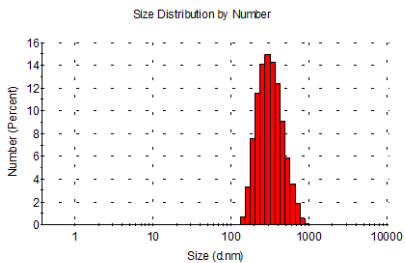
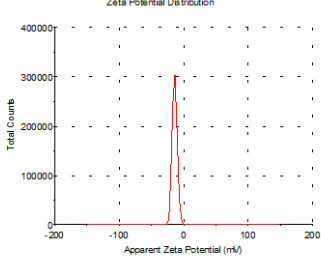
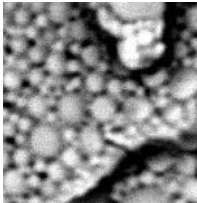
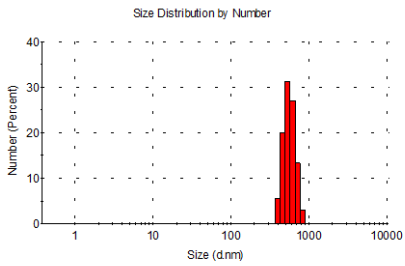
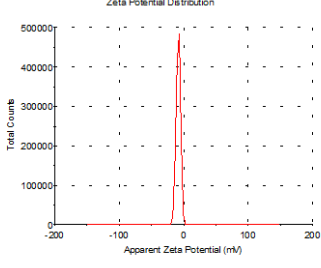
Formulation/ SEM image	Size distribution chart		Zeta potential (mV)
	Size (d.nm)	PDI	
MP-02 			
	2690 ±596	0.801 ±0.024	-13.8 ±4.70
Dex-02 Met 			
	1860 ±215	0.804 ±0.223	-11.3 ±2.39
Dex-02 DMSO 			
	2388 ±98	0.882 ±0.109	-11.4 ±1.14
Flu-02 			
	2647 ±169	0.589 ±0.039	-21.5 ±0.436

Table 4-4 SEM images, particle size, PDI, histograms, and Zeta potential data of microparticles prepared by high viscosity PLGA (PDLG 7507).

Formulation/ SEM image	Size distribution chart		Zeta potential (mV)
	Size (d.nm)	PDI	
MP-07 			
	2892 ±585	0.950 ±0.21	-14.1 ±0.85
MP-Dex-07 (Met) 			
	3740 ±100	0.913 ±0.04	-16.5.4 ±0.81
MP-Dex-07 (DMSO) 			
	2667 ±111	0.910 ±0.04	-13.2 ±1.41
MP-Flu-07 			
	2948 ±53	0.805 ±0.07	-19.4 ±0.21

From the data observed during the preparation of the microparticles on the effect of the viscosity on the microparticle size, low viscosity PLGA (PDLG 7502) produced smaller particles size and a relatively small PDI. Therefore, it was used to prepare the nanoparticles. A high-frequency probe sonicator was employed in the emulsion preparation. Particle size, PDI, Zeta potential and SEM images of Dex-loaded, blank and fluorescent-labelled nanoparticles prepared with low viscosity PLGA are presented in Table 4-5. Particle size ranged from $393 \text{ nm} \pm 2.23$ and $539 \text{ nm} \pm 11.43$ were produced. Lower PDI values were recorded with the nanoparticles compared to the microparticles. This could be due to the higher power of the ultrasonic wave generated by the sonicator through the dispersion that formed fine uniform droplets compared to the hand turbulence homogeniser, which comes in agreement with the literature. A study has demonstrated a correlation between homogenisation power and particle size [151, 276]. Similar to the surface charge observed with the microparticle, the nanoparticles exhibited a negative Zeta potential as the fabrication components were the same in both cases.

Table 4-5 SEM images, particle size histograms, PDI, and Zeta potential distribution of nanoparticles prepared by low viscosity PLGA (PDLG 7502).

Formulation/ SEM image	Size distribution chart		Zeta potential (mV)
	Size (d.nm)	PDI	
NP 			
	446 ±6.85	0.245 ±0.02	-8.77 ±0.73
NP-Dex 			
	393 ±2.23	0.195 ±0.02	-13.4 ±0.27
NP-Flu 			
	539 ±11.43	0.294 ±0.12	-8.15 ±0.09

4.4.3 % Yield

The percentage of production yield was quantified by weighing the lyophilised particles and comparing them to the input materials' weights.

Figure 4-11 shows the mean percentage yield of at least 6 batches \pm SD of blank and Dex-loaded micro- and nano- particles regardless of the solvent used in the fabrication. From the statistical analysis of the reported data, there was a significant difference ($p < 0.00001$) between the Dex-loaded particles and the blank micro and nano- particles. As expected, the Dex-loaded micro- and nano- particles were significantly lower than the blank counterpart as demonstrated by statistical analysis. The difference observed was due to the Dex loss caused by leaching of the solvent used to dissolve Dex (water-miscible solvent) to the aqueous phase during the emulsion preparation.

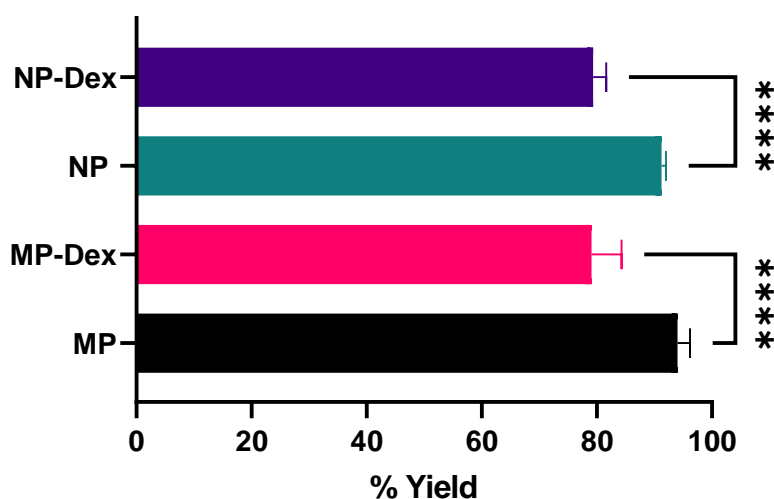


Figure 4-11 Percentage of the production yield of microparticles (MP), Nanoparticles (NP), and Dex-loaded micro- and nano- particles (MP-Dex, NP-Dex) (**** $p < 0.00001$).

4.4.4 Analytical quantification of dexamethasone

A reverse phase (RP)-HPLC method was developed and optimized to detect and quantify Dex dissolved in aqueous PBS (pH 7.4) for the release study and Dex dissolved in ACN organic solvent for particle content determination. The mobile phase composition was optimized using ACN and 0.1% TFA water. A gradient elution was used to adjust the retention time (RT) with an initial higher water ratio to allow the Dex molecules to attach to the RP nonpolar silica surface. Increasing the ratio of the organic solvent gradually allowed for a delay in the RT. TFA was added to the water phase as an organic modifier to improve the peak shape.

With chromatographic conditions mentioned in the method section in Table 4-2, system suitability for the content and the dissolution assays was determined by calculating the parameter presented in Table 4-6. From the table, it was observed that the RT in both assays was similar and the tailing factor (TF) was close to 1 for the Dex peak showing a high degree of symmetry, and the recorded theoretical plates were high (>2000) indicating good column efficiency.

Table 4-6 System suitability parameters for the Dex content and dissolution assays.

	RT (min)	Theoretical plates (N)	Tailing factor (TF)	Quantification precision (RSD%)
Assay: content	7.48 ±0.08	13407.37	0.920	0.190 %
Assay: dissolution	7.76 ±0.01	35943.92	1.030	0.264%

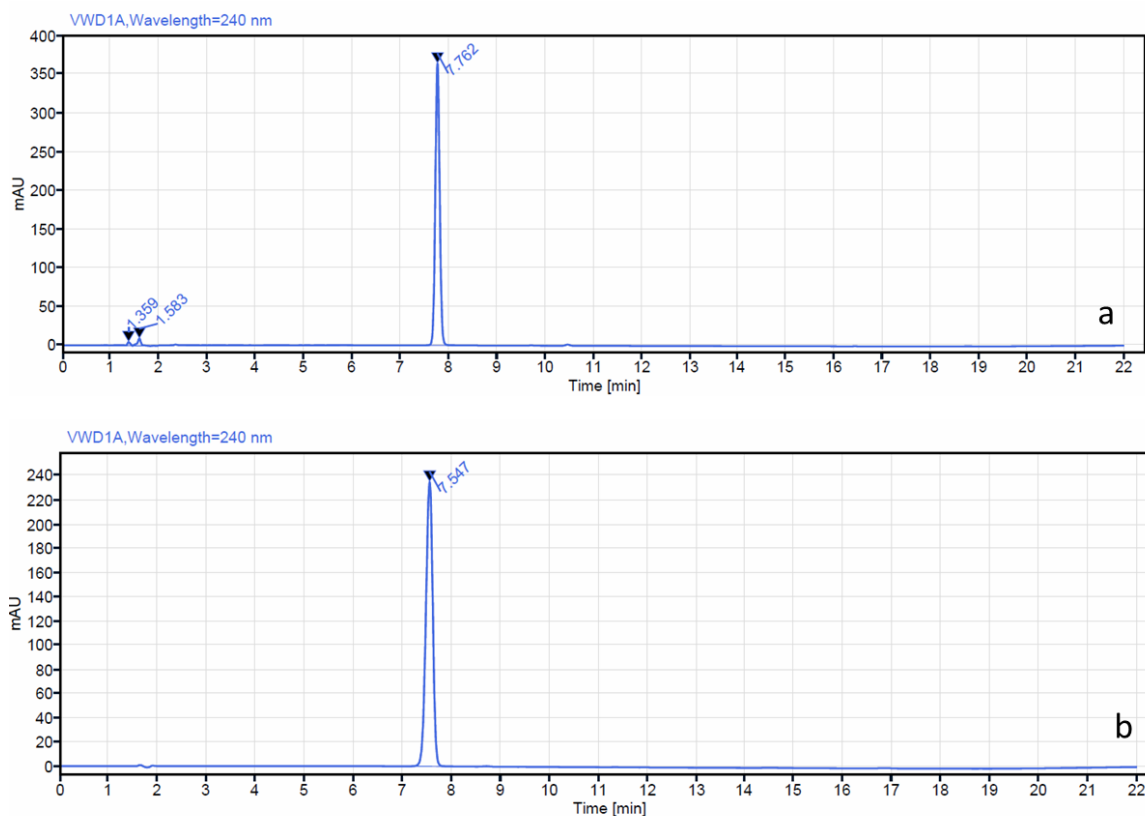


Figure 4-12 Chromatograms of standard Dex solution (100 µg/mL), (a) dissolution assay, (b) content assay.

The method developed was evaluated for specificity, linearity, accuracy, precision, and robustness. The detection wavelength was selected based on the maximum Dex absorbance reported by the supplier [277].

▪ Precision and accuracy

Table 4-7 displays the statistical analysis of data from the repeatability and precision study performed on standard samples in low (50 µg/mL), medium (100 µg/mL), and high (150 µg/mL) concentrations. By combining the intra- and inter-day data, all concentrations showed no significant difference ($p < 0.05$). Moreover, the RSD% values were all less than 2% intraday and 5% interday, which is within the typical acceptance limit by USP43-NF-38 [278]. Further, the accuracy was assessed over the three samples

level. The values of the mean % recovery was found in the range of 99.644 -101.800% indicating the accuracy of the Dex quantification by the method (Table 4-7).

Table 4-7 precision and accuracy analysis of Dex samples performed intra- and inter-day. (n=3)

Repeatability and Precision	Intraday	Interday
Low concentration		
Mean peak area	1164.32	1139.702
STD	2.305	51.012
RSD%	0.197	4.475
Mean % recovery	101.800	99.644
Medium concentration		
Mean peak area	2288.151	2278.355
STD	2.985	70.252
RSD%	0.933	3.083
Mean % recovery	100.113	99.684
High concentration		
Mean peak area	3475.143	3416.335
STD	20.465	157.115
RSD%	0.588	4.598
Mean % recovery	101.395	99.678

▪ Limit of detection and limit of quantification

LOQ was calculated by Equation 4-5 using data obtained from the linearity study, which will be presented in 4.4.4.1. LOQ was 4.172 µg/mL, whereas LOD calculated by the signal-to-noise approach is presented in Table 4-8. Concentration of 0.5 µg/mL produced a peak height 3 times the height of noise detected in the blank chromatogram and 1 µg/mL produced a peak almost 10 times the height of the noise (9.004). Thus, a

concentration of 0.5 µg/mL was considered the lowest concentration for valid detection and 1 µg/mL was the quantitation limit in this study.

Table 4-8 The limit of detection determined by the signal-to-noise approach.

LOD ($S=H/h$)		
Noise (h)	0.258	
	Height (H)	S
0.5 µg/mL	0.866	3.356
1 µg/mL	2.323	9.004
2.5 µg/mL	6.987	27.081

- Specificity

A method's specificity refers to its capacity to distinguish between the target analyte(s) and other elements present in the sample. A chromatogram of the spiked sample with 50 µg/mL Dex with the particle's components (PLGA and PVA) is presented in Figure 4-13. It was confirmed that there were no interferences with any soluble component of the particles or the dissolution medium in the quantification of Dex released from particles by the Student's t-test, which showed no significant difference between the area of the Dex peak of the standard and the spiked samples (Table 4-9).

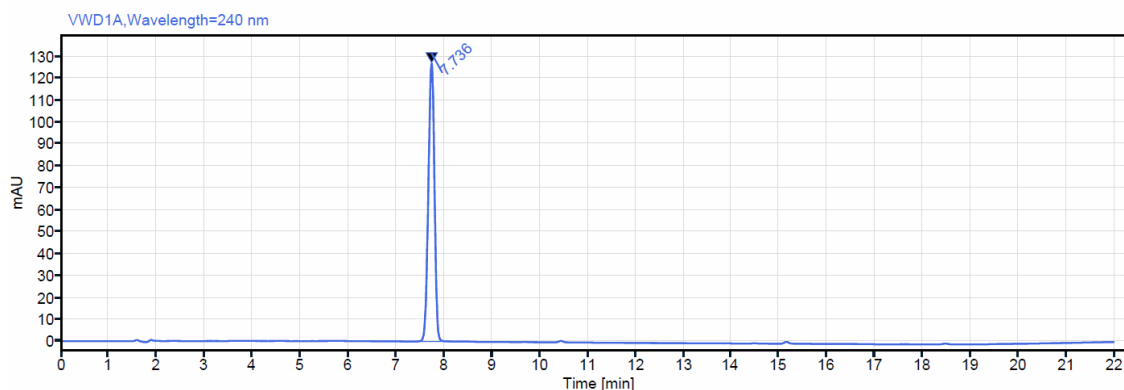


Figure 4-13 Chromatograms acquired in the specificity study of a spiked sample (50 $\mu\text{g/mL}$).

Table 4-9 Statistical calculation of the specificity by a Student's t-test, of the areas of the peaks of standard and spiked samples (50 $\mu\text{g/mL}$) (n=3).

	Peak area	$\pm\text{SD}$	Mean recovery %
Standard solution sample mean area	1164.32	± 2.305	102.187%
Spiked sample mean area	1122.159	± 2.648	99.524%
Student's t-test (p)*	t=18.32, (0.8252)		

*Statistical significant level ($p < 0.05$).

▪ Robustness

To evaluate the method's performance, small intentional changes were made to the method's conditions to measure the method's robustness. This validation parameter's goal was to determine which method criteria if any, were most important for the method to function properly. Table 4-10 shows the mean RT and the mean peak area of analysing 100 $\mu\text{g/mL}$ by variation in the method of the parameter. Typically, the acceptance criterion of the variation is not more than 10 times the %RSD for the system suitability [207]. From Table 4-6, the %RSD value for the system suitability for the content assay is 0.190 %. The %RSD values when the temperature, flow rate and pH

change were all within the acceptance range. The RT %RSD values were less than 5% which was considered acceptable [207].

Table 4-10 Robustness of the HPLC method analysing 100 µg/mL by changing the temperature, flow rate, and pH.

Variables	Mean RT	±SD	% RSD	Mean area	±SD	% RSD	TF
Temperature							
20°C	7.468	0.017	0.227	2287.784	2.184	0.095	0.914
30°C	7.356	0.011	0.154	2287.758	7.111	0.311	0.929
Flow rate							
0.9 mL	7.788	0.164	2.106	2304.326	1.389	0.060	0.907
1.1 mL	7.649	0.179	2.339	2304.697	1.179	0.051	0.928
pH							
2.00	7.758	0.206	2.661	2304.043	0.297	0.013	0.921
2.20	7.564	0.067	0.888	2304.793	0.474	0.021	0.925

4.4.4.1 Standard calibration curve

In order to assess the linearity of the HPLC method and to analyse the concentration of unknown samples, a standard calibration curve was constructed by plotting the concentration against the respective peak area. Serial dilutions ranging from 5 to 150 µg/mL in ACN were analysed. Three separate sets of calibration were prepared. The regression equation and correlation coefficient (R^2) for each set are presented in Table 4-11 and Figure 4-14. The average of the three sets resulted in a regression equation of $y=22.706x + 10.408$ and $R^2=1$ (Figure 4-15).

Table 4-11 HPLC mean peak area of Dex concentrations ($\mu\text{g/mL}$) of three sets (n=3).

Conc. ($\mu\text{g/mL}$)	Overall		1		2		3	
	Mean	SD	Mean	SD	Mean	SD	Mean	SD
5	120.42	2.06	122.68	0.64	118.66	0.34	119.91	0.07
10	236.44	27.35	236.29	1.12	209.16	0.27	263.86	0.36
25	560.37	16.51	575.96	2.72	562.07	0.39	543.08	0.77
50	1143.64	20.52	1163.05	3.46	1122.16	2.64	1145.71	2.81
75	1711.01	17.65	1714.26	3.44	1691.95	0.67	1726.80	0.31
100	2293.23	10.47	2293.07	12.17	2303.79	3.55	2282.84	2.61
150	3425.55	50.18	3470.369	16.71	3371.33	0.64	3434.96	0.30
Equation	$y=22.70x + 10.40$		$y=23.03x + 2.56$		$y=22.64x - 2.58$		$y=23.37x - 11.73$	
R ²	1		0.9999		0.9997		0.9993	

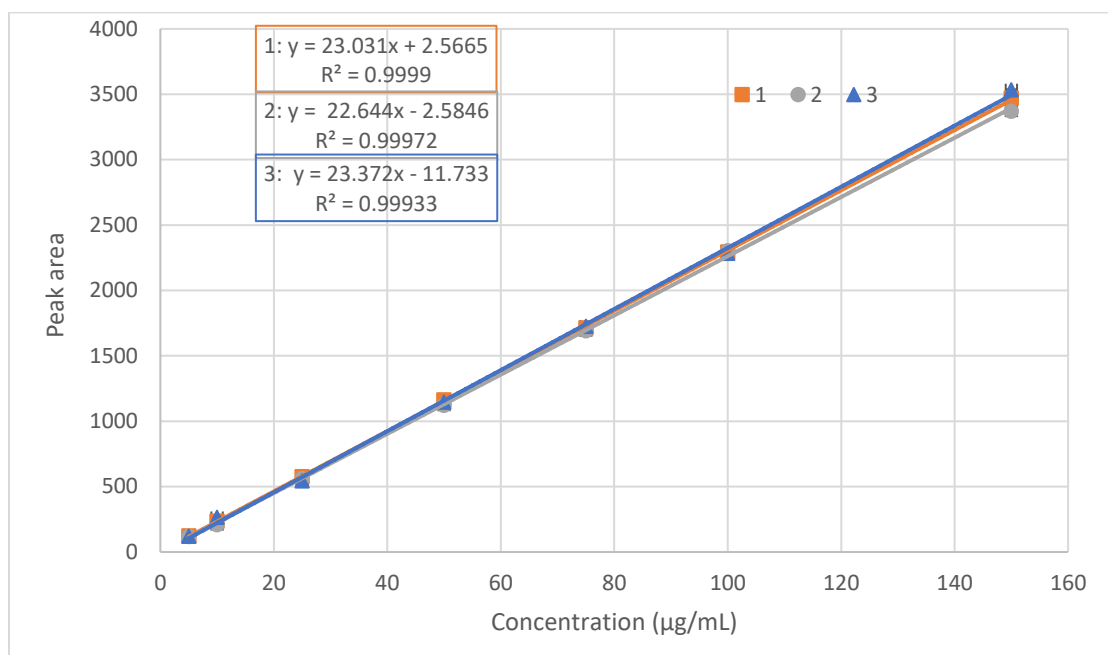


Figure 4-14 Standard calibration curves for Dex on three days (1, 2, and 3) the regression line equation and the correlation coefficient are shown on the top of the curve (mean \pm SD, $n=3$).

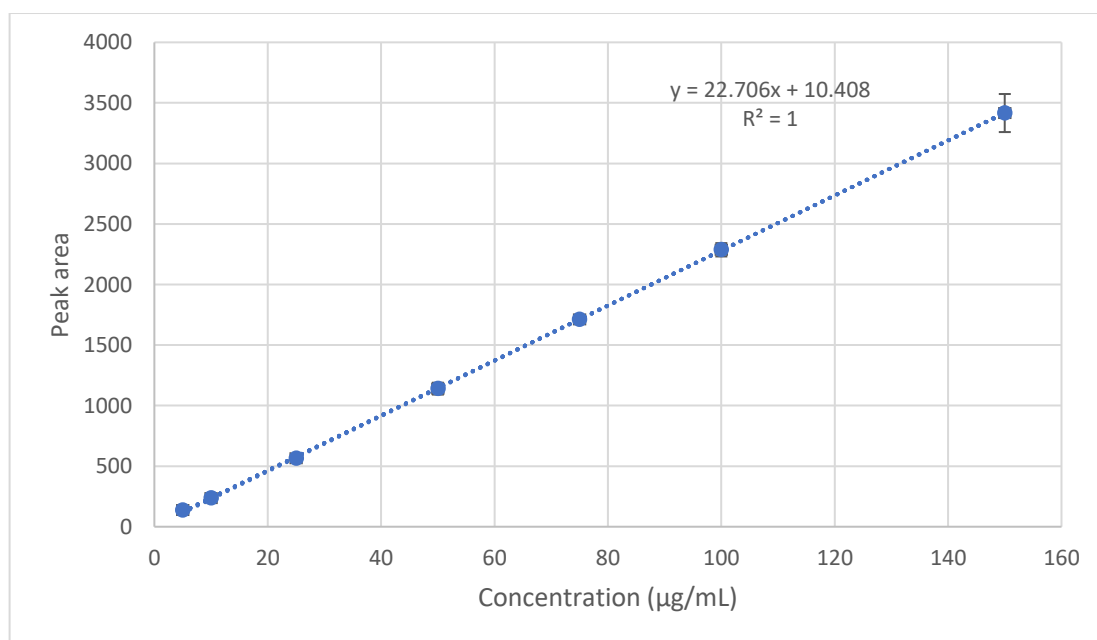


Figure 4-15 Standard calibration curve of Dex in ACN, the regression line equation and the correlation coefficient are shown on the top of the curve (overall mean \pm SD, $n=3$).

This HPLC method was developed in order to measure the amount of Dex in a given sample. The DL%, and EE% in the formulated PLGA particles along with the solubility and release of Dex in PBS were assessed by the developed method.

4.4.5 Encapsulation efficiency and drug loading capacity

Loading drugs in a PLGA particle carrier can offer several advantages over conventional drug delivery systems in terms of biocompatibility, controlled release capability, and targeted delivery [114]. Loading the drug in the microparticles was achieved by using an organic solvent mixture to increase the solubility of Dex in the oil phase. In order to assess the efficiency of the solvent mixture in encapsulating the drug in the PLGA matrix, the DL% and EE% were calculated. Dex DL% and EE% in PLGA microparticles prepared by low and high-viscosity PLGA grades are presented in Figure 4-16 and Figure 4-17, respectively. From the figures, the DL% and EE% were higher when the acetone/DCM mixture was used. However, in section 4.3.1.1, the microparticle preparation and specifically in Figure 4-5, it was observed that free Dex was present in the sample, which implies that the reported values of EE% and DL% were overestimating the amount of encapsulated Dex as they combined the amount of Dex in the particles as well as the amount of free Dex precipitated in the sample.

Moreover, the methanol/DCM mixture produced a significantly higher DL% and EE% compared to the DMSO/DCM mixture ($p < 0.05$). This could be explained by the fact that emulsion is formed with two immiscible liquids. Liquid-liquid miscibility is mainly dependent on the intermolecular forces of attraction. Thus, liquids of similar polarity are more miscible with each other. Here, methanol and DMSO are both miscible with water and DCM. However, DMSO has a higher polarity index ($P' 7.2$) than methanol ($P' 5.1$) which may increase the tendency of DMSO leaching from the organic phase (DCM, $P' 3.1$) to the aqueous phase ($P' 10.2$) resulting in lower DL% and EE% in the case of DMSO/DCM mixture. Also, the high amount of Dex added in the fabrication process and the slight solubility of Dex in water may also contribute to the low encapsulation efficiency in all the mixtures [279, 280].

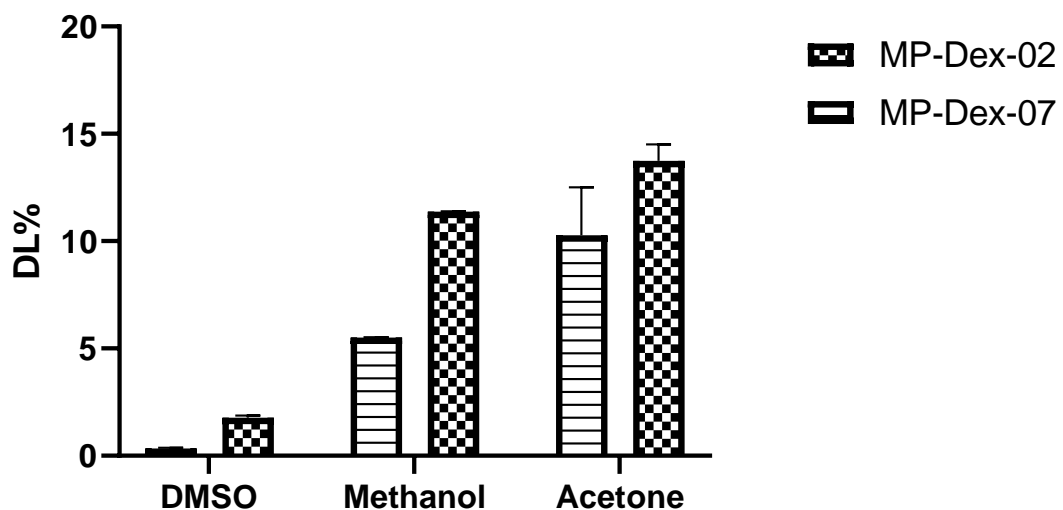


Figure 4-16 DL% of Dex in PLGA microparticles prepared by low (MP-Dex-02) and high viscosity (MP-Dex-07) PLGA grades using different organic mixtures.

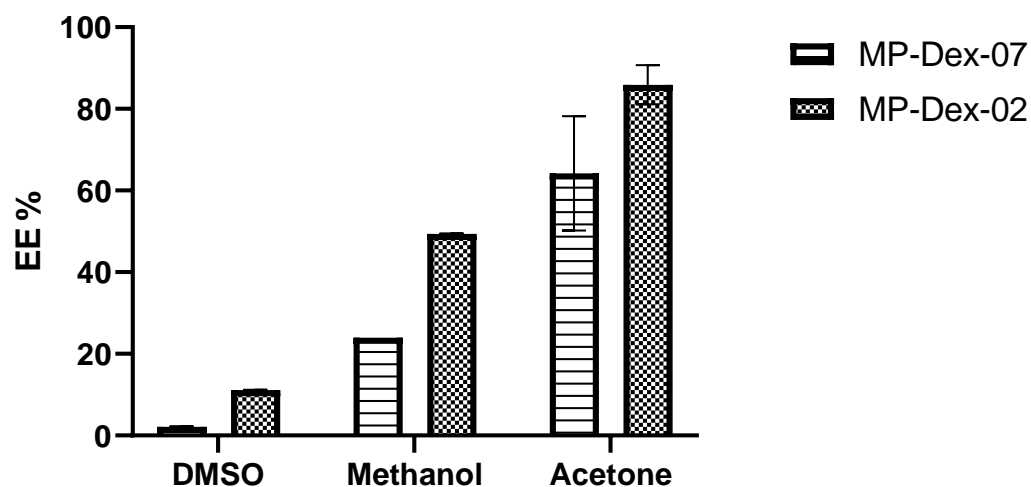


Figure 4-17 EE% of Dex in PLGA microparticles prepared by low (MP-Dex-02) and high viscosity (MP-Dex-07) PLGA grades using different organic mixtures.

Microparticles prepared with DCM/methanol displayed reasonable DL% and EE% and microparticle characteristics. Thus, these particles were further used for drug release assessment and referred to as MP-Dex-02 and MP-Dex-07 for low-viscosity and high-viscosity PLGA grades, respectively.

In the assessment of the Dex-loaded nanoparticles (NP-Dex), the DL% and EE% were $10.153\% \pm 1.518$ and $46.536\% \pm 3.216$, respectively. Figure 4-18 shows a comparison between the microparticles (MP-Dex-02) and the nanoparticles prepared by the same solvent (DCM/methanol). From the figure, it was clear that the Dex DL% and EE% were similar in both the micro- and the nano-sized particles, with no statistically significant differences recorded ($p < 0.05$) between the two sizes.

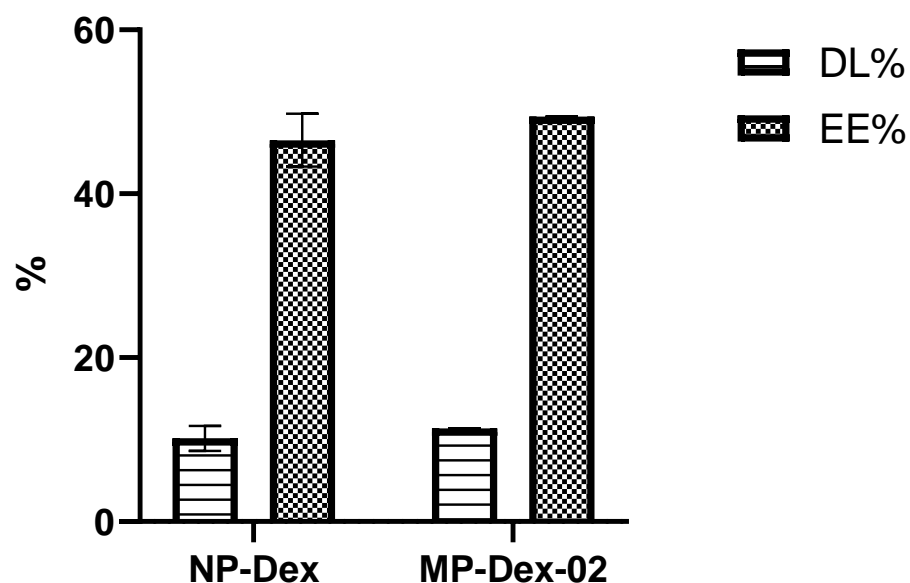


Figure 4-18 Comparisons of the DL% and EE% in Dex-loaded nanoparticles (NP-Dex) and Dex-loaded microparticles (MP- Dex-02) prepared by DCM/methanol organic solvent.

4.4.6 Solubility Study

The saturated solubility of Dex was assessed in deionised water and PBS (pH 7.4) at $37 \pm 0.5^\circ\text{C}$ for 48 h. The solubility was found to be $86.06 \mu\text{g/mL} \pm 1.52 \mu\text{g/mL}$ in deionised water and $88.16 \mu\text{g/mL} \pm 0.25$ in PBS. The solubility of Dex was found in agreement with the reported Dex solubility in Drugbank online [281]. The solubility data were used to estimate the volume of media required to perform the dissolution study in sink conditions.

4.4.7 *In-vitro* release study

In-vitro drug release was performed in PBS (pH 7.4) for both grades of PLGA micropartocels, low viscosity (MP-Dex-02) and high viscosity (MP-Dex-07) for 21 days. As shown in Figure 4-19, the *in-vitro* Dex release profiles of both particles types were observed to be similar, with slightly higher release in MP-Dex-07. An initial burst release effect was observed at 30 min with $36.73\% \pm 10.28$ and $20.72\% \pm 8.57$ for MP-Dex-07 and MP-Dex-02, respectively, followed by an increase to $62.21\% \pm 8.52$ and $51.28\% \pm 12.67$ on the fourth hour of the release study. This rapid initial Dex release indicates the drug was absorbed onto the surface of the particles. Typically in PLGA particle-based systems, a triphasic drug release profile was often observed [282]. From the figure, it was observed that the release from both microparticles followed a three-phase pattern. After the initial fast release over the first 24 h, a controlled release pattern was seen over the next 3 days, which can be attributed to subsurface drug diffusion. Followed by a slow release of Dex from the slowly eroding PLGA matrix. At the end of the release study, on day 21, the percentage released was $98.60\% \pm 0.62$ and $94.23\% \pm 1.56$ for MP-Dex-07 and MP-Dex-02, respectively. A similar pattern was previously reported for Dex release from PLGA microparticles prepared by the same method (o/w emulsion solvent evaporation) using a blend of PLGA grades [259, 267].

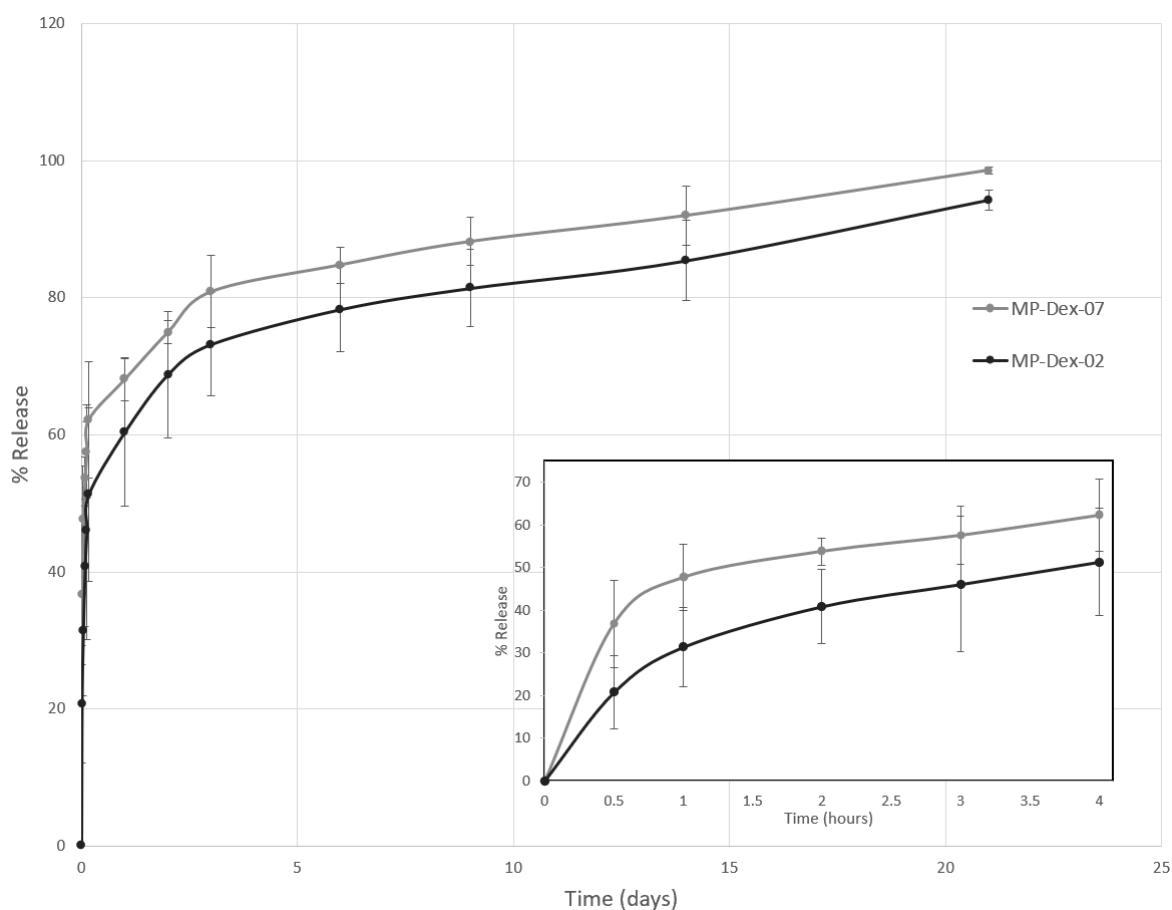


Figure 4-19 *In-vitro* Dex release profiles from microparticles prepared by low viscosity (MP-Dex-02) and high viscosity (MP-Dex-07) PLGA grades.

Based on the previous findings, low viscosity PLGA (PDLG 7502) offered superior microparticle quality, better PDI, and a slightly slower Dex release. Thus, particles prepared by the low viscosity grade (MP-02, MP-Dex-02, and MP-Flu-02) will be investigated and used in the rest of the experimental study.

Moreover, the release of Dex from the nanoparticles showed a similar pattern to the Dex release profile from the microparticles. Initially started with a burst release of $22.28\% \pm 4.80$ at 30 min compared to $20.72\% \pm 8.57$ in the microparticles (Figure 4-20). As mentioned before, the initial fast release could be due to the diffusion of the drug from the particles' surface. Therefore, the high surface area of the nanoparticles was associated with $47.61\% \pm 7.02$ release over the first 4 h. In the last phase of the release profile, a slower rate of Dex release compared to the microparticles was observed

despite the higher surface area of the nanoparticles. In the literature, it was reported that PLGA particles produced by o/w emulsion method using PVA solution as a stabiliser are coated with a PVA layer on the surface and as the particle size decreases the amount of PVA on the surface increases, leading to the formation of a thick gel-like layer around the particles, acting as a release barrier [263, 283]. This could explain the slower release observed with the nanoparticles.

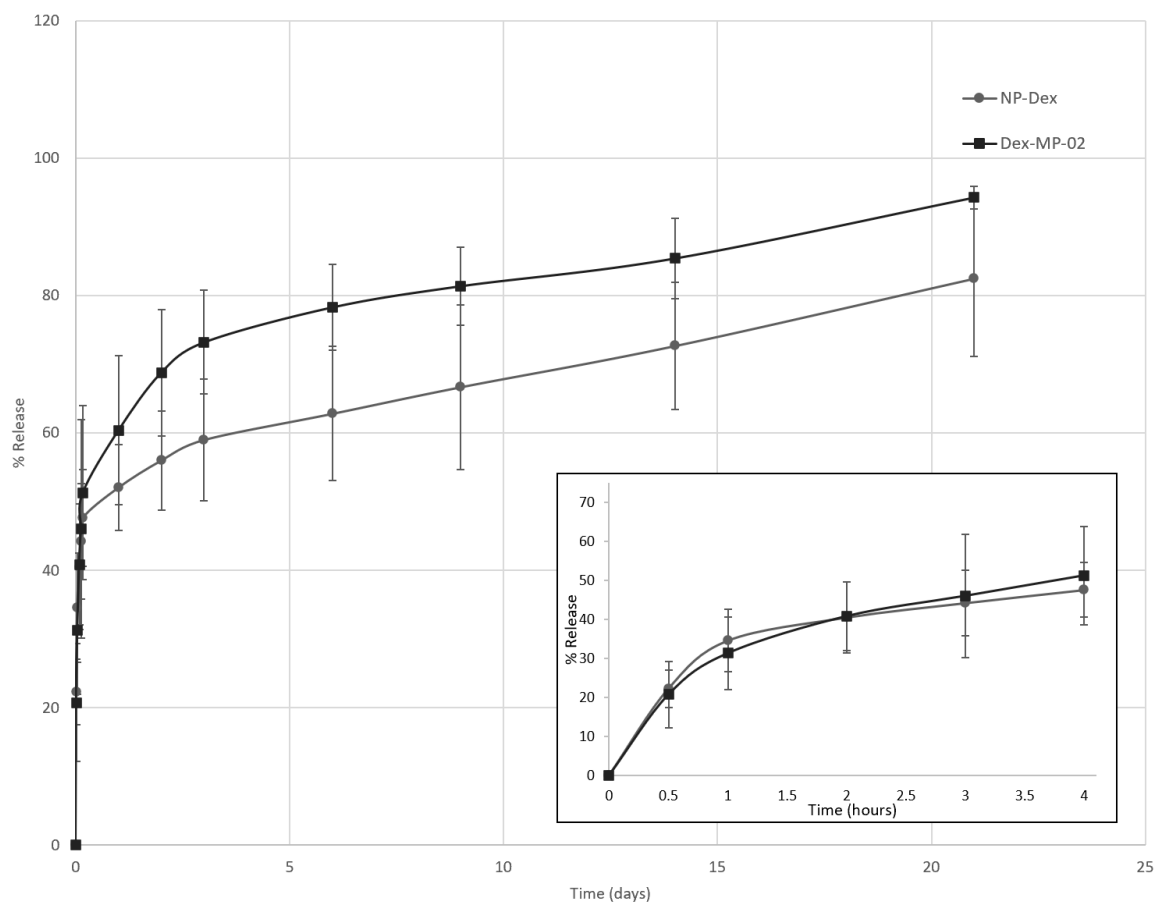


Figure 4-20 *In-vitro* Dex release profiles from nanoparticles (NP-Dex) and microparticles prepared by low viscosity PLGA (MP- Dex-02).

The obtained release profiles of Dex from the micro- and nano- particles were effective for the proposed MN drug delivery model, and controlled release of the drug for over 3 weeks was confirmed.

4.4.8 Differential scanning calorimetry

Dex, free PLGA polymer, physical mixture of the drug and the polymer, and fabricated Dex-loaded and blank microparticles were assessed by DSC. The data are presented in Figure 4-21. The DSC thermogram of Dex displayed a characteristic sharp endothermic transition of melting point (T_m) at 263.5 °C, which confirms the crystalline state of Dex. This comes in agreement with the reported Dex T_m in the literature [136]. The free PLGA powder (as received) recorded a glass transition (T_g) of approximately 53.5 °C, which lies within the range of PLGA T_g reported values [261].

Similarly, the physical mixture thermogram exhibited two endothermic transitions at 55.5 °C and 254.5 °C corresponding to the PLGA T_g and the Dex T_m . The T_g of the PLGA polymer was virtually present in both thermograms of the blank microparticles and Dex-loaded microparticles demonstrating similar endothermic events with a single defined peak at 56.5 °C, which indicates that there was no plasticization effect by Dex loading on the microparticles.

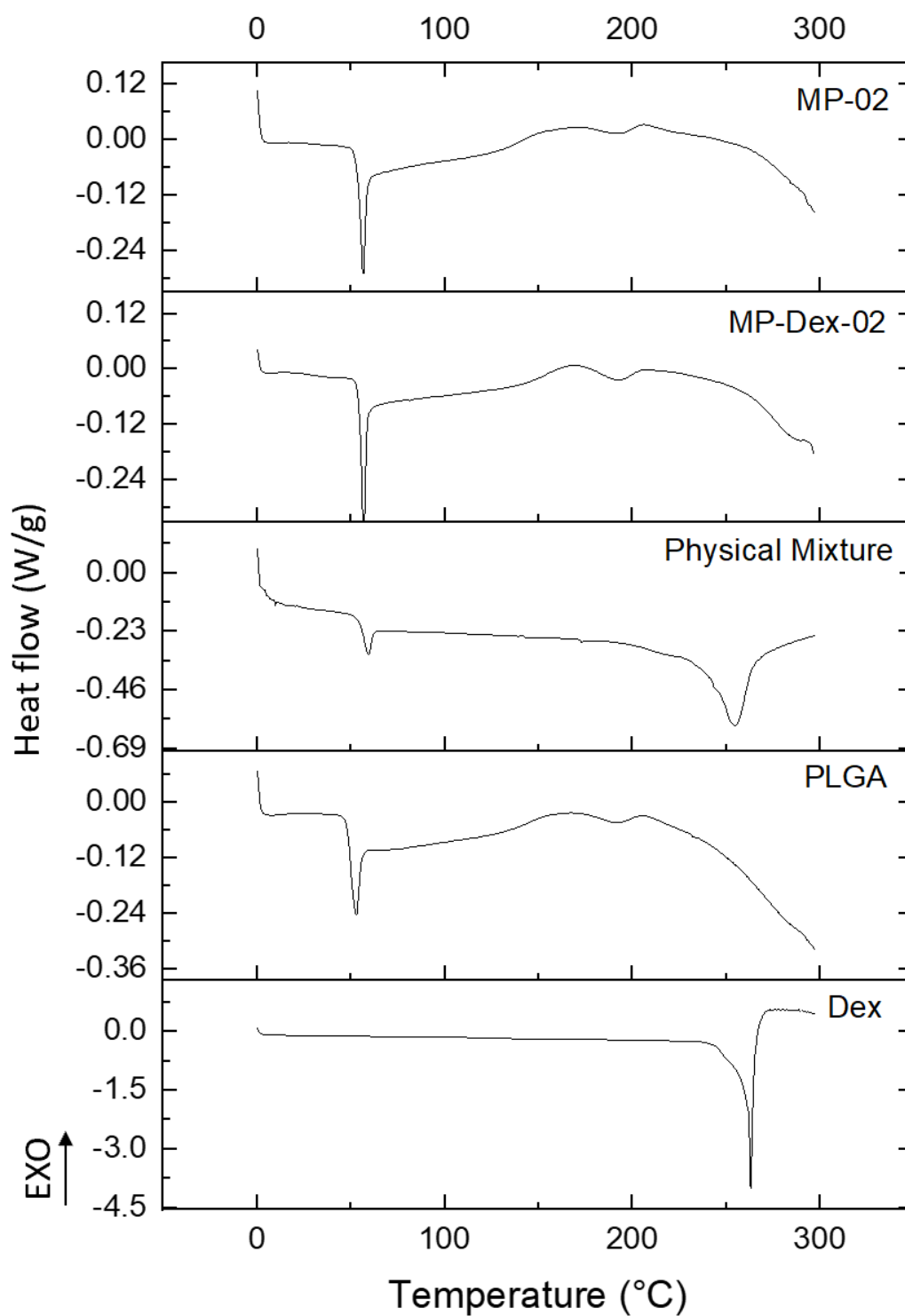


Figure 4-21 DSC thermograms of pure Dex, PLGA (PLDG 7502), physical mixture, MP-Dex-02, and MP-02.

4.4.9 X-ray powder diffraction

In this study, XRD was performed to evaluate the physical state of the encapsulated drug, the polymer, and the PLGA microparticles. Diffractograms of the free Dex, PLGA polymer powder (as received), physical mixture of the drug and the polymer, the blank microparticles (MP-02), and the Dex-loaded microparticles (MP-Dex-02) are presented in Figure 4-22.

The XRD diffractogram of Dex showed characteristic diffraction 2θ peaks values at 13.59° , 16.15° , and 17.75° confirming the crystalline status of Dex, whereas that of PLGA showed no peaks indicating the amorphous state of the polymer. Comparably, the physical mixture showed peaks at the same 2θ values but with lower intensity revealing the presence of Dex crystals in the mixture diluted with the PLGA polymer. However, the Dex diffraction peaks were absent in the MP-Dex-02, which might be attributed to Dex molecular dispersion within the polymeric matrix. Broad halos similar to the PLGA polymer diffractogram were exhibited with MP-02. Comparable patterns have been reported in the literature with Dex-loaded PLGA microspheres [261].

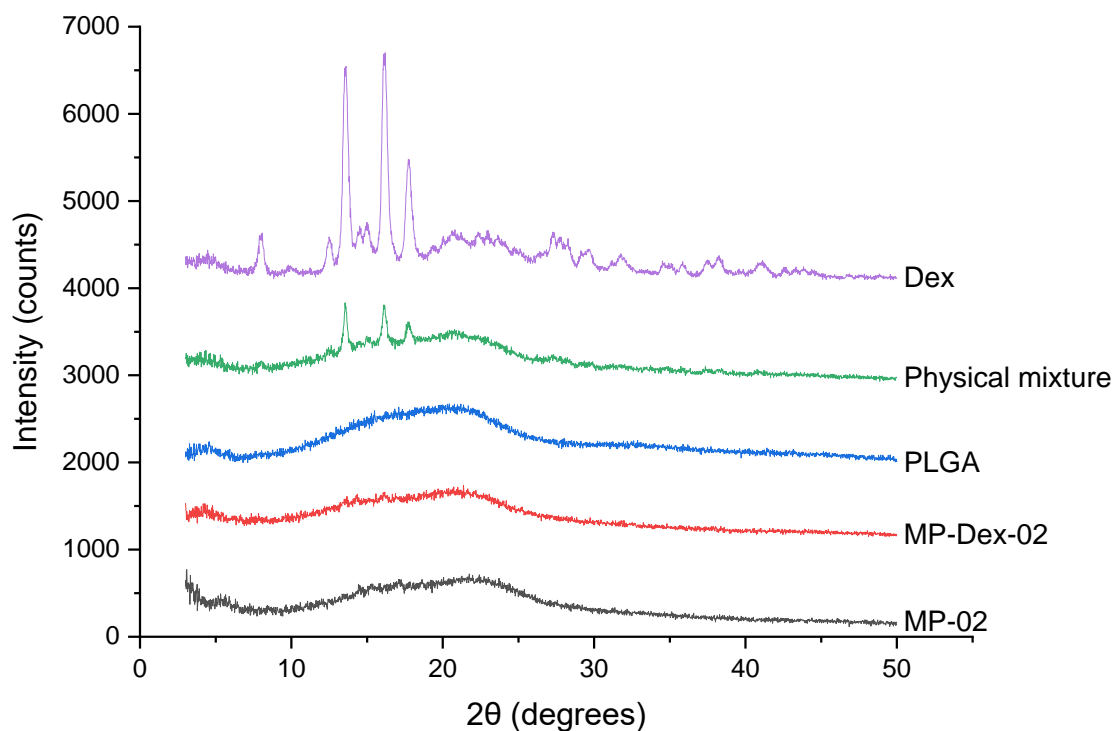


Figure 4-22 XRD diffractograms of Dex, PLGA, physical mixture, MP-Dex-02, and MP-Dex-02.

4.4.10 Fourier transforms infrared spectroscopy

FTIR was conducted to study the potential interaction between the drug and the polymer. The FTIR spectra of pure Dex, PLGA powder, the physical mixture of the drug and the polymer, blank (MP-02) and the Dex-loaded microparticles (MP-Dex-02) are presented in Figure 4-23.

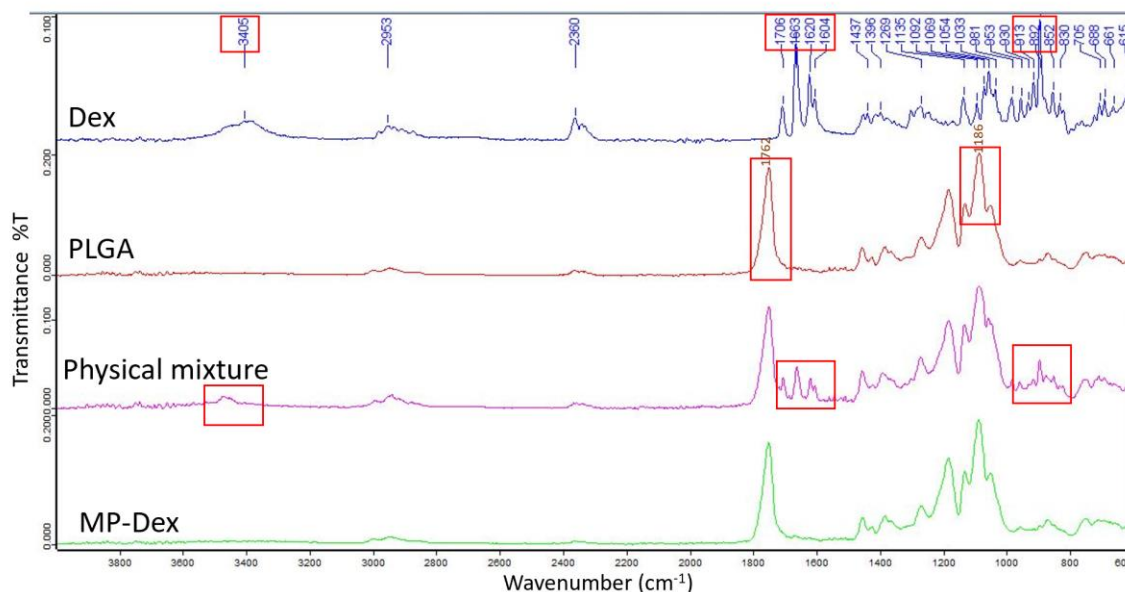


Figure 4-23 FTIR spectra of free Dex, PLGA (PLGD 7502) powder, physical mixture, MP-Dex-02.

From the Dex spectrogram, the peak at 3405 cm^{-1} is for -NH stretching vibration. Functional group peaks at 1706 , 1663 , 1620 , and 1604 cm^{-1} attributed to carboxyl -C=O stretching vibration linked to C3-cyclic and C20 carbonyl groups on Dex. While C-F group axial deformation showed peaks at 981 and 892 cm^{-1} [284]. PLGA spectrogram showed a distinctive peak at 1762 cm^{-1} for carboxyl -C=O stretching and a peak at 1186 for C-O stretching [285]. Dex characteristics peaks were observed in the physical mixture spectrogram however not in the MP-Dex-02, suggesting an involvement of these functional groups in the polymeric matrix and only PLGA peaks were observed with no additional peaks appeared.

4.4.11 Cell viability assay

ARPE-19 is a commonly used cell line for *in-vitro* evaluation of the biocompatibility of an ophthalmic preparation by measuring the cytotoxicity and the cellular uptake to propose future use [286]. ARPE-19 cell line was successfully cultured following the American Type Culture Collection (ATCC) protocol [136]. ARPE-19 has an adherent growth property. Image of the cells adhered to the bottom of the culture flask is shown in Figure 4-24.

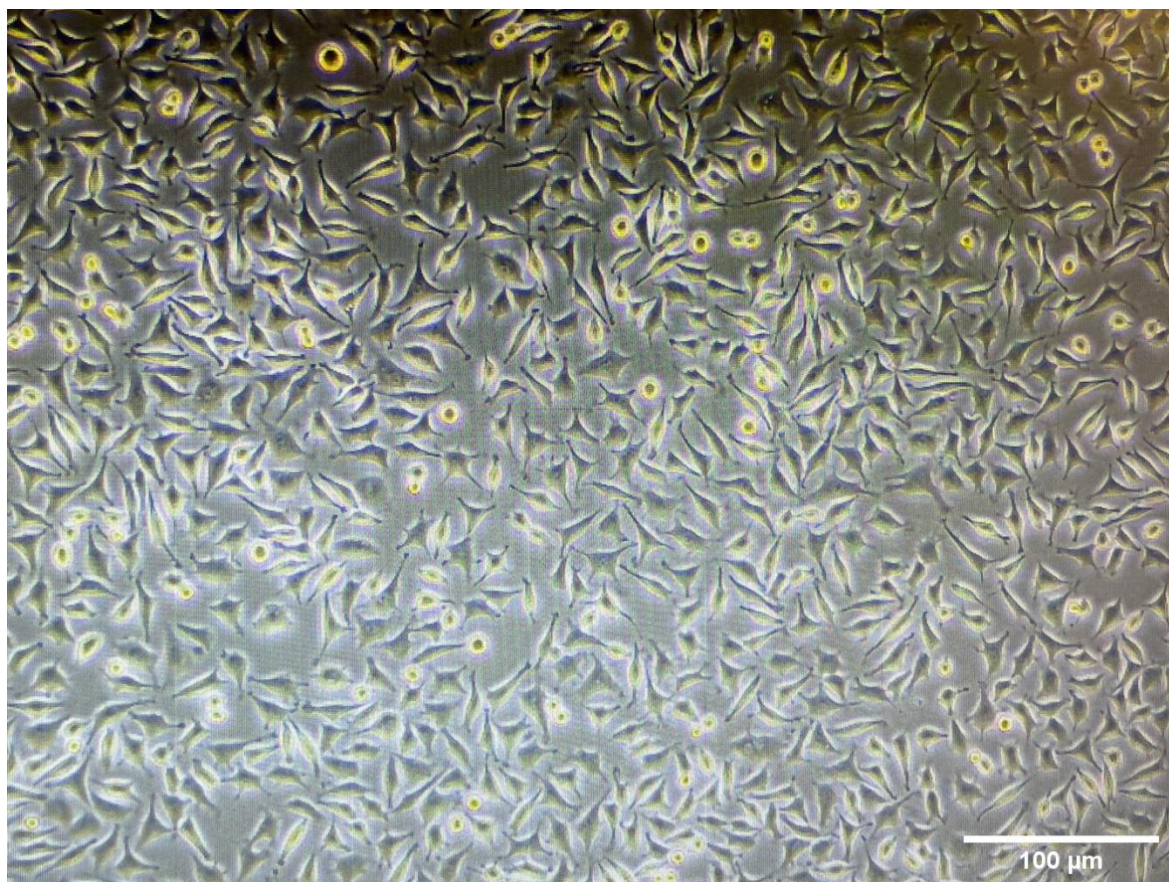


Figure 4-24 Digital image of ARPE-19 cell line adhered to the bottom of the culture flask after 48 h incubation.

Cell viability was assessed at 24 and 48 h of exposure to Dex suspension to evaluate Dex toxicity in the ARPE-19 cells. The concentrations of the drug at which cell viability decreased by 20% and 50% inhibitory concentration (IC₂₀, IC₅₀) were determined. The concentration of Dex leading to 80% viability, and more which equates to IC₂₀ was acceptable for further studies. Figure 4-25 shows the values for IC₂₀ and IC₅₀ 24 h and 48 h post-Dex solution exposure. At 24 h, cell viability greater than 80% was observed with a concentration of up to 125 $\mu\text{g/mL}$. Concentrations up to 15.62 $\mu\text{g/mL}$ maintained more than 80% viability after 48 h. This finding comes in line with the reported IC₂₀ in the literature [287]. Furthermore, exposing the cells to Dex concentrations ranging from 3.9 to 500 $\mu\text{g/mL}$ for 24 h, showed cell viability higher than IC₅₀. However, the concentrations of 250 and 500 $\mu\text{g/mL}$ appeared to be toxic to the cells (above the IC₅₀) at 48 h.

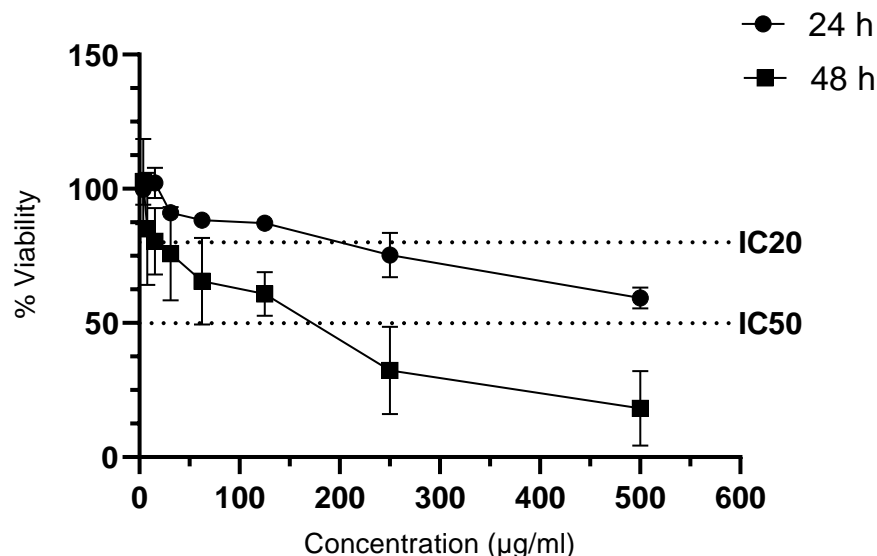


Figure 4-25 The IC20 and IC50 values determined by MTT reagent for Dex in 96 well plates treated with different concentrations at 24 and 48 h.

This study indicates that Dex exhibited dose and time-dependent effects on ARPE-19 cell viability. Concentrations ~ 15 $\mu\text{g/mL}$ can be used safely ($>\text{IC}_{20}$) on the ARPE-19 cells with no toxic effect over 24 and 48 h, respectively. Dex-loaded micro- and nano-particles containing amounts equivalent to ~ 20 $\mu\text{g/mL}$ were used to study the cytotoxic effect of fabricated particles on cell viability.

The interaction of drug delivery carriers with biological systems at the cellular level is essential for understanding the safety and efficacy of a fabricated system on the target cells. PLGA as a polymer has demonstrated a good safety profile and has been approved for ocular use [114]. However, the effect of the micro- and nano- systems on ARPE-19 cells was studied to assess the cellular toxicity and uptake of the particles.

Prepared PLGA micro- and nano-particles, either blank (NP and MP) or Dex-loaded (NP-Dex and MP-Dex) were tested for toxic effects on the cells. Seeded in 96 well plates, ARPE-19 cells were exposed to sterilised suspension of NP, NP-Dex, MP, and MP-Dex-02 for 24 and 48 h. The % cell viability is presented in Figure 4-26. In the case of the blank particles, which were used as a negative control to the Dex-loaded particles,

showed minimum or no toxicity at 24 h as compared to untreated cells with $96.61\% \pm 10.87$ and $101.1\% \pm 12.54$ for NP and MP, respectively. However, after 48 h the cell viability decreased to $91.74\% \pm 7.06$ for NP and to $95.05\% \pm 5.92$ for MP, which is consistent with data was reported in the literature [288]. This slight reduction in the cell viability with the nanoparticles is expected due to the inherent biological toxicity of nanosystems that affect the cells by lodging in the mitochondria and triggering injurious responses [289].

Furthermore, Dex-loaded PLGA particles showed cellular viability of $89.18\% \pm 13.33$ for NP-Dex and $93.77\% \pm 9.12$ for MP-Dex, this was followed by a decrease in the cellular viability to $76.55\% \pm 12.01$ for NP-Dex and $81.122\% \pm 9.36$ for MP-Dex when incubated for 48 h. In general, cell viability over 48 h was above 75% in all the cases indicating the formulated particles presented good cellular biocompatibility for ocular drug delivery.

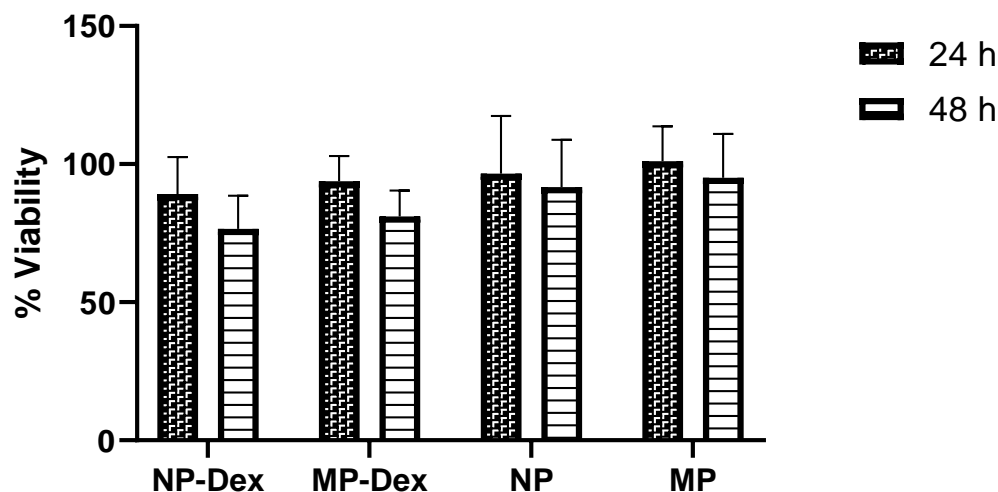


Figure 4-26 Effect of Dex-loaded particles (NP-Dex and MP-Dex) and blank particles (NP and MP) on ARPE-19 % viability.

4.4.12 Cellular uptake

The efficiency of cellular uptake of the fluorescent labelled PLGA micro- and nano-particles (MP-Flu and NP-Flu) was evaluated upon incubation with ARPE-19 cells at

37°C. Scanning the fluorescent intensity of the cells using the plate reader after extracting the fluorescent material from the cells by breaking the cell walls and exposing the fluorescent markers is shown in Figure 4-27-a. NP-Flu cellular uptake was higher than MP-Flu with 546.590 ± 30.404 and 377.854 ± 89.572 , respectively.

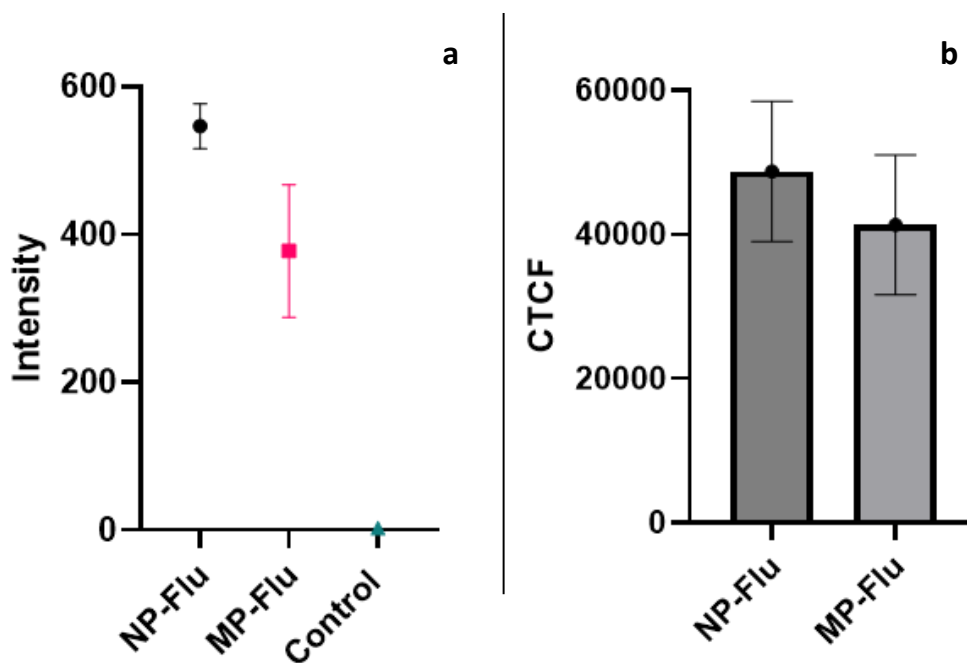


Figure 4-27 Cellular uptakes of NP-Flu and MP-Flu after exposing ARPE-19 cells for 1 h (a) the fluorescent intensity detected extracting the fluorescent markers, (b) CTCF measured in ARPE-19 cells.

Next, the cellular uptake was evaluated by analysing the pixel intensity to quantify the cellular uptake by ImageJ and the corrected total cell fluorescence (CTCF) was determined. Figure 4-27-b shows the CTCF values, NP-Flu showed higher fluorescent intensity compared to MP-Flu. These observations were in agreement with quantitative estimates of the fluorescent intensity. The present study displayed the influence of size on the extent of cellular uptake. It has been proposed that the particle size plays a key role in cellular adhesion and interaction with the cellular component [290]. Nanoparticles may be taken up more readily than microparticles mediated by

phagocytic process in the ARPE-19 cell line. However, studies had showed evidence that ARPE-19 cells avidly ingest microparticles 2.0 μm in size [291, 292].

Generally, studying the cellular uptake of micro- and nano- particles by ARPE-19 cells can provide valuable insights into the mechanisms of drug delivery and the potential therapeutic applications of the particles in the treatment of retinal diseases.

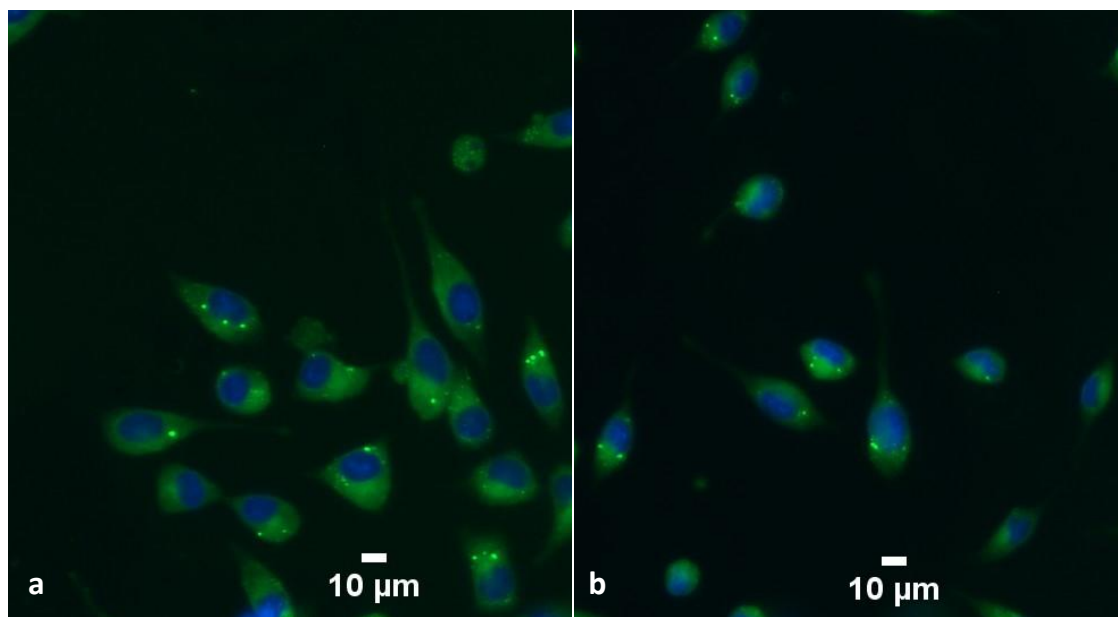


Figure 4-28 Fluorescent microscope images of ARPE-19 cells after 1 h of incubation with (a) NP-Flu, (b)MP-Flu. The cell nucleus was stained blue by DAPI and green, indicating the uptake of the fluorescent marker in the particles.

4.5 Conclusions

In this chapter, an effective method of preparing biodegradable micro- and nano-particles of PLGA has been displayed. An o/w emulsion solvent evaporation method was used to study the effect of the PLGA grade viscosity on the preparation of blank, Dex -loaded and fluorescent labelled microparticles. Dex is a hydrophobic drug that is insoluble in most nonpolar solvents. A mixture of organic solvents was tested to enhance the %EE and %DL. An EE% of more than 45% was recorded with

DCM/methanol solvent. The low viscosity grade of PLGA enhanced the particle size distribution and Dex encapsulation.

In order to assess the Dex content and release from the prepared particles an HPLC method was developed, and the findings confirmed the appropriate accuracy, specificity, and precision of the developed HPLC method. The Dex release from the particles was assessed for 21 days, and the release profile showed multiphasic behaviour, with initial drug burst release followed by sustained Dex release.

The PLGA particles were optimised and fully characterised by DSC, XRD, and FTIR to address the physical state and any possible interaction between the materials. Furthermore, the formulations had no cytotoxic effects on ARPE-19 cells at the tested concentrations. The particles were also tested for cellular uptake, this was essential to confirm the ability of the particle to penetrate the cell as the main target of the system was to deposit the PLGA particles in the ocular tissue and prolong the retention time.

Overall, the various types PLGA particles fabricated in this chapter demonstrated adequate properties and sufficient Dex release profile to be incorporated in the MN system for safe and effective deposition in the scleral tissue offering controlled drug release.

Chapter 5 Preparation and characterisation of microneedle arrays and *ex-vivo* studies

5.1 Introduction

Dissolvable MN systems were recently introduced for ocular delivery, and the approach is gaining great interest among pharmaceutical researchers. However, few studies have been conducted to investigate the feasibility of dissolving MN for ocular delivery [58, 62, 81, 90-92, 147, 293]. To enable its extensive clinical application, further studies in this area are necessary to understand the restrictions and challenges of the dissolving MN application [293].

The mechanical strength of the MN is vital for efficient application; glass or metal MN can sustain greater application forces than polymeric-based MN [293]. Therefore, in order to develop polymeric MN with adequate characteristics, it is crucial to take into account elements such as the type of ocular tissues, and the forces needed for the application. An added challenge in preparing an ocular intended dissolvable MN array is to prepare a polymeric base that possesses sufficient structural strength and controls the dissolution rate in the presence of the natural fluids of the eye, to successfully pierce tough ocular tissues [63].

This study introduces a novel dissolving MN model to deliver and deposit drug-loaded biodegradable PLGA particles into the scleral tissue at which the drug is released and permeates through the sclera. Transscleral permeability has been extensively investigated in the literature [3, 21, 27, 47, 294, 295]. Numerous factors have contributed to the scleral permeability, including molecular weight, lipophilicity, and molecular shape [296]. The scleral matrix is mainly composed of proteoglycans and collagen fibres. This complex structure can hinder particle permeation and diffusion. However, recent studies have demonstrated the potential of transscleral permeability of nanosized particles [297, 298].

At this stage of the study, the MN array moulds were designed and fabricated by 3D printing, and the PLGA particles of various sizes and types, including blank, Dex-loaded, and fluorescent labelled microparticles and nanoparticles were prepared and characterised. Thereafter, the development of the dissolving MN base to incorporate

the prepared particles in the polymeric MN will be the next step to proceed with the research aim and objectives. As proposed, a dissolvable MN array, which permits particle entrapment within the polymeric MN array, is studied in this chapter. Assessment of the MN mechanical strength, the dissolution rate of the polymeric base and *ex-vivo* assessment of the system, including transscleral Dex permeation and particles biodistribution, were carried out.

5.1.1 Aim and objectives

This chapter aims to fabricate and assess a drug delivery system composed of PLGA particles incorporated in a dissolvable polymeric MN array to deliver and localise the PLGA particles within the scleral tissue.

The objectives of the study are:

- Optimise the mechanical strength and the dissolution rate of the dissolvable polymeric base.
- Prepare and characterise the particles incorporated dissolving MN array.
- Study the MN *ex-vivo* performance of the Dex transscleral permeation on porcine scleral tissue.
- Assess the ability of the system to deposit the particles at the scleral tissue.
- Study the behaviour of the drug release from the formulated MN array through the ocular globe.

5.1.2 Chapter graphical overview

A summary of the work conducted in this chapter is illustrated in Figure 5-1.

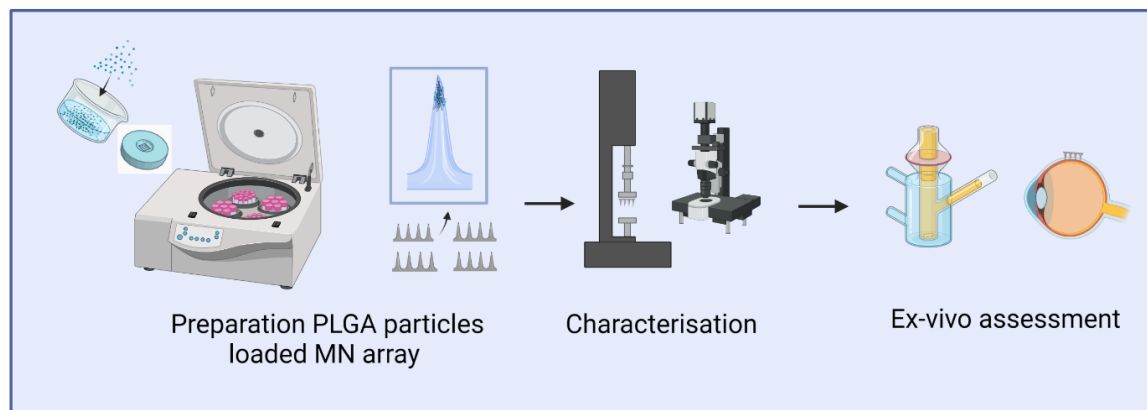


Figure 5-1 Chapter 5 graphical overview (created by Biorender).

5.2 Materials

Polyvinyl pyrrolidone Kollidon®30 and Kollidon®90 grades were purchased from BASF, Germany. Polyvinyl alcohol, gelatin, phosphate buffer saline tablet (pH 7.4), acetonitrile, dexamethasone, and 10% neutral buffered formalin, were purchased from Merck Sigma Aldrich, USA. Methylprednisolone was purchased from Cambridge bioscience, UK. SlowFade™ gold antifade mountant and optimal cutting temperature compound (OCT Cellpath) were purchased from ThermoFisher, UK.

5.3 Methods

5.3.1 Microneedle array preparation

To prepare the dissolvable polymeric MN arrays, moulds of a 3x3 conical MN 900 μm in height and 450 μm in base diameter were fabricated according to the method mentioned in Chapter 3, section 3.3.2. The MN moulds were printed at 0° orientation for all the experiments conducted in this chapter except for the MN array used for Dex ocular diffusion study, whereby the moulds were printed at 45° orientation. The effect of printing on angled positions was discussed in Chapter 3.

Polymeric blends of PVP and PVA at different ratios and grades of PVP were prepared. Initially, the predominant effect of PVP or PVA in the polymers blend on the MN array

dissolution and mechanical strength was assessed. Three ratios of PVP (Kollidon® 30) with PVA were used to prepare 30% w/v solutions as shown in Table 5-1.

Table 5-1 Formulations composition of MN array polymeric base solution (30% w/v) prepared by various ratios of PVP and PVA.

Formulation code	PVP (Kollidon® 30)	PVA
P5A1	25 mg	5 mg
P1A1	15 mg	15 mg
P1A5	5 mg	25 mg

Furthermore, the effect of PVP grade (i.e. viscosity) on the MN dissolution and mechanical behaviour was also assessed. PVP Kollidon 30 or Kollidon 90 with PVA was used to prepare a 30% w/v solution at a different ratio as listed in Table 5-2. Each polymer was accurately weighed then added to deionised water. The mixture was heated to 80 °C and continuously stirred by a magnetic stirrer in a sealed bottle until the polymers were completely dissolved. Subsequently, the polymeric solutions were stored at room temperature for up to 3 days until further use.

Table 5-2 Formulation composition of MN array polymeric base solution (30% w/v) prepared by PVA with PVP-K30 or PVP-K90.

Formulation code	Kollidon® 30 (PVP-K30)	Kollidon® 90f (PVP-K90)	PVA
P30-4	24 mg		6 mg
P30-2	20 mg		10 mg
P90-4		24 mg	6 mg
P90-2		20 mg	10 mg

To prepare the polymeric MN array, moulds were filled with a specified volume of the polymeric solution then the moulds were centrifuged in a horizontal direction at a 90° angle using swinging buckets rotor for 15 min at 9000 rpm, then left to dry for 24 h in a

closed container under ambient conditions. After complete drying, the MN array was gently separated from the mould and excess dry polymer on the mould wall was cut out at the edge of the base by a sharp blade.

For the preparation of PLGA particles incorporated dissolvable MN arrays, various types of particles prepared according to the method described in Chapter 4, section 4.3.1 were used to prepare MN arrays (Table 5-3). An accurate amount of the particles was weighed and mixed with 10 % (w/v) PVP (Kollidon 30) solution with a magnetic stirrer for 10 mins until the particles dispersed in the solution. A volume of the dispersion equivalent to 100 µg of particles was placed in the moulds and centrifuged in a horizontal direction at a 90° angle using a swinging bucket rotor for 15 min at 9000 rpm, then left to dry for 24 h in a closed container under ambient conditions. Next, the dried particles in the moulds were filled with PVP/PVA solution then centrifuged at 90° for 10 mins then left to dry for 24 h in a closed container under ambient conditions. The arrays were gently removed from the moulds and excess polymer on the side was cut off. The MN arrays were stored in a light-protected airtight container until further use.

Table 5-3 Specifications of PLGA particles incorporated in dissolvable MN array.

Size*	Formulation name	PLGA grade	Organic solvent	Loading material
Microparticles	MP	PLGD 7502	DCM	Blank
	MP-Dex	PLGD 7502	DCM/Methanol	Dex**
	MP-Flu	PLGD 7502	DCM	Coumarin-6
Nanoparticles	NP	PLGD 7502	DCM	Blank
	NP-Dex	PLGD 7502	DCM/Methanol	Dex**
	NP-Flu	PLGD 7502	DCM	Coumarin-6

(*) The average size of the particles is mentioned in Chapter 4, section 4.4.2

(**) The percentage of drug loading is mentioned in Chapter 4, section 4.4.5.

5.3.2 Dissolution study

To test the dissolution of the fabricated polymeric MN array, solidified gelatine was used. Gelatine powder was added to deionised water to prepare a 15% (w/v) solution [63]. The solution was gently heated at 70°C until completely dissolved. The solution was poured into a petri dish and left to cool. The MN array was inserted in the solidified gelatine hydrogel using gentle thumb pressure for 15 sec and left in the gelatine for 15 sec then removed by a tweezer and the dissolution was determined by calculating the percentage of height reduction of the MN by taking images before and after insertion. The images were processed by ImageJ to determine the height change. Data are reported as mean \pm SD, n=18.

5.3.3 Mechanical strength testing

To assess the mechanical properties of the MN array, an Instron tensile tester 5567 (Instron, USA) was used (Figure 5-2). MN array was fixed to the lower frame of the instrument by double-sided tape. A compression force was applied using a flathead stainless-steel cylindrical probe attached to the upper frame of the instrument and vertical to the MN array at a speed of 0.1 mm/ sec. The compression force was continuously recorded until a displacement of 500 μ m was reached. Data was collected and analysed by Bluehill 2 (version 2.35) software. Force vs displacement curve was constructed by Origin Pro software (2019b, Originlab, USA) to determine the force required for 500 μ m displacement. Data are reported as mean \pm SD, n=3.



Figure 5-2 MN array mechanical testing setup using an Instron tensile tester. A cylindrical probe attached to the upper instrument frame.

5.3.4 Preparation of ocular tissue

The *ex-vivo* experiments, including adhesion, permeation, insertion, and ocular biodistribution tests were conducted on excised ocular tissue. Fresh porcine eye globes were purchased from Fresh Tissue Supplies (Etchingham, East Sussex, UK). The eye surface was cleaned, and the remaining rectus muscles were carefully removed. The cornea was cut out around the limbus using surgical scissors. Then, the vitreous humour was removed, and the retinal layer was gently detached. A square sample of scleral tissue ($\sim 7 \times 7$ mm) was cut. All the scleral samples were cut at a 5 mm distance from the lumbus to minimise sample thickness variation [62]. This location is where the subconjunctival injection is usually applied, and it is the visible part of the sclera where a self-implantable MN array can be inserted. All the ocular tissue samples were used immediately or frozen in a sealed container at -20 °C for further use. At the time of use,

the tissues were thawed and soaked in phosphate buffered saline (PBS) (pH 7.4) for 30 min at $37^{\circ}\text{C} \pm 0.5$.

5.3.5 Microneedle array adhesion test

To study the degree of adhesion of the prepared MN array to scleral tissue, an Instron tensile tester was used. A $\sim 7 \times 7$ mm square piece of scleral tissue was affixed to the lower stationary frame of the instrument then the tissue was wetted with 20 μl PBS (pH 7.4). The MN array was attached to a moving stainless-steel probe with double-sided adhesive tape. Initially, a compression force of 4 N was applied to insert the MN array into the tissue and the probe was held in position for 10 sec then a tensile force was applied until the MN array was completely separated from the scleral sample [299]. The force corresponding to the MN array detachment was identified as the adhesion force. The test was performed in triplicate and the mean \pm SD was reported.

5.3.6 MN array scleral insertion test

The insertion force study was performed on isolated scleral tissue samples using an Instron tensile tester 5567 (Instron, USA). The scleral sample was hydrated before the experiment for 30 min in PBS (pH 7.4) at $37 \pm 0.5^{\circ}\text{C}$. The scleral samples were pat dried with a paper towel and then affixed to the lower frame of the Instron tester using cyanoacrylate adhesive glue as shown in Figure 5-3. The MN array was mounted on a cylindrical stainless-steel probe with double-sided adhesive tape perpendicular to the tissue sample. The probe was set to move at a rate of 10 $\mu\text{m}/\text{sec}$ until a force of 4 N was reached. The compression force exerted on the ocular tissue by the MN array (N) as a function of its compression distance (mm) was continuously recorded using Bluehill 2 (version 2.35) software. The MN insertion force was determined from the distance vs force curve as the average force when the curve shows a rapid increase in the force as the MN penetrate the tissue [63]. The test was performed in triplicate and the mean \pm SD was recorded.

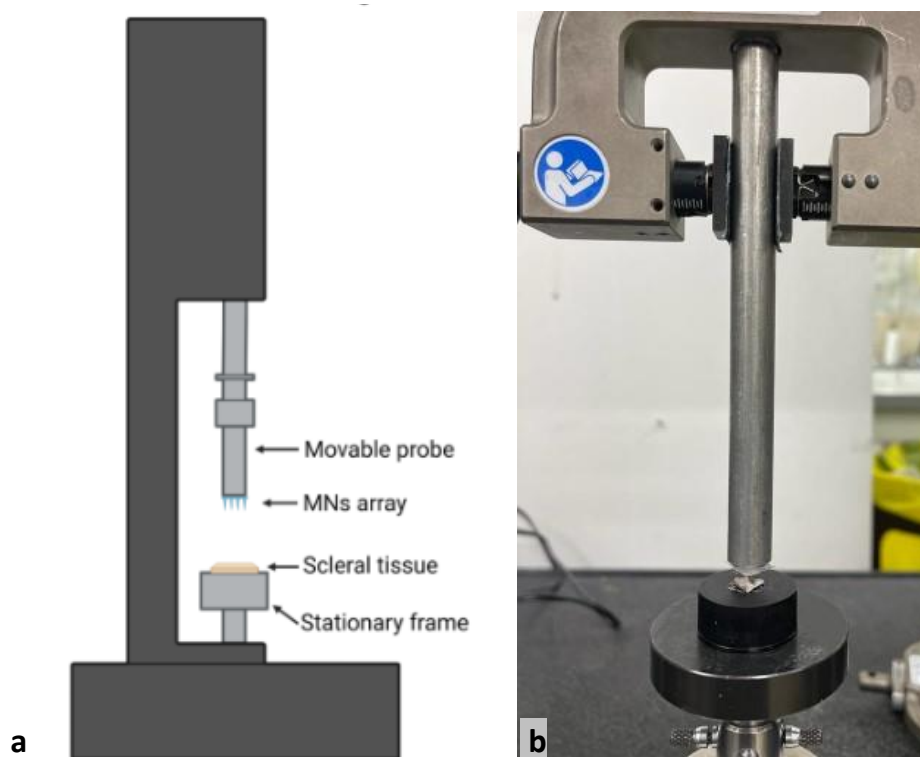


Figure 5-3 Illustration of the instrumental set-up of MN array insertion into porcine scleral tissue (a) graphical illustration, (b) Instron tensile tester.

5.3.7 Analytical quantification of dexamethasone in ocular tissue

Dex detection and quantification method developed and validated in Chapter 4, section 4.3.7 was amended to substantiate the quantity of Dex in biological samples. An internal standard was added to the samples to compensate for the loss during the sample preparation. The internal standard (IS) should be similar in structure to the analyte of interest in the sample [300]. Thus, methylprednisolone was selected as an internal standard. The chromatographic conditions of the HPLC method are mentioned in Chapter 4, Table 4-2. The flow rate was modified to 0.9 mL to improve the separation of Dex and methylprednisolone detected peaks. System suitability, linearity, and specificity were calculated for Dex analysis by the developed method.

To determine the method specificity, sample of the vitreous humour and scleral tissue was spiked with Dex and IS. The sample was homogenised, centrifuged and filtered. The filtrate was analysed and the percentage of mean recovery was calculated.

5.3.8 Dexamethasone transscleral permeation

To study the permeation of Dex through ocular tissue, excised porcine sclera was used. The study was performed using a Franz diffusion cell (PermeGear Inc., USA). The acceptor compartment volume was 3 mL with a 9 mm joint orifice diameter and 0.64 cm² diffusion area. The acceptor compartment was filled with 3 mL PBS (pH 7.4) and maintained at 37 ±0.5 °C under continuous stirring by a magnetic bar. A piece of scleral tissue, large enough to cover the orifice, was fixed to the top of the donor compartment by cyanoacrylate glue with the episcleral layer side facing upwards. The donor compartment was fixed to the acceptor compartment by a clamp exposing the tissue to the donor compartment. The tissue was wetted with 10 µL PBS before adding the samples. Three dosage forms were tested for transscleral permeation, 1% Dex suspension in deionised water, free Dex-loaded microparticles (MP-Dex), and MP-Dex incorporated MN array (Dex-MN). An amount equivalent to ~100 µg of Dex in free MP-Dex or 1% Dex suspension was instilled in the donor compartment post connecting the donor compartment to prevent spilling. While with the Dex-MN, the MN array was inserted in the scleral tissue by gentle thumb pressure before joining the donor compartment with the acceptor compartment to allow the application of force while securing the sides of the tissue on the orifice to avoid detaching it from the acceptor compartment. Afterwards, the donor compartment was attached to the acceptor compartment by a clamp. During the experiment, the top of the donor compartment and sampling arm were covered with Parafilm® to preserve fluid in the tissue and cell. A long stainless-steel needle (20G) attached to a 1 mL syringe was inserted in the sampling arm to withdraw samples (300 µL) from the donor compartment at predetermined time intervals, which was later replaced by fresh PBS buffer maintained at 37 ±0.5°C. Collected samples were kept at 4°C to be later analysed by HPLC. The cumulative percentage of Dex permeated through the sclera was calculated. At the end

of the experiment the scleral tissue was washed thrice with PBS then the edges covering the orifice were cut. Subsequently, the tissue was homogenised with PBS/ ACN mixture by a homogeniser. The homogenised mixture was centrifuged, and the supernatant was filtered and analysed by HPLC. Results were reported as mean \pm SD, n=3.

5.3.9 *Ex-vivo* transscleral particles diffusion

To study the PLGA particles release and diffusion from the needle tip into scleral tissue, fluorescent-labelled micro- (MP-Flu) and nano- (NP-Flu) particles incorporated in MN array were used. The MN array was inserted on $\sim 7 \times 7$ mm square piece of the sclera. The tissue was hydrated for 30 min in PBS (pH 7.4) at 37 ± 0.5 °C before MN array insertion. The MN array was inserted into the tissue by applying gentle thumb pressure for 30 sec. The tissue MN array composite was witted with 50 μ L PBS in a closed container at 37 ± 0.5 °C for 1 h. The sclera was then washed three times in fresh PBS to remove MN array residue. The tissue was fixed in 10% neutral buffered formalin for 2 h. The fixed scleral sample was placed in a 1x1 cm square mould and immersed in optimal cutting temperature (OCT) compound cryo embedding matrix, which was then kept in dry ice for 15 mins allowing the OCT to solidify. The frozen tissue block was transversely sectioned or cross-sectioned by microtome-cryostat (HM525 NX Cryostat, Thermo Scientific, UK) at -20 °C to 12 μ m thick sections then mounted on Superfrost® plus slides (Thermo Scientific, UK) [301]. The sections were either stained with haematoxylin and eosin stain as per the manufacturer protocol or stained with DAPI for 5 min and then washed with PBS. The sections were left to dry under ambient conditions then were mounted with SlowFade™ gold antifade mountant to be imaged by an optical microscope for haematoxylin and eosin staining and fluorescent microscope (EVOS, ThermoFisher, USA) for fluorescent staining.

5.3.10 Dexamethasone ocular biodistribution

This study was designed to study the *ex-vivo* Dex release and distribution from the MN array within the ocular globe. A porcine eye either fresh or thawed from frozen was hydrated for 30 mins in PBS (pH 7.4) at 37 ± 0.5 °C. The eyes were placed in 3D-printed

cups designed to fit porcine eyes to maintain their shape and to keep it equally hydrated. An amount of 200 μ L PBS was added to the cup to keep the eyes hydrated during the experiment. MN array containing Dex-loaded particles (MP-Dex or NP-Dex) was inserted into the eye globe by applying force equal to 5 N using a movable stainless probe attached to a mechanical tester (TA plus texture analyser, Stable Micro System, UK). After the insertion, the cups were covered by Parafilm® and kept at $37 \pm 0.5^\circ\text{C}$ in a shaking incubator (50 rpm) for 4 h. Subsequently, the MN array residual was removed, and the eye was washed thrice in a fresh PBS tub. The vitreous humour (VH) was aspirated slowly from the centre of the eye by a 5 mL syringe attached to a 25 G needle at the equator opposite the MN array insertion site [302, 303]. The eye was dissected around the limbus to isolate the anterior segment (AS), including the cornea, lens, and iris–ciliary body. At this point, any VH remained was withdrawn by a needle and added to the collected VH sample. The site of the MN insertion was cut out. Finally, the rest of the eye globe, including the sclera and the retina was also stored separately.

To extract Dex from VH, a liquid-liquid extraction method was used. A 5 mL ACN with a known concentration of IS was added to the sample, the solution was vortexed for 60 sec and then sonicated for 5 min. The mixture was centrifuged for 15 min at 9000 rpm. The supernatant was withdrawn then the solution was dried under vacuum. The dried extract was resuspended in 0.5 mL ACN then filtered by PTFE filter (0.2 μm) and analysed by HPLC. The anterior segment, the site of MN array insertion and the rest of the eye globe were each homogenised with ACN and PBS mixture (1:4) with IS added to the mixture. The homogenised tissue mixture was sonicated for 10 min then centrifuged for 15 min at 9000 rpm. The supernatant was withdrawn then left to dry under vacuum. The dried extract was resuspended in 0.5 mL ACN and filtered by a PTFE filter (0.2 μm) to be analysed by HPLC.

5.3.11 Statistical analysis

All the results are presented as mean \pm SD. Statistical analysis was performed using one-way ANOVA or Student's *t*-test and *p*-value <0.05 was considered statistically

significant. All statistical analyses were performed using Prism software (GraphPad La Jolla, California).

5.4 Results

5.4.1 Preparation and optimization of the dissolvable polymeric base

The MN array is composed of a dissolvable polymeric base. PVP and PVA are hydrophilic polymers that are most commonly used in the preparation of ocular dosage forms due to their favourable properties, such as tear film stabilisation and lubrication. More details about the ocular uses of the polymers are mentioned in Chapter 2, sections 2.1.1 and 2.1.2. Studies have demonstrated that PVP/PVA blend offers a synergistic effect by combining the properties of each parent polymer into the blended network [304]. Blending PVP with PVA in the presence of water results in the formation of thermodynamically miscible blends due to the intermolecular hydrogen bonding between the PVA hydroxyl group (-OH) with the proton acceptor carbonyl group on the pyrrolidone ring (-C=O) on PVP [304, 305]. PVP/PVA mixture has been frequently used for the fabrication of a dissolvable ocular MN array [58, 90]. The ratio and the grade can highly affect the properties of the MN. Initially, to assess the effect of each polymer on the MN array dissolution and strength, three ratios of PVP Kollidon® 30 (PVP-K30) to PVA (Mwt 31,000-50,000) of 5:1, 1:1, and 1:5 were used to prepare 30% (w/v) solutions. The analysis of the dissolution rate of a dissolvable MN system is crucial, particularly for ocular application, unlike transdermal application where the skin surface is relatively dry. Healthy adult conjunctiva and eye globe surface are covered with a tear film $\sim 7\text{-}9\text{ }\mu\text{L}$ in volume and $0.5\text{-}2.2\text{ }\mu\text{L}/\text{min}$ turnover rate [17]. The presence of fluid on the eye surface will initiate the dissolution process when the MN touch the ocular surface which may hinder the MN insertion into the tissue.

Dissolution of the polymeric base was tested in gelatine to offer an environment that mimics the ocular tissue water content [63]. The MN was easily inserted by applying force with thumb pressure into the solidified gelatine matrix. Images of the MN array before and after the insertion and the percentage of height reduction are presented in

Figure 5-4 and Figure 5-5, respectively. The MN array prepared with P5A1 has a higher portion of PVP than PVA. The MN has partially dissolved, and the average height of the array was reduced by $31.78\% \pm 5.77$, this could be attributed to the higher water solubility nature of PVP polymer than PVA. A study has reported that a high concentration of PVP in PVP/PVA blends results in the formation of large pores in the structure that makes it prone to dissolution [305]. On the other hand, when PVA was predominant in the blend (P1A5) the visual assessment of the MN confirmed that the MN were weak and slightly deformed even before the insertion. The average height of the MN has reduced by $10.52\% \pm 2.79$ after insertion, which is mainly due to tip bending rather than dissolving. This is due to the lower solubility of PVA in water that depends on the degree of hydrolysis of the polymer and the molecular weight [140]. Highly hydrolysed PVA polymer necessitates elevated temperatures and long dissolution time to break the strong hydrogen bonds formed within the PVA molecules [305]. In the case of the equal proportion of PVP and PVA (P1A1), the MN has maintained its shape and minimum height reduction was observed ($5.84\% \pm 1.03$). From the dissolution data, it was evident that the amount of PVA and PVP in the blend can modulate the dissolution rate.

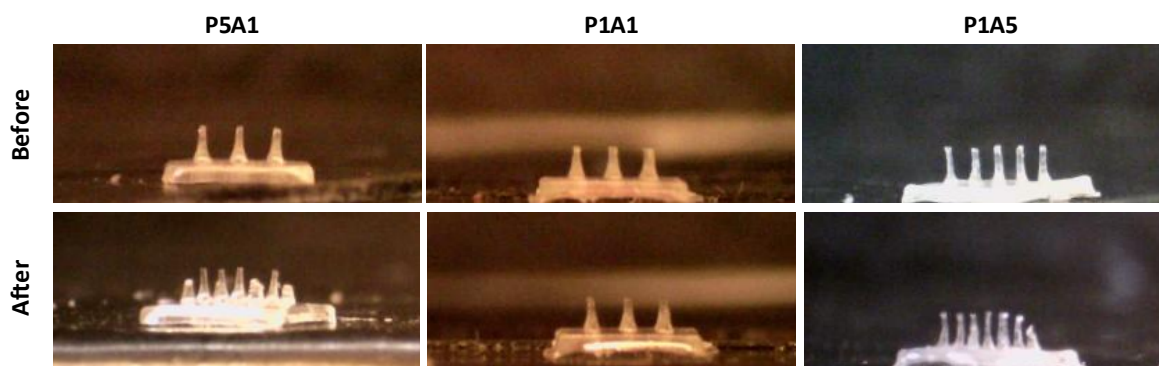


Figure 5-4 Before and after images of MN array dissolution prepared by different ratios of PVP/PVA blend. P5A1, P1A1, and P1A5 MN arrays were inserted in gelatine for 30 sec. (MN are $900\ \mu\text{m}$ in height before insertion).

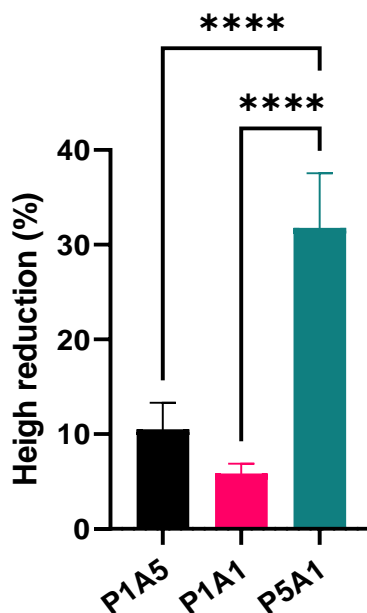


Figure 5-5 Percentage of height reduction of MN arrays formulated by different PVP/PVA blend (P5A1, P1A1, and P1A5) MN arrays after insertion in gelatine. Data presents mean \pm SD (n=18), (**** $p < 0.00001$).

To further investigate the effect of the PVP/PVA polymer blend on the behaviour of the MN, the mechanical strength of the MN array was tested using a texture analyser (TA plus texture analyser, Stable Micro System, UK). The data was obtained as the compression force required for 0.5 mm displacement (Figure 5-6). P5A1 has the highest compression force with $12.12\text{N} \pm 2.00$, while P1A1 blend reduced the force to $5.67\text{N} \pm 0.57$, and the lowest compression force was $2.25\text{N} \pm 0.37$ observed with P1A5. PVA polymer exhibits strength and flexibility, it has viscoelastic mechanical behaviour, which gives it a rubbery-like effect that could explain the low compression force recorded with P1A5 [142]. On the other hand, the high PVP ratio increased the strength significantly ($p < 0.001$). However, the MN were brittle, and the base was breaking easily. From the dissolution and mechanical strength data, combining an equal ratio of the polymers has resulted in the slower dissolution of the MN, yet with a low compression force. Consequently, altering the ratio was further required to achieve a strong and slowly dissolving MN capable of retaining their structural integrity.

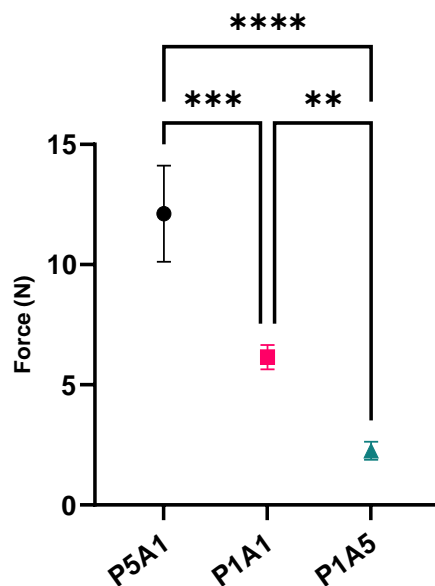


Figure 5-6 Force exerted on MN array prepared by different ratios of PVP/PVA to reach 0.5 mm displacement. The values represent mean \pm SD (** $p < 0.001$, *** $p < 0.0001$, **** $p < 0.00001$).

To further optimise the properties of the polymeric base, the influence of the PVP molecular weight on the properties of the MN array was investigated. High molecular weight PVP-K90 and low molecular weight PVP-K30 were blended with PVA. The ratio of PVP to PVA was set as 4:1 and 2:1 in order to tune the characteristic of the MN array. The formulations dissolution in the gelatine and the percentage of height reduction are presented in Figure 5-7 and Figure 5-8, respectively.

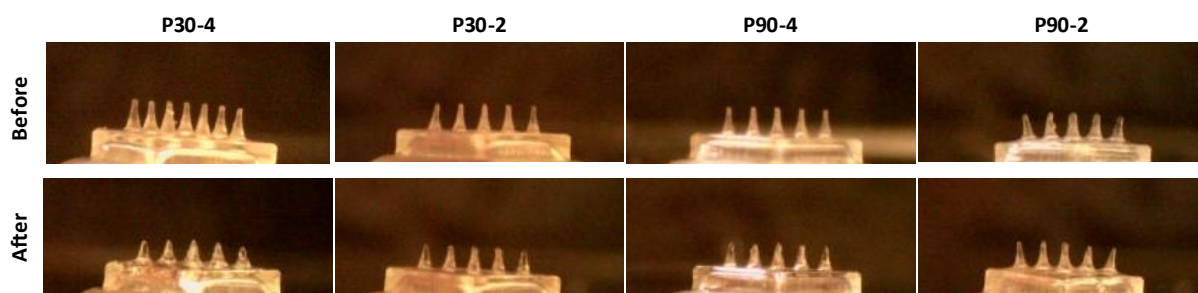


Figure 5-7 Before and after images of MN array dissolution in gelatine after 30 sec prepared by different ratios of PVP/PVA blend (MN are 900 μ m in height before insertion).

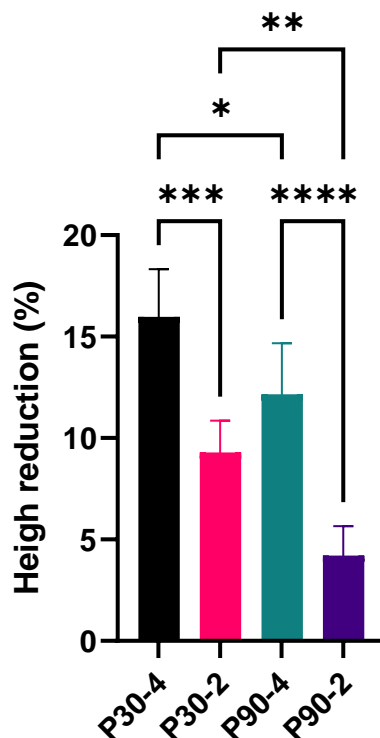


Figure 5-8 Percentage of height reduction of MN formulated by different grades of PVP and ratio of PVP/PVA blend. Data present mean \pm SD (n=18) (* p <0.01, ** p <0.001, *** p <0.0001, **** p <0.00001).

The molecular weight and the proportion of PVP were found to have a significant influence on the dissolution rate and, thus the percentage of the MN height reduction. Higher molecular weight PVP-K90 resulted in slower dissolution and consequently a lower percentage of height reduction compared to PVP-k30. This could be attributed to the higher viscosity of the PVP-K90, which creates a viscous layer around the needles that requires more time for dissolving in the surrounding media. A study in the literature has mentioned the effect of PVP molecular weight on the dissolution rate and the drug release from a PVP matrix and described the formation of a viscous gel-like layer around the dissolving medium limiting the dissolution kinetics with PVP-K90 grade [306]. Also, the lower ratio of PVP (i.e. higher ratio of PVA) regardless of the grade decreased the dissolution significantly.

Moreover, the ratio of PVA has also influenced the rate of the MN array dissolution rate confirming the previous finding (Figure 5-5). Increasing the proportion of PVA from 25% in P90-4 and P30-4 to 33.33% in P90-2 and P30-2 and accordingly reducing PVP from 75% to 66.66% resulted in a significant decrease in the height reduction from 12.15% \pm 2.52 to 4.20% \pm 1.45 with PVP-K30, and from 15.97% \pm 2.34 to 9.29% \pm 1.56 with PVP-K90. This could be attributed to the interaction between PVP and PVA molecules, hence hindering the water interaction with the polymeric chains and thus reserving the matrix integrity [305]. A similar observation was reported in a gel prepared by PVP/PVA blend, increasing the PVP concentration in the formulation resulted in faster chain dissolution and less matrix swelling [307].

The mechanical strength of the MN array prepared by the various PVP/PVA blends was assessed by a compression test presented in Figure 5-9. The force was exerted perpendicular to the MN array and the forces corresponding to 0.5 mm displacement are presented in Table 5-4. Comparing the prepared formulation, P90-2 showed a significantly higher compression force compared to the rest of the prepared PVP/PVA blends ($p < 0.05$). the synergistic effect of blending the two polymers in addition to the use of higher molecular weight PVP has positively influenced the mechanical properties of the MN. Still, the mechanical strength data of all the formulated MN arrays exhibited a strong structure sufficient to penetrate ocular tissue in accordance with the published literature [63].

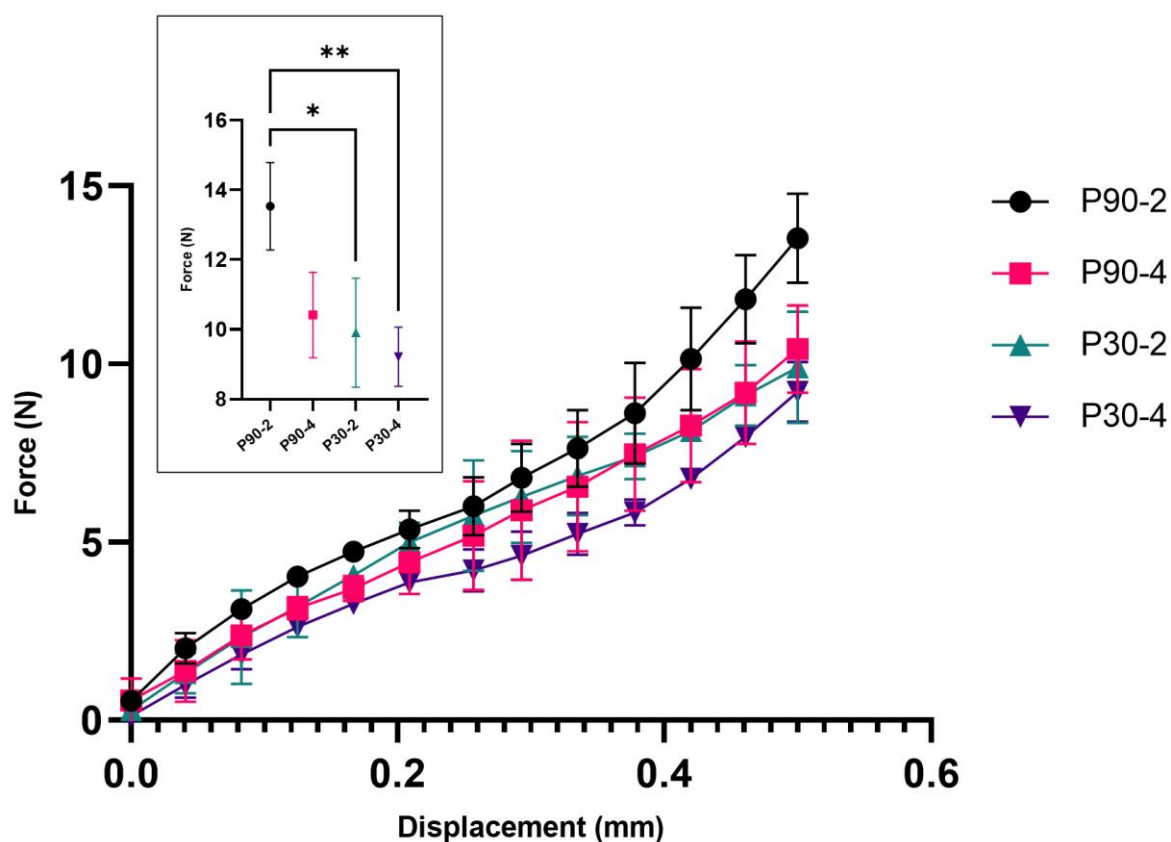


Figure 5-9 MN array (3x3) mechanical strength test of various PVP/PVA blends. In the box, the force exerted to reach 0.5 mm displacement. All values represent mean \pm SD (n=3) (* p <0.01, ** p <0.001).

Table 5-4 Compression force per MN array (3x3) and per needle of various PVP/PVA blends to reach 0.5 mm displacement. values represented as mean value \pm SD (n=3).

Formulation code	Compression force/array (N)	Compression force/needle (N)
P90-2	13.53 \pm 1.25	1.50
P90-4	10.42 \pm 1.22	1.15
P30-2	9.91 \pm 1.56	1.10
P30-4	9.21 \pm 0.85	1.02

The adhesion strengths of the various PVP grades and PVA blends on porcine scleral tissue were investigated using an Instron tensile tester. Generally, both PVA and PVP

exhibit relatively weak mucoadhesive properties [308, 309]. However, polymer properties such as molecular weight, moisture content and hydrogen bonding capacity can affect the degree of adhesion to biological tissue [310]. To assess the adhesion, a tensile force was exerted after applying a compression force to attach the MN array to the scleral sample. The force required to detach the MN array from the tissue was recognised as the adhesion strength (Figure 5-10). Comparing the two ratios from the same PVP grade P90-2 and P90-4, adhesion force showed no statistically significant difference between the ratios of the same grade ($p > 0.05$). However, formulating MN array using PVP-K90 and PVP-K30 revealed a significant difference between the two grades of PVP. Both PVP and PVA demonstrate hydrogen bonding ability that promotes the interaction with the surface mucin layer [311]. It was also reported that the length of the polymer chain is critical for the polymer entanglement with the mucin molecules. Polymers with a molecular weight greater than 100 kDa can demonstrate bioadhesive properties which explain the stronger adhesion forces reported with P90-2 and P90-4 [309].

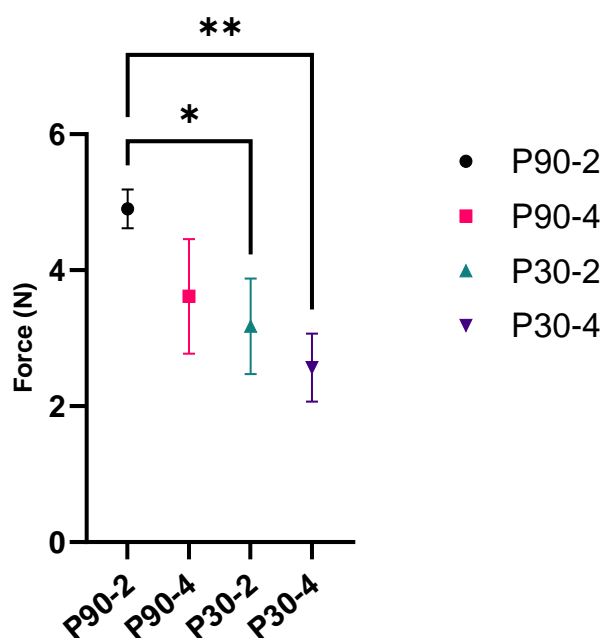


Figure 5-10 Forces recorded to detach MN array prepared by various PVP/PVA blends from porcine scleral tissue. All values represent mean \pm SD (n=3).

From the reported data in the dissolution, mechanical strength and adhesion study, formula P90-2 produced stronger needles with slow dissolution and stronger adhesion capability. Therefore, P90-2 was selected to prepare the particles loaded MN array for the rest of the study.

5.4.2 Preparation and characterisation of particle loaded MN arrays

The selected polymeric base (P90-2) was used to prepare a 3x3 conical MN array of 900 μm height and 450 μm in base diameter needles (Figure 5-11, a and b). The first step to prepare particles incorporated MN array was to mix the particles (MP, MP-Dex, MP-Flu, NP, NP-Dex, and NP-Flu) with 10% (w/v) PVP-K30 solution to form particle dispersion. A specific amount of the dispersion was placed in the mould and centrifuged. A 10% PVP-K30 solution was used to attain a weak binding effect without hindering the release of the particles to the surrounding tissue upon insertion. The second step in the fabrication process was to place the P90-2 polymeric base solution into the dried layer of particles and then centrifuged. The fabrication process has successfully concentrated the particles at the tip of the MN as shown in Figure 5-11-c and d.

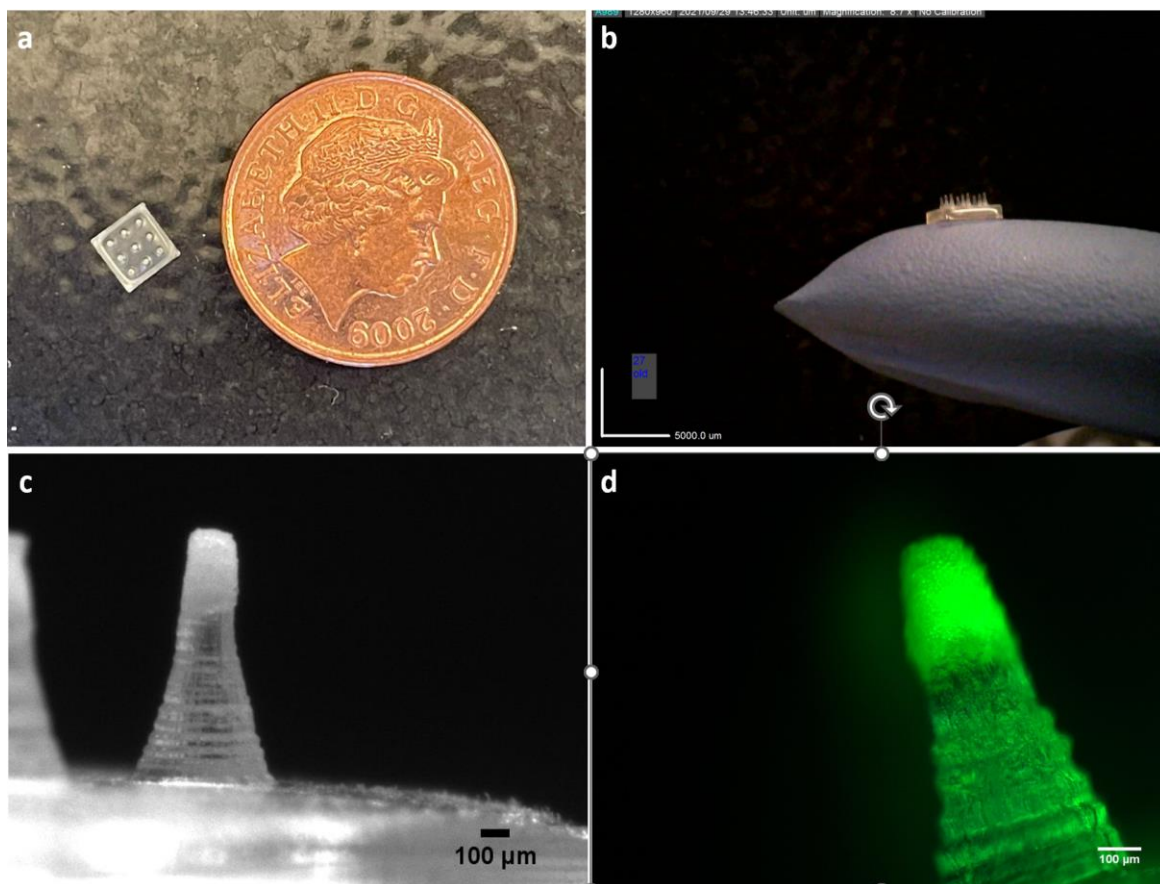


Figure 5-11 Digital images of MN array of (a) top view of the blank MN array compared to British one penny coin (diameter = 20.3 mm), (b) side view, (c) MP concentrated at the tip of the MN, and (d) fluorescent microscope image of MP-Flu incorporated MN array.

SEM images of the prepared MN arrays are presented in Figure 5-12. The polymeric MN array tip and inter-needle space are shown in Figure 5-12-a and b. The tip and the inter-needle space displayed a smooth surface. However, layers were observed on the MN body, which reflected the surface of the 3D printed mould. Meanwhile, SEM images of particles incorporated MN arrays confirmed the concentration of the particles at the tip of the needles. Examining the interneedle space revealed that particles were found on the surface indicating that remnants of the particles did not travel to the tip of the MN during centrifugation. Particles in the inter-needle space may offer drug release to the episcleral surface in the applied region.

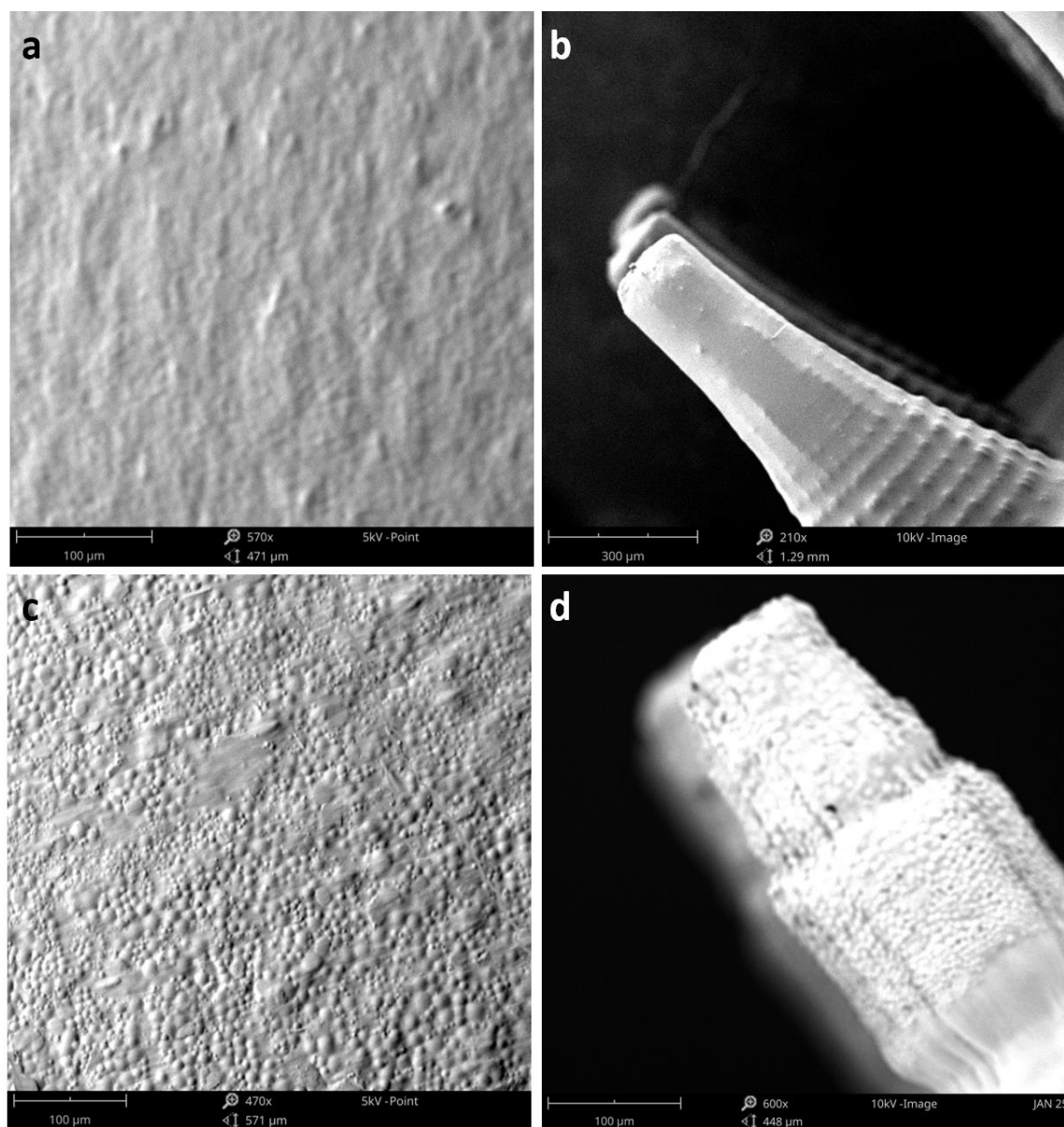


Figure 5-12 SEM images of MN arrays, (a) interneedle space of blank MN array, (b) tip of the blank MN array, (c) interneedle space of microparticles incorporated MN array, (d) MN tip of microparticles incorporated MN array.

The microparticle (MP) incorporated MN array (MP-MN) was tested for mechanical strength, this test was carried out to evaluate the effect of the MP addition on the mechanical strength. Figure 5-13 depicts the mechanical strength of a blank polymeric (P90-2) MN array and the MP-loaded counterpart. The addition of particles has significantly reduced the compression resistance from $13.53 \text{ N} \pm 1.25$ per array (1.5

N/needle) to $8.99 \text{ N} \pm 0.98$ per array (0.99 N/needle). This could be attributed to the low packing density of the particles at the MN tip. Consistent with the data reported in the literature, MP-MN was strong enough to penetrate the ocular tissue [63, 242].

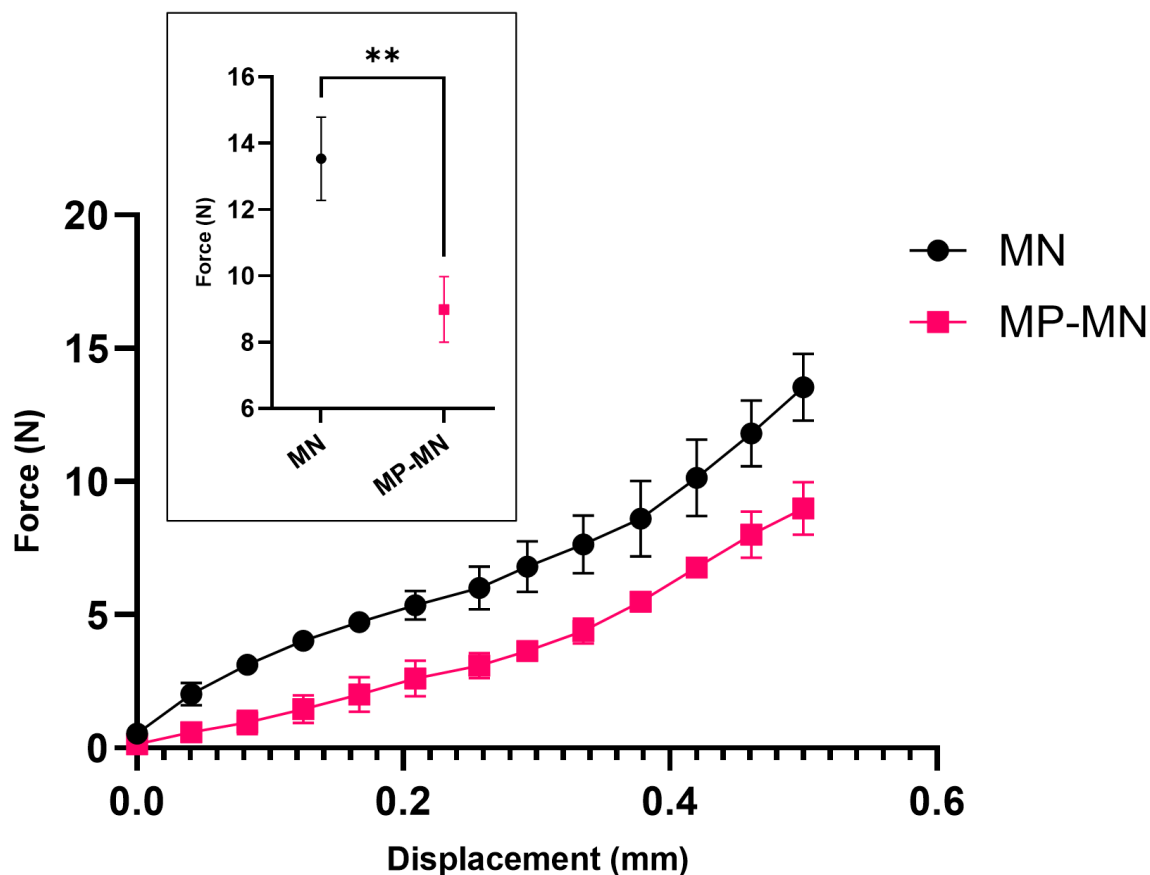


Figure 5-13 MN array (3x3) mechanical strength test of blank polymeric MN (MN) and MP-MN arrays. In the box, forces exerted to reach 0.5 mm displacement. All values represent the mean \pm SD (n=3).

5.4.3 Microneedle array scleral insertion test

The insertion capability of polymeric and MP-loaded MN array into the ocular tissue was estimated from the compression distance vs force curve [63]. The MN array insertion force-distance curve into scleral tissue is shown in Figure 5-14. The forces required to penetrate the sclera were $0.774 \text{ N} \pm 0.241$ and $0.782 \pm 0.246 \text{ N/ array}$ for MN and MP-MN array, respectively (Table 5-5). The force was calculated by averaging 3

points on the distance vs forces curve at the transition region where the curve recorded a rapidly increasing force, demonstrating that resistance employed by the tissue upon MN penetration. In both cases, microparticles loaded (MP-MN) and blank polymeric (MN) arrays showed no significant difference ($p > 0.05$) in the forces required to penetrate the scleral surface. More importantly, the penetration forces recorded were small enough to insert the MN array into the sclera by gentle thumb pressure [63]. Incorporating MP into the MN array has slightly increased the force required for insertion, this could be due to the lower needle strength of MP-MN recorded in the mechanical strength test.

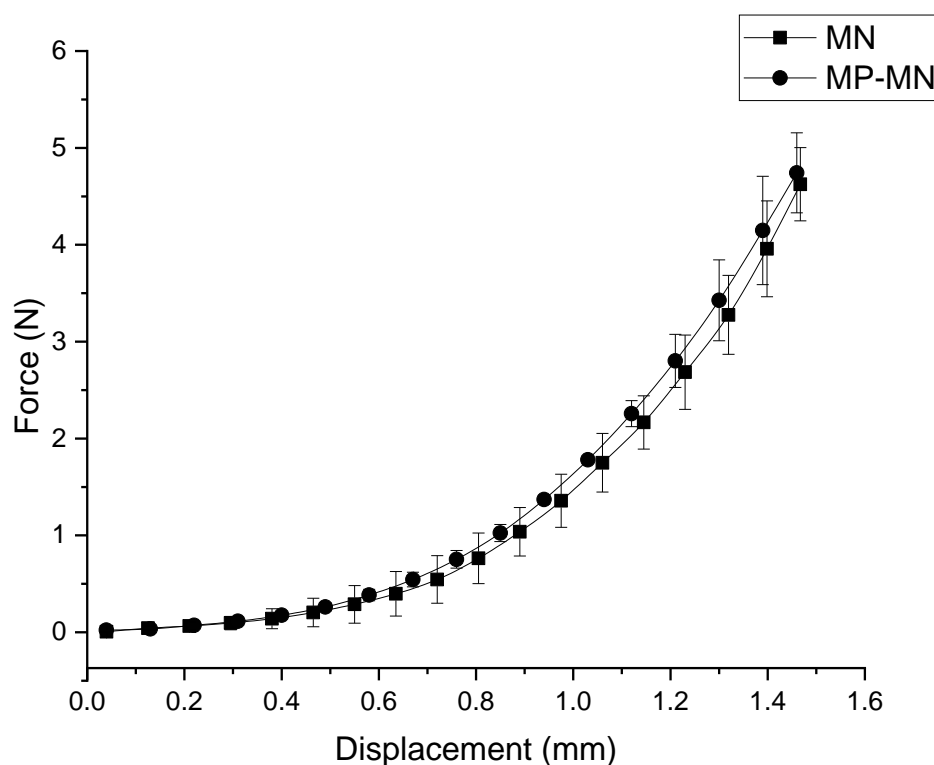


Figure 5-14 *Ex-vivo* scleral insertion test of MN and MP-MN arrays. The data represents mean values \pm SD ($n=3$ arrays).

Table 5-5 Estimation of insertion force into scleral tissue for MN and MP-MN arrays.

MN type	Distance (mm)	Force (N)/ array	Force/ needle
MN	0.760	0.774 \pm 0.241	0.086
MP-MN	0.805	0.782 \pm 0.246	0.087

In the literature, few studies have investigated the penetration force of dissolvable MN arrays into scleral tissue [62, 81, 91]. More studies have reported corneal insertion force [58, 62, 63, 89, 90, 147]. The penetration force is highly influenced by several factors, including the material used, needle geometry, tip size, and tissue type [240]. A similar finding was reported in a study using an 11x11 MN array prepared by PVP K30, a 0.08 N/needle force was recorded for scleral insertion [91]. While another study tested a 3x3 MN array of 800 μ m in height fabricated by PVP K29-32 polymeric base has recorded an insertion force of 0.148 N/ needle on porcine scleral tissue and a threefold higher force of 0.413N/needle for corneal tissue for full MN penetration [62].

5.4.4 Analytical quantification of dexamethasone in ocular tissue

In order to quantify Dex extracted from ocular tissues, the validated HPLC method in Chapter 4, section 4.3.7, was further modified to adapt to the presence of soluble biological components in the sample and the intricate extraction process.

Although the UV detector is the most versatile detector employed in HPLC and is usually preferred due to the linearity and rapid quantitative analysis, the detector lacks specificity, which necessitates a high resolution of the analyte separation [312]. To achieve a good separation quality between the Dex and IS detected peaks, a resolution (R_s) ≥ 2 was considered ideal [313]. The retention time (R_T) of Dex and IS as well as the resultant R_s are displayed in Table 5-6, and the corresponding chromatograms are presented in Figure 5-15. The original method has resulted in a resolution of peak separation of 1.946 (Figure 5-15-a). To improve the resolution, two modifications have

been tested. First, the time of mobile phase gradient change from 70:30 to 30:70 was increased from 12 to 14 min, the change resulted in overlapped peaks (Figure 5-15-b) and thus, lower R_s (1.399) was obtained. Second, the flow rate was decreased from 1 mL/min to 0.9 mL/min. This change has improved the selectivity and R_s of the method to 2.25, as shown in Figure 5-15-c. Consequently, a 0.9 mL/min flow rate was used for the Dex quantification in ocular tissue.

Table 5-6 Effect of HPLC method modification on peaks separation R_s and R_T of Dex and IS.

Modification	Original method	IS R_T	Dex R_T	R_s
Original method	No change	6.828 ± 0.009	7.499 ± 0.008	1.946 ± 0.007
Mobile phase gradient change conducted over 14 min	12 min	5.849 ± 0.018	6.838 ± 0.014	1.399 ± 0.001
Flow rate 0.9 mL/min	Flow rate 1 mL/min	7.143 ± 0.002	7.734 ± 0.001	2.251 ± 0.003

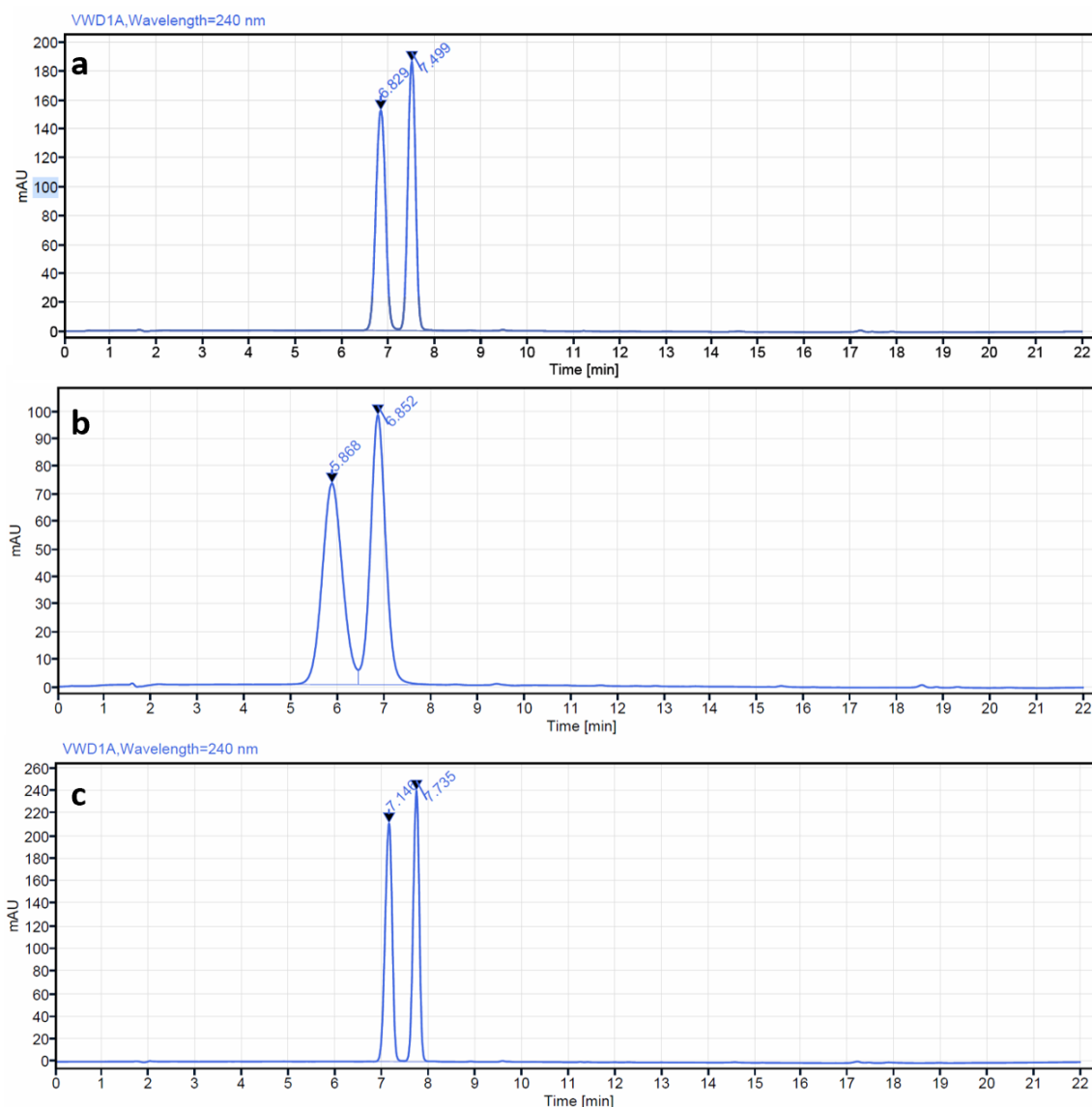


Figure 5-15 Chromatograms of standard Dex solution (100 µg/mL) and IS (100 µg/mL). (a) original developed method, (b) mobile phase gradient change over 14 min, (c) flow rate of 0.9 mL.

System suitability for the modified method was determined by calculating the parameter presented in Table 5-7, reported R_T of both Dex and IS showed that IS eluted before Dex and calculated RSD% values were less than 1%, which lies within the acceptance limit stated by USP43-NF-38 [278]. The tailing factor is close to 1 for Dex and IS peaks showing a high degree of symmetry, and the recorded theoretical plates were high (>2000), indicating good column efficiency.

Table 5-7 System suitability parameters for Dex and IS standard samples.

Analyte	R _T (min)	Theoretical plates (N)	TF	Quantification precision (RSD%)
Dex	7.734 ±0.001	10158.15	0.917	0.163%
IS	7.143 ±0.002	16371.15	0.923	0.349%

The capacity of the method to distinguish between Dex and any soluble components present in the ocular tissue samples was tested by spiking ocular extracted sample with 50 µg/mL Dex and IS with scleral extract in ACN presented in Figure 5-16. It was confirmed that there was no interference peak of any soluble component in the biological sample with Dex and IS peaks. Studying the difference between the spiked biological sample and standard sample by the Student's t-test, showed no significant difference between the area of the Dex/IS peak ratio of the standard and spiked samples and the recovery percentage was adequate (<5%) to accurately determine the Dex concentration in biological samples (Table 5-8).

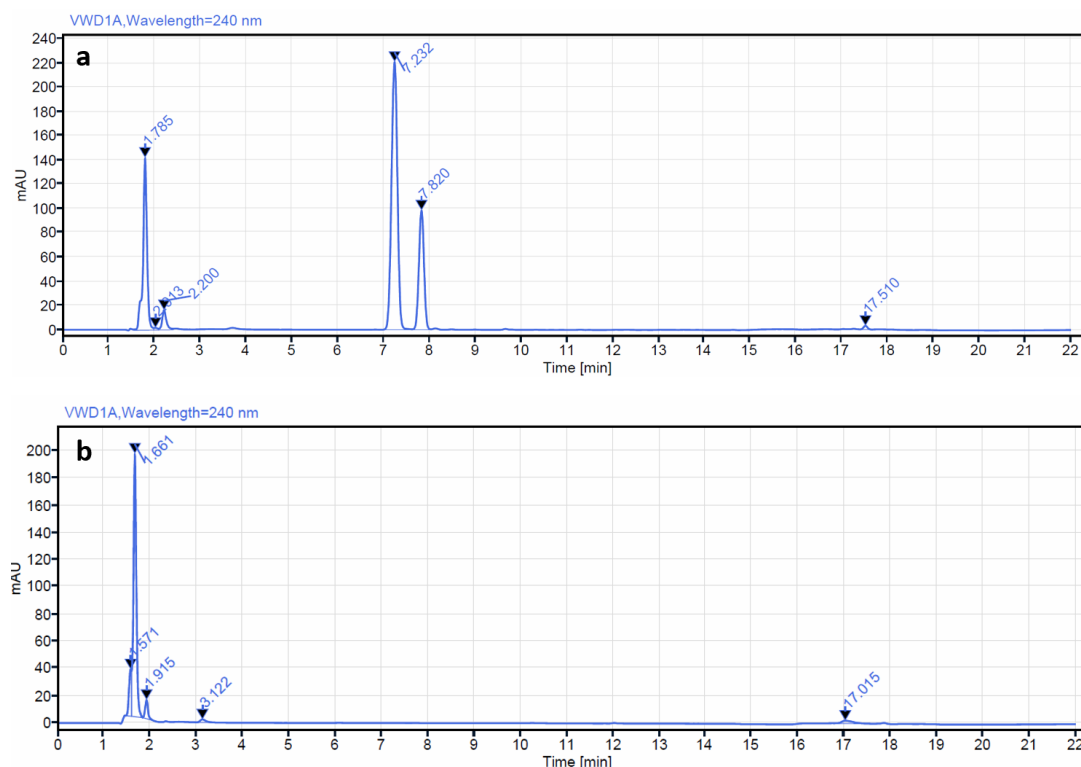


Figure 5-16 Chromatogram of scleral tissue extract. (a) Dex spiked sample (50 µg/mL) of scleral extract, (b) blank scleral extract.

Table 5-8 Statistical calculation of the specificity by a Student's t-test, of the areas of the peaks of standard solution and Dex spiked samples (50 µg/mL) (n=3).

	Peak area ratio	±SD	Mean % recovery
Standard solution sample mean area	0.491	0.019	96.415%
Spiked sample mean area	0.531	0.026	104.346%
Student's t-test (p)*	t=2.177, (0.095)		

*Statistical significant level ($p < 0.05$).

The linearity of the method was tested by analysing a series of Dex concentrations with IS, and a standard calibration curve was constructed by plotting the concentration against the respective ratio of Dex peak area to IS peak area. Serial dilutions ranging from 5 to 150 µg/mL of Dex in ACN with a constant amount of IS (100 µg/mL) were analysed. Three separate sets of calibration were tested. The regression equation and correlation coefficient (R^2) for each set are presented in Table 5-9. The standard calibration curve resulted in a regression equation of $y = 0.0102x + 0.0075$ and $R^2 = 0.9983$ (Figure 5-17).

Table 5-9 Mean ratios of peak area (Dex/IS) of Dex concentration (µg/mL) of three sets (n=3).

Conc. (µg/mL)	Overall		1	2	3
	Mean	SD	Mean	Mean	Mean
5	0.053	0.001	0.054	0.052	0.053
10	0.105	0.006	0.103	0.103	0.101
25	0.257	0.007	0.255	0.254	0.251
50	0.546	0.010	0.541	0.541	0.540
75	0.779	0.011	0.774	0.773	0.773
100	0.982	0.013	0.977	0.977	0.974
150	1.543	0.020	1.537	1.536	1.528
Equation	$y = 0.0102x + 0.0075$		$y = 0.0101x + 0.0066$	$y = 0.0101x + 0.0058$	$y = 0.0101x + 0.0057$
R^2	0.9983		0.9984	0.9984	0.9984

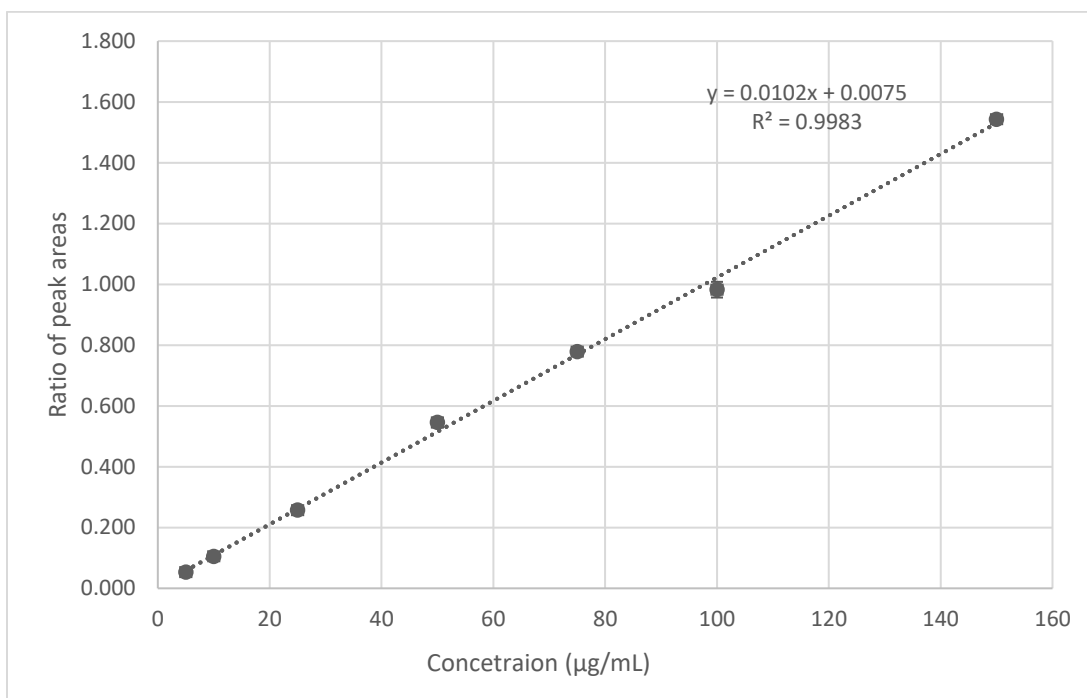


Figure 5-17 Standard calibration curve of Dex/IS in ACN, the regression line equation and the correlation coefficient are shown on the top of the curve (data present mean \pm SD, n=3).

The developed HPLC method was modified to quantify the amount of Dex extracted from biological samples in experiments, including transscleral permeation study and Dex ocular biodistribution.

5.4.5 Dexamethasone transscleral permeation

To determine Dex transscleral permeation, excised porcine sclera was mounted in a Franz cell diffusion chamber. Dex permeation from different dosage forms was studied, namely, Dex suspension, Dex-loaded PLGA microparticles (MP-Dex), and Dex-loaded microparticles incorporated in MN array (Dex-MN). Transscleral Dex permeation profile is presented in Figure 5-18. Dex permeation was significantly higher from the Dex-MN compared to free MP-Dex and Dex suspension. At 4 h post application, 34.93% \pm 2.44 permeated from Dex-MN, 14.89% \pm 4.26 from Dex suspension, and 4.75% \pm 3.45 from MP-Dex. At 24 h, Dex permeation was 45.12% \pm 5.39 from Dex-MN, 25.96% \pm 4.35 from Dex suspension and 9.75% \pm 4.06 from free MP-Dex. This significant difference between

Dex-MN and the other dosage forms could be attributed to the fact that the MN pierces the tissue surface overcoming the scleral barrier. The permeation of Dex suspension was significantly greater than the free MP-Dex, which was predicted. Studies have shown that the sclera provides a posterior drug delivery route for large molecules up to 150 kDa in molecular weight. Dex molecules (MW: 392 Da, molecular radius: 5.2 Å) can pass through the relatively porous scleral membrane more readily [3]. Although the release profile of free MP-Dex has shown initial burst release (reported in Chapter 4, section 4.4.7), in the permeation experiment limited fluid content was added to the surface of the tissue in the donor chamber, which may constrain Dex release from the particles and hence its permeation.

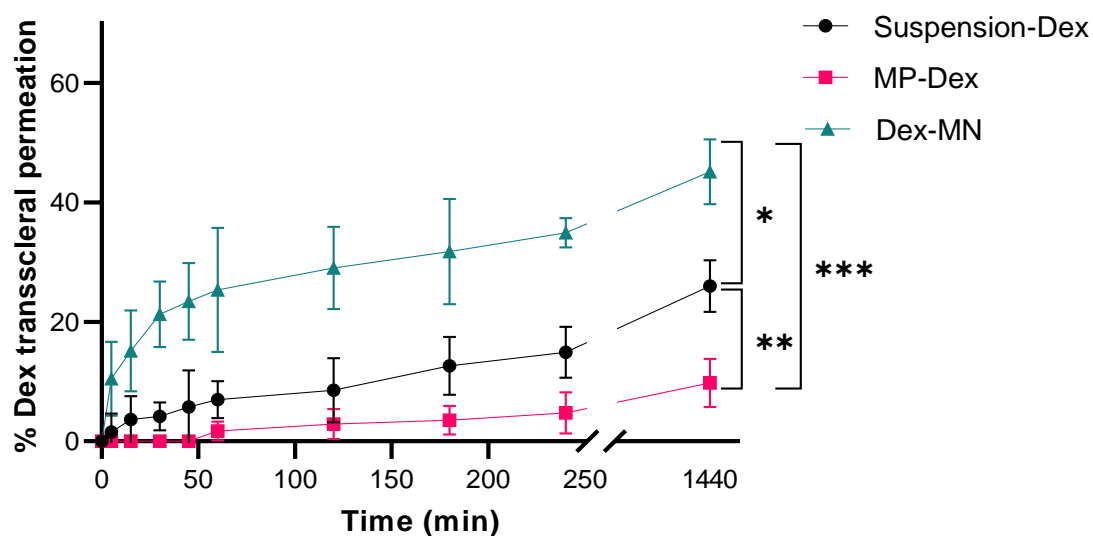


Figure 5-18 *In-vitro* transscleral permeation profile of Dex from Dex suspension, Dex-loaded microparticles (MP-Dex), and MP-Dex incorporated MN array (Dex-MN) (* $p < 0.01$, ** $p < 0.001$, and *** $p < 0.0001$).

At the end of the permeation study, scleral tissue was homogenised, and Dex was extracted by ACN liquid-liquid extraction method then quantified by HPLC analysis. ACN can dissolve free Dex and MP-Dex within the sclera freeing unreleased Dex from the PLGA particles. Figure 5-19 shows the percentage of Dex retained within the sclera. From the displayed data, the amount of Dex detected in the sclera was significantly

higher in the case of Dex-MN ($37.00\% \pm 9.51$) compared to the free MP-Dex ($8.95\% \pm 3.18$) and Dex suspension ($11.19\% \pm 4.05$). This is potentially due to Dex-MN tissue penetration and microparticle dispositioning within scleral tissue opposing the anatomical barriers.

A similar finding was reported with a corneal application of besifloxacin-loaded PVP/PVA dissolvable MN array. The amount of besifloxacin detected in the cornea post MN application was almost fourfold higher than the amount detected after topical solution instillation [58].

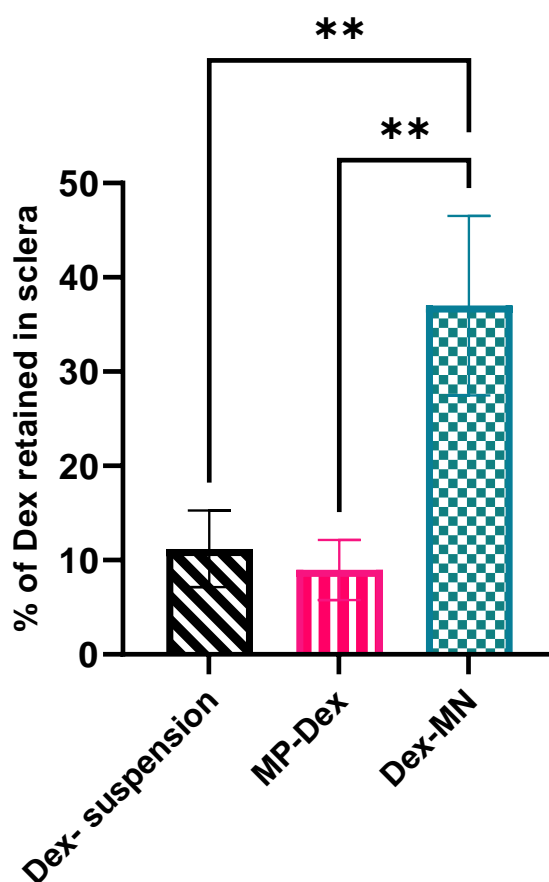


Figure 5-19 Dex retained in sclera post the permeation study. Values are mean \pm SD (** $p < 0.001$).

5.4.6 *Ex-vivo* trans-scleral particles diffusion

To evaluate the particle release and diffusion through porcine scleral tissue, fluorescent labelled microparticles (MP-Flu) and nanoparticles (NP-Flu) were incorporated in P90-2 polymeric base MN array. Porcine eyes exhibit the most suitable model to study ocular diffusion according to studies, as porcine sclera has a high degree of homology with human sclera compared to any other animal model. It shows a resemblance to the human sclera in terms of water content, histological structure, and collagen bundle arrangement [295].

Scleral samples were examined under the microscope to confirm the capability of the MN to pierce the episcleral surface. The crack wound in the tissue was imaged by a light microscope and fluorescence microscope, as shown in Figure 5-20-a, b. The images confirm that the MN has created a crack on the scleral tissue surface and released the MP-Flu around the insertion crack confirming the dissolution of the MN tip.

To evaluate the particle diffusion across the scleral structure, after MP-Flu or NP-Flu incorporated MN array was inserted in scleral samples. The tissue was fixed and frozen to be cryosectioned. The sections were stained with DAPI as shown in Figure 5-20-c, d. In Figure 5-20-c, NP-Flu incorporated MN array showed a high intensity of fluorescent marker at the area of insertion, which indicates that NP-Flu has diffused into the surrounding tissue. Meanwhile, MP-Flu incorporated MN array shown in Figure 5-20-d displays that the MP-Flu has also permeated through scleral tissue. Histological images of scleral sections stained with haematoxylin and eosin (Figure 5-20-e, f) have further confirmed the particle diffusion showing that MP-Flu has diffused laterally within collagen and elastin fibres of the scleral matrix.

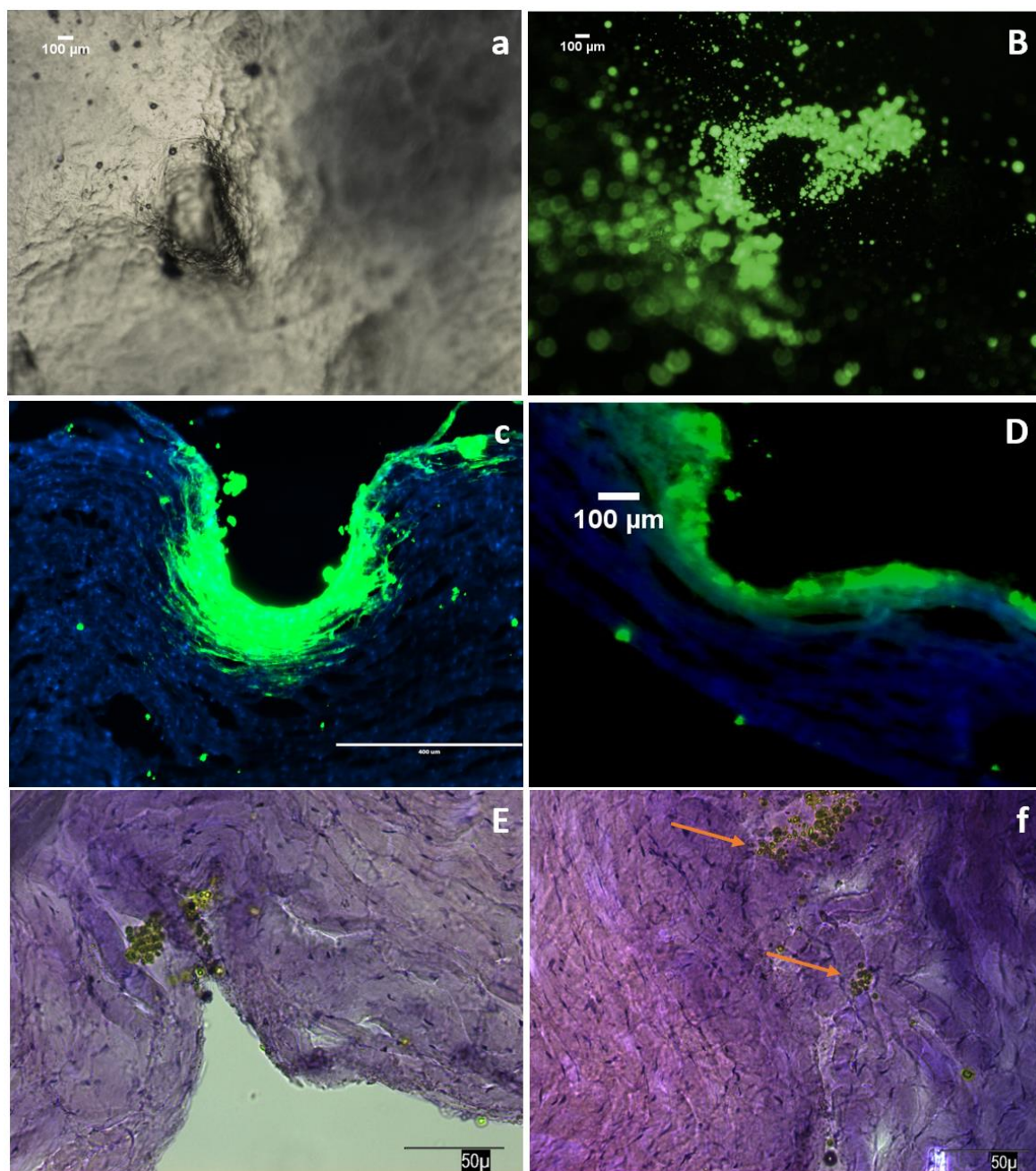


Figure 5-20 Images of *ex-vivo* particle diffusion in scleral tissue (a) light microscope image of MN produced crack wound on the scleral surface, (b) fluorescent microscopy image of MP-Flu release on the scleral surface, (c) fluorescent microscopy image of DAPI stained cross-sectioned sclera post MN array loaded with NP-Flu insertion, (d) MP-Flu insertion, (e) light microscopy image of cross-sectioned haematoxylin and eosin stained sclera post MN array loaded with MP-Flu insertion showing MN-produced crack and MP-Flu dispositioning, (f) MP-Flu detected within the tissue (indicated by orange arrows).

For a better understanding of particle diffusion, scleral samples were sectioned transversely. Fluorescent microscope images of the transverse sections are displayed in Figure 5-21 and Figure 5-22 for MP-Flu and NP-Flu loaded MN arrays, respectively. From the images in both cases, MP-Flu and NP-Flu transverse diffusion into the scleral matrix were observed. Demonstrating the ability of particles, regardless of their size to penetrate the sclera fibrous tissue. However, the magnitude could be different and more work could be conducted to evaluate the particles diffusion in the scleral tissue. Furthermore, a few particles have been detected in deeper scleral layers collected from beneath the MN crack confirming that the particles diffused in transverse and lateral directions.

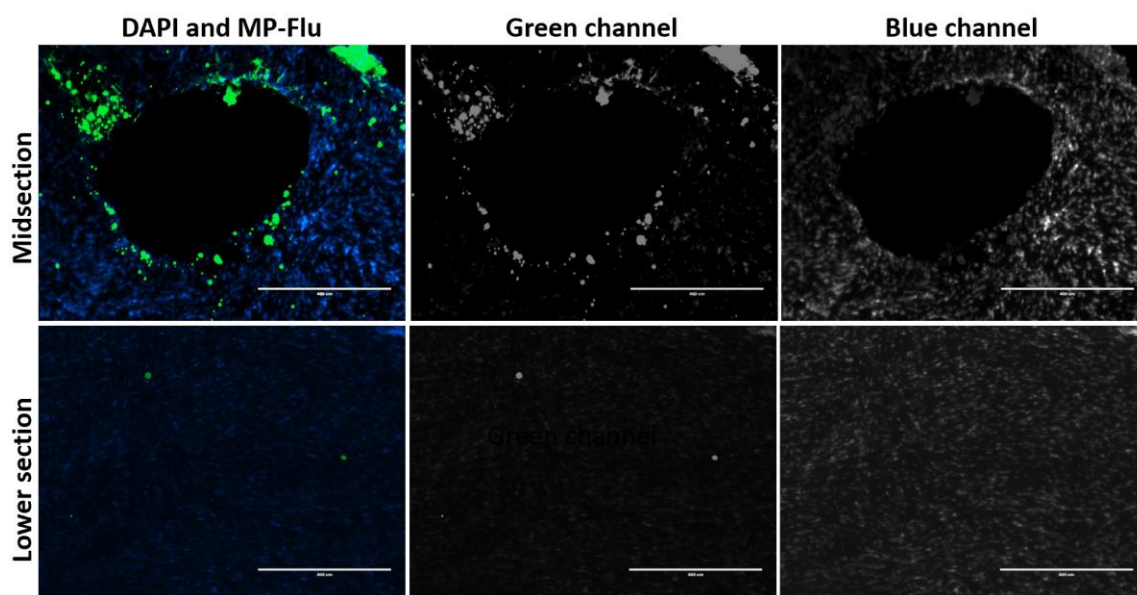


Figure 5-21 Fluorescent microscope images of middle and bottom region transverse sections of *ex-vivo* MP-Flu diffusion study 1 h post insertion. Blue represents nucleus and green represents MP-Flu. The green channel shows MP-Flu and the blue channel shows the tissue nucleus (scale bar=400 μm).

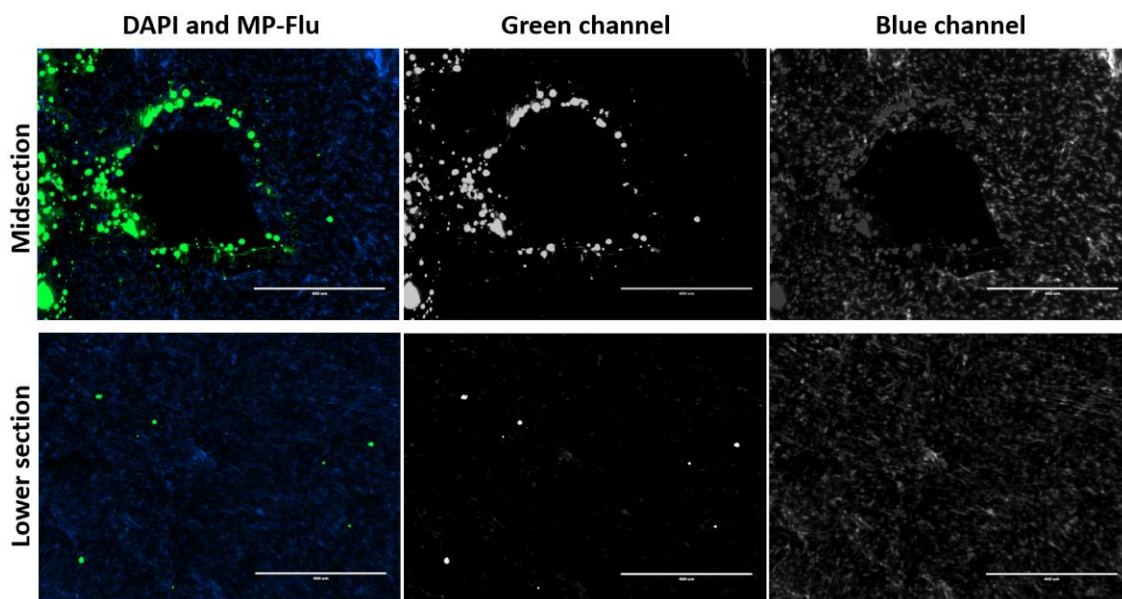


Figure 5-22 Fluorescent microscope images of middle and bottom region transverse sections of *ex-vivo* NP-Flu diffusion study 1 h post insertion. Blue represents nucleus and green represents NP-Flu. Green channel shows MP-Flu and blue channel shows the tissue nucleus (scale bar=400 μm).

The sclera has a porous membrane with water-filled channels between collagen bundles. As a consequence, passive diffusion may be the main method of transport into the sclera, while active transport is unlikely due to the absence of a cellular barrier [314]. Data indicates that smaller particles (<500 nm) can diffuse through scleral channels and suprachoroidal space due to the small spacing between the collagen fibre in the sclera, whereas larger particles (>500nm) flow between the collagen fibre is more constrained due to the scleral sieving effect [77]. A study was conducted to compare the delivery of microparticles and nanoparticles to the suprachoroidal space using a solid, hollow microneedle. The nanoparticles showed a significant transscleral diffusion, whereas the microparticles remained trapped in the suprachoroidal space [77]. There is not enough evidence in the literature to support the hypothesis that microparticles travel across the sclera and reach the retinal layer. However, with restricted particle diffusion into the deeper scleral layer, particle retention and localisation in the scleral matrix can serve as a drug delivery depot where the drug can be released from the particles and permeate through the sclera.

It is worth noting that the scleral matrix is primarily composed of negatively charged collagen bundles, making it more permeable to anionic molecules [18]. In this study, the fabricated MP-Flu and NP-Flu have negative surface charges as reported in Chapter 4, section 4.4.2, which implies that the particles tend to be less aggregated and more flexible to permeate between the collagen bundles. Moreover, the spherical shape of the prepared particles could be adding an advantageous factor to improve particle diffusion. As the shape was also reported to influence the particle's permeability [294]. In the literature, a study was conducted to evaluate the effect of MN shape and surface charge on the transscleral interaction and diffusion. The globular-shaped and negatively charged macromolecules demonstrated high permeability across the sclera compared to positively charged linear or branched macromolecules [295]. Overall, the collected data demonstrated the potential of particle release and localisation within the scleral matrix.

5.4.7 Dexamethasone ocular biodistribution

This study was designed to fully comprehend Dex diffusion across the ocular globe. MN array loaded with MP-Dex or NP-Dex was inserted on the porcine eye globe. The eye was kept hydrated under gentle shaking (50 rpm) at $37^{\circ}\text{C} \pm 0.5$. Dex transscleral diffusion was estimated by quantifying the amount detected in each region. Generally, the eye is divided into posterior and anterior segments. The eye globe in the experiment was segmented into the anterior segment (AS), vitreous humour (VH), MN array insertion site (MN), and the rest of the posterior segment (Sc) as shown in Figure 5-23. The total amount of Dex detected in the eye globe was used as the comparative reference to calculate the percentage detected in each part of the eye. However, if the total percentage of Dex detected in the eye globe was calculated as a percentage based on the estimation of drug loading, the total percentage detected in each eye would be $79.56 \pm 14.3\%$ and $75.61\% \pm 8.64$ for MP-Dex and NP-Dex-loaded MN arrays, respectively.

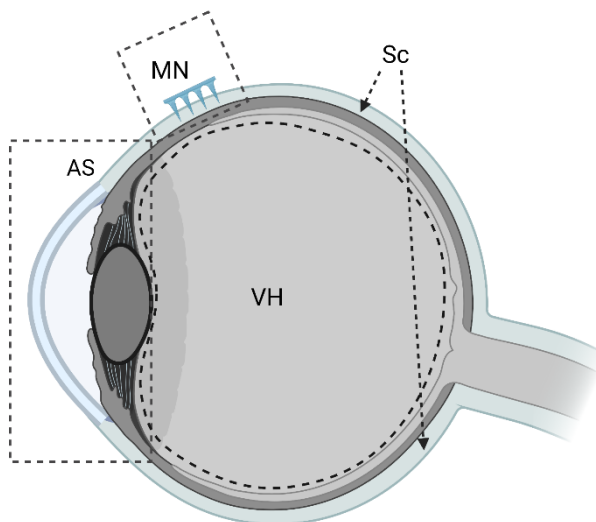


Figure 5-23 Schematic illustration of the segmentation of the eye globe for Dex extraction (created by Biorender).

The percentages of Dex detected in each of the sections of the eye globe post MP-Dex and NP-Dex-loaded MN array application is displayed in Figure 5-24-a. In both cases, Dex percentages were similar in terms of the relative value of distribution. The highest percentage of Dex detected was at the site of the MN insertion, with $42.4\% \pm 4.47$ and $63.33\% \pm 9.43$ for MP-Dex and NP-Dex, respectively, which was expected due to the direct particle's deposition in the scleral matrix. The Dex percentage reported at MN insertion site was a net of the amount of Dex released from the particles and the amount of Dex still encapsulated in the particles and yet to be released.

Currently, the major challenge in treating posterior ocular diseases is delivering an effective dose that overcomes the ocular barrier and reaches the target tissue [3]. This novel drug delivery was able to deliver $19.21\% \pm 11.870$ with MP-Dex and $9.15\% \pm 2.39$ with NP-Dex to VH in 4 h. Moreover, the Dex percentage at the rest of the sclera, the choroid, and the retina (excluding the insertion site) was $25.9\% \pm 12.16$ in MP-Dex and $21.56\% \pm 5.75$ in NP-Dex, which could be attributed to drug and particles diffusion in the transverse direction. The scleral collagen fibres are known to have a lateral orientation that facilitates transverse diffusion [295]. Between these two regions, 30.71% to

38.38% have reached the posterior segment. The lowest amount was detected at AS with 12.48% \pm 3.05 in MP-Dex and 5.94% \pm 2.53 in NP-Dex, which could be diffused through the episcleral surface and moisture surrounding the eye globe.

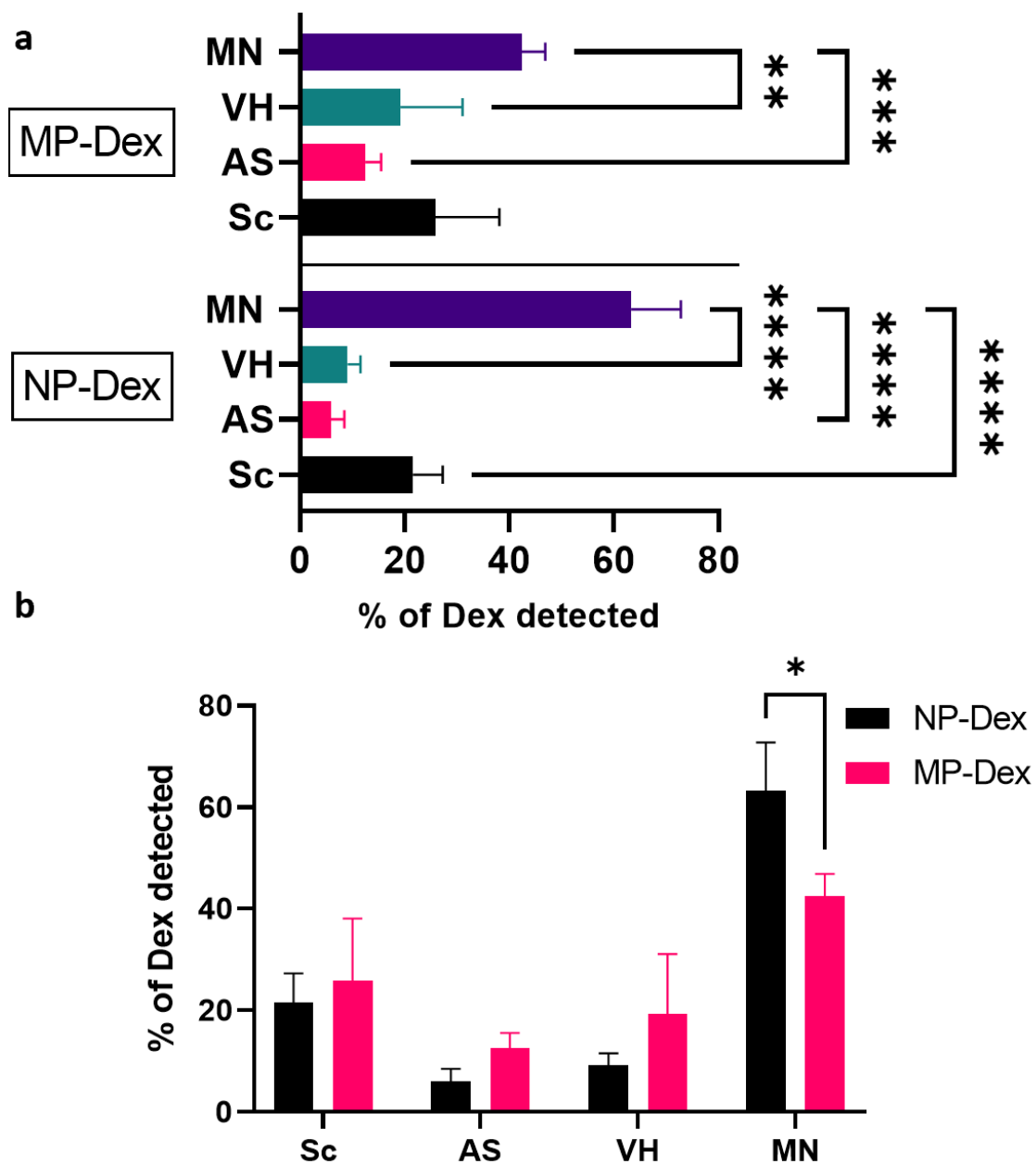


Figure 5-24 Dex ocular diffusion presented as a percentage of Dex detected in each region post MN application (a) MP-Dex-loaded MN array and NP-Dex-loaded MN array, and (b) represent a comparison between MP-Dex and NP-Dex, (Sc= sclera, AS= anterior segment, VH= vitreous humour, MN= MN insertion site). Data presented as mean \pm SD.

To allow comparison between the MP-Dex and NP-Dex and identify the effect of size on the drug distribution, the percentage of Dex detected in each section of the globe is presented in Figure 5-24-b. The percentage of Dex detected in ocular regions was higher in the case of MP-Dex except at the site of MN insertion. This finding confirms the data was reported of Dex *in-vitro* release profile from the free particles in Chapter 4, section 4.4.7. Dex is a small molecule that can diffuse readily through the scleral matrix [3]. On the contrary, particles were mainly condensed at the site of application (MN). Therefore, faster release from the particles results in a greater extent of permeation and this was observed with MP-Dex where the percentage detected in AS, VH, and Sc were greater than NP-Dex. On the other hand, NP-Dex displayed a higher percentage of Dex at MN insertion site and a lower percentage of Dex in the rest of the regions reflecting the sustained release of Dex from NP-Dex.

5.5 Conclusions

In this chapter, the main aim of the study was captured and investigated. PLGA particles incorporated in a dissolvable polymeric MN array were prepared, characterised and their *ex-vivo* performance was studied. Various PVP/PVA blends were tested for dissolution, strength, and adhesion. A ratio of 2:1 PVP K90 to PVA was selected. Micro- and nano- particles were successfully concentrated at the tips of MN array. The MN array displayed sufficient strength to penetrate ocular tissue. Insertion force was determined, and it was found to be small enough to pierce the sclera with gentle thumb pressure.

The validated HPLC method previously mentioned in Chapter 4 was amended to adapt the extraction of Dex from biological tissue and Dex permeation and diffusion across ocular tissue were displayed. Dex has permeated the sclera from MP-Dex incorporated MN array at a higher flux compared to Dex suspension and free MP-Dex. MN array

incorporated with MP-Dex or NP-Dex was able to deliver Dex to the posterior segment with considerably high concentration.

Finally, to exhibit transscleral particle distribution, fluorescent labelled particles (MP-Flu and NP-Flu) incorporated into the MN array were inserted into the excised porcine sclera. Both sizes of the particles demonstrated particle diffusion and localisation, indicating the potential success of the platform to be used to treat posterior segment diseases.

Chapter 6 *In-vivo* studies of dexamethasone-loaded microneedle patches

6.1 Introduction

Following the development and fabrication of the PLGA particles incorporated into the dissolvable MN system, the *in-vitro* and *ex-vivo* performances were studied. The studies showed potential success in localising the particles in the sclera and delivering Dex to the ocular tissue. Consequently, an *in-vivo* study was designed to investigate the irritancy and the therapeutic activity of the Dex-loaded particles incorporated in the MN array in an animal model of endotoxin-induced ocular inflammation.

The eye is a delicate organ, and chemicals and materials may harm the eye in ways ranging from mild discomfort due to irritation or inflammation to more severe tissue damage that can lead to permanent blindness. The application of tough solid material to the eye may cause mechanical injury [315]. To ensure that the hazards connected with the application of the MN system meet appropriate safety standards, eye toxicity testing is necessary.

Dissolvable polymeric MN arrays are widely investigated for transdermal delivery. However, their application in the ocular drug delivery field is relatively new. Until recently, few studies had been conducted to study the *in-vivo* performance of the dissolvable MN system in ocular tissue [63, 316], and no studies had been carried out to assess the irritancy of the dissolving MN system. Therefore, for the MN systems developed here, studying the irritancy effect *in-vivo* is crucial to validate the suitability of the system. Albino rabbits are the standard animal model for the *in-vivo* irritancy study as this is the breed of choice for such a test due to the lack of melanin in ocular tissue, which facilitates the monitoring of the irritation symptoms [227].

Uveitis signifies a diverse disease of ocular inflammatory conditions that involve the uvea [230]. Ocular inflammation, specifically uveitis, is linked to autoimmune diseases, bacterial and viral infections, chemical injuries, and metabolic problems. Currently, the mechanism underlying uveitis is not fully understood. Nonetheless, recent research firmly indicates a link between oxidative stress and inflammation in the pathogenesis of uveitis [230]. Moreover, cellular infiltration appears to contribute to the breakdown

of the blood-aqueous barrier in uveitis, which increases protein permeability, cytokine upregulation, chemokines, and adhesion molecules in the aqueous humour and vitreous regions[231]. Consequently, ocular tissues close to the blood-aqueous barrier are exposed to inflammatory cytokines and chemokines, which can induce a variety of autocrine/paracrine effects [231]. Lipopolysaccharide (LPS) is a component in the outer envelope of gram-negative bacteria. A potent pro-inflammatory endotoxin. LPS is secreted from the surface of gram-negative bacteria that are reproducing and enters the bloodstream [231]. Intravitreal injection of LPS results in inflammation that typically peaks 24 h following the injection [317]. Initially, endotoxin-induced uveitis served as a model for anterior uveitis. Nevertheless, mounting data indicates that it also induces inflammation in the posterior segment of the eye [230].

Dexamethasone (Dex) is a potent immunosuppressant and anti-inflammatory corticosteroid that is commonly used to treat ocular inflammation [318]. In this study, endotoxin-induced uveitis was chosen as a disease model to test the pharmacological efficacy of the developed system.

It should be noted that the *in-vivo* study was performed with an external collaborator in the college of pharmacy at King Saud University in Riyadh, Saudi Arabia, by a research group led by Prof. Aws Alshamsan, including the ocular irritancy test, the *in-vivo* anti-inflammatory assessment, and the histopathological evaluation. The fabrication of the MN array was carried out at the UCL School of Pharmacy. Blank and Dex-loaded PLGA nanoparticles were incorporated in the dissolving MN array and cut out to create a patch. The prepared MN patches were sealed in an airtight container, protected from light, and sent for the *in-vivo* study. The *in-vivo* study was conducted by the external collaborator in the animal house care centre at the college of pharmacy, King Saud University. Data collection was performed by the external collaborator. Analysis and interpretation of the data were performed by Ms Fitaihi.

6.1.1 Aim and objectives

This chapter aims to assess the ocular toxicity of the newly developed MN system in a healthy rabbit model and also to evaluate the *in-vivo* efficacy of the Dex-loaded particles incorporated in MN array in a rabbit model of uveitis.

The objectives of the study are:

- Design and 3D print of a customised master to prepare MN array mould suitable for animal application.
- Prepare a blank and Dex-loaded MN array patch by incorporating blank, and Dex-loaded nanoparticles in the dissolvable polymeric base.
- Test the potential ocular irritancy of the developed MN patches using the Draize irritancy test on albino rabbits.
- Assess the pharmacological activity of Dex-loaded MN patches in an endotoxin-induced uveitis animal model.
- Analysis of the histopathology of the ocular tissue in uveitis animal model with and without Dex MN patch application.

6.1.2 Graphical overview

A summary of the work conducted in this chapter is illustrated in Figure 6-1.

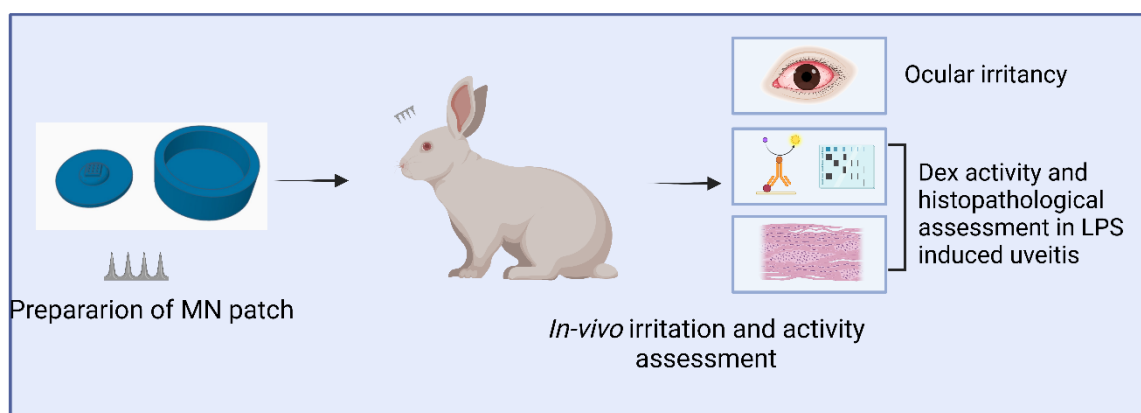


Figure 6-1 Chapter 6 graphical overview (created by Biorender).

6.2 Materials

UV curable liquid resin, Clear[®], purchased from Formlabs[®], USA. Polydimethylsiloxane (PDMS) SYLGARD[®] 184 Silicone Elastomer kit purchased from Dow, USA. PLGA 75:25 grades, Purasorb[®] PDLG 7502 were obtained from Corbion Purac Biomaterials, Netherlands. Dexamethasone, polyvinyl alcohol, isopropyl alcohol and methanol were purchased from Merck Sigma Aldrich, France. Polyvinyl pyrrolidone Kollidon[®] 90 were purchased from BASF, Germany. Poly(methyl methacrylate) and polyvinyl alcohol, natural buffered formalin, and bovine serum albumin, were purchased from Merck Sigma Aldrich, USA.

Normal saline (0.9% NaCl solution) was obtained from Pharmaceutical Solutions Laboratory (Jeddah, Saudi Arabia). Ketamine hydrochloride (TEKAM[®], 50 mg/mL) obtained from Hikma Pharmaceuticals, Jordan. Lipopolysaccharide (LPS) Escherichia coli was purchased from Santa Cruz Biotechnology, Inc., USA. Trans-Blot[®]Turbo[™] Transfer System from BIO-RAD Laboratories, Inc. Singapore. Rabbit Tumor Necrosis Factor Alpha ELISA kit, Rabbit Interleukin 6 receptor ELISA kit, Rabbit Myeloperoxidase ELISA kit, Nuclear Factor KappaB p65 ELISA kit, anti-TNF- α antibody: Hamster TNF- α Monoclonal Antibody, anti-NF κ B p65 antibody, anti-TLR4 antibody, anti-BCL2 antibody, Rabbit anti-Human Bax Antibody, and anti-Caspase3 antibody were purchased from MyBiosource, Inc., USA.

6.3 Methods

6.3.1 Preparation of animal microneedle moulds

To fabricate PLGA particles incorporated in a dissolvable MN patch, a master containing a 5x5 MN array was designed by Fusion 360[™]. The needles were conical in shape with 500 μ m height and 300 μ m base diameter. The array was on a 3.1x3.1 mm and 0.1 mm thick square base, as shown in Figure 6-2-a, b. The square was held on a cylinder 10 mm in diameter to create a depth in the reverse mould for material filling Figure 6-2, d. The cylinder was placed on a 23 mm round disk (Figure 6-2-c) to fit inside a cup with a 25 mm internal diameter. The master was designed to produce a reverse mould that fits inside the centrifugal tube; more details about the mould fabrication were discussed in

Chapter 3. The CAD design of the master was uploaded to the SLA 3D printer (Form 3, Formlabs) and a support structure was added to print the design at 67.5° orientation using Clear resin. The masters were washed in an IPA tub for 30 min then cured by LED light curer (Form Cure, USA). Next, the reverse mould was created by pouring the PDMS solution into the master, then vacuumed for 10 min and cured at 65°C for 4 h (Nuve vacuum oven, EV 018, Turkey).

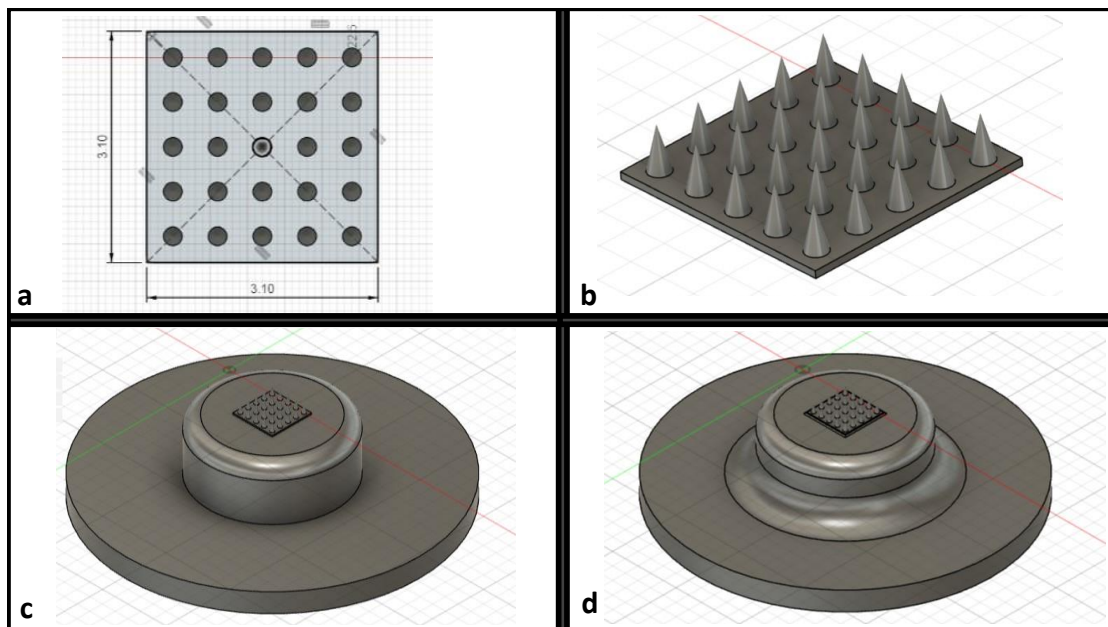


Figure 6-2 CAD design of the master to prepare the mould to fabricate MN patches for animal use, (a) sketch of the MN array, (b) 3D design of the MN array, (c) MN array on cylinder filleted top on 23 mm disk, (d) the final design of the master.

6.3.2 Preparation of microneedle patches

A polymeric mixture of PVP (PVP K90) and PVA in a 2:1 ratio was prepared by dissolving the polymers powder in deionised water to make a 30% (w/v) solution. The polymer and water mixture was heated to 80 °C and continuously mixed with a magnetic stirrer until all the polymers completely dissolved. The polymeric solution was cooled and stored at 4°C until further use. A 10% (w/v) PVP solution was also prepared by the same method PVP/PVA mixture was prepared. Next, Dex-loaded or blank PLGA nanoparticles prepared according to the method mentioned in Chapter 4, section 4.3.1.2, were accurately weighed and mixed with a 10% PVP K30 (w/v) solution. A volume of the

mixture equivalent to 100 µg of the nanoparticles was added to each mould. The moulds were centrifuged at 9000 rpm for 20 mins to concentrate the nanoparticles at the tip of the needles. The mixture was left to dry in the mould under ambient conditions for 24 h. Subsequently, the moulds were refilled with the PVP/PVA mixture solution and then centrifuged for 5 mins to remove any air bubbles trapped in the solution and ensure proper mould filling. Then, the moulds were left to dry for 24 h in a closed container under ambient conditions. The formulations of the patches used in the *in-vivo* study are listed in Table 6-1.

Table 6-1 Formulation of the MN patches prepared for *in-vivo* animal study

Patch code	Nanoparticles type	Nanoparticles formulation code	Polymeric base
Dex-MN	Dex-loaded nanoparticles	NP-Dex	PVP K90/PVA (2:1) 30% (w/v)
Blank-MN	Blank nanoparticles	NP	PVP K90/PVA (2:1) 30% (w/v)

To create patches with a water insoluble backing layer, poly(methyl methacrylate) (PMMA) was dissolved in acetone to make a 10% (w/v) solution. After complete drying of the PVP/PVA solution, 50 µL of a 5% PMMA solution was added by pipette to each mould. The moulds were left to dry for 1 h. After drying, the dried polymeric structure was carefully removed from the moulds and cut by 7 mm punch tool to create the patch.

6.3.3 Animals

New Zealand albino rabbits weighing 1.5-2.0 kg were obtained from the experimental animal house care centre at the college of pharmacy, King Saud University (Riyadh, Saudi Arabia). The protocol for animal use was approved by the Research Ethics Committee (REC) at King Saud University (No. SE-19-90). The rabbits were maintained in accordance with the guidelines for laboratory animal use and care of the association for research in vision and ophthalmology (ARVO). The rabbits were housed in a clean

cage under 12 h of light and dark cycles with free access to food and water. All the rabbits were examined for any pre-existing conditions before any experiment.

6.3.4 Ocular irritancy

The guidelines of the ARVO for animal use in ophthalmic and vision research were followed for the experiments. The right eye of all rabbits was chosen for testing purposes, while the left eye was served as negative control and only treated with 0.9% NaCl. The experiment was performed by following Draize's eye test to assess the potential of the ocular irritation (if any) of the Dex-loaded MN patch (Dex-MN) and the blank MN patch (Blank-MN) [137]. Twelve New Zealand albino rabbits were divided into two groups, each containing six rabbits ($n=6$) for testing the Dex-MN patch (Group I) as compared to the blank-MN patch (Group II). Before insertion, the MN patches were sterilized by UV radiation. The UV sterilization of the patch was performed by exposing the patches to UV light for 2 h at a 254 nm wavelength [319].

The patch of Dex-MN and Blank-MN were inserted into the sclera under the upper eyelid of each rabbit of the two groups. Around 1 h post insertion of the MN array, the treated eyes of the rabbits were observed at different time points for any injury or clinical signs and symptoms of irritation in the cornea, iris, and conjunctiva. Also, at each observation, an image of the eye was taken, and an assessment for scoring the irritation (if any) was performed.

The irritation scoring was performed according to the theoretical scoring and grading systems as shown in Table 6-2, based on the signs and symptoms of eye irritation such as swelling, redness, chemosis, haemorrhage, cloudiness, oedema and/or any abnormal ocular discharge which may occur in the treated eyes [320].

Table 6-2 Grading system for ocular lesion severity in irritation tests [320].

Cornea		
Lesion		Score
A. Opacity-degree of density		
No ulceration or opacity		0
Scattered or diffuse area – details of the iris is clearly visible		1
Easily discernible translucent areas, details of iris slightly obscured		2
Opalescent areas, no details of the iris is visible, size of pupil barely discernible		3
Opaque, iris is invisible		4
B. Area of cornea involved		
One quarter (or less) but not zero		1
Greater than one quarter but less than one half		2
Greater than one half but less than three quarters		3
Greater than three quarters up to the whole area		4
Score equals (A x B x 5):	Total =	80
Iris		
Lesion		Score
A. Values		
Normal		0
Folds above normal, congestion, swelling, circumcorneal injection (one, all of these or combination of any), iris still reacting to light (sluggish reaction is positive)		1
No reaction to light, haemorrhage, gross destruction (one of these or all)		2
Score equals (A x 5):	Total =	10
Conjunctiva		
Lesion		Score
A. Redness (refers to palpebral conjunctiva only)		
Vessels normal		0
Vessels injected above normal		1
More diffuse, deeper crimson red, individual vessels not easily discernible		2
Diffuse beefy red		3
B. Chemosis		
No swelling		0
Any swelling above normal (includes nictitating membrane)		1
Obvious swelling with partial eversion of the lids		2
Swelling with lids about half closed		3
Swelling with lids half closed to completely closed		4

C. Discharge		
No discharge		0
Any amount different from normal (does not include small amount observed in the inner canthus of normal animals)		1
Discharge with moistening of the lids and hairs just adjacent to the lids		2
Discharge with moistening of the lids and considerable area around the eye		3
Score equals (A + B + C) x 2:	Total =	20

The type of irritation was classified as per the Kay and Calandra eye irritation scoring system by calculating the maximum mean total score (MMTS), which is mentioned in Table 6-3 [321].

Table 6-3 Classification of the eye irritation scoring system.

Classification of Irritation	Maximum Mean Total Score (MMTS*)
None	0.0-0.5
Practically none	0.6-2.5
Minimally	2.6-15.0
Mildly	15.1-25.0
Moderately	25.1-50.0
Severely	50.1-80.0
Extremely	80.1-100.0
Maximally	100.1-110.0

6.3.5 *In-vivo* activity of dexamethasone in LPS-induced uveitis

The endotoxin (LPS) from *Escherichia coli* was used to induce uveitis in rabbits. Based on a previously reported dose-response study, 100 ng of LPS was determined as a sufficient dose to induce uveitis in rabbits [322]. LPS was dissolved in sterile water for injection to prepare a concentration of 1 mg/200 mL. The aqueous solution of LPS was injected intravitreally in the right eye of the rabbits, which was considered as the

experimental eye, and the left eye as the control. The rabbits were sedated with intravenous injection (in the ear vein) of ketamine.HCl; 15 mg/kg of body weight. Thereafter, the upper eyelid was retracted, and 100 ng (20 μ L) of LPS solution was injected via the intravitreal route using a 29 G needle attached to a disposable syringe.

Nine rabbits were divided into three groups (3 rabbits in each group). Group-I animals were treated with the Blank-MN patch only and termed as normal control. Only the rabbits of Group-II and Group-III were injected with LPS solution as endotoxin through intravitreal injection, while Group-I animals were left without inducing inflammation. In Group-II, animals were treated with Blank-MN patch, and Group-III animals received Dex-loaded MN patch (Dex-MN). After induction of the experimental uveitis (around 24 h post LPS injection), only one patch of Dex-MN or Blank-MN patch was inserted topically under the upper eyelids of the respective group animals. After applying the MN patch, the eyes were examined for a further 24 h for clinical grading. Thereafter, approximately 100 μ L of aqueous humour (AqH) were collected to determine the cell count, total protein, tumour necrosis factor-alpha (TNF- α), Interleukin 6 (IL-6), myeloperoxidase (MPO), and nuclear factor-kappa B (NF- κ B) DNA bindings [322, 323]. Subsequently, an overdose of ketamine.HCl injection was given to the rabbits and sacrificed. The treated eyes were enucleated immediately for histopathological examinations.

The clinical signs and symptoms for ocular inflammatory conditions were graded on a 0 to 4 scale, as per the described scoring system by Ruiz-Moreno et al. [324]. The grading scale was set as follows: "0 = no inflammatory response observed; 1 = discrete inflammatory response; 2 = moderate inflammatory response; 3 = intense iridial hyperaemia with aqueous flare in the anterior segment; and 4 = the presence of fibrinoid exudation in the pupil with a strong flare in the anterior segment. The grading of clinical signs of uveitis was done at 24 h and 48 h after intravitreal injection of LPS [323, 324].

To estimate the total protein count in AqH samples, 10 μ L of the extracted AqH was diluted to 1 mL with 1N NaOH solution 1N and mixed with 5 mL of copper reagent. Next, 0.5 mL of Folin's reagent was added to the sample and then vortexed, the samples were kept for 30 min in the dark. The sample absorbance was analysed by a UV-spectrophotometer at 450 nm. Bovine Serum Albumin (BSA) was used as a standard protein for the AqH sample protein content calculation [325]. The cell count and protein estimation were performed on the same day as the AqH collection. The levels of TNF- α and IL-6 in the AqH sample were determined by an ELISA kit as per the manufacturer's instructions.

Eye tissues were frozen then homogenised in a 0.5% (w/v) bromide solution, dissolved in a 10 mM potassium phosphate buffer (pH 7), and centrifuged at 6,500 rpm for 30 min at 4°C. The concentration of the protein in the tissue sample was measured by Bradford assay method [326]. 20 μ g of the protein sample was separated by gel electrophoresis (10% w/v polyacrylamide) and used for SDS-PAGE [327]. The western blot assay for Caspase-3, Bax, BCL-2 and β -actin protein expression was performed according to the protocol previously reported by Towbin *et al.* [328-330].

6.3.6 Histopathological evaluation

After the AqH samples were aspirated, the rabbits' eyes were enucleated 48 h post intravitreal injection of LPS. The eyes were fixed in 10% neutral buffered formalin for 24 h before the histopathological examinations. Later, the eyes were embedded in paraffin then sectioned. Sections of the eye tissue 6 to 8 μ m in thickness were cut and stained with haematoxylin and eosin stain. Subsequently, the intensity of oedema, vasodilatation, and inflammatory cell infiltration was next assessed in the structures close to the LPS injection site, including the anterior chamber, posterior chamber, and ciliary body. The histological assessment of the eye structures was conducted using light microscopy. The following scale was used to score the inflammatory alterations brought on by lymphocyte, polymorph-nuclear leukocyte, and macrophage infiltrates in the ocular tissue: no inflammation is represented by a score of 0, mild inflammation

by a score of 1, distinct inflammation by a score of 2, moderate inflammation by a score of 3, severe inflammation by a score of 4, and intense inflammation by a score of 5 [38, 137].

6.3.7 Statistical analysis

The data are presented as mean \pm SD. The differences between the mean values were compared by one-way ANOVA followed by Tukey's multiple comparison tests. *P*-value <0.05 was considered statistically significant. All statistical analyses were performed using Prism software (GraphPad La Jolla, California).

6.4 Results

6.4.1 Preparation of microneedle patch

To prepare a customised MN patch for rabbit use, a 3D model was designed to fit the rabbit eye, and a 5x5 array was selected to increase the loading capacity. Thereafter, a 3D printed master and the reverse PDMS mould were created, as shown in Figure 6-3. The rabbit sclera is less than 200 μ m in thickness [331], and it is well known that smaller particles are better tolerated *in-vivo* than larger particles [18]. Therefore, PLGA nanoparticles were selected for the *in-vivo* studies. The moulds were filled with PLGA particles (NP or Dex-NP) and PVP/PVA polymeric solution. After drying, the polymeric structure was gently removed, as shown in Figure 6-4-a. Then, the excess dry polymer was cut with a 7mm metal punch tool to create the MN patches, as shown in Figure 6-4-b, c.

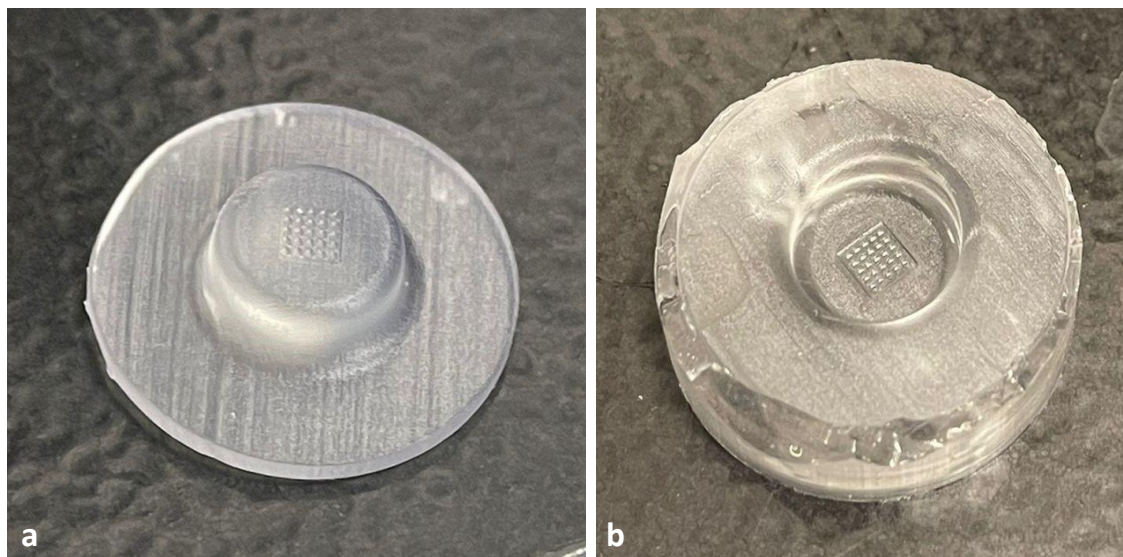


Figure 6-3 Digital images of moulds prepared for *in-vivo* animal studies (a) 3D printed master (base 23 mm in diameter) (b) PDMS reverse mould (23 mm in diameter).

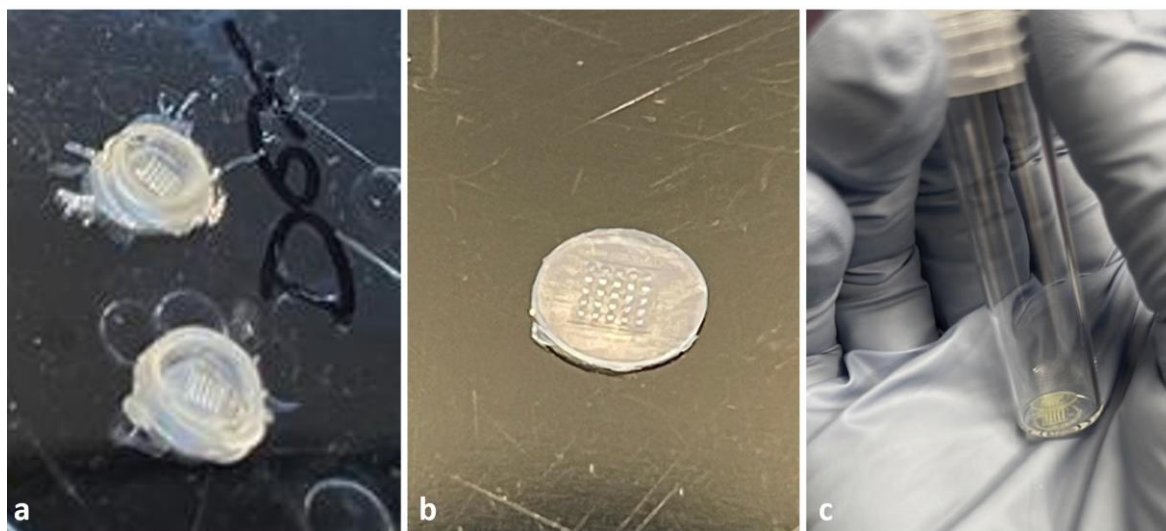


Figure 6-4 Preparation of customised animal MN patch (a) the dried polymeric base containing nanoparticles in the MN removed from the moulds, (b) a 5x5 MN patch prepared by punch tool (7 mm in diameter), (c) MN patches in a glass container.

At the preliminary stage, the MN patches composed mainly of PVP/PVA blend were prepared without the insoluble PMMA backing layer. The patch got dissolved within 15 minutes and could not retain its shape, as shown in Figure 6-5. The remaining parts of

the patch on the ocular surface were found to be sticky and dislocated from the insertion site as it moved on the ocular surface with eyelid blinking movement.

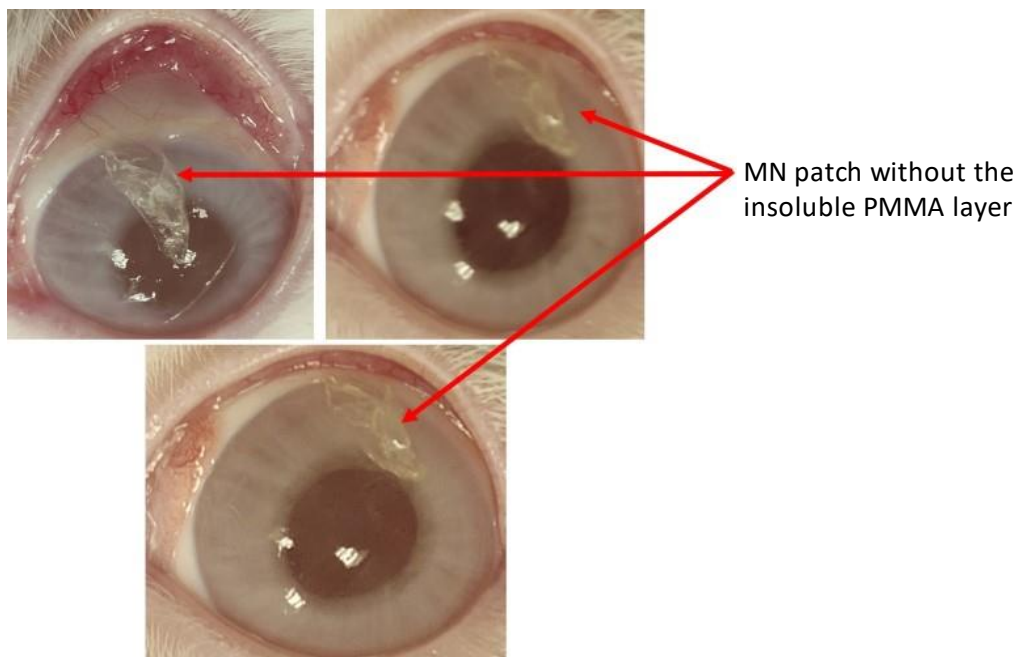


Figure 6-5 The remaining portion of the MN patches without an insoluble PMMA backing layer on the rabbit ocular surface.

Subsequently, an insoluble outer layer was added to the back of the patch to prevent unspecific adhesion to the eyelid and to maintain the patch at the site of application to enhance residence time and enable particles diffusion. PMMA has been used for decades in the fabrication of intraocular lenses [141]. PMMA is a thermoplastic biocompatible polymer with strong mechanical strength, it is an FDA approved polymer for ocular use. When processed, the polymer maintains the shape of the prepared product [332]. Therefore, MN patches with the insoluble PMMA backing layer were prepared. The patch retained its shape after application and was found to have good surface adhesion and resisted the movement from the inserted area for up to 2 h after application, as shown in Figure 6-6.

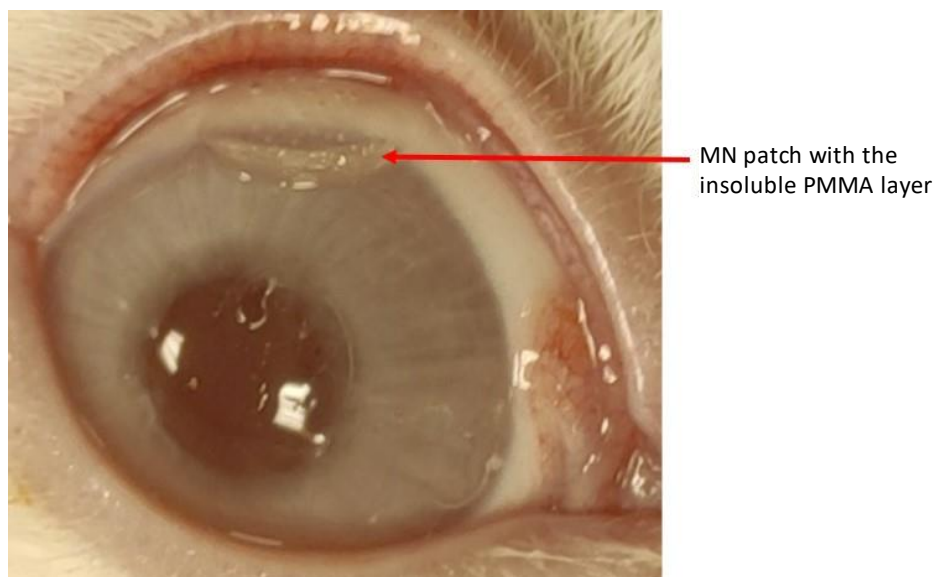


Figure 6-6 The MN patch remaining with an insoluble PMMA backing layer maintained the shape and integrity of the patch 2 h after application. The MN are visible under the patch.

6.4.2 Ocular irritation

By following Draize's test protocol, the eye irritation potential of the developed Dex-MN patch compared to the Blank-MN patch was investigated for 24 h [225]. The observations were noted after the insertion of the Dex-MN into the right eyes of Group-I rabbits in parallel to the Blank-MN patch in Group-II. The changes in the cornea, iris and conjunctiva of the treated eyes were visually observed and assessed [333]. The obtained scores and signs of discomfort during the irritation experiment for the tested MN patches are shown in Table 6-4.

Table 6-4 Weighted scores for the eye irritation test of the Dex-MN patch and Blank-MN patch.

Lesions in the treated eyes	Individual scores for eye irritation											
	Dex-MN patch (Group-I)						Blank-MN patch (Group-II)					
	Rabbit numbers						Rabbit numbers					
	1 st	2 nd	3 rd	4 th	5 th	6 th	1 st	2 nd	3 rd	4 th	5 th	6 th
Cornea												
A. Opacity (degree of density)	1	0	0	0	0	0	0	0	0	1	0	1
B. Area of cornea	4	4	4	4	4	4	4	4	4	4	4	4
Total score= (A x B x 5)=	20	0	0	0	0	0	0	0	0	20	0	20
Iris												
A. Lesion values	1	0	0	0	0	0	0	0	0	1	0	1
Total score= (A x 5)=	5	0	0	0	0	0	0	0	0	5	0	5
Conjunctiva												
A. Redness	1	0	0	0	0	1	0	0	0	1	0	1
B. Chemosis	0	0	0	0	0	0	0	0	0	0	0	0
C. Mucoidal discharge	0	0	0	0	1	0	0	1	0	1	0	1
Total score= (A + B + C) x2=	2	0	0	0	2	2	0	2	0	4	0	4

Neither the Blank-MN patches nor the Dex-MN patches caused any clear sign or indication of discomfort in the rabbits upon the application of the patches during the irritation experiment. The representative images of the rabbit eyes at the time of the patch insertion (i.e. at 0 h) are shown in Figure 6-7. The eyes treated with 0.9% NaCl (control) are shown in Figure 6-7-a, whereas the MN patch treated eye is shown in Figure 6-7-b.

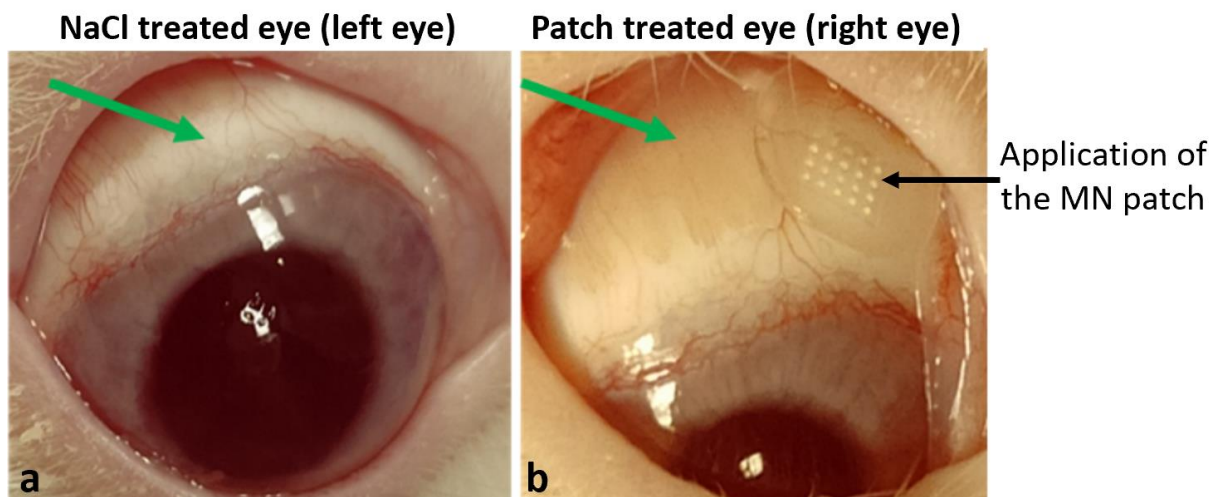


Figure 6-7 Images of rabbit eye (a) NaCl treated eyes, (b) MN patch treated eye, at the time of the patch insertion (0 h). Green arrows indicate the normal features of the eye.

Figure 6-8 displays the ocular irritation reaction over 6 h post application, with mild redness of the conjunctiva and no inflammation or abnormal discharge observed 1 h post the insertion of the Blank-MN and the Dex-MN patches. Among the six rabbits of Group-II, two have shown mild abnormal discharge at 3 h, and in the Dex-MN patch treated group one rabbit has shown mild watery discharge at 3 h. The abnormal discharge from the Blank-MN treated eyes might occur due to the ocular surface abrasion caused by the polymeric MN, which activates natural physiological responses i.e. secretions to overcome episcleral disruption [226]. In the Dex-MN treated group, only mild watery discharge (not mucoidal) in one animal was recorded. The surface abrasion has also occurred in Dex-MN treated animals, but due to the anti-inflammatory effect of Dex released from the PLGA nanoparticles, the irritation has been restored to normal by suppressing the immunological responses [334].

Redness and slight inflammation were observed in both the Blank-MN and Dex-MN patch treated eyes (Figure 6-8). The symptom persisted for 6 h with the Blank-MN treated eyes then the intensity of the irritation declined. Whereas in Dex-MN treated eyes, the redness has disappeared, and no sign of inflammation was observed at 6 h,

as shown in Figure 6-8 (signified by the green arrow). All signs of the inflammation have subsided 12 h post the insertion of both Blank-MN and Dex-MN, as shown in the figure, and the treated eyes have completely returned to their normal conditions at 24 h.

The recovery from the irritation symptoms could be attributed to the natural defensive mechanism of the eye in the treated animals [30]. In addition, all the polymers used in the fabrication of the MN patches, including the PLGA nanoparticles have recognised good biocompatibility and safety profiles [114, 335]. In fact, both PVP and PVA exhibit several advantageous ocular effects [305]. PVP has been widely used to treat dry eye syndrome by relieving conjunctival vascular congestion. PVP is a polar dipole molecule that enhances the interaction with the ocular surface mucin by hydrogen or electrostatic bonds. The high polarity and dipole enable the interaction with water molecules that helps maintain a stable tear film by bonding to mucin on one side and water from the other side [336]. Along with PVP, PVA has been used as an ocular lubricant and in artificial tears formulation due to the wettability effect and the surfactant properties that stabilise the tear film for a long time [335].

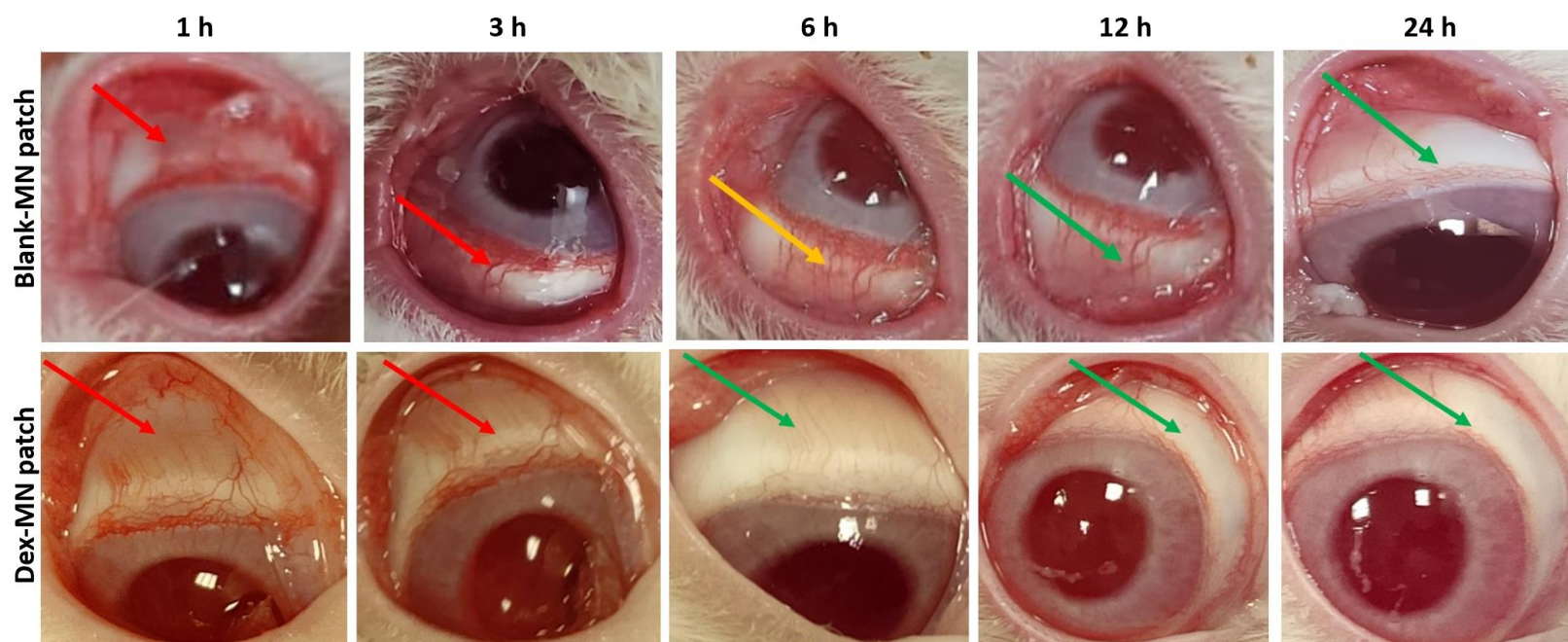


Figure 6-8 Images taken during irritation study on albino rabbit eyes. Post insertion of Blank-MN and Dex-MN patches over 24 h. Red arrows indicate visible signs of inflammation, orange arrow indicates mild signs, and green arrows indicate the normal features of the eye.

By considering the recorded ocular irritation scored according to the Draize scale for eye lesion scoring (Table 6-4), MMTS was calculated according to the descriptive Kay and Calandra eye irritation scoring system [321]. The calculated MMTS during visual observation after 24 h of insertion is displayed in Table 6-5. The MMTS of the Blank-MN patch was 9.998, and that for the Dex-MN patch was 5.166 (i.e., > 2.6 but < 15). Thus, both the Blank-MN and the Dex-MN patches were considered “minimally irritating” to the rabbit eyes in this study. The comparatively lower MMTS for the Dex-MN suggests some benefits of Dex-loaded nanoparticles over the blank nanoparticles.

Table 6-5 Calculation of MMTS for the Blank-MN and Dex-MN patches according to the scores mentioned in Table 6-4.

Dex-MN patch								
Animal number	1st	2nd	3rd	4th	5th	6th	SUM	Average
Cornea	20	0	0	0	0	0	20	3.333
Iris	5	0	0	0	0	0	5	0.833
Conjunctiva	2	0	0	0	2	2	6	1.000
SUM =	27	0	0	0	2	2	31	5.166
Blank-MN patch								
Animal number	1st	2nd	3rd	4th	5th	6th	SUM	Average
Cornea	0	0	0	20	0	20	40	6.666
Iris	0	0	0	5	0	5	10	1.666
Conjunctiva	0	2	0	4	0	4	10	1.666
SUM =	0	2	0	29	0	29	60	9.998

All the rabbits used in this experiment remained active and healthy with no abnormal signs of toxicity during the study, except those as mentioned and scored in Table 6-4. Additionally, no eye irritation was noted due to mechanical injury by the patches or due to any corneal abrasion/scar development during the insertion of the patches.

6.4.3 *In-vivo* activity of dexamethasone in LPS-induced uveitis

In order to assess the *in-vivo* activity of Dex-MN, an endotoxin-induced uveitis rabbit model was used. Nine rabbits were divided into three groups. Group-I animals were treated with the Blank-MN patch only and termed as normal control (NC). Uveitis was only induced in Group-II and Group-III. Group-II animals were treated with a Blank-MN patch, and Group-III animals received Dex-MN. Figure 6-9-a displays the clinical score in all the cases. In Group-I the normal control, the clinical score was 0 since no inflammation was induced. Whereas in Group-II, LPS intravitreal injection induced uveitis led to a significant ($p < 0.05$) increase in the inflammation clinical stage score from 0 to 2.66 ± 0.053 . However, the treatment with Dex-MN in LPS-induced uveitis led to a significantly ($p < 0.05$) reduced clinical stage score from 2.66 ± 0.053 to 1.83 ± 0.083 over the next 24 h after the patch application.

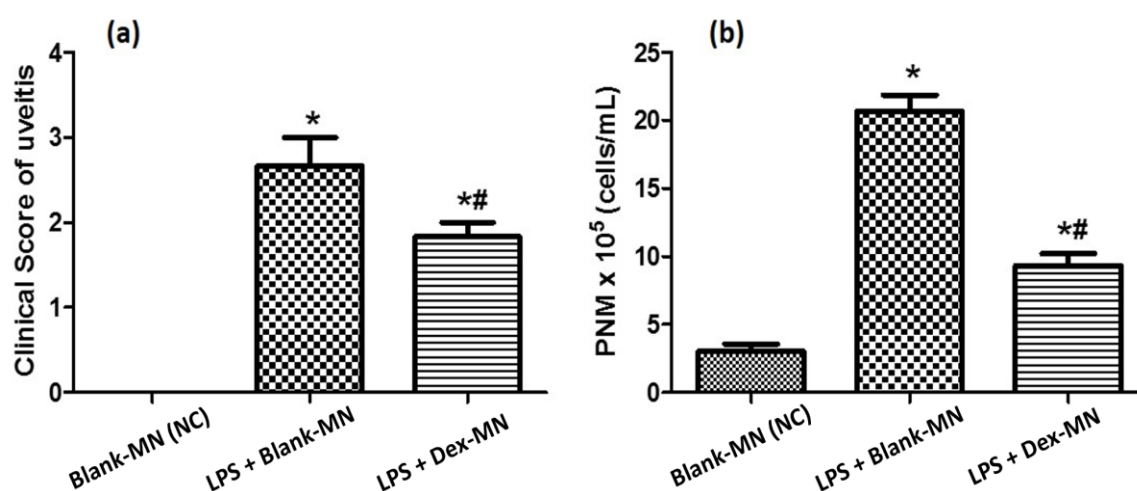


Figure 6-9 The effect of Dex-MN on LPS-induced uveitis. (a) clinical scores of LPS-induced uveitis in rabbit eyes (b) polymorphonuclear infiltration cytology in AqH samples. All values represent mean \pm SD of three animals per group * $p < 0.05$ (Blank-MN); # $p < 0.05$ (LPS + Blank-MN).

In addition to the previous finding, assessing the rabbit, AqH sample cytology revealed that Group-I had a low number of polymorphonuclear (PMN) cellular infiltration in

AqH with only $3 \times 10^5 \pm 0.44 \times 10^5$ cells/mL. While the number has significantly increased in Group-II to $20.66 \times 10^5 \pm 0.93 \times 10^5$ cells/mL. Treatment with Dex-MN in Group-III significantly ($p < 0.05$) reduced the PMN cellular infiltration indicating amelioration of LPS-induced uveitis as compared to Group-II (Figure 6-9-b).

In Group-II, rabbits exhibit macroscopic signs of inflammation, such as redness of the conjunctiva and swelling of the eyes. The AqH samples of Group-II showed a significant ($p < 0.05$) increase in the pro-inflammatory cytokines, including TNF- α , IL-6 and MPO. The induction of inflammatory mediator-encoding genes by stimulation and localisation of monocytes and macrophages results in the subsequent infiltration of neutrophils and mononuclear cells and, thus, upregulation of the inflammatory markers [230]. As shown in Figure 6-10, a-c, Group-II recorded 67.56 ± 3.73 pg/mL, 322.87 ± 14.70 pg/mL and 1.51 ± 0.06 ng/mL for TNF- α , IL-6, and MPO, respectively, indicating high expression of pro-inflammatory cytokines due to untreated uveitis. Whereas Group-I displayed 21.39 ± 1.20 pg/mL, 120.45 ± 3.74 pg/mL and 0.53 ± 0.05 ng/mL for the same markers in the normal control group, which are normal values in healthy animals [330].

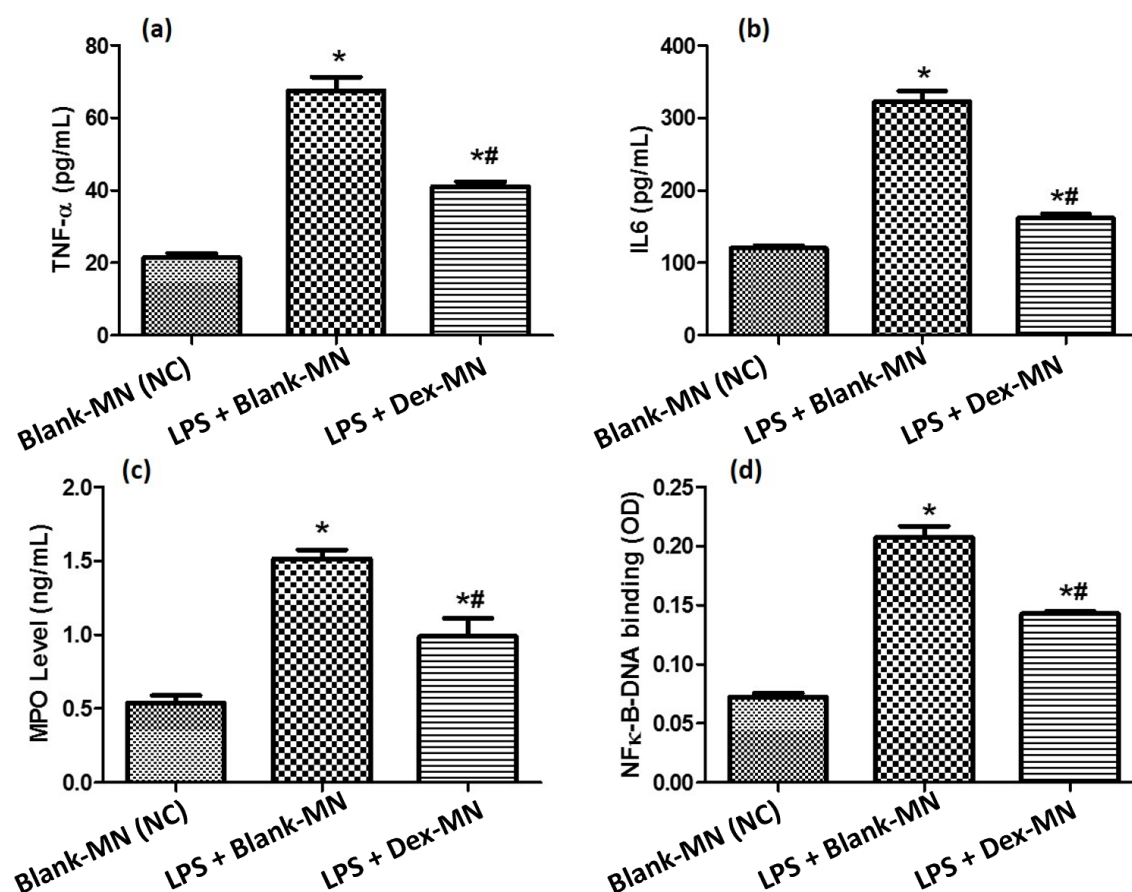


Figure 6-10 Effect of Dex-MN on LPS-induced uveitis on inflammatory cytokines (a) TNF- α , (b) IL-6, (c) pro-inflammatory marker MPO, and (d) NF- κ B DNA-binding. All values represent mean \pm SD of three animals per group * $p < 0.05$ (Blank-MN); # $p < 0.05$ (LPS + Blank-MN).

Treatment with Dex-MN in Group III has significantly ($p < 0.05$) reduced the inflammatory cytokines and markers (TNF- α , IL-6, and MPO) as demonstrated by the results of LPS + Dex-MN (Figure 6-10, a-c). The values were reduced to 41.10 ± 1.36 pg/mL, 161.76 ± 6.10 pg/mL and 0.98 ± 0.12 ng/mL for TNF- α , IL-6 and MPO, respectively. The results of AqH screening demonstrate the potent anti-inflammatory effect of Dex-MN on uveitis-induced inflammation.

The increases in PMN infiltration, total protein concentration, and inflammatory cytokines and inflammatory markers (MPO) have been reported in LPS-induced

uveitis [317]. Several pro-inflammatory cytokines and inflammatory markers (TNF- α , IL-6 and MPO) are involved in the pathogenesis of uveitis, with AqH levels positively correlating with disease severity [323, 337-339]. In the present study, there were approximately 68.33%, 62.69% and 64.41% increases in the levels of TNF- α , IL-6 and MPO, respectively, in the AqH of all treated rabbits by LPS + Blank-MN (Group-II) as compared to those measured in the normal control (Group-I). These results are in corroboration of the previously reported findings [137, 330, 340, 341]. However, LPS-induced uveitis treated with Dex-MN suppressed the upregulated levels of TNF α , IL-6 and MPO by 39.16%, 49.86% and 34.71%, respectively, as compared to LPS + Blank-MN. The reduction in the levels of inflammatory cytokines and biomarkers has shown that Dex-MN has a potent anti-inflammatory effect.

In inflammatory responses, the increased production of cytokines and chemokines is linked to NF- κ B activation. Different intracellular signalling cascades that are triggered by inflammation result in both changes in gene expression and severe physiological impacts. Therefore, understanding NF- κ B signalling is essential for understanding inflammation [342]. LPS intravitreal injection increased the NF- κ B DNA binding activity due to the translocation of NF- κ B from the cytoplasm to the nucleus [343]. The results of AqH obtained from Group-II (LPS + Blank-MN) demonstrate an increase in NF- κ B DNA binding activity from 0.072 ± 0.0006 to 0.20 ± 0.002 as compared to the normal control group (Group-I). Treatment with Dex-MN in Group-III uveitis significantly ($p < 0.05$) downregulated the NF- κ B DNA binding activity, a further sign in the improvement of uveitis (Figure 6-10-d).

The downregulation of uveal pro-apoptotic and upregulation of anti-apoptotic protein expression activities by Dex-MN in LPS-induced uveitis rabbits are represented in Figure 6-11, a-e.

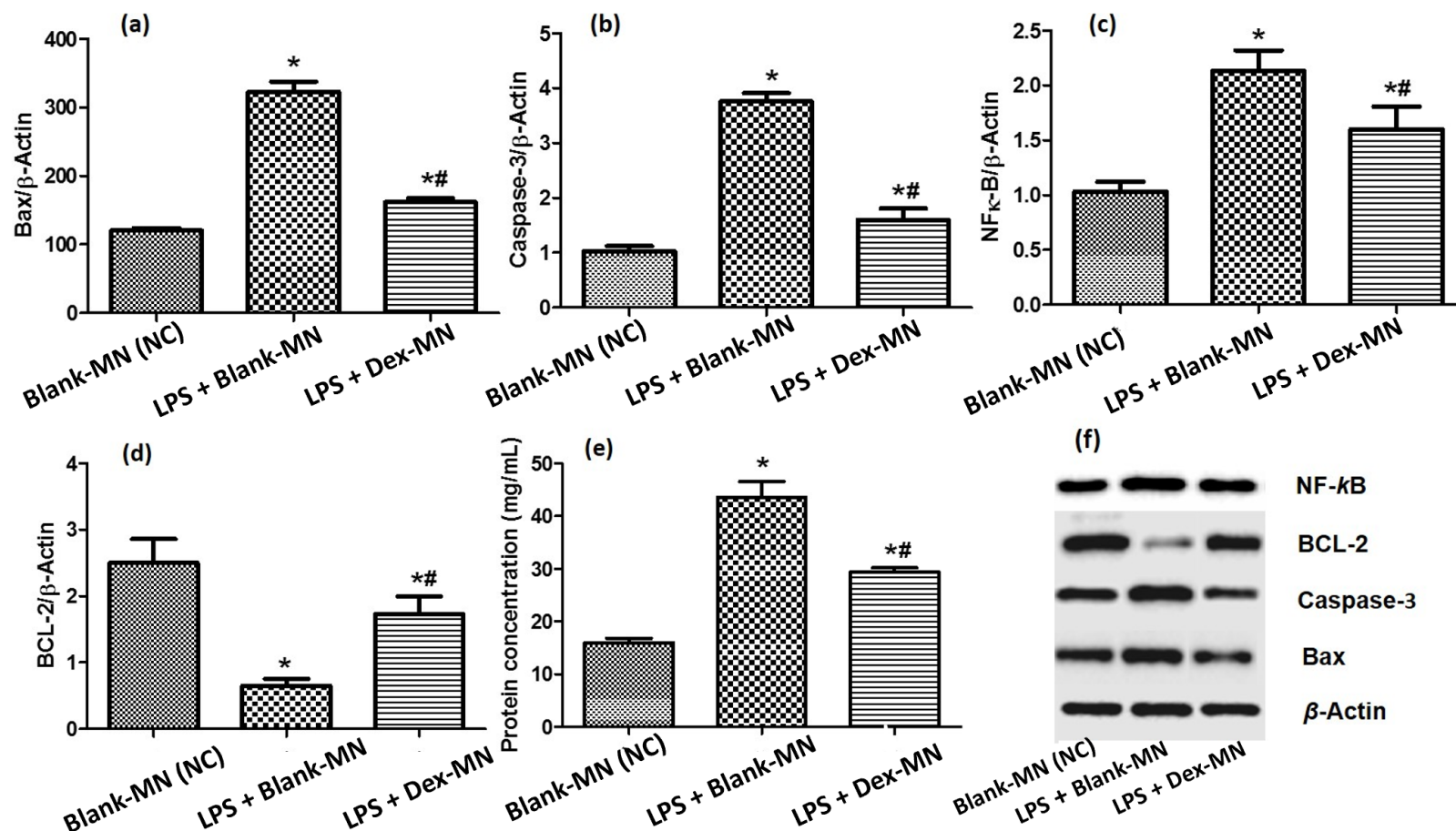


Figure 6-11 Effect of Dex-MN on LPS- induced uveitis on apoptotic markers in ocular tissues of rabbit. (a) the protein expression of Bax, (b) Caspase-3, (c) NF- κ B phosphorylation proteins, (d) BCL-2 β -actin, and (e) protein levels in AqH, and (f) western blot of all proteins. All values represent mean \pm SD of three animals per group * $p < 0.05$ (Blank-MN); # $p < 0.05$ (LPS + Blank-MN).

In Group-II, LPS significantly ($p < 0.05$) upregulated the expression of Bax gene, Caspase-3 and NF- κ B phosphorylation proteins and significantly ($p < 0.05$) downregulated BCL-2 protein expression compared to their expression in the normal control (Blank-MN). The treatment with Dex-MN in LPS induced uveitis rabbits significantly ($p < 0.05$) downregulated the expression of Bax, Caspase-3 and NF- κ B phosphorylation proteins and upregulated the expression of the BCL-2 protein level as compared to LPS + Blank-MN (Figure 6-11, a-d). The total proteins levels significantly ($p < 0.05$) upregulated in LPS + Blank-MN is 43.56 ± 2.33 mg/mL as compared to normal control (Blank-MN), which is 15.92 ± 0.69 mg/mL; however, Dex-MN in LPS-induced uveitis rabbits significantly ($p < 0.05$) reduced the level of total proteins in LPS + Dex-MN to 29.35 ± 1.05 mg/mL that is a sign of improvement in LPS-induced uveitis (Figure 6-11-e).

The expression of different apoptosis mediators, including Bax, BCL-2, and Caspase-3, in the ocular tissues, was assessed using immunoblot. Protein bands corresponding to antibodies were identified in the ocular tissues of healthy rabbits as well as all rabbits from all treated groups are presented in Figure 6-11,f.

Densitometry analysis showed that Bax, Caspase-3, and NF- κ B phosphorylation proteins levels were significantly ($p < 0.05$) increased, while the expression of BCL2 was considerably decreased in LPS-induced uveitis group (LPS + Blank-MN) as compared to normal control. Group-III treated with Dex-MN demonstrated significant ($p < 0.05$) downregulation of Caspase-3, and Bax levels while upregulation of BCL-2, indicating the inhibition of apoptotic injuries to uveal and ciliary bodies. Moreover, the treatment with Dex-MN inhibited nuclear phosphorylation, which reduced the activity of DNA binding due to the translocation of NF- κ B DNA binding activity from the cytoplasm to the nucleus. These results demonstrate that Dex-MN has the ability to inhibit apoptotic injuries in rabbit eyes. The results are consistent with previous reports in the literature [137, 330, 340, 341].

In this *in-vivo* pharmacological activity study, the data demonstrated a significant ($p < 0.05$) upregulation of activated NF- κ B in the AqH during the ocular inflammation that occurred in LPS-induced uveitis. Inhibition of this *in-vivo* activation by Dex improves the clinical signs of uveitis. These results are entirely consistent with the suggestion that the activation of NF- κ B is a critical participation in the pathogenesis of uveitis [342]. NF- κ B is a family of transcription factors that plays an important role in the regulation of immune and inflammatory responses [342, 344-346]. It is recognised that the synthesis and secretion of inflammatory chemokines play important roles in the pathophysiology of ocular inflammation. The expression of inducible genes leading to the formation of these proteins relies on transcription factors. NF- κ B plays a key role in the regulation of the genes responsible for the generation of mediators or proteins in inflammation. There is increasing evidence that NF- κ B is involved in the regulation of chemokine gene expression [346]. These results of ELISA NF- κ B DNA binding, cytokines (TNF α , IL-6 and MPO) and immunoblot of NF- κ B demonstrated that the LPS-induced expression of cytokines and NF- κ B in LPS + Blank-MN. However, LPS + Dex-MN AqH results demonstrate a significant ($p < 0.05$) inhibition of NF- κ B and cytokines (TNF α , IL-6 and MPO). These results are consistent with previously reported data [347]. Overall, the displayed finding shows that application of Dex-MN was able to deliver Dex to the posterior segment and enhance LPS-induced uveitis.

6.4.4 Histopathological evaluation

Histological examination of the enucleated eyes after the *in-vivo* activity test in LPS-induced uveitis is shown in Figure 6-12. In the normal control group (Group-I), where the animal only treated with the Blank-MN patch showed normal tissue histology and no cellular infiltrate nor hyperaemia was found.

In line with clinical observation, the histopathological signs on the rabbit eye of Group-II (LPS + Blank-MN) after 48 h of intravitreal injection of LPS exhibited marked inflammatory reactions characterized by cellular infiltrate, hyperaemia, and perivascular exudates. Neutrophils are prominent cells along with mononuclear cells.

LPS induced uveitis in the eyes of rabbits showed infiltration of inflammatory cells in the anterior chamber of the eye adhering to the endothelial surface (Figure 6-12-b, c). On the other hand, Group-III (LPS + Dex-MN treated groups) exhibited less infiltration of protein and inflammatory cells with slight hyperaemia (Figure 6-12-d). The Dex-MN treatment in Group-III significantly ($p < 0.05$) augmented the uveitis as compared to Group-II which was evidenced by the obtained histological scores of LPS-induced uveitis in rabbits as illustrated in Figure 6-13.

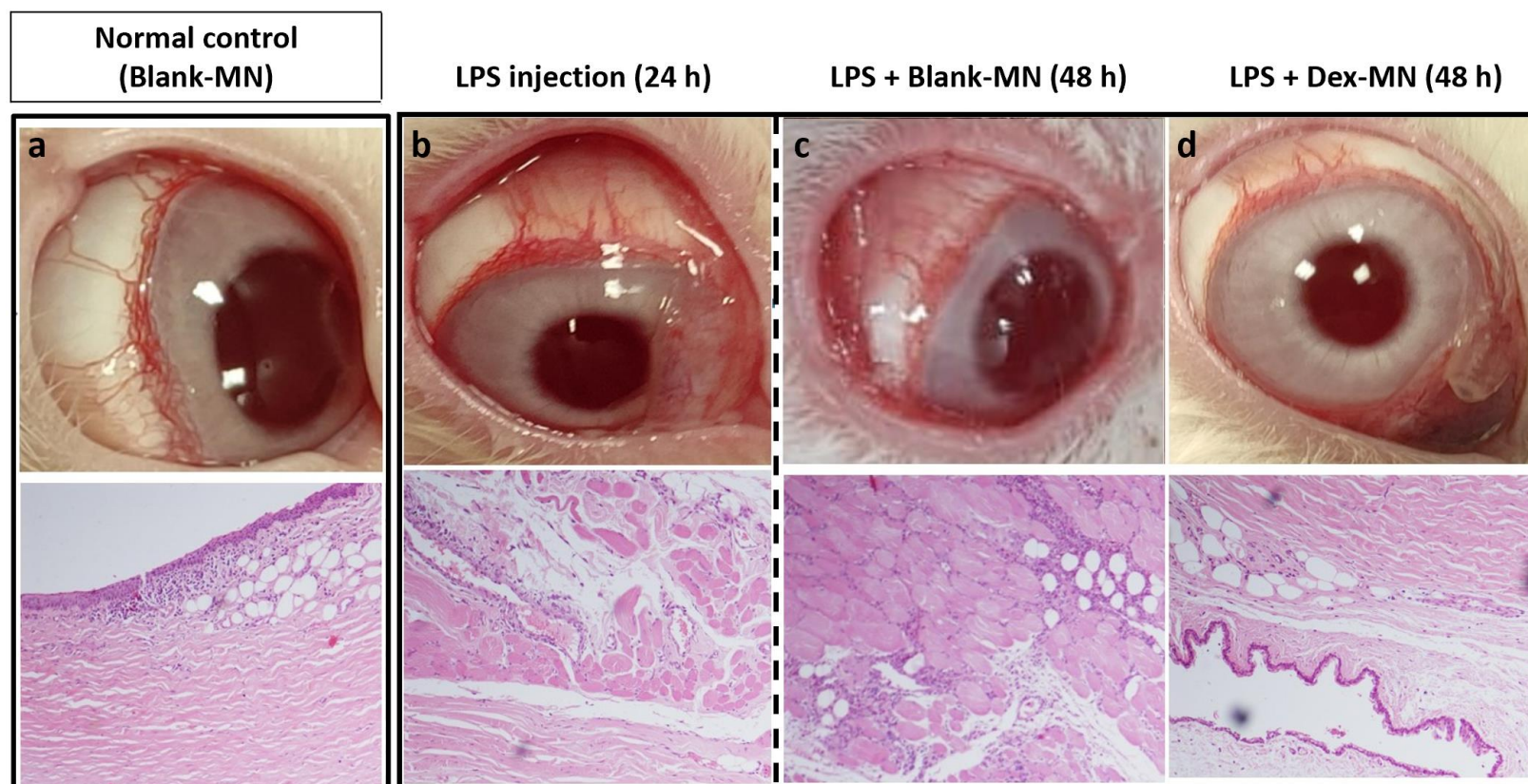


Figure 6-12 Images and micrographs of hematoxylin and eosin–stained sections of rabbit eyes for *in-vivo* activity in LPS-induced uveitis. (a) Group-I, normal control group (Blank-MN). No cellular infiltrate, and conjunctival hyperaemia were observed, (b) LPS-induced uveitis (24 h), (c) Group-II, numerous inflammatory cells infiltrated the extravascular uveal tissue in the LPS + Blank-MN and (d) Group-III, inflammatory cellular infiltration was reduced by treatment with Dex-MN. Section magnification $\times 100$.

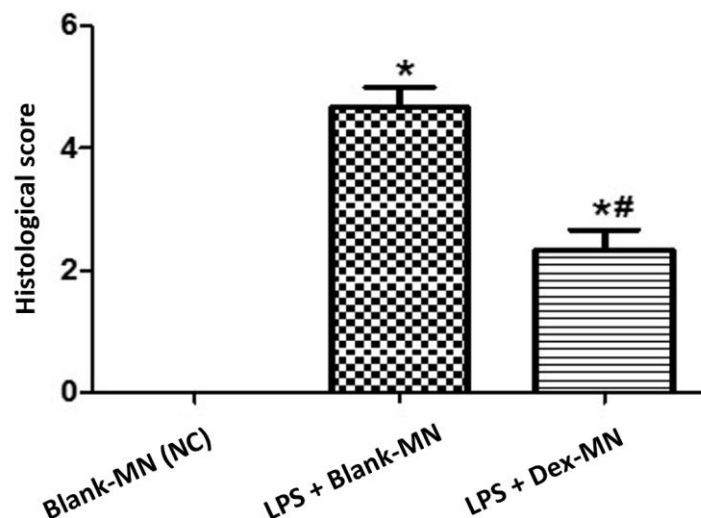



Figure 6-13 Histological score of the normal control group, LPS-induced uveitis with Blank-MN and Dex-MN administration. (The values represent mean \pm SD of three animals per group * $p < 0.05$ (Blank-MN); # $p < 0.05$ (LPS + Blank-MN)).

Histological examination of eye tissue further validated the above results that intravitreal LPS injection exhibited a marked inflammatory response characterized by hyperaemia, cellular infiltrate, and fibrinous exudates along with the infiltration of inflammatory cells in the anterior chamber adherent to the endothelial surface. Similar histopathological changes in LPS-induced uveitis were previously reported [348, 349]. Treatment with Dex-MN has significantly ($p < 0.05$) improved the apoptosis and inflammation induced cell damage.

6.5 Conclusions

In this chapter, an *in-vivo* study of Blank-MN patch and Dex-MN patch was successfully performed to evaluate the ocular toxicity and the anti-inflammatory activity of the system. The ocular irritancy test revealed that both Blank-MN patches and Dex-MN patches exhibited minimum irritation to the rabbit eye, and no mechanical injury by the MN developed upon the insertion of the patches. However, Dex-MN showed a lower irritation score compared to the blank-MN patch, and the eye cleared all the signs of irritation 6 h post patch application, whereas Blank-MN lasted for more than 6 h.

Moreover, the application of Dex-MN patches to an endotoxin-induced uveitis rabbit model displayed an anti-inflammatory effect and significantly reduced the clinical score of the uveitis over 24 h after the Dex-MN patch insertion compared to the normal control group (Blank-MN). This was further confirmed by AqH sample analysis, cytology revealed lower PMN cellular infiltration compared to the treatment with Blank-MN group and the pro-inflammatory markers TNF- α , IL-6, and MPO were also reduced. The expression of various apoptosis mediators, including Bax, BCL2, NF- κ B and Caspase3 in the ocular tissues, was investigated, and Dex-MN has significantly normalised apoptosis and inflammation induced cells. Histopathological assessment has further supported the previous finding, which revealed that endotoxin-induced uveitis caused severe inflammatory reactions characterised by cellular infiltrate, hyperaemia, and fibrinous exudates. Dex-MN has significantly reduced the histological score and reduced the changes caused by the induction of inflammation. The results obtained from the in-vivo study suggested that the system has the potential to serve as a safe and effective drug delivery platform.



Chapter 7 Conclusions and future direction

7.1 Conclusions

Due to the unique anatomy and physiology of the eye, ocular drug delivery has faced major challenges. The delivery of a free drug or drug in a dosage form, particularly to the posterior segment of the eye, is significantly hindered by the combination of anatomical barriers (including the cornea, sclera, retina BAB, and BRB) and the dynamic physiological barriers (including choroidal and conjunctival blood absorption, lymphatic elimination, tear dilution, and efflux pumps) [25]. Numerous posterior ocular diseases cannot be treated by conventional ophthalmic preparation, hence, more invasive approaches such as intravitreal injection are employed to deliver the drug effectively. Therefore, advanced drug delivery techniques are required to overcome ocular delivery obstacles and to maintain drug levels at the target region.

The principal aim of this thesis was to develop a minimally invasive dissolving MN system loaded with PLGA particles to overcome the ocular static and dynamic barriers and to deposit the drug-loaded biodegradable particles in the ocular tissue offering sustained transscleral drug delivery.

The experimental work in Chapter 3 focused on the development of a customisable master to prepare the reverse moulds for the fabrication of the dissolving MN arrays. The master was prepared by a simple and low-cost SLA 3D printer. SLA printers are based on the photopolymerization of liquid resin by a laser beam to build an object layer-by-layer. The use of 3D printing for the fabrication of MN facilitates rapid prototyping and contributes towards the on-demand customisation of therapy approach.

The flexibility and simplicity of 3D printing method was key to enable the study of the effects of different MN designs. Cone, pyramid, and triangular pyramid MN in different aspect ratios were fabricated. All the MN were highly accurate in terms of height and base dimensions. However, the MN tips were wide and blunt. A parametric study was conducted to improve the overall printing resolution and to reduce the tip size of the MN. The stair-stepping surface phenomenon inherent to the layer edges has markedly

improved with decreasing the thickness of the layers. Printing at a 25 μm layer height resulted in a smooth surface finish. Furthermore, the printing orientation has significantly affected the tip size. Changing the printing angle will affect the size and shape of the layer corresponding to the MN tip printing. Consequently, printing at 45°, 67.5°, and 90° angles produced a sharper tip compared to horizontal 0° orientation. The effect of printing at an angled position on the MN dimensions and geometries was further assessed by 3D scanning. In concept, printing at an angled position would also provide high accuracy printing. However, the lack of support structures on the MN body can cause printing deformation. The 3D scanning revealed that printing MN at an angled position also exhibited a significant impact on the MN volume and surface area. After assessment of the accuracy of the MN, printing at 67.5° was deemed to be suitable for producing sharp tips with minimum effect on the MN body.

Despite the fact that SLA 3D printing offers a high degree of accuracy and precision of the printed objects, printing microstructure with fine details requires smaller dimensional tolerance. In the study, all the printed MN shapes with different aspect ratios were accurate in terms of height and base dimensions. The 3D scanning of the printed shapes in a 1:2 aspect ratio revealed that the cone shaped 3D printed MN was more accurate in volume and surface area compared to the pyramid and the triangular pyramid shapes. The assessment of the MN insertion depth revealed that a cone shaped and smaller tip MN penetrated to a greater depth. The conducted 3D printing study demonstrated a method to significantly reduce the MN tip size by using an SLA printer.

In Chapter 4, the preparation and characterisation of PLGA particles were assessed. Initially, the fabrication of the PLGA microparticles focused on studying the influence of the PLGA grade, i.e., viscosity, on the microparticle characteristics. The low viscosity PLGA grade produced a more uniform particle distribution compared to the higher viscosity grade with no significant difference in the average particle size. For the Dex-loaded particles, combinations of organic solvents were prepared to improve the Dex encapsulation in the PLGA particles. Along with the effect of PLGA viscosity, the

composition of the oil phase had a significant effect on the Dex encapsulation. A mixture of DCM and methanol (9:1) using low viscosity PLGA offered a significantly higher Dex encapsulation $49.41\% \pm 0.02$ compared to $23.97\% \pm 0.01$ in high viscosity grade, and consequently higher drug loading.

Comparing the Dex release profile between the two grades of PLGA, the release from the particles prepared with the low viscosity PLGA displayed a slower release than the high viscosity particles. A triphasic Dex release profile was observed with all prepared particles. An initial burst release was followed by accelerated and controlled release phases over 21 days. The Dex release from the low viscosity grade particles was slightly slower than the high viscosity PLGA grade. Therefore, the low viscosity PLGA was selected for further study.

For the preparation of the nanoparticles, a similar method with different mixing tools was utilised, and various types of particles ranging in size from ~ 400 to ~ 540 nm were successfully produced. A slower Dex release rate was reported from the Dex-loaded nanoparticles compared to the microparticles. Moreover, the characterisation of the particles displayed no interaction between the drug and the polymer and confirmed Dex dispersion in the polymeric matrix. In the cell culture study, particles showed a high safety profile in ARPE-19 cell line and confirmed cellular uptake with micro- and nanoparticles with higher internalisation of the nanoparticles.

PLGA carriers are very versatile with regard to their drug encapsulation capacity and release behaviour. The design of the PLGA particles could be controlled to overcome barriers and enhance precision therapy by tailoring the properties of the particles. Therefore, advanced engineering of the PLGA particles to meet the specific application requirements can open new opportunities when loaded in the MN system.

Chapter 5 focused on the development, fabrication, and assessment of the PLGA particles incorporated into dissolvable MN system. The polymeric base was first studied, PVP/PVA blends of different ratios and PVP grades (PVP K90 and PVP K30) were

studied. The polymeric base with PVP K90 and PVA in a 2:1 ratio exhibited mechanically strong MN with controlled MN dissolution and stronger adhesion to porcine scleral tissue. Therefore, it was selected to prepare the MN system. The various types of particles prepared in Chapter 4 were incorporated into the MN array. The addition of the PLGA particles has reduced the mechanical strength of the array and increased the scleral insertion force. Still, the PLGA particles loaded MN array demonstrated sufficient mechanical strength to penetrate the porcine scleral tissue with gentle thumb pressure.

The amount of Dex permeated after the MN application was significantly higher compared to free Dex microparticles and Dex suspension. Similarly, the amount of Dex that remained in the scleral tissue after the MN application was threefold higher than the amount detected after the installation of Dex-loaded microparticles and Dex suspension. Moreover, tracking the fluorescent labelled particles has revealed both microparticles and nanoparticles were capable of diffusing through the scleral matrix in lateral and transverse directions. It should be highlighted that determining the magnitude of the particle's distribution was challenging in this study. Therefore, to take the approach forward, advanced imaging instruments could be utilised to quantitatively study the particle distribution. In addition, the influence of the duration of the MN array application could also be useful in understanding the capacity of the system to deposit the particles.

Tracking Dex ocular distribution after the MN administration showed great potential for posterior drug delivery. Extracting Dex from various ocular parts proved the delivery of the drug to the vitreous humour and to the scleral tissues, indicating that the drug was released from the particles and permeated through the scleral, reaching the inner parts of the eye. It should also be emphasized that the estimated amount of Dex-loaded in the MN array was not completely detected, indicating that part of the particles had not permeated through the scleral tissue.

The final experimental chapter depicted the *in-vivo* performance of the developed system. The ocular irritancy test on albino rabbit model, confirmed minimum irritation

of the blank and Dex-loaded nanoparticles incorporated in the MN patch and all the signs of irritation were cleared in less than 12 h post MN application. In addition, the MN incorporated with Dex-loaded particles displayed a significant improvement in the symptoms associated with the endotoxin-induced uveitis model and reduced the histological changes caused by the inflammation. The result demonstrated the safety and potential efficacy of the MN system *in-vivo*.

In conclusion, this research described a comprehensive approach to design and fabricate PLGA particles incorporated into a dissolvable MN array to overcome the ocular barriers and improve bioavailability using customisable 3D printed mould. 3D printing in the pharmaceutical industry is expected to be transformative, with the capacity to revolutionize drug development, manufacturing, and delivery. The research further provided insight to confirm the potential application of the system to localise the PLGA particles at the insertion site and to deliver the drug through the sclera. The synergistic combination of MN and the PLGA biodegradable carrier showed great possibility to deliver drugs to the posterior segment of the eye in a minimally invasive application and potentially controlled release drug delivery. Additionally, the *in-vivo* assessments determined the potential safety and efficacy of the MN system for ocular application, and the study outcome can benefit the development of this technology for future use in clinical practice.

7.2 Future direction

This project involves multiple areas of investigation, from the creation and optimisation of the 3D printed moulds to the fabrication and characterisation of PLGA particle carriers and finally to the construction and assessment of the dissolvable MN system. From there, several suggested future works could be considered.

In Chapter 3, the reported method of 3D printing the MN master mould has demonstrated an improved printing resolution by reducing the needle tip size. 3D technology offers an advantageous potential to overcome the limitation of other manufacturing technologies. The emerging 3D technology enables desirable MN personalisation [97]. Master mould can be further enhanced to create a customised MN patch using micromoulding and 3D printing techniques.

Conventional MN patches are fabricated with plane bases. Application of the flat MN patch on the curved eyeball surface could reduce the MN insertion capability and limit the efficacy. The utilisation of 3D printing allows the fabrication of personalized curved micromould for a perfect fit on the ocular surface. Methods to scan the eye curvature, such as slit-scan topography and cranial MRI scan, can be used to design a personalised curved MN patch. Multifunctional features will be made possible by the use of 3D printing in ocular patch manufacturing. In an integrated production process, spherical, symmetrical, and asymmetrical shaped bases can be produced. In the literature, studies have been reported on the fabrication of personalised contact lenses through the utilisation of 3D printing techniques [350].

Moreover, the developed MN system in this work has displayed sufficient mechanical strength for ocular insertion; however, the stability of the system has not been studied. Investigation of the mechanical properties and insertion ability of the polymeric MN under different temperature and humidity conditions is important to understand the mechanical stability of the developed system. Stability studies of pharmaceutical products should be designed in the light of the properties and stability characteristics of the dosage form as well as the climatic zone of the intended market. Designing an

experiment to study the influence of storage time, temperature, and humidity on the mechanical stability of the polymeric MN system is essential. The stability of the prepared PLGA particles was also not assessed. A real time stability study and accelerated study at $40^{\circ} \pm 2$ and $75\% \pm 5$ for 3 or 6 months based on the region of use could also be investigated; the morphology, the size, and the drug release from the particle could be assessed.

In Chapter 5, an investigation of the particle's transscleral distribution was carried out to prove the concept of the possibility of using the MN system to deposit various sizes of the PLGA particles in the scleral matrix; however, the magnitude and particles residency time within the tissue were not assessed. The fate and behaviour of the particles in the scleral tissue, along with the pharmacokinetics study of the payload release from the particles, can be investigated *in-vivo*.

A further area of research interest is investigating the effect of the spreading enzymes, i.e. hyaluronidase and collagenase, on particle distribution. The spreading enzymes allow the disruption of the scleral microstructure to overcome the rate limiting ocular anatomical barriers [76]. The administration of the spreading enzymes may expand the delivery coverage and enhance micro- and nano- particles distribution at the target area [351]. Coadministration spreading enzymes with nano- or micro- particles by hollow MN has been reported to enhance the delivery of particles to the posterior segment [76, 351]. Exploring the potential of the spreading enzymes to improve transscleral particle distribution by incorporating the spreading enzymes in the polymeric MN has not been reported in the literature.

References

1. Thrimawithana, T.R., et al., *Drug delivery to the posterior segment of the eye*. Drug Discovery Today, 2011. **16**(5): p. 270-277.
2. Janoria, K.G., et al., *Novel approaches to retinal drug delivery*. Expert Opinion on Drug Delivery, 2007. **4**(4): p. 371-388.
3. Geroski, D.H. and H.F. Edelhauser, *Transscleral drug delivery for posterior segment disease*. Advanced Drug Delivery Reviews, 2001. **52**(1): p. 37-48.
4. Patel, A., et al., *Ocular drug delivery systems: An overview*. World J Pharmacol, 2013. **2**(2): p. 47-64.
5. Falavarjani, K.G. and Q.D. Nguyen, *Adverse events and complications associated with intravitreal injection of anti-VEGF agents: a review of literature*. Eye (London, England), 2013. **27**(7): p. 787-794.
6. Moffatt, K., et al., *Microneedles for enhanced transdermal and intraocular drug delivery*. Current Opinion in Pharmacology, 2017. **36**: p. 14-21.
7. Galloway N.R., et al., *Basic Anatomy and Physiology of the Eye*, in *Common Eye Diseases and their Management*. 2006, Springer, Cham. p. 7-15.
8. Cholkar, K., et al., *1 - Eye: anatomy, physiology and barriers to drug delivery*, in *Ocular Transporters and Receptors*, A.K. Mitra, Editor. 2013, Woodhead Publishing. p. 1-36.
9. Olsen, T.W., et al., *Human sclera: Thickness and surface area*. American Journal of Ophthalmology, 1998. **125**(2): p. 237-241.
10. Cholkar K, et al., *Ocular Drug delivery*, in *Drug delivery*. 2014, Jones & Bartlett Learning. p. 219-263.
11. McCaa, C.S., *The eye and visual nervous system: anatomy, physiology and toxicology*. Environ Health Perspect, 1982. **44**: p. 1-8.
12. Arranz-Romera, A., et al., *Simultaneous co-delivery of neuroprotective drugs from multi-loaded PLGA microspheres for the treatment of glaucoma*. Journal of Controlled Release, 2019. **297**: p. 26-38.
13. Tsai, C.H., et al., *Ocular Drug Delivery: Role of Degradable Polymeric Nanocarriers for Ophthalmic Application*. Int J Mol Sci, 2018. **19**(9).
14. Agrahari, V., et al., *A comprehensive insight on ocular pharmacokinetics*. Drug Deliv Transl Res, 2016. **6**(6): p. 735-754.
15. Maurice, D.M. and S. Mishima, *Ocular Pharmacokinetics*, in *Pharmacology of the Eye*, M.L. Sears, Editor. 1984, Springer Berlin Heidelberg: Berlin, Heidelberg. p. 19-116.
16. Urtti, A., *Challenges and obstacles of ocular pharmacokinetics and drug delivery*. Advanced Drug Delivery Reviews, 2006. **58**(11): p. 1131-1135.
17. Bachu, R.D., et al., *Ocular Drug Delivery Barriers-Role of Nanocarriers in the Treatment of Anterior Segment Ocular Diseases*. Pharmaceutics, 2018. **10**(1).
18. Achouri, D., et al., *Recent advances in ocular drug delivery*. Drug Development and Industrial Pharmacy, 2013. **39**(11): p. 1599-1617.

19. Varela-Fernández, R., et al., *Drug Delivery to the Posterior Segment of the Eye: Biopharmaceutic and Pharmacokinetic Considerations*. Pharmaceutics, 2020. **12**(3).
20. Hornof, M., E. Toropainen, and A. Urtti, *Cell culture models of the ocular barriers*. European Journal of Pharmaceutics and Biopharmaceutics, 2005. **60**(2): p. 207-225.
21. Ambati, J., et al., *Diffusion of High Molecular Weight Compounds through Sclera*. Investigative Ophthalmology & Visual Science, 2000. **41**(5): p. 1181-1185.
22. Maurice, D., *Review: Practical Issues in Intravitreal Drug Delivery*. Journal of Ocular Pharmacology and Therapeutics, 2001. **17**(4): p. 393-401.
23. Ghate, D. and H.F. Edelhauser, *Ocular drug delivery*. Expert Opinion on Drug Delivery, 2006. **3**(2): p. 275-287.
24. Pitkänen, L., et al., *Permeability of Retinal Pigment Epithelium: Effects of Permeant Molecular Weight and Lipophilicity*. Investigative Ophthalmology & Visual Science, 2005. **46**(2): p. 641-646.
25. Gaudana, R., et al., *Ocular drug delivery*. Aaps j, 2010. **12**(3): p. 348-60.
26. Chen, H., *Recent developments in ocular drug delivery*. Journal of Drug Targeting, 2015. **23**(7-8): p. 597-604.
27. Moisseiev, E. and A. Loewenstein, *Drug Delivery to the Posterior Segment of the Eye*. Dev Ophthalmol, 2017. **58**: p. 87-101.
28. Kuno, N. and S. Fujii, *Recent Advances in Ocular Drug Delivery Systems*. Polymers, 2011. **3**(1): p. 193-221.
29. Bourges, J.L., et al., *Intraocular implants for extended drug delivery: Therapeutic applications*. Advanced Drug Delivery Reviews, 2006. **58**(11): p. 1182-1202.
30. Lee, D.J., *Intraocular Implants for the Treatment of Autoimmune Uveitis*. J Funct Biomater, 2015. **6**(3): p. 650-66.
31. Chan, A., L.-S. Leung, and M.S. Blumenkranz, *Critical appraisal of the clinical utility of the dexamethasone intravitreal implant (Ozurdex) for the treatment of macular edema related to branch retinal vein occlusion or central retinal vein occlusion*. Clinical ophthalmology (Auckland, N.Z.), 2011. **5**: p. 1043-1049.
32. Souto, E.B., et al., *Advanced Formulation Approaches for Ocular Drug Delivery: State-Of-The-Art and Recent Patents*. Pharmaceutics, 2019. **11**(9).
33. Lee, S.Y., et al., *Surodex in paediatric cataract surgery*. British Journal of Ophthalmology, 2003. **87**(11): p. 1424.
34. *Ocular Therapeutix. DEXTENZA® (dexamethasone ophthalmic insert) 0.4 mg, for intracanalicular use.* [cited 2022 13 Sep]; Available from: <https://www.dextenza.com/>.
35. Shirley, M., *Bimatoprost Implant: First Approval*. Drugs Aging. Drugs Aging, 2020. **37**(6): p. 457-462.
36. Cao, Y., et al., *Recent advances in intraocular sustained-release drug delivery devices*. Drug Discovery Today, 2019. **24**(8): p. 1694-1700.
37. Allergan, a.A.c. *Ozurdex (dexamethasone intravitreal implant)*. 2022 [cited 2022; Available from: <https://www.ozurdex.com/>.

38. Jaffe, G.J., et al., *Fluocinolone Acetonide Implant (Retisert) for Noninfectious Posterior Uveitis: Thirty-Four-Week Results of a Multicenter Randomized Clinical Study*. Ophthalmology, 2006. **113**(6): p. 1020-1027.
39. Wang, J., et al., *Drug Delivery Implants in the Treatment of Vitreous Inflammation*. Mediators of Inflammation, 2013. **2013**: p. 8.
40. Haghjou, N., M. Soheilian, and M.J. Abdekhodaie, *Sustained release intraocular drug delivery devices for treatment of uveitis*. Journal of ophthalmic & vision research, 2011. **6**(4): p. 317-329.
41. Barnett, P.J., *Mathematical modeling of triamcinolone acetonide drug release from the I-vation intravitreal implant (a controlled release platform)*. Conf Proc IEEE Eng Med Biol Soc, 2009: p. 3087-90.
42. Desai, A.R., et al., *Multiple drug delivery from the drug-implants-laden silicone contact lens: Addressing the issue of burst drug release*. Materials Science and Engineering: C, 2020. **112**: p. 110885.
43. Madni, A., et al., *Non-invasive strategies for targeting the posterior segment of eye*. International Journal of Pharmaceutics, 2017. **530**(1): p. 326-345.
44. *Effectiveness and Safety of Timolol and Dorzolamide Loaded Contact Lenses*. 2016 1/9/2019]; [NCT02852057](https://clinicaltrials.gov/ct2/show/NCT02852057). Available from: <https://clinicaltrials.gov/ct2/show/NCT02852057>.
45. Ross, A.E., et al., *Topical sustained drug delivery to the retina with a drug-eluting contact lens*. Biomaterials, 2019. **217**: p. 119285.
46. *Amorphex Therapeutics. TODDD™*. 1/9/2019]; Available from: <https://www.amorphexusa.com/>.
47. Myles, M.E., D.M. Neumann, and J.M. Hill, *Recent progress in ocular drug delivery for posterior segment disease: emphasis on transscleral iontophoresis*. Advanced drug delivery reviews, 2005. **57**(14): p. 2063-2079.
48. Santer, V., Y. Chen, and Y.N. Kalia, *Controlled non-invasive iontophoretic delivery of triamcinolone acetonide amino acid ester prodrugs into the posterior segment of the eye*. Eur J Pharm Biopharm, 2018. **132**: p. 157-167.
49. Davies, J.B., et al., *Delivery of several forms of DNA, DNA-RNA hybrids, and dyes across human sclera by electrical fields*. Mol Vis, 2003. **9**: p. 569-78.
50. Molokhia, S.A., et al., *Transscleral iontophoretic and intravitreal delivery of a macromolecule: study of ocular distribution in vivo and postmortem with MRI*. Experimental eye research, 2009. **88**(3): p. 418-425.
51. Jung, J.H., et al., *Ocular drug delivery targeted by iontophoresis in the suprachoroidal space using a microneedle*. Journal of Controlled Release, 2018. **277**: p. 14-22.
52. Prausnitz, M.R., S. Mitragotri, and R. Langer, *Current status and future potential of transdermal drug delivery*. Nature Reviews Drug Discovery, 2004. **3**(2): p. 115-124.
53. Yang, J., et al., *Recent advances of microneedles for biomedical applications: drug delivery and beyond*. Acta Pharmaceutica Sinica B, 2019. **9**(3): p. 469-483.
54. Cheng, H., et al., *Recent progress of micro-needle formulations: Fabrication strategies and delivery applications*. Journal of Drug Delivery Science and Technology, 2019. **50**: p. 18-26.

55. Sharma, S., et al., *Recent advances in microneedle composites for biomedical applications: Advanced drug delivery technologies*. Materials Science and Engineering: C, 2019. **103**: p. 109717.
56. A. Machekposhti, S., et al., *Biocompatible polymer microneedle for topical/dermal delivery of tranexamic acid*. Journal of Controlled Release, 2017. **261**: p. 87-92.
57. Sharma, S., et al., *Evaluation of a minimally invasive glucose biosensor for continuous tissue monitoring*. Analytical and bioanalytical chemistry, 2016. **408**(29): p. 8427-8435.
58. Bhatnagar, S., et al., *Corneal delivery of besifloxacin using rapidly dissolving polymeric microneedles*. Drug Delivery and Translational Research, 2018. **8**(3): p. 473-483.
59. Niu, L., et al., *Intradermal delivery of vaccine nanoparticles using hollow microneedle array generates enhanced and balanced immune response*. Journal of Controlled Release, 2019. **294**: p. 268-278.
60. Ma, Y., et al., *Vaccine Delivery to the Oral Cavity Using Coated Microneedles Induces Systemic and Mucosal Immunity*. Pharmaceutical Research, 2014. **31**(9): p. 2393-2403.
61. Pradeep, N.S. and S. Raghavan, *Solid silicon microneedles for drug delivery applications*. The International Journal of Advanced Manufacturing Technology, 2017. **93**(1): p. 407-422.
62. Thakur, R.R.S., et al., *Rapidly dissolving polymeric microneedles for minimally invasive intraocular drug delivery*. Drug delivery and translational research, 2016. **6**(6): p. 800-815.
63. Than, A., et al., *Self-implantable double-layered micro-drug-reservoirs for efficient and controlled ocular drug delivery*. Nature Communications, 2018. **9**(1): p. 4433.
64. Luzuriaga, M.A., et al., *Biodegradable 3D printed polymer microneedles for transdermal drug delivery*. Lab Chip, 2018. **18**(8): p. 1223-1230.
65. Mylien, T.H., B.I. Kevin, and A.B. Daniel, *Solid Microneedles for Transdermal Delivery of Amantadine Hydrochloride and Pramipexole Dihydrochloride*. Pharmaceutics, 2015. **7**(4): p. 379-396.
66. Jiang, J., et al., *Coated microneedles for drug delivery to the eye*. Invest Ophthalmol Vis Sci, 2007. **48**(9): p. 4038-43.
67. Ma, Y. and H.S. Gill, *Coating Solid Dispersions on Microneedles via a Molten Dip-Coating Method: Development and In Vitro Evaluation for Transdermal Delivery of a Water-insoluble Drug*. Journal of Pharmaceutical Sciences, 2014. **103**(11): p. 3621-3630.
68. Vora, L.K., et al., *Novel bilayer dissolving microneedle arrays with concentrated PLGA nano-microparticles for targeted intradermal delivery: Proof of concept*. Journal of Controlled Release, 2017. **265**: p. 93-101.
69. Eltayib, E., et al., *Hydrogel-forming microneedle arrays: Potential for use in minimally-invasive lithium monitoring*. European Journal of Pharmaceutics and Biopharmaceutics, 2016. **102**: p. 123-131.
70. Wilke, N., et al., *Silicon microneedle electrode array with temperature monitoring for electroporation*. Sensors and Actuators A: Physical, 2005. **123-124**: p. 319-325.

71. Gittard, S.D., et al., *Two-photon polymerization of microneedles for transdermal drug delivery*. Expert Opinion on Drug Delivery, 2010. **7**(4): p. 513-533.
72. Xenikakis, I., et al., *Fabrication and finite element analysis of stereolithographic 3D printed microneedles for transdermal delivery of model dyes across human skin in vitro*. European Journal of Pharmaceutical Sciences, 2019. **137**: p. 104976.
73. Economidou, S.N., et al., *3D printed microneedle patches using stereolithography (SLA) for intradermal insulin delivery*. Materials Science and Engineering: C, 2019. **102**: p. 743-755.
74. Cordeiro, A.S., et al., *Two-Photon Polymerisation 3D Printing of Microneedle Array Templates with Versatile Designs: Application in the Development of Polymeric Drug Delivery Systems*. Pharm Res, 2020. **37**(9): p. 174.
75. Jiang, J., et al., *Coated Microneedles for Drug Delivery to the Eye*. Investigative Ophthalmology & Visual Science, 2007. **48**(9): p. 4038-4043.
76. Jiang, J., et al., *Intrascleral drug delivery to the eye using hollow microneedles*. Pharmaceutical research, 2009. **26**(2): p. 395-403.
77. Patel, S.R., et al., *Suprachoroidal drug delivery to the back of the eye using hollow microneedles*. Pharmaceutical research, 2011. **28**(1): p. 166-176.
78. Gardeniers, H.J., et al., *Silicon micromachined hollow microneedles for transdermal liquid transport*. Journal of Microelectromechanical systems, 2003. **12**(6): p. 855-862.
79. Allen, E.A., et al., *Dissolvable microneedle fabrication using piezoelectric dispensing technology*. International Journal of Pharmaceutics, 2016. **500**(1): p. 1-10.
80. Peng, K., et al., *Dissolving microneedle patches loaded with amphotericin B microparticles for localised and sustained intradermal delivery: Potential for enhanced treatment of cutaneous fungal infections*. Journal of Controlled Release, 2021. **339**: p. 361-380.
81. Amer, M. and R.K. Chen, *Self-Adhesive Microneedles with Interlocking Features for Sustained Ocular Drug Delivery*. Macromolecular Bioscience, 2020. **20**(6): p. 2000089.
82. Gupta, P. and K.S. Yadav, *Applications of microneedles in delivering drugs for various ocular diseases*. Life Sciences, 2019. **237**: p. 116907.
83. Song, H.B., et al., *Impact insertion of transfer-molded microneedle for localized and minimally invasive ocular drug delivery*. Journal of Controlled Release, 2015. **209**: p. 272-279.
84. Yeh, S., et al., *Efficacy and Safety of Suprachoroidal CLS-TA for Macular Edema Secondary to Noninfectious Uveitis: Phase 3 Randomized Trial*. Ophthalmology, 2020. **127**(7): p. 948-955.
85. Prausnitz, M.R., N. Jiang, and H.F. Edelhauser, *Method for drug delivery to ocular tissue using microneedle*, U.S. Patent, Editor. 2011.
86. Habot-Wilner, Z., G. Noronha, and C.C. Wykoff, *Suprachoroidally injected pharmacological agents for the treatment of chorio-retinal diseases: a targeted approach*. Acta Ophthalmologica, 2019. **97**(5): p. 460-472.

87. Gilger, B.C., et al., *Treatment of Acute Posterior Uveitis in a Porcine Model by Injection of Triamcinolone Acetonide Into the Suprachoroidal Space Using Microneedles*. Investigative Ophthalmology & Visual Science, 2013. **54**(4): p. 2483-2492.
88. Palakurthi, N.K., et al., *Toxicity of a biodegradable microneedle implant loaded with methotrexate as a sustained release device in normal rabbit eye: a pilot study*. J Ocul Pharmacol Ther, 2011. **27**(2): p. 151-6.
89. Datta, D., et al., *Ocular delivery of cyclosporine A using dissolvable microneedle contact lens*. Journal of Drug Delivery Science and Technology, 2022. **70**: p. 103211.
90. Roy, G., et al., *Microneedle ocular patch: fabrication, characterization, and ex-vivo evaluation using pilocarpine as model drug*. Drug Development and Industrial Pharmacy, 2020. **46**(7): p. 1114-1122.
91. Suriyaamporn, P., et al., *Computer-aided rational design for optimally Gantrez® S-97 and hyaluronic acid-based dissolving microneedles as a potential ocular delivery system*. Journal of Drug Delivery Science and Technology, 2021. **61**: p. 102319.
92. Wu, Y., et al., *Long-acting nanoparticle-loaded bilayer microneedles for protein delivery to the posterior segment of the eye*. European Journal of Pharmaceutics and Biopharmaceutics, 2021. **165**: p. 306-318.
93. Wohlers, T. and T. Gornet, *History of additive manufacturing*. Wohlers report, 2014. **24**(2014): p. 118.
94. Capel, A.J., et al., *3D printing for chemical, pharmaceutical and biological applications*. Nature Reviews Chemistry, 2018. **2**(12): p. 422-436.
95. Yu, D.G., et al., *Three-Dimensional Printing in Pharmaceutics: Promises and Problems*. Journal of Pharmaceutical Sciences, 2008. **97**(9): p. 3666-3690.
96. Jamróz, W., et al., *3D Printing in Pharmaceutical and Medical Applications – Recent Achievements and Challenges*. Pharmaceutical Research, 2018. **35**(9): p. 176.
97. Yang, Q., et al., *Recent progress of 3D-printed microneedles for transdermal drug delivery*. International Journal of Pharmaceutics, 2021. **593**: p. 120106.
98. Robles Martinez, P., A.W. Basit, and S. Gaisford, *The history, developments and opportunities of stereolithography, in 3D Printing of Pharmaceuticals*. 2018, Springer. p. 55-79.
99. Chiulan, I., Ş.I. Voicu, and D. Batalu, *The Use of Graphene and Its Derivatives for the Development of Polymer Matrix Composites by Stereolithographic 3D Printing*. Applied Sciences, 2022. **12**(7): p. 3521.
100. Deshmane, S., et al., *Stereolithography 3D printing technology in pharmaceuticals: a review*. Drug Development and Industrial Pharmacy, 2021. **47**(9): p. 1362-1372.
101. Xu, X., et al., *Vat photopolymerization 3D printing for advanced drug delivery and medical device applications*. Journal of Controlled Release, 2021. **329**: p. 743-757.
102. Wang, J., et al., *Stereolithographic (SLA) 3D printing of oral modified-release dosage forms*. International Journal of Pharmaceutics, 2016. **503**(1): p. 207-212.
103. Pere, C.P.P., et al., *3D printed microneedles for insulin skin delivery*. International Journal of Pharmaceutics, 2018. **544**(2): p. 425-432.

104. Krieger, K.J., et al., *Simple and customizable method for fabrication of high-aspect ratio microneedle molds using low-cost 3D printing*. Microsystems & Nanoengineering, 2019. **5**(1): p. 42.
105. Economidou, S.N., D.A. Lamprou, and D. Douroumis, *3D printing applications for transdermal drug delivery*. International Journal of Pharmaceutics, 2018. **544**(2): p. 415-424.
106. Goyanes, A., et al., *Patient acceptability of 3D printed medicines*. International Journal of Pharmaceutics, 2017. **530**(1): p. 71-78.
107. West, T.G. and T.J. Bradbury, *3D Printing: A Case of ZipDose® Technology – World's First 3D Printing Platform to Obtain FDA Approval for a Pharmaceutical Product*, in *3D and 4D Printing in Biomedical Applications*. 2019. p. 53-79.
108. Lim, S.H., J.Y. Ng, and L. Kang, *Three-dimensional printing of a microneedle array on personalized curved surfaces for dual-pronged treatment of trigger finger*. Biofabrication, 2017. **9**(1): p. 015010.
109. Lee, J.-S., et al., *3D printing of composite tissue with complex shape applied to ear regeneration*. Biofabrication, 2014. **6**(2): p. 024103.
110. Zuniga, J., et al., *Cyborg beast: a low-cost 3d-printed prosthetic hand for children with upper-limb differences*. BMC research notes, 2015. **8**(1): p. 1-9.
111. Murphy, S.V. and A. Atala, *3D bioprinting of tissues and organs*. Nature Biotechnology, 2014. **32**(8): p. 773-785.
112. Vukicevic, M., et al., *Cardiac 3D Printing and its Future Directions*. JACC Cardiovasc Imaging, 2017. **10**(2): p. 171-184.
113. Arribada, R.G., et al., *The Use of Polymer Blends in the Treatment of Ocular Diseases*. Pharmaceutics, 2022. **14**(7).
114. Allyn, M.M., et al., *Considerations for Polymers Used in Ocular Drug Delivery*. Frontiers in Medicine, 2022. **8**.
115. Sapino, S., et al., *Ocular Drug Delivery: A Special Focus on the Thermosensitive Approach*. Nanomaterials (Basel), 2019. **9**(6).
116. Zhang, L., et al., *Sustained intravitreal delivery of dexamethasone using an injectable and biodegradable thermogel*. Acta Biomater, 2015. **23**: p. 271-281.
117. Sheshala, R., et al., *In situ forming phase-inversion implants for sustained ocular delivery of triamcinolone acetonide*. Drug Delivery and Translational Research, 2019. **9**(2): p. 534-542.
118. Hu, C.C., et al., *Controlled release bevacizumab in thermoresponsive hydrogel found to inhibit angiogenesis*. Biomed Mater Eng, 2014. **24**(6): p. 1941-50.
119. Zhou, C., et al., *Sustained Subconjunctival Delivery of Infliximab Protects the Cornea and Retina Following Alkali Burn to the Eye*. Investigative Ophthalmology & Visual Science, 2017. **58**(1): p. 96-105.
120. Osswald, C.R. and J.J. Kang-Mieler, *Controlled and Extended In Vitro Release of Bioactive Anti-Vascular Endothelial Growth Factors from a Microsphere-Hydrogel Drug Delivery System*. Curr Eye Res, 2016. **41**(9): p. 1216-22.
121. Gupta, H., et al., *Sparfloxacin-loaded PLGA nanoparticles for sustained ocular drug delivery*. Nanomedicine: Nanotechnology, Biology and Medicine, 2010. **6**(2): p. 324-333.

122. Bode, C., et al., *In-situ forming PLGA implants for intraocular dexamethasone delivery*. International Journal of Pharmaceutics, 2018. **548**(1): p. 337-348.
123. Herrero-Vanrell, R., *Intraocular administration of biodegradable microspheres to increase drug bioavailability and extend therapeutic effect*. Acta Ophthalmologica, 2012. **90**(s249): p. 0-0.
124. Makadia, H.K. and S.J. Siegel, *Poly Lactic-co-Glycolic Acid (PLGA) as Biodegradable Controlled Drug Delivery Carrier*. Polymers, 2011. **3**(3): p. 1377-1397.
125. Hernández-Giottonini, K.Y., et al., *PLGA nanoparticle preparations by emulsification and nanoprecipitation techniques: effects of formulation parameters*. RSC Advances, 2020. **10**(8): p. 4218-4231.
126. Hua, F.J., T.G. Park, and D.S. Lee, *A facile preparation of highly interconnected macroporous poly(D,L-lactic acid-co-glycolic acid) (PLGA) scaffolds by liquid-liquid phase separation of a PLGA-dioxane-water ternary system*. Polymer, 2003. **44**(6): p. 1911-1920.
127. Berkland, C., et al., *Uniform double-walled polymer microspheres of controllable shell thickness*. Journal of Controlled Release, 2004. **96**(1): p. 101-111.
128. Yun, W., et al., *Electrospray Production of Nanoparticles for Drug/Nucleic Acid Delivery*, in *The Delivery of Nanoparticles*, A.H. Abbass, Editor. 2012, IntechOpen: Rijeka. p. Ch. 10.
129. Fessi, H., et al., *Nanocapsule formation by interfacial polymer deposition following solvent displacement*. International Journal of Pharmaceutics, 1989. **55**(1): p. R1-R4.
130. Alshamsan, A., *Nanoprecipitation is more efficient than emulsion solvent evaporation method to encapsulate cucurbitacin I in PLGA nanoparticles*. Saudi Pharmaceutical Journal, 2014. **22**(3): p. 219-222.
131. Raizman, M., *Corticosteroid Therapy of Eye Disease: Fifty Years Later*. Archives of Ophthalmology, 1996. **114**(8): p. 1000-1001.
132. Gaballa, S.A., et al., *Corticosteroids in ophthalmology: drug delivery innovations, pharmacology, clinical applications, and future perspectives*. Drug Delivery and Translational Research, 2021. **11**(3): p. 866-893.
133. van der Velden, V.H., *Glucocorticoids: mechanisms of action and anti-inflammatory potential in asthma*. Mediators Inflamm, 1998. **7**(4): p. 229-37.
134. Amano, Y., S.W. Lee, and A.C. Allison, *Inhibition by glucocorticoids of the formation of interleukin-1 alpha, interleukin-1 beta, and interleukin-6: mediation by decreased mRNA stability*. Molecular Pharmacology, 1993. **43**(2): p. 176-182.
135. Tripathi, R.C., et al., *Corticosteroids and Glaucoma Risk*. Drugs & Aging, 1999. **15**(6): p. 439-450.
136. Rodríguez Villanueva, J., et al., *Optimising the controlled release of dexamethasone from a new generation of PLGA-based microspheres intended for intravitreal administration*. European Journal of Pharmaceutical Sciences, 2016. **92**: p. 287-297.
137. Barcia, E., et al., *Downregulation of endotoxin-induced uveitis by intravitreal injection of polylactic-glycolic acid (PLGA) microspheres loaded with dexamethasone*. Experimental Eye Research, 2009. **89**(2): p. 238-245.

138. Kiddee, W., et al., *Intraocular pressure monitoring post intravitreal steroids: a systematic review*. *Surv Ophthalmol*, 2013. **58**(4): p. 291-310.
139. Gaaz, T.S., et al., *Properties and Applications of Polyvinyl Alcohol, Halloysite Nanotubes and Their Nanocomposites*. *Molecules* (Basel, Switzerland), 2015. **20**(12): p. 22833-22847.
140. Hassan, C.M.a.P., N.A. , *Structure and Applications of Poly(Vinyl Alcohol) Hydrogels Produced by Conventional Crosslinking or by Freezing/Thawing Methods*. *Advances in Polymer Science*, 2000. **153**: p. 37-65.
141. Rowe, R.C., A. American Pharmacists, and A. American Pharmaceutical, *Handbook of pharmaceutical excipients*. 7th ed. ed. 2012, London, Washington, D.C.: Pharmaceutical Press.
142. Karimi, A. and M. Navidbakhsh, *Mechanical properties of PVA material for tissue engineering applications*. *Materials Technology*, 2014. **29**(2): p. 90-100.
143. Vandervoort, J. and A. Ludwig, *Biocompatible stabilizers in the preparation of PLGA nanoparticles: a factorial design study*. *International Journal of Pharmaceutics*, 2002. **238**(1): p. 77-92.
144. Haaf, F., A. Sanner, and F. Straub, *Polymers of N-Vinylpyrrolidone: Synthesis, Characterization and Uses*. *Polymer Journal*, 1985. **17**(1): p. 143-152.
145. Gade, S.K., et al., *Effect of Mucoadhesive Polymeric Formulation on Corneal Permeation of Fluoroquinolones*. *J Ocul Pharmacol Ther*, 2018. **34**(8): p. 570-578.
146. Buhler, V., *Kollidon® Polyvinylpyrrolidone excipients for the pharmaceutical industry.*, B.S.P.I. Services, Editor. 2008: Germany.
147. Roy, G., et al., *Amphotericin B containing microneedle ocular patch for effective treatment of fungal keratitis*. *International Journal of Pharmaceutics*, 2019. **572**: p. 118808.
148. Siepmann, J., R.A. Siegel, and M.J. Rathbone, *Fundamentals and Applications of Controlled Release Drug Delivery*. 2012, Springer, Boston, MA.
149. Houchin, M.L. and E.M. Topp, *Physical properties of PLGA films during polymer degradation*. *Journal of Applied Polymer Science*, 2009. **114**(5): p. 2848-2854.
150. Ding, D. and Q. Zhu, *Recent advances of PLGA micro/nanoparticles for the delivery of biomacromolecular therapeutics*. *Materials Science and Engineering: C*, 2018. **92**: p. 1041-1060.
151. Taylor, K.M. and M.E. Aulton, *Aulton's Pharmaceutics E-Book: The Design and Manufacture of Medicines*. 2021: Elsevier Health Sciences.
152. Mata, A., A.J. Fleischman, and S. Roy, *Characterization of polydimethylsiloxane (PDMS) properties for biomedical micro/nanosystems*. *Biomed Microdevices*, 2005. **7**(4): p. 281-93.
153. DOW, *SYLGARD™ 184 Silicone Elastomer , Technical data sheet*. 2017.
154. Finke, J.H., et al., *Coumarin 6 as a fluorescent model drug: How to identify properties of lipid colloidal drug delivery systems via fluorescence spectroscopy?* *European Journal of Lipid Science and Technology*, 2014. **116**(9): p. 1234-1246.
155. Vardanyan, R.S. and V.J. Hruby, *27 - Corticosteroids*, in *Synthesis of Essential Drugs*, R.S. Vardanyan and V.J. Hruby, Editors. 2006, Elsevier: Amsterdam. p. 349-363.

156. Solomon, S.D., et al., *Diabetic retinopathy: a position statement by the American Diabetes Association*. Diabetes care, 2017. **40**(3): p. 412-418.
157. Pan, Q., et al., *Corticosteroid-loaded biodegradable nanoparticles for prevention of corneal allograft rejection in rats*. Journal of Controlled Release, 2015. **201**: p. 32-40.
158. Adcock, I.M. and G. Caramori, *Cross-talk between pro-inflammatory transcription factors and glucocorticoids*. Immunol Cell Biol, 2001. **79**(4): p. 376-84.
159. Mogensen, T.H., et al., *Mechanisms of Dexamethasone-Mediated Inhibition of Toll-Like Receptor Signaling Induced by Neisseria meningitidis and Streptococcus pneumoniae*. Infection and Immunity, 2008. **76**(1): p. 189-197.
160. Djalilian, A.R., et al., *Inhibition of inflammatory cytokine production in human corneal cells by dexamethasone, but not cyclosporin*. Cornea, 2006. **25**(6): p. 709-714.
161. Information, N.C.f.B. *PubChem Compound Summary for CID 5743, Dexamethasone*. (2022); Available from: <https://pubchem.ncbi.nlm.nih.gov/compound/Dexamethasone>.
162. Formlabs. *Guide to Clear 3D Printing*. [cited 2022 Sep]; Available from: <https://formlabs.com/uk/blog/3d-printing-transparent-parts-techniques-for-finishing-clear-resin/>.
163. Krebs, J., *CAD. Basics*. 2017: Birkhauser.
164. Su, A. and S.J. Al'Aref, *Chapter 1 - History of 3D Printing*, in *3D Printing Applications in Cardiovascular Medicine*, S.J. Al'Aref, et al., Editors. 2018, Academic Press: Boston. p. 1-10.
165. Gabbrielli, R., I. Turner, and C.R. Bowen. *Development of modelling methods for materials to be used as bone substitutes*. in *Key Engineering Materials*. 2008. Trans Tech Publ.
166. Melchels, F.P.W., J. Feijen, and D.W. Grijpma, *A review on stereolithography and its applications in biomedical engineering*. Biomaterials, 2010. **31**(24): p. 6121-6130.
167. Gibson, I., et al., *Additive manufacturing technologies*. Vol. 17. 2021: Springer.
168. Mansour, S., M. Gilbert, and R. Hague, *A study of the impact of short-term ageing on the mechanical properties of a stereolithography resin*. Materials Science and Engineering: A, 2007. **447**(1-2): p. 277-284.
169. Mi, X., et al., *Toughness and its mechanisms in epoxy resins*. Progress in Materials Science, 2022. **130**: p. 100977.
170. Formlabs. *Guide to Stereolithography (SLA) 3D Printing*. [cited 2022 Sep]; Available from: <https://formlabs.com/eu/blog/ultimate-guide-to-stereolithography-sla-3d-printing/>.
171. Mapili, G., et al., *Laser-layered microfabrication of spatially patterned functionalized tissue-engineering scaffolds*. Journal of Biomedical Materials Research Part B: Applied Biomaterials: An Official Journal of The Society for Biomaterials, The Japanese Society for Biomaterials, and The Australian Society for Biomaterials and the Korean Society for Biomaterials, 2005. **75**(2): p. 414-424.

172. Arshady, R., *Preparation of biodegradable microspheres and microcapsules: 2. Polyactides and related polyesters*. Journal of Controlled Release, 1991. **17**(1): p. 1-21.
173. Arshady, R. and A. Ledwith, *Suspension polymerisation and its application to the preparation of polymer supports*. Reactive Polymers, Ion Exchangers, Sorbents, 1983. **1**(3): p. 159-174.
174. Blehn, G.F. and M.L. Ernsberger, *Polyvinyl Alcohol as an Emulsifying Agent*. Industrial & Engineering Chemistry, 1948. **40**(8): p. 1449-1453.
175. Jain, R.A., *The manufacturing techniques of various drug loaded biodegradable poly(lactide-co-glycolide) (PLGA) devices*. Biomaterials, 2000. **21**(23): p. 2475-2490.
176. Wu, X.S., *Synthesis, Characterization, Biodegradation, and Drug Delivery Application of Biodegradable Lactic/Glycolic Acid Polymers: Part III. Drug Delivery Application*. Artificial Cells, Blood Substitutes, and Biotechnology, 2004. **32**(4): p. 575-591.
177. Taha, A., et al., *Ultrasonic emulsification: An overview on the preparation of different emulsifiers-stabilized emulsions*. Trends in Food Science & Technology, 2020. **105**: p. 363-377.
178. Ruiz, E., et al., *Study of sonication parameters on PLA nanoparticles preparation by simple emulsion-evaporation solvent technique*. European Polymer Journal, 2022. **173**: p. 111307.
179. Franks, F., *Freeze-drying of bioproducts: putting principles into practice*. European Journal of Pharmaceutics and Biopharmaceutics, 1998. **45**(3): p. 221-229.
180. Abdelwahed, W., et al., *Freeze-drying of nanoparticles: Formulation, process and storage considerations*. Advanced Drug Delivery Reviews, 2006. **58**(15): p. 1688-1713.
181. Garcia-Amezquita, L.E., et al., *Freeze-drying: The Basic Process*, in *Encyclopedia of Food and Health*, B. Caballero, P.M. Finglas, and F. Toldrá, Editors. 2016, Academic Press: Oxford. p. 104-109.
182. Chung, N.-O., M.K. Lee, and J. Lee, *Mechanism of freeze-drying drug nanosuspensions*. International Journal of Pharmaceutics, 2012. **437**(1): p. 42-50.
183. Graham, J., *Biological centrifugation*. 2020: Garland Science.
184. Olatunde, A., M.S. Obidola, and H. Tijjani, *Chapter 3 - Centrifugation techniques*, in *Analytical Techniques in Biosciences*, C. Egbuna, et al., Editors. 2022, Academic Press. p. 43-58.
185. Tajarudin, H.A., M.I. Ahmad, and M.N. Ismail, *Centrifugation*, in *Unit Operation in Downstream Processing*. 2018, Penerbit Universiti Sains Malaysia.
186. Holtzhauer, M., *Centrifugation*, in *Basic Methods for the Biochemical Lab*, M. Holtzhauer, Editor. 2006, Springer Berlin Heidelberg: Berlin, Heidelberg. p. 161-180.
187. Beckman Coulter, I. [cited 2022 Sep]; Available from: <https://www.beckman.com/resources/technologies/centrifugation/principles/rotor-types>.

188. Akhtar, K., et al., *Scanning Electron Microscopy: Principle and Applications in Nanomaterials Characterization*, in *Handbook of Materials Characterization*, S.K. Sharma, Editor. 2018, Springer International Publishing: Cham. p. 113-145.
189. Vladár, A.E. and V.-D. Hodoroaba, *Chapter 2.1.1 - Characterization of nanoparticles by scanning electron microscopy*, in *Characterization of Nanoparticles*, V.-D. Hodoroaba, W.E.S. Unger, and A.G. Shard, Editors. 2020, Elsevier. p. 7-27.
190. Leong, S.S., et al., *Dynamic Light Scattering: Effective Sizing Technique for Characterization of Magnetic Nanoparticles*, in *Handbook of Materials Characterization*, S.K. Sharma, Editor. 2018, Springer International Publishing: Cham. p. 77-111.
191. Falke, S. and C. Betzel, *Dynamic Light Scattering (DLS)*, in *Radiation in Bioanalysis: Spectroscopic Techniques and Theoretical Methods*, A.S. Pereira, P. Tavares, and P. Limão-Vieira, Editors. 2019, Springer International Publishing: Cham. p. 173-193.
192. Bhattacharjee, S., *DLS and zeta potential – What they are and what they are not?* Journal of Controlled Release, 2016. **235**: p. 337-351.
193. Xia, Z., et al., *Surface Zeta Potential of ALD-Grown Metal-Oxide Films*. Langmuir, 2021. **37**(39): p. 11618-11624.
194. Selvamani, V., *Chapter 15 - Stability Studies on Nanomaterials Used in Drugs*, in *Characterization and Biology of Nanomaterials for Drug Delivery*, S.S. Mohapatra, et al., Editors. 2019, Elsevier. p. 425-444.
195. Lu, G.W. and P. Gao, *CHAPTER 3 - Emulsions and Microemulsions for Topical and Transdermal Drug Delivery*, in *Handbook of Non-Invasive Drug Delivery Systems*, V.S. Kulkarni, Editor. 2010, William Andrew Publishing: Boston. p. 59-94.
196. Höhne, G., W.F. Hemminger, and H.J. Flammersheim, *Differential Scanning Calorimetry / by Günther Höhne, Wolfgang F. Hemminger, H.-J. Flammersheim*. 2nd ed. 2003. ed. 2003, Berlin, Heidelberg: Springer Berlin Heidelberg.
197. Gill, P., T.T. Moghadam, and B. Ranjbar, *Differential scanning calorimetry techniques: applications in biology and nanoscience*. J Biomol Tech, 2010. **21**(4): p. 167-93.
198. Craig, D.Q.M. and M. Reading, *Thermal Analysis of Pharmaceuticals*. 2006, Baton Rouge: CRC Press.
199. Gumustas, M., et al., *Chapter 5 - Effect of Polymer-Based Nanoparticles on the Assay of Antimicrobial Drug Delivery Systems*, in *Multifunctional Systems for Combined Delivery, Biosensing and Diagnostics*, A.M. Grumezescu, Editor. 2017, Elsevier. p. 67-108.
200. Unruh, D.K. and T.Z. Forbes, *X-ray Diffraction Techniques*, in *Analytical Geomicrobiology: A Handbook of Instrumental Techniques*, D.S. Alessi, H. Veeramani, and J.P.L. Kenney, Editors. 2019, Cambridge University Press: Cambridge. p. 215-237.
201. Raval, N., et al., *Chapter 10 - Importance of Physicochemical Characterization of Nanoparticles in Pharmaceutical Product Development*, in *Basic Fundamentals of Drug Delivery*, R.K. Tekade, Editor. 2019, Academic Press. p. 369-400.

202. Dutta, A., *Chapter 4 - Fourier Transform Infrared Spectroscopy*, in *Spectroscopic Methods for Nanomaterials Characterization*, S. Thomas, et al., Editors. 2017, Elsevier. p. 73-93.
203. Titus, D., E. James Jebaseelan Samuel, and S.M. Roopan, *Chapter 12 - Nanoparticle characterization techniques*, in *Green Synthesis, Characterization and Applications of Nanoparticles*, A.K. Shukla and S. Irvani, Editors. 2019, Elsevier. p. 303-319.
204. Robards, K. and D. Ryan, *Chapter 5 - High performance liquid chromatography: Instrumentation and techniques*, in *Principles and Practice of Modern Chromatographic Methods (Second Edition)*, K. Robards and D. Ryan, Editors. 2022, Academic Press. p. 247-282.
205. Moldoveanu, S. and V. David, *Chapter 1 - Introductory information regarding HPLC*, in *Essentials in Modern HPLC Separations (Second Edition)*, S. Moldoveanu and V. David, Editors. 2022, Elsevier. p. 3-20.
206. LaCourse, M.E. and W.R. LaCourse, *Chapter 17 - General instrumentation in HPLC**, in *Liquid Chromatography (Second Edition)*, S. Fanali, et al., Editors. 2017, Elsevier. p. 417-429.
207. Lister, A.S., *7 - Validation of HPLC Methods in Pharmaceutical Analysis*, in *Separation Science and Technology*, S. Ahuja and M.W. Dong, Editors. 2005, Academic Press. p. 191-217.
208. Chen, Y., Z. Gao, and J.Z. Duan, *Chapter 13 - Dissolution Testing of Solid Products*, in *Developing Solid Oral Dosage Forms (Second Edition)*, Y. Qiu, et al., Editors. 2017, Academic Press: Boston. p. 355-380.
209. Adrianto, M.F., et al., *In vitro dissolution testing models of ocular implants for posterior segment drug delivery*. Drug Delivery and Translational Research, 2022. **12**(6): p. 1355-1375.
210. Gray, V.A. and T.W. Rosanske, *Chapter 18 - Dissolution*, in *Specification of Drug Substances and Products (Second Edition)*, C.M. Riley, T.W. Rosanske, and G. Reid, Editors. 2020, Elsevier. p. 481-503.
211. Ahearne, M., *4 - Mechanical testing of hydrogels*, in *The Mechanics of Hydrogels*, H. Li and V. Silberschmidt, Editors. 2022, Woodhead Publishing. p. 73-90.
212. Timmie Topoleski, L.D., et al., *3 - Fundamental principles of mechanical testing*, in *Mechanical Testing of Orthopaedic Implants*, E. Friis, Editor. 2017, Woodhead Publishing. p. 33-47.
213. Shrivastava, A., *3 - Plastic Properties and Testing*, in *Introduction to Plastics Engineering*, A. Shrivastava, Editor. 2018, William Andrew Publishing. p. 49-110.
214. Peacock, A.J. and A. Calhoun, *Solid State Properties of Polymers*, in *Polymer Science*, A.J. Peacock and A. Calhoun, Editors. 2006, Hanser. p. 137-170.
215. Chakraborty, B.C. and D. Ratna, *Chapter 6 - Experimental techniques and instruments for vibration damping*, in *Polymers for Vibration Damping Applications*, B.C. Chakraborty and D. Ratna, Editors. 2020, Elsevier. p. 281-325.
216. Cabrera-Pérez, M.Á., et al., *2 - Importance and applications of cell- and tissue-based in vitro models for drug permeability screening in early stages of drug development*, in *Concepts and Models for Drug Permeability Studies*, B. Sarmiento, Editor. 2016, Woodhead Publishing. p. 3-29.

217. Ng, S.F., et al., *A Comparative Study of Transmembrane Diffusion and Permeation of Ibuprofen across Synthetic Membranes Using Franz Diffusion Cells*. Pharmaceutics, 2010. **2**(2): p. 209-223.
218. PermeGear. *Franz Cell*. 2022; Available from: <https://permegear.com/franz-cells/>.
219. Uysal, O., et al., *Chapter 17 - Cell and Tissue Culture: The Base of Biotechnology*, in *Omics Technologies and Bio-Engineering*, D. Barh and V. Azevedo, Editors. 2018, Academic Press. p. 391-429.
220. Ligasová, A. and K. Koberna, *DNA Dyes—Highly Sensitive Reporters of Cell Quantification: Comparison with Other Cell Quantification Methods*. Molecules, 2021. **26**(18): p. 5515.
221. Augustine, R., et al., *Cellular uptake and retention of nanoparticles: Insights on particle properties and interaction with cellular components*. Materials Today Communications, 2020. **25**: p. 101692.
222. Rees, P., *Chapter 5 - Uptake and Toxicology of Nanoparticles*, in *Frontiers of Nanoscience*, H. Summers, Editor. 2013, Elsevier. p. 123-138.
223. Sun, R., et al., *Size-dependent cellular uptake and sustained drug release of PLGA particles*. Particuology, 2023. **73**: p. 1-7.
224. Hsiao, I.L., et al., *Quantification and visualization of cellular uptake of TiO₂ and Ag nanoparticles: comparison of different ICP-MS techniques*. Journal of Nanobiotechnology, 2016. **14**(1): p. 50.
225. Draize, J.H., G. Woodard, and H.O. Calvery, *Methods for the study of irritation and toxicity of substances applied topically to the skin and mucous membranes*. Journal of Pharmacology and Experimental Therapeutics, 1944. **82**(3): p. 377-390.
226. Baran, K.P. and S.C. Gad, *Eye Irritancy Testing*, in *Encyclopedia of Toxicology (Third Edition)*, P. Wexler, Editor. 2014, Academic Press: Oxford. p. 577-580.
227. Gad, S.C. and C.P. Chengelis, *CHAPTER 4 - Ocular Irritation Testing*, in *Acute Toxicology Testing (Second Edition)*, S.C. Gad and C.P. Chengelis, Editors. 1998, Academic Press: San Diego. p. 57-84.
228. Peiffer, R.L., L. Pohm-Thorsen, and K. Corcoran, *CHAPTER 19 - Models in Ophthalmology and Vision Research*, in *The Biology of the Laboratory Rabbit (Second Edition)*, P.J. Manning, D.H. Ringler, and C.E. Newcomer, Editors. 1994, Academic Press: San Diego. p. 409-433.
229. Zeiss, C.J., *Translational models of ocular disease*. Veterinary Ophthalmology, 2013. **16**(s1): p. 15-33.
230. Yadav, U.C.S. and K.V. Ramana, *Endotoxin-Induced Uveitis in Rodents*, in *Mouse Models of Innate Immunity: Methods and Protocols*, I.C. Allen, Editor. 2019, Springer New York: New York, NY. p. 161-168.
231. Rosenbaum, J.T., et al., *Endotoxin-induced uveitis in rats as a model for human disease*. Nature, 1980. **286**(5773): p. 611-613.
232. Johnson, A.R. and A.T. Procopio, *Low cost additive manufacturing of microneedle masters*. 3D Printing in Medicine, 2019. **5**(1): p. 2.
233. Indermun, S., et al., *Current advances in the fabrication of microneedles for transdermal delivery*. Journal of Controlled Release, 2014. **185**: p. 130-138.

234. Chen, J.-K., et al., *Using imprinting technology to fabricate three-dimensional devices from moulds of thermosetting polymer patterns*. Semiconductor science and technology, 2006. **21**(9): p. 1213.
235. Gittard, S.D., et al., *Fabrication of Polymer Microneedles Using a Two-Photon Polymerization and Micromolding Process*. Journal of Diabetes Science and Technology, 2009. **3**(2): p. 304-311.
236. Nejad, H.R., et al., *Low-cost and cleanroom-free fabrication of microneedles*. Microsystems & nanoengineering, 2018. **4**(1): p. 1-7.
237. Tang, T.O., et al., *Design and fabrication of transdermal drug delivery patch with milliprojections using material extrusion 3D printing*. Journal of Applied Polymer Science, 2020. **137**(23): p. 48777.
238. Choo, S., S. Jin, and J. Jung, *Fabricating High-Resolution and High-Dimensional Microneedle Mold through the Resolution Improvement of Stereolithography 3D Printing*. Pharmaceutics, 2022. **14**(4): p. 766.
239. Li, Y., et al., *Bioinspired Functional Surfaces Enabled by Multiscale Stereolithography*. Advanced Materials Technologies, 2019. **4**(5): p. 1800638.
240. Avcil, M. and A. Çelik, *Microneedles in Drug Delivery: Progress and Challenges*. Micromachines, 2021. **12**(11): p. 1321.
241. Gill, H.S., et al., *Effect of microneedle design on pain in human volunteers*. The Clinical journal of pain, 2008. **24**(7): p. 585-594.
242. Davis, S.P., et al., *Insertion of microneedles into skin: measurement and prediction of insertion force and needle fracture force*. Journal of Biomechanics, 2004. **37**(8): p. 1155-1163.
243. Bodhale, D.W., A. Nisar, and N. Afzulpurkar, *Structural and microfluidic analysis of hollow side-open polymeric microneedles for transdermal drug delivery applications*. Microfluidics and Nanofluidics, 2010. **8**(3): p. 373-392.
244. Chang, K.-T., et al., *Optimal design and fabrication of a microneedle arrays patch*. Journal of Manufacturing Processes, 2020. **54**: p. 274-285.
245. Hartman, R.R. and U.B. Kompella, *Intravitreal, Subretinal, and Suprachoroidal Injections: Evolution of Microneedles for Drug Delivery*. J Ocul Pharmacol Ther, 2018. **34**(1-2): p. 141-153.
246. El-Sayed, N., L. Vaut, and M. Schneider, *Customized fast-separable microneedles prepared with the aid of 3D printing for nanoparticle delivery*. European Journal of Pharmaceutics and Biopharmaceutics, 2020. **154**: p. 166-174.
247. Pouran, H.M., *Engineered Nanomaterials in the Environment, their Potential Fate and Behaviour and Emerging Techniques to Measure Them*, in *Handbook of Environmental Materials Management*, C.M. Hussain, Editor. 2018, Springer International Publishing: Cham. p. 1-15.
248. Bribiesca, E., *An easy measure of compactness for 2D and 3D shapes*. Pattern Recognition, 2008. **41**(2): p. 543-554.
249. Hanon, M.M., L. Zsidai, and Q. Ma, *Accuracy investigation of 3D printed PLA with various process parameters and different colors*. Materials Today: Proceedings, 2021. **42**: p. 3089-3096.

250. Makvandi, P., et al., *Engineering Microneedle Patches for Improved Penetration: Analysis, Skin Models and Factors Affecting Needle Insertion*. Nano-Micro Letters, 2021. **13**(1): p. 93.
251. Verbaan, F.J., et al., *Improved piercing of microneedle arrays in dermatomed human skin by an impact insertion method*. Journal of Controlled Release, 2008. **128**(1): p. 80-88.
252. Römgens, A.M., et al., *Monitoring the penetration process of single microneedles with varying tip diameters*. Journal of the Mechanical Behavior of Biomedical Materials, 2014. **40**: p. 397-405.
253. Li, Y., et al., *Dissolving Microneedle Arrays with Optimized Needle Geometry for Transcutaneous Immunization*. European Journal of Pharmaceutical Sciences, 2020. **151**: p. 105361.
254. Park, K., et al., *Formulation composition, manufacturing process, and characterization of poly(lactide-co-glycolide) microparticles*. Journal of Controlled Release, 2021. **329**: p. 1150-1161.
255. Tawfik, E.A., et al., *In vitro and in vivo biological assessment of dual drug-loaded coaxial nanofibers for the treatment of corneal abrasion*. International Journal of Pharmaceutics, 2021. **604**: p. 120732.
256. Astete, C.E. and C.M. Sabliov, *Synthesis and characterization of PLGA nanoparticles*. J Biomater Sci Polym Ed, 2006. **17**(3): p. 247-89.
257. Galeska, I., et al., *Controlled release of dexamethasone from PLGA microspheres embedded within polyacid-containing PVA hydrogels*. The AAPS journal, 2005. **7**(1): p. E231-E240.
258. Rençber, S., F. Aydın Köse, and S.Y. Karavana, *Dexamethasone loaded PLGA nanoparticles for potential local treatment of oral precancerous lesions*. Pharmaceutical Development and Technology, 2020. **25**(2): p. 149-158.
259. Hickey, T., et al., *Dexamethasone/PLGA microspheres for continuous delivery of an anti-inflammatory drug for implantable medical devices*. Biomaterials, 2002. **23**(7): p. 1649-1656.
260. Shim, Y.-B., et al., *Fabrication of hollow porous PLGA microspheres using sucrose for controlled dual delivery of dexamethasone and BMP2*. Journal of Industrial and Engineering Chemistry, 2016. **37**: p. 101-106.
261. Gasmi, H., et al., *Towards a better understanding of the different release phases from PLGA microparticles: Dexamethasone-loaded systems*. International Journal of Pharmaceutics, 2016. **514**(1): p. 189-199.
262. Stefani, R.M., et al., *Sustained low-dose dexamethasone delivery via a PLGA microsphere-embedded agarose implant for enhanced osteochondral repair*. Acta Biomaterialia, 2020. **102**: p. 326-340.
263. Dawes, G.J.S., et al., *Size effect of PLGA spheres on drug loading efficiency and release profiles*. Journal of Materials Science: Materials in Medicine, 2009. **20**(5): p. 1089-1094.
264. Wang, Y., B. Gu, and D.J. Burgess, *Microspheres Prepared with PLGA Blends for Delivery of Dexamethasone for Implantable Medical Devices*. Pharmaceutical Research, 2014. **31**(2): p. 373-381.

265. Dawes, G.J.S., et al., *Release of PLGA-encapsulated dexamethasone from microsphere loaded porous surfaces*. Journal of Materials Science: Materials in Medicine, 2010. **21**(1): p. 215-221.
266. Gu, B. and D.J. Burgess, *Prediction of dexamethasone release from PLGA microspheres prepared with polymer blends using a design of experiment approach*. Int J Pharm, 2015. **495**(1): p. 393-403.
267. Gu, B., Y. Wang, and D.J. Burgess, *In vitro and in vivo performance of dexamethasone loaded PLGA microspheres prepared using polymer blends*. International Journal of Pharmaceutics, 2015. **496**(2): p. 534-540.
268. Moosavi, S.M., *Linearity of Calibration Curves for Analytical Methods: A Review of Criteria for Assessment of Method Reliability*. 2018: IntechOpen.
269. Gavet, O. and J. Pines, *Progressive activation of CyclinB1-Cdk1 coordinates entry to mitosis*. Developmental cell, 2010. **18**(4): p. 533-543.
270. Ansari, N., et al., *Chapter 13 - Quantitative 3D Cell-Based Assay Performed with Cellular Spheroids and Fluorescence Microscopy*, in *Methods in Cell Biology*, P.M. Conn, Editor. 2013, Academic Press. p. 295-309.
271. United States Pharmacopeial Convention, *The United States pharmacopeia: USP43 The National formulary: NF38*. 2020: United States Pharmacopeial Convention, Rockville, MD.
272. Wu, J., et al., *A facile strategy for controlling porous PLGA microspheres via o/w emulsion method*. Journal of Polymer Research, 2022. **29**(12): p. 508.
273. Sharifi, F., et al., *Continuous in-line homogenization process for scale-up production of naltrexone-loaded PLGA microparticles*. Journal of Controlled Release, 2020. **325**: p. 347-358.
274. Win, K.Y. and S.S. Feng, *Effects of particle size and surface coating on cellular uptake of polymeric nanoparticles for oral delivery of anticancer drugs*. Biomaterials, 2005. **26**(15): p. 2713-22.
275. Govender, T., et al., *PLGA nanoparticles prepared by nanoprecipitation: drug loading and release studies of a water soluble drug*. Journal of Controlled Release, 1999. **57**(2): p. 171-185.
276. Kwon, H.-Y., et al., *Preparation of PLGA nanoparticles containing estrogen by emulsification-diffusion method*. Colloids and Surfaces A: Physicochemical and Engineering Aspects, 2001. **182**(1): p. 123-130.
277. Sigma-Aldrich. *Dexamethasone (D6645) - Datasheet*. Available from: <https://www.sigmaaldrich.com/deepweb/assets/sigmaaldrich/product/documents/389/294/d6645dat.pdf>.
278. Orna, R.M. and M.W. Dong, *2 - Key Concepts of HPLC in Pharmaceutical Analysis*, in *Separation Science and Technology*, S. Ahuja and M.W. Dong, Editors. 2005, Academic Press. p. 19-45.
279. Wang, Q., et al., *Injectable PLGA based colloidal gels for zero-order dexamethasone release in cranial defects*. Biomaterials, 2010. **31**(18): p. 4980-4986.
280. Snyder, L.R., *Classification of the solvent properties of common liquids*. Journal of Chromatography A, 1974. **92**(2): p. 223-230.

281. online, D. *Dexamethasone*, DB01234. [cited 2022 Sep]; Available from: <https://go.drugbank.com/drugs/DB01234>.
282. Siepmann, J. and F. Siepmann, *Microparticles used as drug delivery systems*, in *Smart colloidal materials*. 2006, Springer. p. 15-21.
283. Sahoo, S.K., et al., *Residual polyvinyl alcohol associated with poly (d,l-lactide-co-glycolide) nanoparticles affects their physical properties and cellular uptake*. *Journal of Controlled Release*, 2002. **82**(1): p. 105-114.
284. Long, J., et al., *Controlled release of dexamethasone from poly(vinyl alcohol) hydrogel*. *Pharmaceutical Development and Technology*, 2019. **24**(7): p. 839-848.
285. Singh, G., et al., *Recent biomedical applications and patents on biodegradable polymer-PLGA*. *Int J Pharmacol Pharm Sci*, 2014. **1**(2): p. 30-42.
286. Buosi, F.S., et al., *Resveratrol encapsulation in high molecular weight chitosan-based nanogels for applications in ocular treatments: Impact on human ARPE-19 culture cells*. *International Journal of Biological Macromolecules*, 2020. **165**: p. 804-821.
287. Luthra, S., et al., *Toxicity of Dexamethasone on Neurosensory Retinal Cells*. *Investigative Ophthalmology & Visual Science*, 2005. **46**(13): p. 428-428.
288. Xiong, S., et al., *Size influences the cytotoxicity of poly (lactic-co-glycolic acid) (PLGA) and titanium dioxide (TiO₂) nanoparticles*. *Arch Toxicol*, 2013. **87**(6): p. 1075-86.
289. Nel, A., et al., *Toxic Potential of Materials at the Nanolevel*. *Science*, 2006. **311**(5761): p. 622-627.
290. Foster, K.A., M. Yazdanian, and K.L. Audus, *Microparticulate uptake mechanisms of in-vitro cell culture models of the respiratory epithelium*. *Journal of pharmacy and pharmacology*, 2001. **53**(1): p. 57-66.
291. Ainscough, S.L., et al., *Discovery and characterization of IGFBP-mediated endocytosis in the human retinal pigment epithelial cell line ARPE-19*. *Experimental Eye Research*, 2009. **89**(5): p. 629-637.
292. Irschick, E.U., et al., *Phagocytosis of Human Retinal Pigment Epithelial Cells: Evidence of a Diurnal Rhythm, Involvement of the Cytoskeleton and Interference of Antiviral Drugs*. *Ophthalmic Research*, 2006. **38**(3): p. 164-174.
293. Thakur Singh, R.R., et al., *Minimally invasive microneedles for ocular drug delivery*. *Expert Opin Drug Deliv*, 2017. **14**(4): p. 525-537.
294. Ambati, J. and A.P. Adamis, *Transscleral drug delivery to the retina and choroid*. *Progress in retinal and eye research*, 2002. **21**(2): p. 145-151.
295. Srikantha, N., et al., *Influence of molecular shape, conformability, net surface charge, and tissue interaction on transscleral macromolecular diffusion*. *Experimental Eye Research*, 2012. **102**: p. 85-92.
296. Kim, S.H., et al., *Transport barriers in transscleral drug delivery for retinal diseases*. *Ophthalmic Res*, 2007. **39**(5): p. 244-54.
297. Swetledge, S., et al., *Stability and ocular biodistribution of topically administered PLGA nanoparticles*. *Scientific Reports*, 2021. **11**(1): p. 12270.
298. Uğurlu, N., et al., *Transscleral Delivery of Bevacizumab-Loaded Chitosan Nanoparticles*. *J Biomed Nanotechnol*, 2019. **15**(4): p. 830-838.

299. Fitaihi, R.A., et al., *Role of chitosan on controlling the characteristics and antifungal activity of bioadhesive fluconazole vaginal tablets*. Saudi Pharmaceutical Journal, 2018. **26**(2): p. 151-161.
300. Samtani, M.N. and W.J. Jusko, *Quantification of dexamethasone and corticosterone in rat biofluids and fetal tissue using highly sensitive analytical methods: assay validation and application to a pharmacokinetic study*. Biomed Chromatogr, 2007. **21**(6): p. 585-97.
301. Mun, E.A., et al., *On the Barrier Properties of the Cornea: A Microscopy Study of the Penetration of Fluorescently Labeled Nanoparticles, Polymers, and Sodium Fluorescein*. Molecular Pharmaceutics, 2014. **11**(10): p. 3556-3564.
302. Shafaie, S., et al., *Diffusion through the ex vivo vitreal body – Bovine, porcine, and ovine models are poor surrogates for the human vitreous*. International Journal of Pharmaceutics, 2018. **550**(1): p. 207-215.
303. Bazmi, E., et al., *Quantitative analysis of benzodiazepines in vitreous humor by high-performance liquid chromatography*. SAGE Open Med, 2016. **4**: p. 2050312116666243.
304. Lilleby Helberg, R.M., et al., *PVA/PVP blend polymer matrix for hosting carriers in facilitated transport membranes: Synergistic enhancement of CO₂ separation performance*. Green Energy & Environment, 2020. **5**(1): p. 59-68.
305. Teodorescu, M., M. Bercea, and S. Morariu, *Biomaterials of PVA and PVP in medical and pharmaceutical applications: Perspectives and challenges*. Biotechnology Advances, 2019. **37**(1): p. 109-131.
306. Banchemo, M., et al., *Supercritical solvent impregnation of piroxicam on PVP at various polymer molecular weights*. The Journal of Supercritical Fluids, 2009. **49**(2): p. 271-278.
307. Teodorescu, M., et al., *Viscoelastic and structural properties of poly (vinyl alcohol)/poly (vinylpyrrolidone) hydrogels*. RSC advances, 2016. **6**(46): p. 39718-39727.
308. Solomonidou, D., et al., *Effect of carbomer concentration and degree of neutralization on the mucoadhesive properties of polymer films*. Journal of Biomaterials Science, Polymer Edition, 2001. **12**(11): p. 1191-1205.
309. Ludwig, A., *The use of mucoadhesive polymers in ocular drug delivery*. Adv Drug Deliv Rev, 2005. **57**(11): p. 1595-639.
310. Salamat-Miller, N., M. Chittchang, and T.P. Johnston, *The use of mucoadhesive polymers in buccal drug delivery*. Advanced Drug Delivery Reviews, 2005. **57**(11): p. 1666-1691.
311. Suknuntha, K., et al., *Characterization of muco- and bioadhesive properties of chitosan, PVP, and chitosan/PVP blends and release of amoxicillin from alginate beads coated with chitosan/PVP*. Drug development and industrial pharmacy, 2011. **37**: p. 408-18.
312. Nikolin, B., et al., *High performance liquid chromatography in pharmaceutical analyses*. Biomolecules and Biomedicine, 2004. **4**(2): p. 5-9.
313. Bicking, M.K.L., *Integration errors in chromatographic analysis, Part I: Peaks of approximately equal size*. LC-GC North America, 2006. **24**: p. 402+.

314. Amrite, A.C. and U.B. Kompella, *Size-dependent disposition of nanoparticles and microparticles following subconjunctival administration*. J Pharm Pharmacol, 2005. **57**(12): p. 1555-63.
315. Wilson, S.L., M. Ahearne, and A. Hopkinson, *An overview of current techniques for ocular toxicity testing*. Toxicology, 2015. **327**: p. 32-46.
316. Shi, H., et al., *A Rapid Corneal Healing Microneedle for Efficient Ocular Drug Delivery*. Small, 2022. **18**(4): p. 2104657.
317. Csukas, S., et al., *Time course of rabbit ocular inflammatory response and mediator release after intravitreal endotoxin*. Investigative Ophthalmology & Visual Science, 1990. **31**(2): p. 382-387.
318. Rodríguez Villanueva, J., L. Rodríguez Villanueva, and M. Guzmán Navarro, *Pharmaceutical technology can turn a traditional drug, dexamethasone into a first-line ocular medicine. A global perspective and future trends*. International Journal of Pharmaceutics, 2017. **516**(1): p. 342-351.
319. Box, J.A., J.K. Sugden, and N.M.T. Younis, *An Examination of the Sterilization of Eye Drops Using Ultra-Violet Light*. 1984. **38**(3): p. 115-121.
320. Falahee, K.J., et al., *Eye Irritation Testing: an Assessment of Methods and Guidelines for Testing Materials for Eye Irritancy*. Office of Pesticides and Toxic Substances., U.S.E.P. Agency, Editor. October 1981: Washington DC-20460.
321. Kay, J.H. and J.C. Calandra, *Interpretation of eye irritation tests*. J. Soc. Cosmet. Chem., 1962. **13**: p. 281-289.
322. Verma, M.J., et al., *Endotoxin-Induced Uveitis is Partially Inhibited by Anti-IL-8 Antibody Treatment*. Investigative Ophthalmology & Visual Science, 1999. **40**(11): p. 2465-2470.
323. Gupta, S.K., et al., *The Anti-inflammatory Effects of Curcuma longa and Berberis aristata in Endotoxin-Induced Uveitis in Rabbits*. Investigative Ophthalmology & Visual Science, 2008. **49**(9): p. 4036-4040.
324. Ruiz-Moreno, J.M., B. Thillaye, and Y. de Kozak, *Retino-choroidal changes in endotoxin-induced uveitis in the rat*. Ophthalmic Res, 1992. **24**(3): p. 162-8.
325. Stastna, M., et al., *Analysis of protein composition of rabbit aqueous humor following two different cataract surgery incision procedures using 2-DE and LC-MS/MS*. Proteome Science, 2011. **9**(1): p. 8.
326. Lo, C.-A., et al., *Quantification of Protein Levels in Single Living Cells*. Cell Reports, 2015. **13**(11): p. 2634-2644.
327. Rossi, S., et al., *Protection from endotoxic uveitis by intravitreal Resolvin D1: involvement of lymphocytes, miRNAs, ubiquitin-proteasome, and M1/M2 macrophages*. Mediators Inflamm, 2015. **2015**: p. 149381.
328. Towbin, H., *Origins of Protein Blotting*, in *Methods in Molecular Biology*. 2009, Humana Press. p. 1-3.
329. Ansari, M.A., et al., *Sinapic acid mitigates gentamicin-induced nephrotoxicity and associated oxidative/nitrosative stress, apoptosis, and inflammation in rats*. Life Sciences, 2016. **165**: p. 1-8.
330. Alshamsan, A., et al., *Treatment of endotoxin-induced uveitis by topical application of cyclosporine a-loaded PolyGel in rabbit eyes*. Int J Pharm, 2019. **569**: p. 118573.

331. Barathi, A., M.K. Thu, and R.W. Beuerman, *Dimensional growth of the rabbit eye*. Cells Tissues Organs, 2002. **171**(4): p. 276-85.
332. Luo, C., et al., *Recent Advances of Intraocular Lens Materials and Surface Modification in Cataract Surgery*. Frontiers in Bioengineering and Biotechnology, 2022. **10**.
333. Kennah, H.E., 2nd, et al., *An objective procedure for quantitating eye irritation based upon changes of corneal thickness*. Fundam Appl Toxicol, 1989. **12**(2): p. 258-68.
334. Coursey, T.G., et al., *Dexamethasone nanowafer as an effective therapy for dry eye disease*. J Control Release, 2015. **213**: p. 168-174.
335. Forrester, J.V., et al., *Chapter 6 - General and ocular pharmacology*, in *The Eye (Fourth Edition)*, J.V. Forrester, et al., Editors. 2016, W.B. Saunders. p. 338-369.e1.
336. Ehrenberg, M., et al., *Combining Sodium Hyaluronate and Polyvinylpyrrolidone Therapies for the Rabbit Cornea: A New Approach to Relief of the Human Dry Eye Syndrome*. Current Eye Research, 2015. **40**(9): p. 913-922.
337. Gupta, C. and A. Chauhan, *Ophthalmic delivery of cyclosporine A by punctal plugs*. Journal of Controlled Release, 2011a. **150**(1): p. 70-76.
338. Liu, X.F., et al., *Curcumin, A Potential Therapeutic Candidate for Anterior Segment Eye Diseases: A Review*. Front Pharmacol, 2017. **8**: p. 66.
339. Yu, X., et al., *High drug payload nanoparticles formed from dexamethasone-peptide conjugates for the treatment of endotoxin-induced uveitis in rabbit*. Int J Nanomedicine, 2019. **14**: p. 591-603.
340. Anfuso, C.D., et al., *Gabapentin Attenuates Ocular Inflammation: In vitro and In vivo Studies*. Front Pharmacol, 2017. **8**: p. 173.
341. Gupta, S.K., et al., *Prevention of endotoxin-induced uveitis in rabbits by Triphala, an Ayurvedic formulation*. 2011b. **1**(2): p. 20-23.
342. Srivastava, S.K. and K.V. Ramana, *Focus on molecules: nuclear factor-kappaB*. Exp Eye Res, 2009. **88**(1): p. 2-3.
343. Kumar, A., et al., *Nuclear factor- κ B: its role in health and disease*. Journal of Molecular Medicine, 2004. **82**(7): p. 434-448.
344. Varfolomeev, E. and D. Vucic, *Intracellular regulation of TNF activity in health and disease*. Cytokine, 2018. **101**: p. 26-32.
345. Oeckinghaus, A. and S. Ghosh, *The NF-kappaB family of transcription factors and its regulation*. Cold Spring Harb Perspect Biol, 2009. **1**(4): p. a000034.
346. Li, Q. and I.M. Verma, *NF-kappaB regulation in the immune system*. Nat Rev Immunol, 2002. **2**(10): p. 725-34.
347. Barcia, E., et al., *Downregulation of endotoxin-induced uveitis by intravitreal injection of polylactic-glycolic acid (PLGA) microspheres loaded with dexamethasone*. Exp Eye Res, 2009. **89**(2): p. 238-45.
348. Serif, N., et al., *Evaluation of Neopterin Levels in an Endotoxin-Induced Experimental Uveitis Model*. Semin Ophthalmol, 2016. **31**(3): p. 256-60.
349. Altinsoy, A., et al., *A cannabinoid ligand, anandamide, exacerbates endotoxin-induced uveitis in rabbits*. J Ocul Pharmacol Ther, 2011. **27**(6): p. 545-52.

- 350. Alam, F., et al., *Prospects for Additive Manufacturing in Contact Lens Devices*. Advanced Engineering Materials, 2021. **23**(1): p. 2000941.
- 351. Jung, J.H., et al., *Collagenase injection into the suprachoroidal space of the eye to expand drug delivery coverage and increase posterior drug targeting*. Experimental Eye Research, 2019. **189**: p. 107824.